Development of new bioactive systems for regenerative medicine using 3D printing and microfluidic technologies

by

Ana Mora Boza

A dissertation submitted by in partial fulfillment of the requirements for the degree of Doctor of Philosophy in

Materials Science and Engineering

Universidad Carlos III de Madrid

Advisors:

Julio San Román del Barrio
Blanca Vázquez Lasa

Tutor:

Diego Velasco Bayón

May 2020

To my parents, my sister and all the women of my life.

ACKNOWLEDGMENTS/AGRADECIMIENTOS

Si me llegan a contar hace 4 años en qué condiciones iba a escribir estos agradecimientos no lo hubiera creído… Pero aquí estamos, Paula, Raquel y yo confinadas en Guzmán el Bueno por una pandemia mundial. Es un final muy épico para un camino que ha sido duro y gratificante a partes iguales. Tengo que empezar agradeciendo el esfuerzo, dedicación y cariño de mis directores de tesis. Julio, gracias por darme la oportunidad de realizar mi tesis con vosotros. Gracias por transmitirme tu pasión por este trabajo, enseñarme que hay que tener siempre fe, y que las cosas fáciles no son tan gratificantes como los grandes retos. Pero sobre todo, gracias por enseñarme que este trabajo es compatible con la alegría, la empatía y la generosidad. Blanca, gracias por tu fuerza y tu dedicación constante, por estar siempre al teléfono y cuidarme en todos los sentidos. Todo se hace más fácil con personas como vosotros al mando. Gracias también a mi tutor, Diego, por su colaboración y apoyo durante estos años.

Gracias al grupo de Biomateriales del ICTP: Curra, Rosana, Raquel, Dani, Gloria, Eva, Luis Rojo y todos los demás compañeros. Gracias a Marisa por su ayuda y predisposición. Muchos de estos experimentos no hubieran salido adelante sin tu apoyo. Gracias LuisGar por ayudarnos siempre que lo necesitábamos (después de protestar un poco) y por sacarnos del pozo cuando estamos agobiadas. No sé cuántas cañas tendrás ya apuntadas en la lista.

María, no puedo imaginar este recorrido sin ti. Hubiera sido, como mínimo, mucho menos feliz. Te doy las gracias por tu paciencia, tu generosidad, tu empatía, tu alegría, tus consejos (científicos y no) y tu risa. Gracias de corazón, siempre. Y gracias a la vida por ponerte en mi camino. La seguiremos viviendo juntas.

Agradecer a la Residencia de Estudiantes y a toda la gente maravillosa que trabaja allí donde pasé mis dos primeros años en Madrid. Siempre me sentiré afortunada por haber tenido el privilegio de vivir en un sitio tan mágico. Gracias a Araceli, Marian, Aycardo, José Luis, Marcelo… Gracias infinitas a Florín, por sus cafés especiales llenos de cariño y sus palabras bonitas. Gracias a los compañeros y amigos, que esta experiencia me permitió conocer y con los que aprendí a disfrutar de Madrid: Pilar, Arantxa, Myriam, María Elena, Alberto, Sergio, Paula... Gracias a mi vecino de primer año, Paco, por hacerme sentir que las cosas siempre son más sencillas de lo que yo creo. Gracias a Carmen por su cariño incondicional y tener siempre un hueco para un audio infinito preocupándose por mí. Gracias a Miguel por sus chistes malos, siempre seré tu mayor fan. Sois familia para mí. Gracias a Miguel Alirangues por sentirse siempre tan orgulloso de mí. Gracias a mi mejor amigo, Mariano, por cogerme de la mano. Gracias a Juan por los bambús, por su cariño y por esas tardes divertidas de estilismo. Gracias por soportar mis riñas y devolvérmelas con amor. Y, por último, no tengo páginas suficientes para agradecerles a Andriu y Ra su amor incondicional y su fortaleza. Me habéis hecho la vida más bonita y fácil trayéndome una magia y

sororidad que nunca hubiera esperado. Gracias Ra, por ser torbellino y paz a la vez; por ser hogar en Madrid. Gracias Andriu por peinarme, acompañarme y guiarme. Seguiremos haciéndonos felices, gracias infinitas.

Gracias por supuesto a mi tropa de La Caixa. Siempre recordaré con cariño esas semanas de retiro en las que me hacíais reír tan tan fuerte. Gracias a Patxi, Laura, Andrea, Jorge, Pablo, las Marías, Dana, Jesús, Alberto. Especialmente a Ander y Simón por sus memes personalizados que me hacen tan feliz. Gracias a Luis, mi trapero favorito. Y por supuesto, gracias infinitas a Juanma y a mi flamenco preferido, Víctor, sois muy especiales para mí. Gracias por intentar siempre hacerme feliz.

I would like to thank Prof. Aránzazu del Campo for gave me the opportunity to join her group for some months. Thank you to the Dynamic Biomaterials group of the INM (Julieta, Essak, Mitchell, Roshna, Jun…) for their help and kindness. Thanks always to Gosia. It was a pleasure to work and enjoy my time with you and your family in Saarbrücken and the other many cities we visited together. Thank you for your kindness and love. Looking forward to meeting Anna and having fun with Zosia. Thank you to stop in Espartinas to meet my family, you will be always in my heart. En Saarbrücken tengo que hacer otra parada y darle gracias infinitas a mi querido clan sevillano: Alberto, David, María, Lola y Manuel. Gracias por vuestra acogida, descubrirme el mejor *pulled pork* del universo, los arroces de Alberto, los almuerzos con el grupo de *Structure Formation*, los mercados de navidad, las pizzas *light*, los viernes de nachos, y los paseos por *Wild Park*. Gracias a Lola, Manuel y Alberto por ese fin de semana de kilómetros en coche con nieve para descubrir castillos. Gracias a Lola por superar conmigo la barrera espaciotemporal del Saarland. Y gracias a Manuel, David y María por cumplir mi sueño de ver *puffins*.

I am profoundly grateful to Prof. Andrés García for the amazing experience I enjoyed at Georgia Tech, and for his dedication and motivation. Thank you for giving me the opportunity to join your group and remembering me what I like the most of this work. Thank you to the group: Becky, for her patience and kindness; Woojin, for his help, warm welcome and funny plans; Elijah, for his nice words, English lessons and teaching me how to pronounce "phytic acid" correctly; Adriana, for her *alegría*, music, dances and big smiles; Pranav, Marc, Michael, Karen, Juan…Thank you so much! And of course, Lina, mi ángel de la guardia en Atlanta. Gracias por tu generosidad, por tu ayuda y por regalarme esta maravillosa familia colombiana. ¡No te vayas nunca de mi lado, tía! Gracias infinitas, chicos, por hacer de mi estancia en Atlanta una experiencia que superó infinitamente mis expectativas. Gracias Lina, Oliver, Jorge, Mónica y Andrés por vuestra ayuda, predisposición y generosidad, por los miércoles de pola, las noches de rumba y vuestra cálida compañía. Gracias Andrés por recordarme lo mucho que me gusta patinar y por llevarme a escuchar música en directo.

Para vosotros no tengo palabras porque sabéis perfectamente lo que significáis para mi después de casi diez años de amistad. Gracias por soportarme, por enseñarme tanto y por quererme tal y como soy. No creo que vuelva a vivir una época más feliz que el año que viví con mis tres mejores amigas. Gracias Maca, Carmen y Paula por hacerlo todo tan divertido y especial. Gracias Pablo, por tu humor y por tu amor incondicional. Gracias Maca por dejarme re-descubrirte y acompañarte. Gracias Carmen por las noches de peli y pizza. Gracias Pauli, por todo, siempre. Por estar a mi (de mi) lado y crecer juntas. Sabes que eres una hermana para mí. No hay mejor regalo que me haya podido dar la tesis que vuestra compañía estos años. Me siento muy afortunada por haberos tenido tan cerca. Y gracias al resto del *Team* por supuesto: Juan Juin, Joseju y Andrés, uno de los mayores regalos que me ha dado la vida.

Viajo ahora a Sevilla. Muchas gracias a mis amigos del ICMS, que me acogieron con mucho amor y confianza a pesar de mi juventud. Gracias Ana Gómez, María, Ana García, y Manuel por vuestro apoyo y amistad. Gracias María por hacerme las cosas más fáciles con tus consejos y tu confianza, por nuestras meriendas de máquina expendedora y tu cariño incondicional. Y a ti Manuel, nunca supe muy bien como agradecerte todo, nada hubiera sido lo mismo sin ti. Gracias también al grupo de *Sincaf* por iniciarme en el mundo de la investigación y por impulsarme para llegar hasta aquí.

Gracias a mi adorable "Chupipandi" (Irene, Alba, Carmen, Isa, Chary, Maca, Jesús) por vuestro cariño y apoyo todos estos años. Gracias por ficharme hace trece años y hacerme reír tanto. A mis niñas de Espartinas (Irene, Lorena, Maru y Cristina) por vuestro amor incondicional todos estos años, por sacar un rato para verme cada vez que visitaba mi casa, y no dejar que esto se apague. Os he necesitado mucho durante este tiempo en la distancia. Gracias a todas por estar ahí siempre.

Gracias a Javier por apoyarme siempre en lo que me hiciera feliz. Este trabajo también es tuyo.

Y por último, y muy importante, gracias a mi familia. Gracias a mis tíos, mis primos, mi abuela, mis gatas. Gracias por dedicarme tiempo cada vez que bajaba desde Madrid. Gracias infinitas a mis padres, por enseñarme el valor del esfuerzo, la constancia, la paciencia y el trabajo. Gracias por no decirme nunca que no era capaz de hacer algo, por confiar en mi ciegamente y entender lo feliz que me hace mi trabajo, aunque eso signifique tenernos lejos. Gracias por darme la mejor herencia del mundo: mi hermana y el saber valorar lo que uno tiene. Gracias Laura, por ser el ejemplo a seguir de mi vida. Os quiero muchísimo. Este trabajo os pertenece, sin vosotros nunca hubiera sido posible.

PUBLISHED AND SUBMITTED CONTENT

This work is presented for consideration as a Doctoral Thesis as a compendium of the following publications

1. **Glycerylphytate compounds with tunable ion affinity and osteogenic properties.**
   Ana Mora-Boza, María Luisa López-Donaire, Laura Saldaña, Nuria Vilaboa, Blanca Vázquez-Lasa, Julio San Román. Scientific Reports 9, Article number: 11491 (2019).
   DOI: 10.1038/s41598-019-48015-5.
   - This item is wholly included in this thesis in Chapter 2 and partly reproduced in Chapter 1.
   - As co-author of this publication together with Dr. María Luisa López-Donaire, we conducted the physicochemical and biological characterization of GPhy derivatives, except the experiments of differential gene expression by RT-qPCR that were carried out in collaboration with the Hospital Universitario La Paz-IdiPAZ. I also contributed to the analysis and discussion of the results and wrote the main draft manuscript text.
   - Whenever material from this source is included in this thesis, it is singled out with typographic means and an explicit reference.

2. **Glycerylphytate crosslinker as a potential osteoinductor of chitosan-based systems for guided bone regeneration.**
   Ana Mora-Boza, Luis García-Fernández, Filipe A. Barbosa, Ana Leite Oliveira, Blanca Vázquez-Lasa, Julio San Román. Carbohydrate Polymers, Volume 241, 116269 (2020).
   DOI: 10.1016/j.carbpol.2020.116269.
   - This item is wholly included in this thesis in Chapter 3 and partly reproduced in Chapter 1.
   - As the first author of this publication I conducted all the physicochemical and biological experiments. I also contributed to the analysis and discussion of the results and wrote the main draft manuscript text.
   - Whenever material from this source is included in this thesis, it is singled out with typographic means and an explicit reference.

3. **Glycerylphytate as an ionic crosslinker for 3D printing of multi-layered scaffolds with improved shape fidelity and biological features.**
   Ana Mora-Boza, Małgorzata K. Włodarczyk-Biegun, Aránzazu del Campo, Blanca Vázquez-Lasa, Julio San Román. Biomaterials. Science 8: 506-516 (2020).
   DOI: 10.1039/C9BM01271K.

- This item is wholly included in this thesis in Chapter 5 and partly reproduced in Chapter 1.
- As the first author of this publication I conducted all the physicochemical and biological experiments. I also contributed to the analysis and discussion of the results and wrote the main draft manuscript text. This work was carried out in collaboration with Prof. Aránzazu del Campo during my first research stay at Leibniz-Institute for New Materials (Saarbrücken, Germany).
- Whenever material from this source is included in this thesis, it is singled out with typographic means and an explicit reference.

4. **Preparation of polymeric and composite scaffolds by 3D Bioprinting.**
Ana Mora-Boza, Maria Luisa Lopez-Donaire. Adv Exp Med Biol 1058: 221-245 (2018) DOI: 10.1007/978-3-319-76711-6_10.

- This item is wholly included in this thesis in Appendix I and partly reproduced in Appendix A.
- As the first author of this publication I wrote the main draft manuscript text together with Maria Luisa Lopez-Donaire.
- Whenever material from this source is included in this thesis, it is singled out with typographic means and an explicit reference.

OTHER RESEARCH MERITS

Other publications

1. **Contribution of bioactive hyaluronic acid and gelatin to regenerative medicine. Methodologies of gels preparation and advanced applications.**
Ana Mora-Boza*, María Puertas-Bartolomé, Blanca Vázquez-Lasa, Julio San Román, Antonio Pérez-Caballer, Marta Olmeda-Lozano. European Polymer Journal 95: 11-26 (2017).

2. **pH-Responsive Polymers: Properties, Synthesis, and Applications**.
Luis García-Fernández, **Ana Mora-Boza**, Felisa Reyes-Ortega. Chapter 3 of the book "Smart Polymers and Their Applications" (2nd edition). WoodHead Publishing, Elsevier (2019).

Short-research stays

2017 – Leibniz-Institute for New Materials (3.5 months). Saarbrücken, Germany.
Dynamic Biomaterials Group (Prof. Aránzazu del Campo).
DAAD short-research grant.
Project: Bioactive and biodegradable 3D scaffolds for Tissue Engineering and Regenerative Medicine.

2018 – Leibniz-Institute for New Materials (1.5 months). Saarbrücken, Germany.
Dynamic Biomaterials Group (Prof. Aránzazu del Campo).
SFB1027 programme short stay (Saarland University).
Project: Bioactive and biodegradable 3D scaffolds for Tissue Engineering and Regenerative Medicine.

2019 – Georgia Institute for Technology (3 months). Atlanta, EEUU.
García Lab (Prof. Andrés García).
CIBER-BNN Movilidad grant.
Project: Application of phytate crosslinker in microgels and organoids platforms.

Table of contents

Chapter 1

General Introduction and Thesis Report

State of the art

1. Natural polymers in regenerative medicine

Regenerative medicine is an interdisciplinary field that combines different principles of engineering and life sciences to potentially promote the regeneration and healing of injured tissues [1]. The use of biomaterials to replace damaged tissues or to contribute to their healing is an important component of current regenerative medicine strategies. Biomaterials are defined as any material intended to interface with biological systems [2, 3] to treat or replace any tissue, organ, or function in the body [2]. They can be classified in metals, ceramics, polymers, and composites depending on chemical composition [3]. Natural-derived polymers are highly attractive to regenerative medicine because of their biodegradability, biocompatibility, non-toxicity, low cost, and availability [3, 4]. These biomaterials can mimic the extracellular matrix (ECM) of native tissues due to their innate structural and chemical similarities, which contribute to resemble the structure and functionality of the developed tissue [1, 5]. Moreover, they can be combined with exogenous biochemical factors (e.g. growth and differentiation factors, bioactive molecules) and/or living cells to create tissue-like structures (Figure 1) [6]. Natural-derived polymers have been applied in different biomedical fields and continue to be studied worldwide [5]. Many natural-occurring polymers, which can be categorized into proteins (e.g. collagen, gelatin) and polysaccharides (e.g. chitosan, hyaluronic acid, alginate), are used in tissue engineering [7]. In this thesis, we focused on three main natural-derived polymers, e.g. chitosan, hyaluronic acid and gelatin, for the development of supports for tissue engineering applications in the regenerative medicine field.

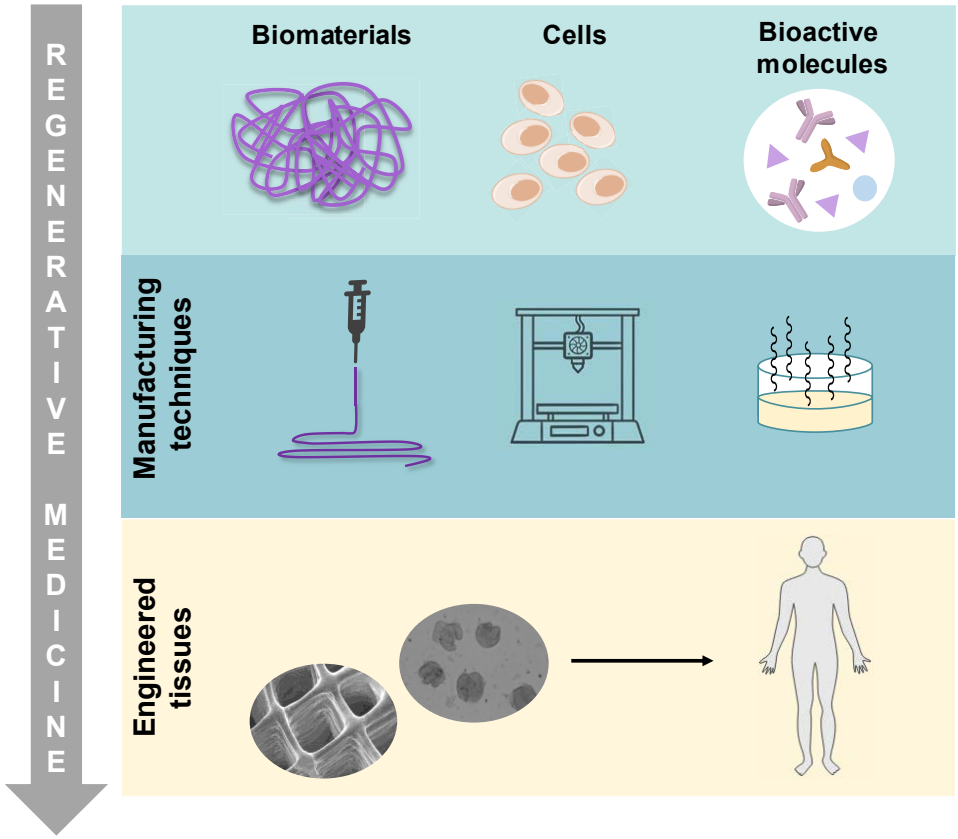

Figure 1. Scheme representing the three main elements that are combined in regenerative medicine (i.e. biomaterials, cells, and bioactive molecules) and the key steps to achieve clinical translation.

Chitosan is a linear polysaccharide obtained from the partial deacetylation reaction of chitin in alkaline conditions. Chitin is abundant in the exoskeleton of crustaceous and insects. Specifically, chitosan is composed of β-(1→4)-linked D-glucosamine (deacetylated unit) and *N*-acetyl-D-glucosamine (acetylated unit), randomly distributed (Figure 2a). Chitosan properties are mainly defined by the presence of amino groups in its structure, whose protonation at acidic conditions allows the solution of the polymer [4]. In fact, chitosan exhibits a pKa value of 6.2, which means that below this pH, amino groups (NH_2) of chitosan chains are protonated (NH_3^+) and the polymer becomes cationic and soluble (Figure 2a) [8]. These positive charges, which are present in chitosan chains at acidic pH, are reactive groups susceptible to interact with different

species of opposite charge. Besides of amino groups, chitosan chains exhibit plentiful hydroxyl groups which allow the introduction of several functionalities along the polymer backbone. This covalent bonding of chemical groups enables the modulation of chitosan properties [4]. Chemical structure and properties of chitosan are quite similar to those of glycosaminoglycans (GAG) of native ECM. In addition, chitosan exhibits remarkable biological features, including antibacterial, hemostatic, analgesic, mucoadhesive, as well as excellent cytocompatibility and biodegradability [8, 9]. Moreover, chitosan is a substance *generally recognized as safe* (GRAS) by Food and Drug Administration (FDA) [10]. Hence, these characteristics make chitosan a suitable candidate for tissue engineering and regenerative medicine applications [8, 9]. Nevertheless, chitosan is characterized by weak mechanical properties, specially under hydrated conditions [8]. Thus, numerous efforts have been made to improve its mechanical strength via crosslinking processes or complexation with other polymers [2]. Besides, its scarce solubility at physiological conditions limits its use for some biomedical applications that require cell encapsulation [11]. In this context, different chemical functionalization reactions are being explored to improve chitosan solubilization (e.g. alkylation, acetylation, and carboxymethylation) [4].

Hyaluronic acid (HA) is an essential component of ECM and participates in several biological processes related to matrix organization, cellular signaling, wound repair, angiogenesis, and morphogenesis [2, 5]. HA can be recognized by a wide variety of cell receptors and it specifically binds to hyaluronan receptors (e.g. CD44 and CD168) [2, 12]. HA is composed of alternating units of *N*-acetyl-D-glucosamine and glucuronic acid (Figure 2b), and it is obtained by an easy and controllable microbial fermentation that can be produced at large scale [5]. Among its main features, HA is characterized by a high hydrophilicity, non-adhesiveness, and excellent biodegradability as it can be completely reabsorbed via different metabolic pathways [2, 7]. These properties make HA an ideal biomaterial for tissue engineering applications.

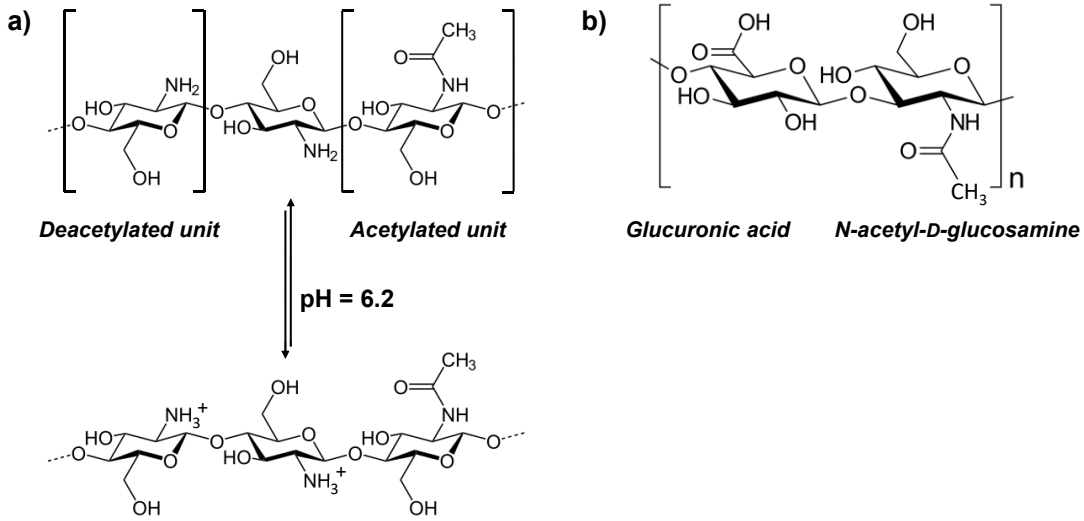

Figure 2. (a) Chitosan chemical structure and pH-sensitive transition from insoluble to soluble form; **(b)** Hyaluronic acid chemical structure.

Gelatin is a natural protein obtained through the denaturalization of the triple helix of collagen. There are two types of gelatin depending on the method of obtaining: type A, which is processed at acidic pH; and type B, which is processed at alkaline conditions, being type A the most preferable for tissue engineering applications [5]. Gelatin is a thermosensitive polymer that contains the specific arginine-glycine-aspartic acid (RGD) peptide sequences, as well as matrix metalloproteases (MMP) sequences that promote cell adhesion and remodelling processes [12]. Thus, gelatin shows excellent biocompatibility, biodegradability, and low antigenicity due to its intrinsic properties derived from its origin [5]. However, gelatin exhibits rapid degradation kinetics and poor mechanical properties, which limit its application in the biomedical field. Hence, functionalization of gelatin with methacryloyl groups is a widely used strategy to improve its strength properties by inducing covalent crosslinking under light irradiation [12].

Due to the all above-mentioned attractive properties of these natural-occurring polymers, they have been widely applied for the fabrication of hydrogels with different applications in regenerative medicine [5, 13].

2. Hydrogel synthesis

Hydrogels are three-dimensional (3D) polymeric networks that are crosslinked through covalent and/or noncovalent interactions to form insoluble matrices [5, 13, 14]. Hydrogels are characterized by the ability to absorb and retain large amounts of water (at least not less than 20 %) due to their hydrophilic nature [5, 14, 15]. The amount of water they can absorb is determined by several factors, such as crosslinking density, composition, fabrication technique or hydrogel structure [5]. Hydrogels exhibit remarkable features that make them appealing materials for regenerative medicine. These features include excellent biocompatibility due to its similarity to ECM, tunable physical, chemical, and biological properties, as well as versatility of manipulation through different biofabrication techniques [14]. In fact, their versatility relies on the easy tunability of their physical and chemical properties to adapt them for the required application [5, 7, 14]. Moreover, their characteristic aqueous environment enhanced the transport of nutrients and biomolecules between cells, promoting cellular interactions and signal transduction [16]. Nevertheless, natural-based hydrogels show some limitations related to poor mechanical properties, potential immunogenicity, and low control over degradation kinetics [7, 14, 16]. In the latest years, many efforts have been made to overcome these limitations by the development of novel crosslinking mechanisms or biofabrication methodologies [2, 3, 13, 17].

As mentioned above, crosslinking is mandatory to obtain the hydrophilic network to be used as a stable support in an aqueous environment [17]. Crosslinking implies a sol-gel transition of the polymer solution to a solid state [5]. In this context, different crosslinking strategies, including physical and chemical, are being developed in the last years for the preparation of hydrogels (Figure 3) [14, 17].

2.1. Physically crosslinked hydrogels

Reversible or physical crosslinking is based on physical interactions between polymers chains, which can be due to molecular entanglements and/or secondary forces like ionic and proteins interactions, pH/temperature changes, and hydrogen bonds (Figure 3) [14, 16]. This type of gelation is claimed to be a safe method for hydrogel synthesis, since it can occur in aqueous solution and in absence of toxic chemical crosslinking agents. However, physically

crosslinked gels exhibit low mechanical strength that limits its application in tissue engineering, above all for load bearing tissues [17, 18].

Ionic crosslinking is widely applied for hydrogel synthesis based on the physical interaction between molecules of opposite electric charges. Divalent cations (e.g. Ca^{+2}, Mg^{+2} or Ba^{+2}) are traditionally used for the physical gelation of polysaccharides. Alginate, for example, is a well-known example of a ionically crosslinked polymer using $CaCl_2$ solution at mild conditions [17, 18]. Electrostatic interactions between anionic and cationic groups exhibited by different macromolecules are also used to form polyelectrolyte complexes (PEC). Some examples of these PECs are those based on chitosan, whose positively charged amino groups can easily interact with anionic polymers like alginate or chondroitin sulphate [18]. Chitosan can also be ionically crosslinked through electrostatic interactions with a wide variety of molecules, such as tripolyphosphate (TPP), sodium sulfate, or cyclodextrin [4, 8, 9, 19]. Electrostatic interactions between amino groups present in chitosan and phosphate groups of TPP have been widely exploited for the preparation of polysaccharide-based membranes [20, 21], polymeric micro- and nanogels [22], and nanoparticles [19, 23]. Finally, hydrogels formed through the mixture of chitosan and β-glycerolphosphate have been extensively studied and clinically applied in the latest years. Interestingly, when β-glycerolphosphate is added to chitosan solution at room temperature, the polymer solution remains liquid and it starts gelling when the temperature increased above 37 ºC. This mechanism of gelling has attracted considerable attention for the development of injectable chitosan-based hydrogels [18, 24].

Among all non-covalent interactions, hydrogen bonds are the most common ones. Different chemical groups (e.g. carboxylic, hydroxyl, amide groups) can form hydrogen bonds among them or interact with other electron donor groups. Although a single hydrogen bond is not enough to lead to hydrogel formation, multiple hydrogen bonds can stabilize network structures when other crosslinking process takes place, and they are usually present in polymeric mixtures [18]. Other crosslinking mechanisms used for physically formed hydrogels are those mediated by hydrophobic interactions, crystallization, metal coordination, and host-guest interactions (e.g. proteins and antibody-antigen interactions) (Figure 3) [13, 17, 18].

2.2. Chemically crosslinked hydrogels

Permanent or chemical crosslinking is mediated by covalent bonds between polymer chains, which can be generated by radical polymerization, chemical reactions, energy irradiation, and enzymatic crosslinking, among other processes (Figure 3) [14]. Unlike physical crosslinking, the linkages formed by chemical crosslinking mechanisms are stronger and irreversible, showing improved stability at physiological conditions and enhanced mechanical properties [18]. Some examples of chemical crosslinking processes include free radical polymerization, enzymatic crosslinking, Schiff base formation, Michael type-addition, or oxime formation. However, chemical gelation mechanisms show some limitations regarding biomedical safety in comparison to physical crosslinking due mainly to the potential cytotoxicity derived from remaining unreacted crosslinking agents [17, 18].

Photo-activated crosslinking is usually mediated by double bonded carbons of methacrylated groups incorporated into the polymer chains. These groups, are highly reactive and trigger free radical chain-growth polymerization under light irradiation in presence of a photoinitiator [12]. The advantages of crosslinking via photopolymerization are: (i) rapid hydrogel formation at mild conditions, (ii) tunable mechanical properties by controlling crosslinking reaction conditions, and (iii) high spatiotemporal accuracy by the precise adjustment of irradiated zones and time of exposure [12, 17, 18]. However, radical polymerization crosslinking shows some drawbacks related to the inhibitory effect of oxygen, since the production of peroxy radicals decreases polymerization rate and reaction yield, leading to unreacted double bonds that can provoke cytotoxicity. Moreover, the free radicals produced by photoinitiators can cause DNA and cellular damage by interacting with cell components (e.g. proteins, nucleic acids) and decrease cell viability [12, 25]. The choice of a suitable photoinitiator is an essential aspect to ensure an appropriate photopolymerization reaction. Photoinitiators are categorized in two main groups: radical and cationic, being the last one not appropriate for tissue engineering applications because of the cytotoxicity of the generated cationic acids, which have a strong harmful effect for cellular environment. Irgacure 2959 (1-[4-(2-hydroxyethoxy)-phenyl]-2-hydroxy-2-methyl-1-propane-1-one) is the most commonly used photoinitiator for biomedical applications due to its low cytotoxicity and immunogenicity. It is sensitive to ultraviolet (UV)

light wavelengths and exhibits moderate water solubility [12]. Despite the attributed drawbacks to UV light photocuring related to triggered cytotoxicity and inflammation reactions [14, 25-27], many authors claim its safe use [14, 27-29]. In recent years, several efforts have been focused on the development of photocrosslinkable systems using visible light-sensitive photoinitiators (e.g. Eosin-Y, riboflavin). Although these photoinitiators are less cytotoxic than UV-sensitive ones, advanced studies are needed to improve their performance since the energy level of visible light is lower than that of UV light, which leads to faster and less controllable crosslinking reactions [12].

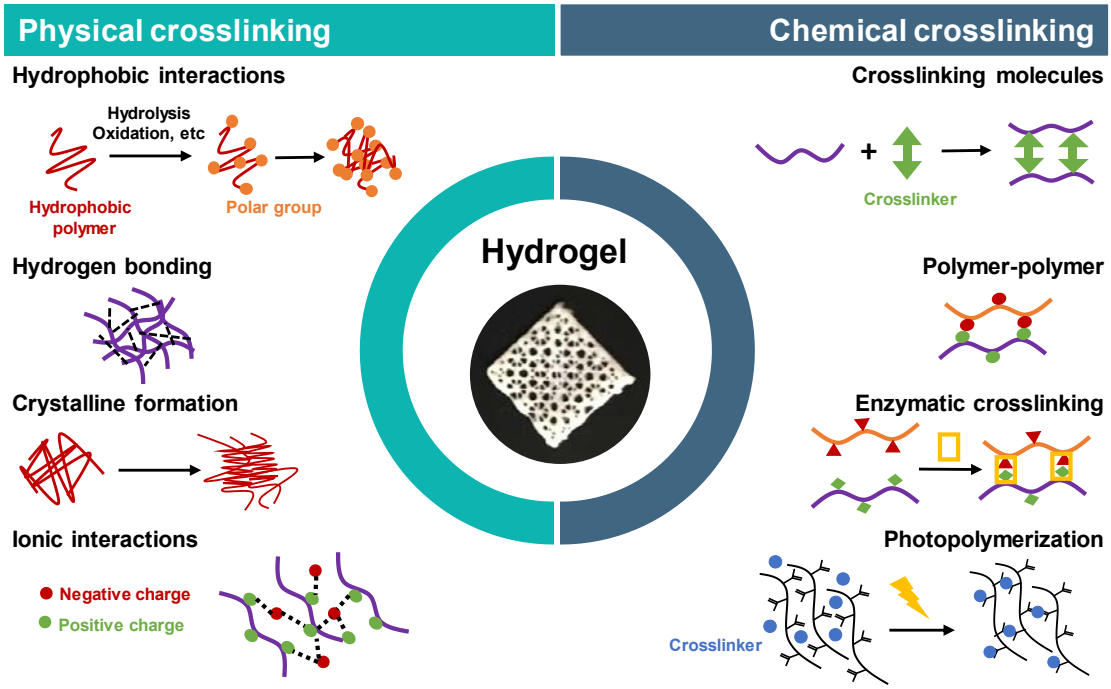

Figure 3. Overview of physical and chemical crosslinking mechanisms for the synthesis of hydrogels.

Currently, one priority objective in regenerative medicine research is focused on the development of bioactive hydrogels to be applied as functional tissues in regenerative medicine [5, 30, 31]. Thus, many efforts are being made for the obtaining of new crosslinking agents and strategies [17, 18] that provide suitable hydrogel matrices for effective tissue regeneration. In this

thesis, we focused on the synthesis and application of novel natural-occurring crosslinkers derived from phytic acid for the fabrication of bioactive systems with promising applications in the biomedical field. In this sense, we applied physical (i.e. ionic) and chemical (i.e. photopolymerization) crosslinking methodologies, either individually or combined, for the development of hydrogel-based structures with bioactive properties for tissue engineering.

3. Phytic acid and its derivatives as natural and bioactive crosslinking agents

Phytic acid (PA), or myo-inositol hexakisphosphate (Figure 4a), is a natural antioxidant compound which constitutes up to 85% of reserve of phosphorus (P) in cereals and legumes [32, 33]. PA is also endogenously synthetized in mammalian cells and participates in several biological processes [34-38]. In the recent years, PA has attracted much attention in the biomedical field because of its attributed beneficial properties [33, 39-44]. PA is claimed to act as an anticancer agent especially in colon and digestive tracts [43, 44], as a lipid peroxidation inhibitor [42, 45, 46], as a preventive agent of calcifications in biological fluids [47, 48], and as an antiosteoporotic compound [39, 49]. PA antioxidant power lies in its ability to form stable chelating complexes with multivalent cations due to the presence of twelve ionizable protons in its structure. Thus, PA is known to form insoluble complexes with positively charged ions [32, 38, 50-52], being the ones formed with Zn^{2+} the most stable, followed by those with Fe^{2+}, Ca^{2+}, Zn^{+2} or Mg^{2+}, among others (Figure 4b) [53]. Moreover, due to its ability to coordinate all iron sites, PA can potentially prevent Fenton reaction, emerging as a powerful lipid peroxidation inhibitor [42, 45, 46, 54, 55].

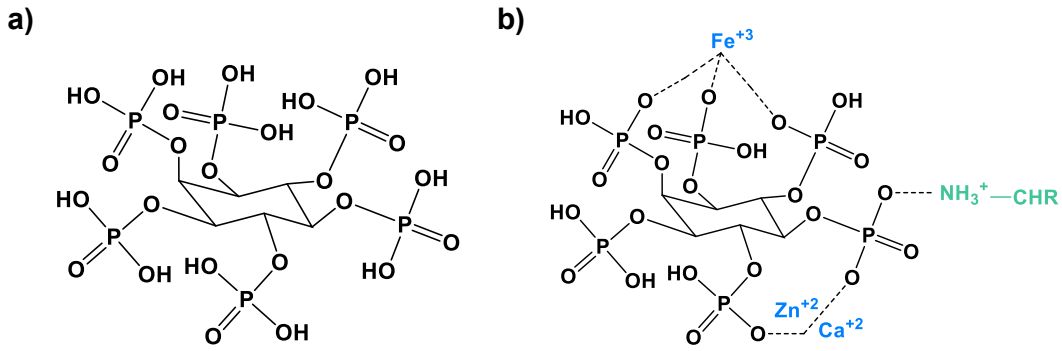

Figure 4. **(a)** Chemical structure of PA; **(b)** Examples of chelating complexes formed by PA and multivalent cations, as well as amino groups present in e.g. polysaccharides and proteins.

The modulatory role of PA in bone remodelling and biomineralization processes has been widely studied in the latest years. PA has been claimed to be an inhibitor of bone resorption processes [56] due to its strong chelating capacity against hydroxyapatite, avoiding its further solution [36]. Moreover, PA has been suggested to inhibit osteoclastogenesis without impairing the osteogenic differentiation at cellular level [49, 57], but its mechanism of action in osteoblasts activity remains unclear and could depend on the cell type [34, 49, 57]. Given all these features related to biomineralization and osteogenesis processes, PA has been widely incorporated to different formulations of bioactive glasses for bone cement applications [58-60], and has been used for the functionalization of titanium surfaces to improve the osteointegration of graft-like surfaces [36, 61]. Currently, PA is considered a *GRAS* substance by FDA, and it is already applied in dietary supplements as phytin (i.e. the calcium salt of PA). Capsules containing PA together with Vitamin A and Zn, which are administered to prevent calcium and phosphocalcic lithiasis, are already commercialized. PA is also used in mouthwashes products to prevent tartar. Other medical formulations containing PA focused on the treatment of cardiovascular calcifications are still in clinical trials. For example, SNF422 is an intravenous formulation that would reduce vascular detrimental effects in dialysis patients and can be also applied as calciphylaxis treatment [48]. Nevertheless, PA has been traditionally considered as an antinutritional agent because of its strong capacity to form stable chelating complexes with mineral ions, compromising supposedly their bioavaibility [38, 62-65]. In addition, PA strong negative density would have a detrimental effect on its cellular interaction and bioassimilation in

the organism [66]. Despite there is no general consensus in this issue, PA-based compounds which exhibit less phosphorylated groups have demonstrated to increase mineral absorption [51, 52].

Ionizable protons of PA structure can interact not only with transition metals, but also with cationic groups present in some natural polymers. Hence, PA has been used as a crosslinking agent of proteins and polysaccharides through ionic interactions [33, 67-71]. For example, PA has been used to fabricate chitosan nanoparticles via ionic gelation for oral delivery of insulin [70], and PA-crosslinked scaffolds consisting of hemoglobin/gelatin/fibrinogen have been proposed for cardiac tissue engineering [71]. In other interesting work, PA was used as crosslinking agent of gelatin and polycaprolactone scaffolds for skin tissue engineering. The PA-crosslinked scaffolds showed improved mechanical properties in comparison to the non-treated materials [72]. Wang et al. [73] also used PA as crosslinking agent for the fixation of decellularized animal derived tissues. These authors agreed in the importance of using natural-derived crosslinking agents to avoid the traditional application of crosslinkers with higher cytotoxicity such as glutaraldehyde, whose biodegradation produces toxic by-products. Genipin, for example, was introduced as a promising alternative to chemical crosslinkers, but its high price and low availability have limited its application [72, 73]. In this context, PA is a promising candidate for the development of naturally crosslinked scaffolds.

Given all the above-mentioned beneficial features and bioactive properties of PA, and in an attempt of overcoming its limitations, we propose in this thesis the **development of hydroxylic derivatives of PA** as bioactive and biocompatible crosslinking agents for the preparation of hydrogel supports oriented to enhance tissue regeneration processes. These novel PA hydroxylic derivatives, named glycerylphytates (**G_xPhy**), were synthetized through a condensation reaction between PA and glycerol. The conjugation of glyceryl residues to phytic acid is an interesting approach to improve the cytocompatibility and bioassimilation properties of the precursor, tuning its biological features [69]. The presence of glyceryl moieties into the chemical structure of the derivatives synthetized here affected the properties of PA by: (i) reducing the negative density of the molecule and (ii) modulating its strong chelating activity, which are both properties

derived from the presence of six phosphoric groups in the inositol ring. The protection of active phosphate esters is a commonly used strategy to increase the bioavailability or to enhance the delivery of these molecules to the cells [66, 69]. In particular, the novel bioactive crosslinker agents G_xPhy have been applied to the fabrication of bidimensional (2D) and 3D hydrogel-based supports with bioactive properties, arising as attractive platforms for tissue engineering applications.

4. Hydrogels as tissue regeneration supports: manufacturing techniques

Hydrogels are appealing materials for the development of matrices with regenerative medicine applications due to their biomechanical similarities to native ECM and easy processability at mild conditions [15, 74]. In this sense, hydrogels-based structures and their combination with bioactive molecules and/or living cells (i.e. constructs) provide mechanical support for *in vivo* implantation and can guide functional tissue repair [75]. As it is known, an ideal scaffold must meet some requirements to be functional such as: (i) to support cell adhesion, proliferation, and differentiation, (ii) to provide an appropriate mechanical and physicochemical environment, and (iii) to facilitate nutrient and oxygen exchange, as well as waste removal and cell signal transduction [3, 15, 76]. Biomaterials can be transformed into matrices of different morphologies and shapes (e.g. fibers, membranes, 3D multilayered scaffolds, microgels) through several manufacturing methods such as solvent casting, freeze-drying, 3D printing, photolithography techniques, microfluidics, among others [77]. These fabrication methods consist of physical and/or chemical processes that are carried out on biomaterials to obtain suitable supports for tissue engineering. As mentioned in section 2, hydrogels are especially attractive materials for the fabrication of polymeric matrices for regenerative medicine applications due to their described advantages [16]. From a practical point of view, the final properties of the support will directly depend on the used crosslinking and biofabrication methods. In this context, it is important to highlight that not all biomaterials possess the adequate properties for every fabrication technique. Thus, biomaterials can be modified or combined with each other to adapt their properties for the application of a desired fabrication

technique [3]. Current biofabrication methodologies provide the possibility of tuning the features of the developed structures to fulfill the specific requirements (e.g. biodegradability, porosity, size, shape, or bioactivity) regarding to the properties of the target tissue [3, 15]. As stated above, chemical crosslinking is usually applied to obtain stable networks with adequate mechanical properties, while physical gelation methods are attractive due to their high cytocompatibility. Thus, the combination of both methodologies is interesting for the obtaining of hydrogel matrices with the desirable properties [13, 18]. Moreover, polymers can be combined to form PECs, semi- and interpenetrated polymer networks (IPNs), or blends [76]. Semi- and IPNs have demonstrated attractive characteristics in terms of enhanced stability and mechanical properties, mainly due to the molecular reinforcement resulted from the combination of different polymers and crosslinking mechanisms [78-80]. Specifically, an IPN consists of the mixture of two (or more) polymer networks which are physically or chemically crosslinked and entangled with each other. For its part, in a semi-IPN, only one of the polymers is crosslinked [78].

In this thesis, different biofabrication strategies were applied for the preparation of polymeric supports. Specifically, we used: (i) conventional **solvent casting methodology** for the preparation of polymeric membranes, semi and -IPN systems, (ii) **3D printing technology** for the fabrication of multi-layered scaffolds, and (iii) **microfluidics** for the synthesis of cell microcarriers.

4.1. Conventional manufacturing techniques for the preparation of polymeric membranes

Conventional manufacturing techniques, including solvent casting, freeze drying or gas foaming, among others, have been traditionally applied for the development of polymeric structures with different applications in regenerative medicine [81]. These techniques usually involve the evaporation of the solvent, in which the polymer is previously dissolved, by applying heat and/or pressure. Thus, the desired shape is obtained by dipping the solution into a mould [82]. The main advantages of these techniques rely on their low cost and relatively easy manufacturing methodology [81]. Currently, several systems obtained through these techniques are commercially available for cartilage and guided bone regeneration (GBR) applications [83-85].

For example, Bio-Gide® is a commercial collagen membrane from porcine skin consisting of a bilayered structure that combines a dense and a porous layer. Thus, the dense layer avoids the infiltration of epithelial cells in bone while the porous layer enables tissue integration [83]. In the field of cartilage regeneration, matrix-induced autologous chondrocyte implantation (MACI) is the most commonly applied strategy. MACI involves the implantation of a biodegradable polymeric construct that promotes cell differentiation and the formation of hyaline cartilage [84]. Chondro-Gide®, which consists of a natural collagen matrix, is an example of a commercial polymeric membrane used in MACI approach [84, 85]. Although current available matrices are being applied with certain degree of success, the development of biomimetic systems that recapitulate better the join microenvironment is still necessary. In this thesis, we have developed polymeric matrices for GBR and cartilage regeneration applications using the novel G_xPhy crosslinkers and combining different crosslinking methodologies for the fabrication of crosslinked, semi- and IPN systems with bioactive properties that can contribute to enhance the regenerative processes.

4.2. 3D printing for the fabrication of hydrogel-based scaffolds

A raising awareness about the importance of recapitulating the complex and dynamic 3D microenvironment of native tissues has promoted the development of scaffolds with complex structures that resemble more precisely tissue heterogeneity [78] and mimic better relevant physiological environment [86-89]. Thus, several efforts are being made in the development of novel biofabrication techniques that would pave a road towards engineering functional tissues [14]. In this context, 3D printing is an attractive technique to fabricate scaffolds with well-defined geometries at macro- and microscale [90]. 3D printing is an additive manufacturing methodology consisting of the layer-by-layer deposition of biomaterials to create 3D structures while reducing material waste generated with traditional fabrication techniques that usually lead to arbitrary geometries [3, 91]. This manufacturing technique exhibits several advantages such as the ability to fabricate complex shapes and morphologies using a wide range of biomaterials, as well as the obtaining of structures with high resolution through an easy and low-cost manner [3]. Furthermore, 3D printing provides the fabrication of scaffolds with interconnected macro and micro-porosity which improves nutrients diffusion and removal of waste products, and facilitates

ECM deposition and vasculogenesis [92, 93]. 3D printing methods can be categorized into printing of cellular constructs (e.g. laser-assisted, extrusion-based or inkjet-based) and acellular techniques (e.g. stereolithography, powder fusion) [90]. An extensive review about 3D cellular and acellular printing techniques, and their applications for the fabrication of polymeric scaffolds can be found in **Appendix A** [94]. Although the variety of biomaterials that can be printed is extensive, synthetic polymers have been traditionally applied because of their mechanical strength enables 3D deposition without the collapse of the consecutive printed layers. However, they do not exhibit suitable properties regarding biocompatibility and biodegradability in contrast to natural-derived polymers [1, 5, 6, 14, 75]. Hydrogels are preferred materials for the fabrication of scaffolds for regenerative medicine because of all the properties above described. However, their high water content leads to poor processability for 3D printing methodologies [95] since their intrinsic softness is insufficient for self-supporting of the printed structures [96-101]. Current trends to overcome these limitations consist of combining different materials and crosslinking mechanisms to fulfil the essential requirements for good printability [102-105], which includes: (i) shear-thinning behavior while printing, (ii) mechanical stability for keeping shape fidelity after printing, (iii) good structural integrity at physiological conditions, and (iv) cytocompatibility [91, 106].

In this thesis, we prepared a blend ink formulation composed of chitosan and methacrylated gelatin (GelMA) that was successfully applied in a dual-step 3D printing approach, which consisted of a first photopolymerization reaction of GelMA followed by an ionic crosslinking step with the novel G_xPhy crosslinkers. Thus, we obtained 3D printed scaffolds with high resolution that displayed adequate stability and physicochemical properties along with excellent biological performance to support fibroblasts as to have a place in the tissue regeneration medicine.

4.3. Microfluidic technology for the fabrication of microgels with stem cells delivery applications

Microfluidics is an attractive technology for the fabrication of microengineering hydrogels with tunable morphologies (e.g. microgels, microfibers) and physicochemical properties [14].

Microgels are defined as 3D-crosslinked particles that provide a porous polymeric network to be applied in several biomedical applications such as drug/cell delivery, cell imaging, and tissue engineering [107-109]. Microfluidics offers different advantages for the fabrication of microgels in comparison to conventional techniques (e.g. precipitation, emulsion-based or atomization methods) regarding low polydispersity of the particles and high-throughput fabrication [108, 110]. Moreover, the size and chemical composition of the generated microgels can be easily controlled by tuning the flow rates and concentrations of the components in the microfluidic channels [14]. Specifically, microgels are synthetized in microfluidic devices by the generation of polymer droplets through water/oil emulsions followed by physical or chemical crosslinking. The most frequently used geometry configurations to generate the droplets in the devices are: T-junction, flow-focusing, and co-flowing laminar streams, which are illustrated in Figure 5 [14, 110].

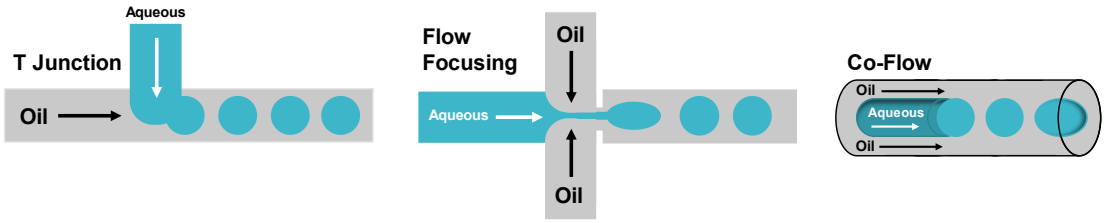

Figure 5. Schematic illustration of different types of droplet generators including T-Junction, flow-focusing, and co-flow configurations.

Microgels fabricated by microfluidic technologies have attracted much attention in the latest years for the development of stem cell microcarriers [107-109]. Stem cell-based therapy is recognized as a promising approach in regenerative medicine since it can induce the healing of damaged tissues [111, 112]. Stem cells are an attractive cell source because of their self-renewal capacity and potential to differentiate into different lineages, as well as the set of secretory bioactive factors (i.e. secretome) that has demonstrated to play an essential therapeutic effect by promoting angiogenesis and enhancing tissue regeneration [111, 113]. However, stem cell transplantation shows some limitations related to low cell survival and poor engraftment at the site of implantation, which reduce its therapeutic efficacy [112]. Hence, microgels can offer multiple advantages as stem cell carriers, including minimally invasive methods of administration

via injection using small-diameter needles. They also act as biological and physical supports, enhancing cell retention, viability, and therapeutic effect at the target tissue. Finally, microgels provide a high surface area, which allows a more efficient transfer of oxygen, nutrients, and signal transduction [109, 114, 115]. Nevertheless, microencapsulation methods should ensure cell viability. Thus, several efforts are being made in the development of novel cell encapsulation strategies with reduced cytotoxicity that enable stem cell therapeutic performance *in vivo* [114]. In the last part of the thesis, the novel bioactive crosslinkers G_xPhy have been applied for the preparation of microgels in flow-focusing microfluidic devices for encapsulating stem cells, which is another priority topic in regenerative medicine.

Outline of the thesis

This thesis consists of an **introductory chapter (Chapter 1)** that exposes the state of the art of the topic and a **thesis report,** which gathers together the objectives, methodology and general conclusions of the thesis, followed by **five chapters** where the **experimental results** of this research work are displayed. Finally, this thesis includes an **appendix (Appendix A)** where main 3D printing techniques applied for the preparation of polymeric scaffolds are deeply described. A schematic representation of this outline is illustrated in Figure 6.

Chapter 2 describes the **synthesis, physicochemical characterization, and biological features of a family of novel glycerylphytate derivatives**. These compounds were obtained by changing the molar ratio between PA and glycerol in the condensation reaction feed, which determined the average number of glyceryl moieties incorporated to the synthetized molecules. Thus, we developed two hydroxylic derivatives of PA (i.e. **G_1Phy and G_3Phy**) that exhibited tunable chelating properties but maintained the antioxidant properties and biological features of their precursor. Osteogenesis ability was evaluated on human mesenchymal stem cells (hMSCs) culture. This approach offers a library of glycerylphytate derivatives to be used as an alternative to PA in biomedical and pharmaceutical applications [69].

Chapter 3 shows the use of **G_3Phy as crosslinker agent for chitosan membranes** with promising applications in GBR. Physicochemical properties, swelling, and crosslinker release of the systems were deeply evaluated along with the biomineralization behavior in simulated body fluids. Moreover, biological features and osteogenic potential were assessed on hMSCs. G_3Phy demonstrated to improve osteogenic and osteoinductivity potential of chitosan by increasing calcium deposition, and alkaline phosphatase (ALP) activity on cultured hMSCs in absence of any typical osteoinducer agent. Therefore, G_3Phy-crosslinked chitosan membranes provide a suitable environment for hMSCs culture and differentiation into osteoblastic lineage, arising as attractive substrates for GBR [116].

In **Chapter 4**, we explore the use of s**emi- and IPN systems containing chitosan and HA** for cartilage regeneration applications. Specifically, **G_1Phy was applied as ionic crosslinker** for obtaining chitosan membranes, chitosan/HA semi-IPN, and chitosan/methacrylated HA (HAMA) IPN systems. In the latter, ionic crosslinking was combined with photopolymerization reaction of HAMA. Thus, physical and chemical crosslinking processes were combined in the IPN system. Physicochemical properties, swelling, crosslinker release, degradation, and rheological properties of the systems were deeply analyzed. Biological features, like proliferation, cytotoxicity, and cell adhesion were assessed on hMSCs. Differences between semi- and IPN systems were found in terms of composition, surface and mechanical properties, as well as biological performance. Interestingly, Ch/HA semi-IPN ionically crosslinked with G_1Phy showed attractive features (e.g. surface roughness, viscoelastic properties approaching those of cartilage, and enhanced hMSCs culture behaviour) to be proposed as an effective biomimetic ECM system for cartilage repair application.

Chapter 5 focuses on the development and implementation of a **3D printing approach** using a dual crosslinking strategy for natural-based polymer inks based on chitosan and GelMA. The applied methodology consisted of a first UV photopolymerization step simultaneously to 3D deposition, followed by a post-printing **ionic crosslinking treatment with G_1Phy.** This approach enabled the fabrication of 3D scaffolds with high shape fidelity and resolution, without the collapse of the consecutive printed layers. Our G_1Phy ionic crosslinking agent provided adequate swelling and long-term stability properties to the 3D scaffolds and good *in vitro* biological performance of 3D printed multi-layered structures in L929 Fibroblasts cultures, which showed successful results in terms of adhesion, spreading, and proliferation in comparison to other phosphate-based traditional crosslinkers (i.e. TPP) [91].

Finally, **Chapter 6** describes the fabrication of **chitosan-lactate microgels** in a flow-focusing **microfluidic device** via *in situ* crosslinking reaction using combination of TPP and **G_1Phy as ionic crosslinkers** for hMSCs encapsulation applications. The incorporation of G_1Phy to chitosan-based microcarriers provided some remarkable features in terms of enlargement of viability of encapsulated hMSCs and upregulation of paracrine signaling at stress

conditions (e.g. oxidative stress and inflammation). Moreover, G_1Phy presence provided *in vivo* cell survival and persistence in comparison to the traditionally applied TPP alone. Given all beneficial properties of G_1Phy, we envision that our proposed delivery platforms can offer a promising approach on the field of cell therapy based on hMSCs.

Appendix A consists of a deep review about the preparation of polymeric and composite scaffolds by 3D printing techniques for osteochondral regeneration [94].

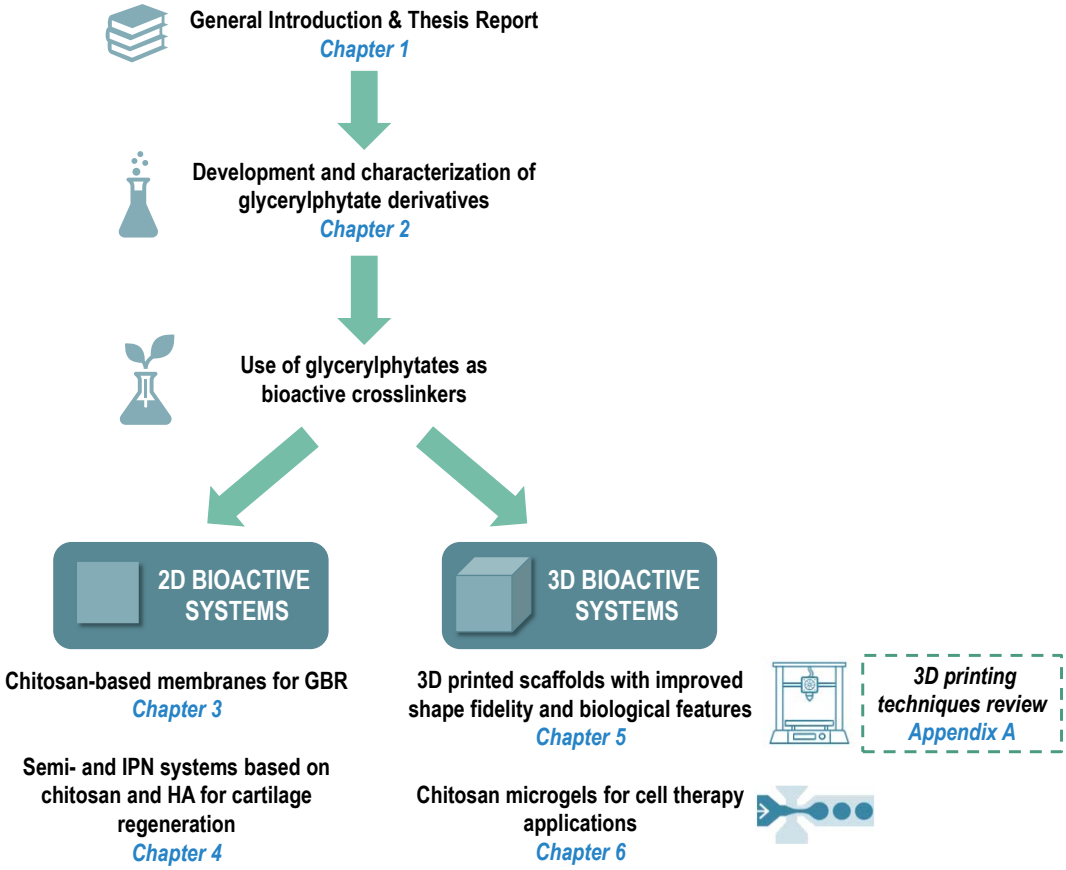

Figure 6. Schematic representation of the outline of the present thesis.

Objectives

This thesis aims to investigate the preparation and use of novel natural phytate derived crosslinking agents (G_xPhy) for the development of 2D and 3D bioactive systems and microgels for regenerative medicine applications. Throughout the different chapters of this thesis, this main aim has been addressed by attaining more specific objectives, as described below:

- Development of two bioactive crosslinking agents (G_1Phy and G_3Phy) of reduced cytotoxicity, taking advantage of antioxidant and biological features described for phytic acid, and evaluation of their chelating activity with divalent cations along with antioxidant behavior.
- Elucidation of hMSCs performance in presence of G_xPhy compounds, in terms of cell viability, proliferation, and differentiation processes compared to those provided by phytic acid, as well as lipid peroxidation inhibition ability when cultured with RAW267.4.
- Analysis the crosslinking potential of G_xPhy compounds to fabricate hydrogel-based systems, specifically by the development of: (i) membranes consisting of G_3Phy-crosslinked chitosan; (ii) semi-IPN systems consisting of G_1Phy-crosslinked chitosan and HA; (iii) IPN systems based on G_1Phy-crosslinked chitosan and UV-crosslinked HAMA, combining both ionic gelation and photopolymerization; (iv) 3D printed scaffolds using an extrusion-based printer and combining physical (G_1Phy ionic crosslinking) and chemical (photocuring of GelMA) gelation; and (iv) microgels developed inside of microfluidic devices by *in situ* ionic gelation (combining G_1Phy and TPP crosslinkers).
- Characterization of physicochemical and surface properties, morphology, and mechanical performance of all developed 2D and 3D bioactive systems.
- Study of the *in vitro* swelling, degradation, and release of the G_xPhy bioactive compounds in physiological conditions for all 2D and 3D scaffolds.
- Evaluation of the biological performance of 2D and 3D systems. In particular:
    - Evaluation of the osteogenic potential of G_3Phy-crosslinked chitosan membranes on hMSCs culture in absence of any osteoinducer agent.

  - Comparison and evaluation of semi- and IPN systems biological performance on hMSCs culture, studying the influence of their respective physicochemical characteristics and focusing on osteochondral regeneration.
  - Evaluation of adhesion and proliferation processes of 3D printed scaffolds using fibroblasts oriented to soft tissue regeneration.
- Development of novel cell microcarriers based on a water-soluble chitosan derivative and G_1Phy crosslinker using microfluidics technology, and analysis of the impact of the bioactive properties of G_1Phy-based microgels on hMSCs culture, differentiation, and secretome modulation.

Methodology

1. Synthesis

1.1. G_xPhy derivatives synthesis

Glycerylphytate (G_xPhy) derivatives were synthetized by a condensation reaction between PA and glycerol (G). A family of hydroxylic derivatives were developed by changing the molar ratio between the two precursors in the reaction feed to obtain products with different number of glyceryl moieties incorporated to PA molecules. In this thesis, two G_xPhy derivatives were prepared using PA:G molar ratios of 5:1 and 1:7, which were named G_1Phy and G_3Phy, respectively. The synthesis was carried out at 120 ºC in bulk by reacting PA with the corresponding G volume for 12 hours under mechanical stirring. The reaction products were dissolved in distilled water (dH_2O), precipitated twice in 2-propanol, dried under reduced pressure to remove 2-propanol trace, and lyophilized (Chapter 2).

1.2. Polymers functionalization

The functionalization of natural polymers with different chemical groups allows the incorporation of crosslinkable groups (e.g. methacrylate groups), or new physicochemical features. In this thesis, we carried out two types of functionalization: (i) the methacrylation of gelatin and HA to obtain photocrosslinkable hydrogels, and (ii) the condensation of chitosan with lactic acid to improve its solubility properties at physiological conditions.

1.2.2. Polymers methacrylation: GelMA and HAMA synthesis

Light is an excellent external stimulus to fabricate hydrogels with tunable mechanical and chemical properties, as it was mentioned in subsection 2.2. [12, 26, 117]. Methacrylation of polymers is an attractive approach to develop light-sensitive hydrogels. The chemical methacrylation of gelatin (GelMA) and hyaluronic acid (HAMA) converts them into photocrosslinkable precursors for hydrogels synthesis under UV or visible light irradiation in the presence of the appropriate photoinitiator. GelMA and HAMA hydrogels have been widely applied for different applications within regenerative medicine due to their attractive mechanical and biological properties [12, 25, 26, 117].

Gelatin methacrylation

Methacrylation reaction of gelatin consists of the substitution of methacryloyl groups on the hydroxyl and reactive amine groups of gelatin (Figure 7a) [12]. In this thesis, GelMA was synthetized by adapting a method previously reported by O'Connell et al. [28]. Briefly, 5 g of gelatin were dissolved in 50 mL of Dulbecco's phosphate-buffered saline (DPBS) at 50 ºC and stirred for 30 min until completely dissolved. Then, 8 mL of methacrylic anhydride (MA) were added gradually to the solution and the reaction proceeded for 3 h at 50 ºC. The reaction was stopped by adding 150 mL of DPBS. The final solution was dialyzed (3500 Da cut off) against dH_2O at 40 ºC for 7 days. The resulted product was freeze-dried and stored at 4 ºC in a dark container.

Hyaluronic acid methacrylation

Methacrylation reaction of HA is based on the substitution of methacryloyl groups on the hydroxyl and reactive amine groups of HA (Figure 7b) [12]. In this thesis, HAMA was synthesized through an esterification reaction in alkaline conditions following the protocol described by Khunmaneeet et al. [118]. MA was added to a HA aqueous solution at different MA:HA ratios (1:1, 2:1 and 5:1) to obtain HAMA with different methacrylation degrees. The corresponding mixture was kept at 0 ºC using an ice bath and the pH was controlled at 8.5 by adding NaOH (5 M) for 24 h. Due to the high pH sensitivity of the esterification reaction, we implemented the use of an automatized titrator (Metrohm), which provided an accurate control over reaction pH and led to homogeneous substitution degrees. The final product was purified by precipitation in cold ethanol, subsequently centrifuged, re-dissolved in dH_2O, and dialyzed (3500 Da cut off) for 4 days. After freeze drying, a white powder was finally obtained.

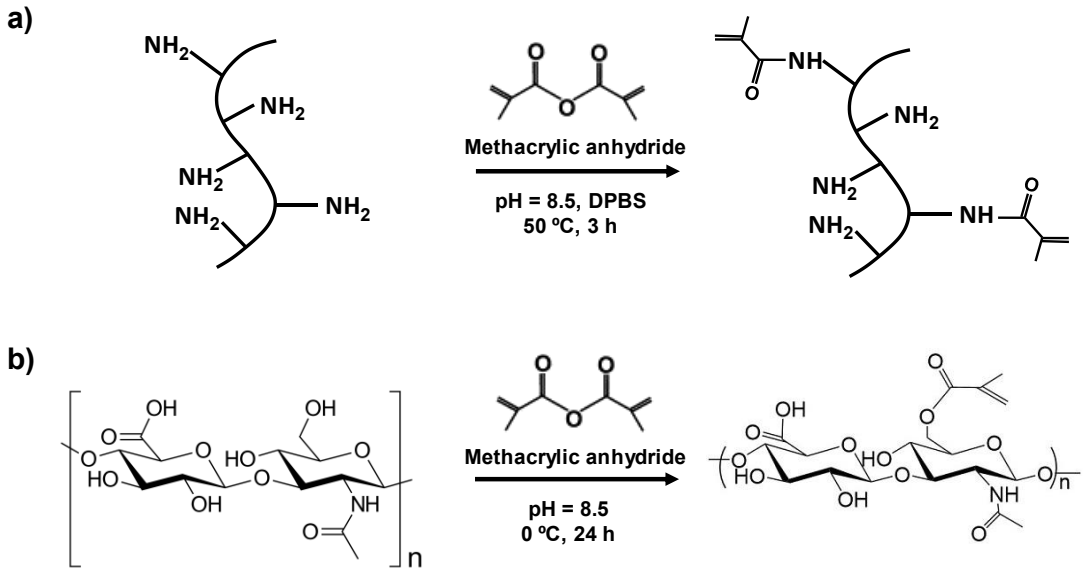

Figure 7. Methacrylation reaction of gelatin **(a)** and HA **(b)**.

1.2.3. Chitosan lactate (ChLA) derivative synthesis

The low solubility of chitosan at physiological pH is a limiting factor for its application for cell encapsulation processes (e.g. bioinks containing cells or cell encapsulating platforms) [2]. Thus, the development of chitosan derivatives with improved solubility properties will extend its use in several biomedical applications [4, 11, 119, 120]. Water soluble chitosan derivatives are obtained through a variety of reactions (e.g. alkylation, acetylation, and carboxymethylation) in order to introduce different functional groups [9, 121]. In this thesis, the water-soluble chitosan derivative, named chitosan lactate (ChLA), was developed. ChLA was synthesized through a condensation reaction of chitosan with lactic acid. Briefly, chitosan powder (1 g) was dissolved in 50 mL of acetic acid solution (1% v/v) and stirred for 24 h to allow complete dissolution of the polymer. Separately, 2-fold excess (0.91 g with respect to lactic acid) of 4-(4,6-dimethoxy-1,3,5-triazin-2-yl)-4-methyl-morpholinium chloride (DMTMM) was dissolved in a lactic acid aqueous solution (122 μL, 30 wt-% respect to chitosan) and stirred for 30 min. This solution was added dropwise to chitosan and the reaction proceeded for 24 h. The final product was purified by precipitation in cold acetone, subsequently filtered, re-dissolved in dH_2O, and dialyzed (3500 Da cut off) for 7 days. After freeze drying, a white powder was obtained.

2. Hydrogel supports fabrication

In this thesis, different fabrication approaches have been employed for the synthesis of 2D and 3D polymeric scaffolds as well as microgels. Specifically, the developed scaffolds present appropriate properties to be applied in soft tissue regeneration processes, in the repair of osteochondral defects, and as membranes for GBR. The synthetized microgels have suitable properties to be proposed as platforms for hMSCs encapsulation.

2.1. 2D membranes fabrication

Polymeric membranes of different composition and structure have been synthetized in this thesis. In Chapter 3, chitosan membranes were prepared by placing 10 mL of chitosan (2 wt-%) acetic acid solution (1 % v/v) into a glass mould and heated in a humid chamber at 37 ºC until complete evaporation of the solvent. The obtained chitosan membranes were neutralized with 1 N NaOH solution and washed with double dH_2O (ddH_2O) until neutral pH. Then, they were ionically crosslinked by their immersion in an aqueous solution of G_3Phy at different concentrations (2.5, 5, and 10 wt-% with respect to chitosan) and kept overnight at 37 ºC.

In Chapter 4, we developed semi-IPN systems consisted of HA and chitosan, in which chitosan was ionically crosslinked with G_1Phy (named Ch/HA,) and IPN systems composed of G_1Phy-crosslinked Ch and HAMA covalently crosslinked through UV light irradiation (named Ch/HAMA). Briefly, Ch/HA or Ch/HAMA were prepared with a content of 75 % of chitosan and 25 % of HA or HAMA, respectively. Either HA or HAMA solution in acetic acid (1% v/v) with $CaCl_2$ (13 wt-% respect to chitosan) was added to the chitosan solution (2 wt-%) together with additional drops of 2 M HCl to achieve the total dissolution of both polymers. For Ch/HAMA membranes, the solution was supplemented with 5 wt-% of polyethylene glycol dimethacrylate (PEGDMA) crosslinker and 2 wt-% Irgacure 2959, both respect to the HAMA content. Then, the corresponding solution was irradiated at 365 nm for 15 min using a UVP chamber photoreactor (CL-1000), equipped with 5 bulbs of 365-nm working at an intensity of 2.9 mW/cm^2. Finally, membranes were immersed in G_1Phy solution (15 mg/mL) and kept overnight at 37 ºC to achieve ionic crosslinking.

2.2. 3D printed scaffolds

In Chapter 5, a dual-step crosslinking 3D printing approach was implemented for the fabrication of 3D scaffolds with good shape fidelity, resolution as well as physicochemical and biological properties. Initially, different ink compositions were evaluated in terms of printability (i.e. self-standing filament) by changing the concentration of chitosan and GelMA in the solution. For the preparation of the polymeric ink, GelMA was dissolved at different concentrations (2 to 5 wt-%) in acetic acid solution (1% v/v) and 1 wt-% of PEGDMA at 40 ºC. Chitosan powder was added to the solutions to obtain different concentrations (1 to 4 wt-%) in the final ink volume. Irgacure 2959 was used as a photoinitiator and added to the ink solutions at a final concentration of 0.5 wt-%. The ink solutions were stirred at 40 ºC for 3 h in dark conditions to obtain a homogeneous mixture and transferred to 10 mL volume cartridges. Finally, the cartridges were centrifuged for 5 min at 800 rpm to remove air bubbles. The selected ink after printability inspection, consisting of 4 wt-% of chitosan and 4 wt-% of GelMA, was first simultaneously deposited and irradiated with UV light to initiate photopolymerization of GelMA in each layer of the scaffold. After printing, the 3D scaffold was immersed in a 15 mg/mL solution of G_1Phy or TPP (used as control) for ionic crosslinking of the amine groups present in chitosan and GelMA. 3D scaffolds were fabricated using a pneumatic extrusion 3D printer (BioScaffolder 3.2, GeSiM, Germany). Metal straight needles with an inner diameter of 150 μm and 200 μm were used. Printing speed and air pressure were adjusted to 5 mm/s and 500 kPa for 150 μm tip, and 8 mm/s and 400 kPa for 200 μm tip, respectively. Further details can be found in Chapter 5.

2.3. Microgels preparation by microfluidics

In Chapter 6, ChLA microgels were synthetized in flow-focusing microfluidic devices via *in situ* crosslinking reaction using mixtures of TPP and G_1Phy as ionic crosslinkers for hMSCs encapsulation. Microfluidic flow-focusing devices with 3 independent flow inlets (ChLA, crosslinker, and continuous phases) were used. Firstly, ChLA and crosslinker phases were merged in a T-junction to enable polymer-crosslinker interaction inside the device. The reactive mixture was then focused to the continuous phase (mineral oil and SPAN80) to allow water/oil

emulsion and droplet generation. The ionic crosslinking reaction was subsequently completed along the serpentine channel of the device. For encapsulated-hMSCs microgels, cells were resuspended in ChLA solution. Flow rates were adjusted to 1.5 μL/min for both polymer and crosslinker phases, and 20 μL/min for continuous phase. Further details can be found in Chapter 6.

3. Characterization

In this thesis, a wide variety of characterization techniques were applied to study the composition, physicochemical properties, morphology, and surface properties of our developed systems. Ion chelating activity with Fe^{2+} and Ca^{2+} was assessed for G_xPhy compounds. *In vitro* experiments were conducted in physiological medium to investigate the swelling and degradation behavior of the scaffolds and release profile of the bioactive G_xPhy compounds.

3.1. Composition and physicochemical characterization

Chemical structure of G_xPhy derivatives and functionalized polymers (GelMA, HAMA, and ChLA) was analyzed by **Nuclear Magnetic Resonance (NMR)**. Proton (^{1}H-NMR) and Carbon 13 (^{13}C-NMR) spectra were recorded in deuterated water (D_2O). ^{1}H chemical shifts were referenced to the residual proton absorption of the solvent, listed as "residual internal" D_2O (δ 4.79). In case of ^{13}C, deuterated dioxane was used as external reference. Chemical structure of G_xPhy derivatives was further analyzed by **2D Heteronuclear Single-Quantum Coherence (HSQC)** performing **Distortionless Enhancement Polarization Transfer (DEPT)** experiments **(2D DEPT-HSQC).**

Chemical structure of G_xPhy derivatives and developed 2D membranes were also studied by **Total Reflection–Fourier Transform Infrared (ATR-FTIR)** spectroscopy.

Chemical composition of G_xPhy derivatives and developed systems (2D membranes and 3D printed scaffolds) was analyzed by **Elemental Analysis (EA)**, **Energy-Dispersive X-Ray (EDX)** and **Inductively Coupled Plasma-Optical Emission (ICP-OES)** spectroscopies.

Thermal properties of G_xPhy compounds were evaluated by **Differential Scanning Calorimetry (DSC)** and **Thermogravimetric Analysis (TGA).** Thermal behavior of the developed 2D membranes was also analyzed by TGA.

Measuring conditions for each system and characterization technique are detailed in their corresponding chapters.

3.2. Morphology and surface properties

Surface morphology is a critical factor for the development of biomaterials that effectively promote cell adhesion and proliferation [122]. In this thesis, morphology of the developed 2D, 3D systems, and microgels was observed by different microscope techniques. **Optical microscopy** was used to evaluate the morphology of 3D printed scaffolds (Chapter 5) using an Olympus (Hamburg, Germany) SZX16 stereomicroscope under opaque illumination, and microgels (Chapter 6) using an EVOS Imaging System (ThermoFisher). **Scanning Electron Microscopy (SEM)** was applied to analyze the surface morphology of G_3Phy-crosslinked chitosan membranes (Chapter 3) and semi- and IPNs systems (Chapter 4) using a Hitachi S-8000 instrument operating in transmission mode at 100 kV. For 3D printed scaffolds (Chapter 5), morphology was evaluated by **cryo-SEM**. Thus, samples were firstly plunged in liquid ethane at -165 ºC using a Gatan (Pleasanton, CA, USA) CP3 cryo plunger and transferred under liquid nitrogen to a FEI (Hilsboro, OR, United States) Quanta 400 FEG microscope. Cryo-SEM observation was performed under high vacuum conditions using accelerating voltage between 1.5 and 5 keV.

Topography of the developed semi- and IPN systems (Chapter 4) was analyzed by **Atomic Force Microscopy (AFM)** with a PicoLE (Molecular Imaging) apparatus operating in the acoustically driven intermittent contact (i.e. tapping) mode using standard silicon AFM probes (NSC11/Cr-Au, Mikromasch, Estonia) with a cantilever spring constant of 48 N/m and a resonance frequency of 330 kHz.

Surface parameters such as wettability are important features that must be studied in order to determine the hydrophilic-hydrophobic balance since it greatly affects cell adhesion and proliferation properties of the scaffolds [123]. Surface-wetting characterization was performed on semi- and IPN systems by **water contact angle (WCA)** measurements using the sessile drop goniometry method. Measuring details can be found in Chapter 4.

3.3. Viscosity of the inks and mechanical properties of the developed systems

Viscosity of the inks used for 3D printing was determined by rheological experiments. Measurements were conducted in oscillatory mode by increasing the shear rate from 1 to 1000 s^{-1} to determine their shear thinning behavior. **Photopolymerization kinetics** of the inks was also studied by *in situ* illumination of the ink formulation in the rheometer using a UV-light source. Further details can be found in Chapter 5.

Viscoelastic properties of the 3D printed scaffolds were evaluated in a rotational rheometer in oscillatory mode at frequency 1 Hz and strain 1%. Particularly, 4 wt-%/4 wt-% GelMA/chitosan solutions were photocrosslinked in 24 well-plates by illuminating them for 5 min at 50 mW/cm^2, and then incubated in 15 mg/mL of G_1Phy or TPP solution for 5 min. Their storage (G') and loss (G") moduli were measured in the rheometer. Further details can be found in Chapter 5.

Mechanical properties of our developed G_3Phy-crosslinked membranes (Chapter 3) and semi, and -IPN systems (Chapter 4) were studied by **rheological measurements** using an advanced rheometer from TA instruments (model AR-G2) equipped with a Peltier and a solvent trap. Thus, the membranes were previously stabilized by their immersion for 24 h in pH 7.4 at 37 °C. Oscillatory shear tests were carried out at a frequency of 0.5 Hz and a strain ranging from 0.01 to 100% to determine the linear viscoelastic region (LVR). Then, frequency sweeping measurements were conducted to determine the G' and G" moduli. Measuring details for each system are exposed in their corresponding chapters.

3.4. Formation of ions chelate complexes by G_xPhy derivatives

3.4.1. Antioxidant activity (Ferrozine assay)

The iron chelate complexes formation was studied by the method of Dinis et al. [55]. PA and G_xPhy compounds at various concentrations (10-300 μg/ml) in dH_2O (0.4 mL) were added to a solution of 2 mM $FeCl_2$ (0.05 mL). The corresponding mixture was vigorously shaken and left at room temperature for 15 min under darkness conditions. Then, 0.2 mL of 5 mM ferrozine solution was added and the total volume was adjusted to 4 mL with ethanol. Absorbance of the

solution was measured spectrophotometrically at 562 nm with a NanoDrop™ spectrophotometer. Further experimental details are exposed in Chapter 2.

3.4.2. Calcium chelating capacity

The binding capacity of PA and G_xPhy derivatives to calcium ions was examined with an adapted method from Saw et al. [124]. Particularly, aliquots of 50 µl at a concentration of 396 mg/mL of each compound were added to a 4 mM solution of $CaCl_2$ (20 mL) in intervals of 2 min until achieving a final concentration of 5.27 mg/mL of each compound in the solution. The pH was controlled by preparing all the solutions in Tris-HCl 0.1M buffer pH 7.5. The pellet was isolated by centrifuging at 4 ºC and washed with dH_2O. The final pellet was digested at 65 ºC with 65% v/v HNO_3. Finally, the P and calcium content of these pellets in 5% v/v HNO_3 solution were measured by ICP-OES. Further experimental details are exposed in Chapter 2.

3.5. *In vitro* performance: swelling, degradation, and crosslinker release

Swelling is a key property to evaluate the capacity of the system for water uptake and diffusion of nutrients and other essential molecules along the scaffold [125, 126]. Thus, in this thesis, swelling degree of 2D developed systems (chitosan, semi- and IPNs membranes) were evaluated gravimetrically over time at physiological conditions (pH 7.4 and 37 ºC). The water uptake was calculated as described in equation 1:

$$\text{Swelling (\%)} = [(W_W - W_0)/W_0] \times 100 \quad (1)$$

where W_w and W_0 are the weights of the swollen membrane at time t and the initial dried weight of the membrane, respectively.

For 3D printed scaffolds, swelling was evaluated by measuring the strand widths of the scaffolds at different times of incubation in PBS at 37 ºC using light microscopy.

Degradation is also an essential property to be analyzed in tissue engineering since it gives information on the stability of the scaffold**.** Degradation of our 2D systems was monitored

gravimetrically at physiological conditions (pH 7.4 and 37 ºC) over time. The percentage of weight loss was calculated following the equation (2):

$$\text{Weight loss (\%)} = [(W_0 - W_t)/W_0] \times 100 \quad (2)$$

where W_0 and W_t are the weights of the initial dry membrane and the dried membrane at time t after incubation in PBS, respectively.

Crosslinker release (TPP and G_xPhy, depending on the system) was followed by measuring the P content in the supernatant after incubating the scaffolds in Tris-HCl 0.1 M buffer (pH 7.4) at 37 °C. P content of the aliquots taken at increasing times was determined by ICP-OES. Tris-HCl buffer was used to avoid interference between P of the samples and PBS. Further experimental details can be found in each chapter.

4. Biological performance

4.1. Cell culture

In this thesis, different cell lines were used to study the biological behavior displayed by the developed systems. The type of cells was selected according to specific assay and the future application of each system. G_xPhy derivatives, 2D membranes, and microgels performance was assessed on hMSCs. The specific cell culture conditions are detailed in Chapters 2, 3, 4 and 6 of the present thesis.

Murine RAW 264.7 macrophages cell line was used for lipid peroxidation experiments to study the antioxidant ability of G_xPhy derivatives. Culture conditions are detailed in Chapter 2.

The biological behavior of the 3D printed scaffolds was assessed on L929 Fibroblasts, whose culture conditions are further explained in Chapter 5.

4.2. Cytotoxicity and cell viability

Alamar Blue assay was conducted to evaluate the cytotoxicity of G_xPhy derivatives and extracts of the scaffolds, as well as cell viability over time after seeding cells directly on the developed systems**.** The Alamar Blue assay is a fluorometric method for the measurement of metabolic activity of cells [127]. The method is based on the reduction of resazurin (oxidized

form; 7-hydroxy-3H-phenoxazin-3-1-10-oxide) to resorufin (reduced form) by mitochondrial enzymes. Fluorescence of both forms can be monitored at 530–560 nm excitation wavelength and at 590 nm emission wavelength [127, 128].

Live/dead assay was used to evaluate the viability of cultured cells on semi- and IPNs, 3D printed scaffolds, and cell viability over time of encapsulated cells in the developed microgels. Detailed live/dead assay parameters are described in Chapters 4, 5, and 6, respectively. Briefly, this assay consists of a double-staining protocol for live and dead cells with two different dyes that emit fluorescence at different wavelengths, which correspond to green and red emission for live and dead cells, respectively. The stained cells are then imaging using microscopic techniques. In this thesis, **fluorescence microscopy** was applied for imaging live and dead cells on 3D scaffolds (Chapter 5), and **confocal microscopy** was used for seeded cells on semi- and IPN systems as well as encapsulated cells in microgels (Chapters 4 and 6, respectively).

4.3. Cell adhesion and morphology

Adhesion and morphology of the cells seeded on the top of the developed systems were evaluated through different visualization techniques. Adhered hMSCs to G_3Phy-crosslinked membranes (Chapter 3) were stained using Calcein AM, which was added in a concentration 1:1000 to the culture media and incubated for 10 min. Fluorescent cells were visualized under **fluorescence microscopy** (Nikon Eclipse Microscopy model TE2000 equipped with a fluorescence light source CooLED model CoolLED's pE-300^{lite}). For hMSCs seeded on semi- and IPN systems (Chapter 4), an **environmental SEM (ESEM)** was used. In this case, samples were fixed with 2% v/v glutaraldehyde, rinsed in 0.1 M cacodylate buffer, and incubated overnight at 4 °C. For critical point the samples were maintained with Osmium tetroxide 1% RT during 1 h and dehydrated in a series of ethanol solutions (50%, 70%, 90%, 100%) by soaking the samples in each solution for 15 min. Morphology of fibroblasts seeded on 3D printed scaffolds (Chapter 5) was observed by **immunohistochemical staining** and **fluorescence microscopy.** Hence, L929 Fibroblasts were fixed with paraformaldehyde 3.7% v/v for 10 min, permeabilized with 0.5% w/v Triton-X 100 (TX) for 10 min, and blocked with 0.1% TX and 5% w/v bovine serum albumin for 20 min. Samples were incubated in 1:1000 vinculin rabbit

antibody solution for cytoskeleton labelling and 1:200 Alexa fluor-546 Phalloidin solution for focal adhesions staining in red color for ~1 h. Then, they were rinsed twice with PBS and incubated with secondary antibody (Alexa flour-488 goat antirabbit) 1:500 solution to visualize cytoskeleton in green. Finally, samples were stained with 1:1000 DAPI (4',6-diamidino-2-phenylindole, dihydrochloride) solution for nuclei visualization in blue color and washed with PBS. Imaging was performed using Nikon Ti-Eclipse (Nikon Instruments Europe B.V., Germany) with a Sola SE 365 II (Lumencor Inc., Beaverton, USA) solid state illumination device and an Andor Clara CCD camera for detection.

4.4. Human MSCs osteogenic differentiation

Alkaline phosphatase (ALP) activity was evaluated on hMSCs cultured in presence of G_xPhy derivatives (Chapter 2) and after seeding cells and cultured them on 2D membranes crosslinked with G_3Phy (Chapter 3). ALP activity was evaluated by measuring p-nitrophenol absorption at 405 nm. In every case, ALP activity per cell was normalized by DNA quantification. Thus, ALP/DNA ratios indicate the amount of ALP activity per cell. Total DNA amount was measured using a PicoGreen dsDNA quantitation kit and following the manufacturer instructions.

Calcium deposition on the G_3Phy-crosslinked membrane surfaces (Chapter 3) was evaluated by **Alizarin red assay.** For this experiment, hMSCs were seeded on the films, and subsequently stained with alizarin red staining solution (pH = 4.2, 40 mM) for 30 min at room temperature. Then, alizarin red dye was extracted from the cell monolayer by incubating the membranes in cetylpyridinium chloride (CPC) buffer (10 wt-%, 10 mM Na_2PO_4) for 15 min. Absorbance values were read at 550 nm. Further experimental details are explained in Chapter 3.

The expression of genes related to osteogenic processes was evaluated by **Reverse Transcription (RT) and Real-Time Quantitative Polymerase Chain Reaction (qPCR)** of hMSCs cultured in presence of G_xPhy derivatives. Specifically, *COL1A1* and *ALPL* expressions were analyzed as detailed in Chapter 2.

4.5. Human MSCs secretome analysis

Paracrine factors secretion of encapsulated-hMSCs in the developed microgels was evaluated under two different conditions: oxidative stress and interferon-γ (IFN-γ) activation. All the samples were analyzed for 23 analytes using a **Luminex® Assay** (R&D Systems) and following the manufacturer's instructions. Further experimental details are described in Chapter 6.

4.6. *In vivo* persistence and survival of encapsulated-hMSCs in microgels

Luciferase-expressing hMSCs ($hMSCs^{Luc}$) were used for evaluating *in vivo* performance of ChLA microcarriers (Chapter 6). $hMSCs^{Luc}$ were generated by transducing hMSCs with lentivirus encoding for fire-fly luciferase as previously described [129]. Cell persistence and survival were evaluated by tracking the bioluminescence of encapsulated $hMSCs^{Luc}$ that were injected in dorsal subcutaneous spaces of immunocompromised mice. NSG male and female mice (5 weeks, Jackson Laboratories) were anesthetized under isoflurane and 100 μL microgel suspensions were injected in the dorsal area. Luciferin salt was dissolved in saline and sterile filtered through 0.22 μm pore membranes. Mice received a 150 mg/kg luciferin dose injected into the intraperitoneal cavity, as previously reported, and bioluminescence signal was measured using the **IVIS Spectrum CT** System at specified time points [129]. All animal experiments were performed with the approval of the Georgia Tech Animal Care and Use Committee with veterinary supervision and within the guidelines of the Guide for the Care and Use of Laboratory Animals.

General conclusions

In this thesis, a family of hydroxylic derivatives of phytic acid have been developed and successfully applied for the fabrication of bioactive polymeric systems with applications in regenerative medicine. G_xPhy compounds not only displayed attractive antioxidant and biological features regarding cell viability, proliferation and differentiation processes, but also excellent crosslinking ability that has been explored using different biofabrication techniques.

1. Synthesis and characterization of G_xPhy derivatives

Conjugation of glycerol to PA in different proportions provided two hydroxylic derivatives (G_1Phy and G_3Phy) of increasing glyceryl moieties, which modulate important biological properties. G_1Phy chelating properties approached those of PA, while G_3Phy showed a reduced capacity to form chelating complexes ascribed to the presence of higher glyceryl moieties. Both hydroxylic derivatives showed excellent antioxidant and *in vitro* lipid peroxidation inhibition properties, which are essential features in tissue remodelling processes.

The new derivatives exhibited reduced cytotoxicity in comparison to PA. Moreover, G_xPhy compounds showed excellent cytocompatibility and osteogenic properties as it was evinced by ALP and RT-qPCR experiments performed on hMSCs cultures. This approach can offer a library of compounds with different compositions to be used as an alternative to PA in biomedical and pharmaceutical applications.

2. G_3Phy-crosslinked chitosan membranes for guided bone regeneration

G_3Phy crosslinker was effectively applied for the development of chitosan membranes varying G_3Phy concentration as confirmed by spectroscopic techniques and TGA analysis.

In vitro studies revealed that membranes swelling and G_3Phy release exhibited a crosslinker content-dependent behavior. Moreover, chitosan membranes crosslinked with 10 wt-% of G_3Phy allowed the deposition of apatite-like aggregates when soaked in simulated body fluid, demonstrating their osteointegration potential.

G_3Phy-crosslinked systems showed to be excellent supports for hMSCs culture, providing osteogenesis features in comparison to uncrosslinked chitosan membranes. Specifically, G_3Phy

incorporation to chitosan membranes enhanced ALP activity and mineralization on hMSCs cultures in absence of any typical osteogenic inducer.

These systems present adequate properties for further bone tissue engineering applications, i.e. GBR.

3. Semi- and IPN systems based on chitosan and HA

Semi-IPN and IPN systems based on HA and crosslinked chitosan were developed for articular cartilage regeneration. Membranes fabrication involved G_1Phy as ionic crosslinker of chitosan and HAMA photopolymerization reaction for the IPNs systems.

Comparison of the properties of both semi- and IPN systems revealed significant differences regarding composition, mechanical and surface properties, as well as biological performance. Particularly, composition results by ICP-EOES and EA suggested a hindered release of HA from the IPN systems attributed to the covalent crosslinking. Granular surfaces were observed by AFM for semi-IPN and IPN systems, being more marked in Ch/HA semi-IPN. Viscoelasticity evaluation showed a loss tangent for the Ch/HA membranes in the range of native cartilage (tan δ=0.17).

Biological performance assessed on hMSCs revealed no cytotoxic effects as the total surface of the membranes was covered by live cells at the end of culture period (21 days). In agreement, cell proliferation increased over time for all the systems. However, Ch/HA semi-IPN notably enhanced cell proliferation respect to IPN. These findings suggest that Ch/HA semi-IPNs ionically crosslinked with G_1Phy best mimic cartilage ECM and are proposed for further studies as an effective promoter systems of cartilage repair.

4. Three-Dimensional printed scaffolds using a dual-step crosslinking approach

An innovative dual-step 3D printing methodology based on ionic crosslinking using G_1Phy and photopolymerization was implemented and optimized with excellent results. This approach allowed the fabrication of 3D gelatin and chitosan-based hydrogel scaffolds with high shape fidelity and resolution, as it was demonstrated by SEM and light microscopy inspection, leading to structures with up to 28 layers. The 3D printed scaffolds were soft, had *in vitro* long-term stability, and adequate swelling behavior as well as good biological performance using L929

Fibroblasts cell line. In this regard, the use of G_1Phy crosslinker enhanced cell adhesion and proliferation on the as-obtained 3D scaffolds in comparison to those fabricated with the widely used TPP crosslinking agent. These results open a door on hydrogel-based inks employing phytate natural-derived crosslinkers for the fabrication of intricate structures with excellent biological properties.

5. Chitosan-based microgels using in situ G_1Phy ionic crosslinking in microfluidic devices for cell encapsulation

Bioactive chitosan microgels were successfully synthetized in a flow-focusing microfluidic device via *in situ* crosslinking reaction using combination of TPP and G_1Phy as ionic crosslinkers. The implemented microfluidic approach allowed hMSCs encapsulation in the bioactive microgels by using the water-soluble chitosan derivative, ChLA.

In particular, ChLA microgels containing only 0.10 wt-% of G_1Phy offered significant advantages as hMSCs delivery platforms, including cell viability maintenance over time, upregulation of paracrine signaling at adverse conditions (e.g. oxidative stress and inflammation), minimally invasive surgery by injection and *in vivo* cell survival and persistence.

In summary, G_1Phy-crosslinked microgels emerge as a suitable cell delivery platform from a novel point of view, since its therapeutic effect is not only due to regenerative capacity and enhancement of viability of encapsulated hMSCs, but also to modulation of hMSCs secretome.

References

[1] A.S. Mao, D.J. Mooney, Regenerative medicine: Current therapies and future directions, Proceedings of the National Academy of Sciences of the United States of America 112(47) (2015) 14452-9.

[2] R. Song, M. Murphy, C. Li, K. Ting, C. Soo, Z. Zheng, Current development of biodegradable polymeric materials for biomedical applications, Drug design, development and therapy 12 (2018) 3117-3145.

[3] U. Jammalamadaka, K. Tappa, Recent Advances in Biomaterials for 3D Printing and Tissue Engineering, Journal of functional biomaterials 9(1) (2018).

[4] P. Domalik-Pyzik, J. Chłopek, K. Pielichowska, Chitosan-Based Hydrogels: Preparation, Properties, and Applications, Cellulose-Based Superabsorbent Hydrogels2018, pp. 1-29.

[5] M.C. Catoira, L. Fusaro, D. Di Francesco, M. Ramella, F. Boccafoschi, Overview of natural hydrogels for regenerative medicine applications, J Mater Sci Mater Med 30(10) (2019) 115.

[6] F. Berthiaume, T.J. Maguire, M.L. Yarmush, Tissue engineering and regenerative medicine: history, progress, and challenges, Annu Rev Chem Biomol Eng 2 (2011) 403-30.

[7] N. Celikkin, C. Rinoldi, M. Costantini, M. Trombetta, A. Rainer, W. Swieszkowski, Naturally derived proteins and glycosaminoglycan scaffolds for tissue engineering applications, Mater Sci Eng C Mater Biol Appl 78 (2017) 1277-1299.

[8] A. Muxika, A. Etxabide, J. Uranga, P. Guerrero, K. de la Caba, Chitosan as a bioactive polymer: Processing, properties and applications, International journal of biological macromolecules 105(Pt 2) (2017) 1358-1368.

[9] M.C.G. Pellá, M.K. Lima-Tenório, E.T. Tenório-Neto, M.R. Guilherme, E.C. Muniz, A.F. Rubira, Chitosan-based hydrogels: From preparation to biomedical applications, Carbohydrate polymers 196 (2018) 233-245.

[10] C. Marques, C. Som, M. Schmutz, O. Borges, G. Borchard, How the Lack of Chitosan Characterization Precludes Implementation of the Safe-by-Design Concept, 8(165) (2020).

[11] T.J. Kean, M. Thanou, Utility of Chitosan for 3D Printing and Bioprinting, Sustainable Agriculture Reviews 352019, pp. 271-292.

[12] J.R. Choi, K.W. Yong, J.Y. Choi, A.C. Cowie, Recent advances in photo-crosslinkable hydrogels for biomedical applications, BioTechniques 66(1) (2019) 40-53.

[13] Y.S. Zhang, A. Khademhosseini, Advances in engineering hydrogels, Science 356(6337) (2017).

[14] N. Annabi, A. Tamayol, J.A. Uquillas, M. Akbari, L.E. Bertassoni, C. Cha, G. Camci-Unal, M.R. Dokmeci, N.A. Peppas, A. Khademhosseini, 25th Anniversary Article: Rational Design and Applications of Hydrogels in Regenerative Medicine, Advanced Materials 26(1) (2014) 85-124.

[15] H. Geckil, F. Xu, X. Zhang, S. Moon, U. Demirci, Engineering hydrogels as extracellular matrix mimics, Nanomedicine (Lond) 5(3) (2010) 469-84.

[16] A.S. Hoffman, Hydrogels for biomedical applications, Advanced drug delivery reviews 64 (2012) 18-23.

[17] W.E. Hennink, C.F. van Nostrum, Novel crosslinking methods to design hydrogels, Advanced drug delivery reviews 54(1) (2002) 13-36.

[18] W. Hu, Z. Wang, Y. Xiao, S. Zhang, J. Wang, Advances in crosslinking strategies of biomedical hydrogels, Biomaterials Science 7(3) (2019) 843-855.

[19] D. Ficai, M.G. Albu, M. Sonmez, A. Ficai, E. Andronescu, Chapter 13 - Advances in the field of soft tissue engineering: From pure regenerative to integrative solutions, in: A.M. Grumezescu (Ed.), Nanobiomaterials in Soft Tissue Engineering, William Andrew Publishing2016, pp. 355-386.

[20] P. Sacco, M. Borgogna, A. Travan, E. Marsich, S. Paoletti, F. Asaro, M. Grassi, I. Donati, Polysaccharide-Based Networks from Homogeneous Chitosan-Tripolyphosphate Hydrogels: Synthesis and Characterization, Biomacromolecules 15(9) (2014) 3396-3405.

[21] P. Sacco, A. Travan, M. Borgogna, S. Paoletti, E. Marsich, Silver-containing antimicrobial membrane based on chitosan-TPP hydrogel for the treatment of wounds, Journal of Materials Science: Materials in Medicine 26(3) (2015) 128.

[22] A. Koc Demir, A.E. Elcin, Y.M. Elcin, Osteogenic differentiation of encapsulated rat mesenchymal stem cells inside a rotating microgravity bioreactor: in vitro and in vivo evaluation, Cytotechnology 70(5) (2018) 1375-1388.

[23] D.R. Bhumkar, V.B. Pokharkar, Studies on effect of pH on cross-linking of chitosan with sodium tripolyphosphate: a technical note, AAPS PharmSciTech 7(2) (2006) E50-E50.

[24] S. Saravanan, S. Vimalraj, P. Thanikaivelan, S. Banudevi, G. Manivasagam, A review on injectable chitosan/beta glycerophosphate hydrogels for bone tissue regeneration, International journal of biological macromolecules 121 (2019) 38-54.

[25] A. Mora-Boza, M. Puertas-Bartolomé, B. Vázquez-Lasa, J. San Román, A. Pérez-Caballer, M. Olmeda-Lozano, Contribution of bioactive hyaluronic acid and gelatin to regenerative medicine. Methodologies of gels preparation and advanced applications, (2017).

[26] B.J. Klotz, D. Gawlitta, A.J. Rosenberg, J. Malda, F.P. Melchels, Gelatin-Methacryloyl Hydrogels: Towards Biofabrication-Based Tissue Repair, Trends Biotechnol 34(5) (2016) 394-407.

[27] W.F. Hynes, N.J. Doty, T.I. Zarembinski, M.P. Schwartz, M.W. Toepke, W.L. Murphy, S.K. Atzet, R. Clark, J.A. Melendez, N.C. Cady, Micropatterning of 3D Microenvironments for Living Biosensor Applications, Biosensors (Basel) 4(1) (2014) 28-44.

[28] C.D. O'Connell, C. Di Bella, F. Thompson, C. Augustine, S. Beirne, R. Cornock, C.J. Richards, J. Chung, S. Gambhir, Z. Yue, J. Bourke, B. Zhang, A. Taylor, A. Quigley, R. Kapsa, P. Choong, G.G. Wallace, Development of the Biopen: a handheld device for surgical printing of adipose stem cells at a chondral wound site, Biofabrication 8(1) (2016) 015019.

[29] G. Camci-Unal, D. Cuttica, N. Annabi, D. Demarchi, A. Khademhosseini, Synthesis and characterization of hybrid hyaluronic acid-gelatin hydrogels, Biomacromolecules 14(4) (2013) 1085-92.

[30] X. Nie, Y.J. Chuah, D. Wang, Bioactive Hydrogels and Their Applications in Regenerative Medicine, in: C. Gao (Ed.), Polymeric Biomaterials for Tissue Regeneration: From Surface/Interface Design to 3D Constructs, Springer Singapore, Singapore, 2016, pp. 57-74.

[31] S. Mantha, S. Pillai, P. Khayambashi, A. Upadhyay, Y. Zhang, O. Tao, H.M. Pham, S.D. Tran, Smart Hydrogels in Tissue Engineering and Regenerative Medicine, Materials (Basel) 12(20) (2019).

[32] L. Oatway, T. Vasanthan, J.H. Helm, Phytic Acid, Food Reviews International 17(4) (2007) 419-431.

[33] E. Graf, J.W. Eaton, Antioxidant functions of phytic acid, Free Radical Biology and Medicine 8(1) (1990) 61-69.

[34] W.N. Addison, M.D. McKee, Inositol hexakisphosphate inhibits mineralization of MC3T3-E1 osteoblast cultures, Bone 46(4) (2010) 1100-7.

[35] K.H. Sun, Z. Liu, C. Liu, T. Yu, T. Shang, C. Huang, M. Zhou, C. Liu, F. Ran, Y. Li, Y. Shi, L. Pan, Evaluation of in vitro and in vivo biocompatibility of a myo-inositol hexakisphosphate gelated polyaniline hydrogel in a rat model, Sci Rep 6 (2016) 23931.

[36] A. Cordoba, M. Hierro-Oliva, M.A. Pacha-Olivenza, M.C. Fernandez-Calderon, J. Perello, B. Isern, M.L. Gonzalez-Martin, M. Monjo, J.M. Ramis, Direct Covalent Grafting of Phytate to Titanium Surfaces through Ti-O-P Bonding Shows Bone Stimulating Surface Properties and Decreased Bacterial Adhesion, ACS Appl Mater Interfaces 8(18) (2016) 11326-35.

[37] L.A. Hanakahi, M. Bartlet-Jones, C. Chappell, D. Pappin, S.C. West, Binding of inositol phosphate to DNA-PK and stimulation of double-strand break repair, Cell 102(6) (2000) 721-729.

[38] B.F. Harland, E.R. Morris, Phytate: A good or a bad food component?, Nutrition Research 15(5) (1995) 733-754.

[39] A.A. Lopez-Gonzalez, F. Grases, N. Monroy, B. Mari, M.T. Vicente-Herrero, F. Tur, J. Perello, Protective effect of myo-inositol hexaphosphate (phytate) on bone mass loss in postmenopausal women, Eur J Nutr 52(2) (2013) 717-26.

[40] S. Meininger, C. Blum, M. Schamel, J.E. Barralet, A. Ignatius, U. Gbureck, Phytic acid as alternative setting retarder enhanced biological performance of dicalcium phosphate cement in vitro, Sci Rep 7(1) (2017) 558.

[41] T. Obata, M. Nakashima, Phytic acid suppresses ischemia-induced hydroxyl radical generation in rat myocardium, Eur J Pharmacol 774 (2016) 20-4.

[42] A. Zajdel, A. Wilczok, L. Weglarz, Z. Dzierzewicz, Phytic acid inhibits lipid peroxidation in vitro, Biomed Res Int 2013 (2013) 147307.

[43] F. Barahuie, D. Dorniani, B. Saifullah, S. Gothai, M.Z. Hussein, A.K. Pandurangan, P. Arulselvan, M.E. Norhaizan, Sustained release of anticancer agent phytic acid from its chitosan-coated magnetic nanoparticles for drug-delivery system, Int J Nanomedicine 12 (2017) 2361-2372.

[44] A. Matejuk, A. Shamsuddin, IP6 in Cancer Therapy: Past, Present and Future, Current Cancer Therapy Reviews 6(1) (2010) 1-12.

[45] A. Bhowmik, D. Ojha, D. Goswami, R. Das, N.S. Chandra, T.K. Chatterjee, A. Chakravarty, S. Chakravarty, D. Chattopadhyay, Inositol hexa phosphoric acid (phytic acid), a nutraceuticals, attenuates iron-induced oxidative stress and alleviates liver injury in iron overloaded mice, Biomed Pharmacother 87 (2017) 443-450.

[46] F. Iemma, G. Cirillo, F. Puoci, S. Trombino, M. Castiglione, N. Picci, Iron (III) chelation and antioxidant properties of myo-inositol phosphorylated polymeric microspheres, The Journal of pharmacy and pharmacology 59(4) (2007) 597-601.

[47] F. Grases, A. Costa-Bauza, Phytate (IP6) is a powerful agent for preventing calcifications in biological fluids: usefulness in renal lithiasis treatment, Anticancer research 19(5a) (1999) 3717-22.

[48] J.M.B. Fuster, P.S. Cortés, J.P. Bestard, F.G. Freixedas, Fosfatos de origen vegetal, fitato y calcificaciones patológicas en la enfermedad renal crónica, nefrologia 37(1) (2017) 20-28.

[49] M. Arriero Mdel, J.M. Ramis, J. Perello, M. Monjo, Inositol hexakisphosphate inhibits osteoclastogenesis on RAW 264.7 cells and human primary osteoclasts, PLoS One 7(8) (2012) e43187.

[50] L. Johnson, M. Tate, Structure of" phytic acids", Canadian Journal of Chemistry 47(1) (1969) 63-73.

[51] U. Konietzny, R. Greiner, PHYTIC ACID| nutritional impact, (2003).

[52] S. Dinicola, M. Minini, V. Unfer, R. Verna, A. Cucina, M. Bizzarri, Nutritional and Acquired Deficiencies in Inositol Bioavailability. Correlations with Metabolic Disorders, Int J Mol Sci 18(10) (2017).

[53] L. Oatway, T. Vasanthan, J.H. Helm, Phytic acid, Food Reviews International 17(4) (2001) 419-431.

[54] F. Iemma, S. Trombino, F. Puoci, G. Cirillo, U.G. Spizzirri, R. Muzzalupo, N. Picci, Synthesis and antioxidant efficiency of a new copolymer containing phosphorylated myo-inositol, Macromol Biosci 5(11) (2005) 1049-56.

[55] T. Dinis, V. Madeira, L. Almeida, Action of phenolic derivatives as inhibitors of membrane lipid peroxidation and as peroxyl radical scavengers, Arch Biochem Biophys 315(161) (1994) 69.

[56] Á.A. López-González, F. Grases, N. Monroy, B. Marí, M.T. Vicente-Herrero, F. Tur, J. Perelló, Protective effect of myo-inositol hexaphosphate (phytate) on bone mass loss in postmenopausal women, European Journal of Nutrition 52(2) (2013) 717-726.

[57] M. Arriero Mdel, J.M. Ramis, J. Perello, M. Monjo, Differential response of MC3T3-E1 and human mesenchymal stem cells to inositol hexakisphosphate, Cellular physiology and biochemistry : international journal of experimental cellular physiology, biochemistry, and pharmacology 30(4) (2012) 974-86.

[58] C.-Y. Cui, S.-N. Wang, H.-H. Ren, A.-L. Li, D. Qiu, Y.-H. Gan, Y.-M. Dong, Regeneration of dental–pulp complex-like tissue using phytic acid derived bioactive glasses, RSC Advances 7(36) (2017) 22063-22070.

[59] H.-H. Ren, H.-Y. Zhao, Y. Cui, X. Ao, A.-L. Li, Z.-M. Zhang, D. Qiu, Poly(1,8-octanediol citrate)/bioactive glass composite with improved mechanical performance and bioactivity for bone regeneration, Chinese Chemical Letters 28(11) (2017) 2116-2120.

[60] T. Zhu, H. Ren, A. Li, B. Liu, C. Cui, Y. Dong, Y. Tian, D. Qiu, Novel bioactive glass based injectable bone cement with improved osteoinductivity and its in vivo evaluation, Sci Rep 7(1) (2017) 3622.

[61] K. Liu, H. Zhang, M. Lu, L. Liu, Y. Yan, Z. Chu, Y. Ge, T. Wang, C. Tang, Enhanced bioactive and osteogenic activities of titanium by modification with phytic acid and calcium hydroxide, Applied Surface Science 478 (2019) 162-175.

[62] Y. Wang, T. Zeng, S.E. Wang, W. Wang, Q. Wang, H.X. Yu, Fructo-oligosaccharides enhance the mineral absorption and counteract the adverse effects of phytic acid in mice, Nutrition 26(3) (2010) 305-11.

[63] T. Hou, W. Liu, W. Shi, Z. Ma, H. He, Desalted duck egg white peptides promote calcium uptake by counteracting the adverse effects of phytic acid, Food Chem 219 (2017) 428-435.

[64] S. Gupta, J. Lakshmi A, J. Prakash, In vitro bioavailability of calcium and iron from selected green leafy vegetables, Journal of the Science of Food and Agriculture 86(13) (2006) 2147-2152.

[65] L.H. Walter, L. Fanny, C. Charles, R. Christian, Minerals and phytic acid interactions: is it a real problem for human nutrition?, International Journal of Food Science & Technology 37(7) (2002) 727-739.

[66] C. Schultz, Prodrugs of biologically active phosphate esters, Bioorganic & Medicinal Chemistry 11(6) (2003) 885-898.

[67] M. Martínez-Tomé, M.A. Murcia, N. Frega, S. Ruggieri, A.M. Jiménez, F. Roses, P. Parras, Evaluation of antioxidant capacity of cereal brans, Journal of Agricultural and Food Chemistry 52(15) (2004) 4690-4699.

[68] M.V. Sidorova, A.K. Martusevich, A.G. Solov'eva, S.P. Peretyagin, A.R. Dorofeeva, L.N. Nistratova, N.B. Mel'nikova, Acid-Base and Antioxidant Properties of Complexes of Phytic Acid-Xymedone in Solution, Pharmaceutical Chemistry Journal 49(1) (2015) 13-20.

[69] A. Mora-Boza, M.L. López-Donaire, L. Saldaña, N. Vilaboa, B. Vazquez-Lasa, J.S. Román, Glycerylphytate compounds with tunable ion affinity and osteogenic properties, Scientific Reports 9 (2019).

[70] H. Lee, C. Jeong, K. Ghafoor, S. Cho, J. Park, Oral delivery of insulin using chitosan capsules cross-linked with phytic acid, Biomed Mater Eng 21(1) (2011) 25-36.

[71] R. Ravichandran, V. Seitz, J. Reddy Venugopal, R. Sridhar, S. Sundarrajan, S. Mukherjee, E. Wintermantel, S. Ramakrishna, Mimicking native extracellular matrix with phytic acid-crosslinked protein nanofibers for cardiac tissue engineering, Macromol Biosci 13(3) (2013) 366-75.

[72] Z. Tashi, M. Zare, N. Parvin, Application of phytic-acid as an in-situ crosslinking agent in electrospun gelatin-based scaffolds for skin tissue engineering, Materials Letters 264 (2020).

[73] X. Wang, K. Wen, X. Yang, L. Li, X. Yu, Biocompatibility and anti-calcification of a biological artery immobilized with naturally-occurring phytic acid as the crosslinking agent, J. Mater. Chem. B 5(40) (2017) 8115-8124.

[74] J.L. Drury, D.J. Mooney, Hydrogels for tissue engineering: scaffold design variables and applications, Biomaterials 24(24) (2003) 4337-4351.

[75] S. Pina, V.P. Ribeiro, C.F. Marques, F.R. Maia, T.H. Silva, R.L. Reis, J.M. Oliveira, Scaffolding Strategies for Tissue Engineering and Regenerative Medicine Applications, Materials (Basel) 12(11) (2019).

[76] B.V. Slaughter, S.S. Khurshid, O.Z. Fisher, A. Khademhosseini, N.A. Peppas, Hydrogels in regenerative medicine, Adv Mater 21(32-33) (2009) 3307-29.

[77] P. Bajaj, R.M. Schweller, A. Khademhosseini, J.L. West, R. Bashir, 3D biofabrication strategies for tissue engineering and regenerative medicine, Annu Rev Biomed Eng 16 (2014) 247-76.

[78] S. Suri, C.E. Schmidt, Photopatterned collagen-hyaluronic acid interpenetrating polymer network hydrogels, Acta Biomater 5(7) (2009) 2385-97.

[79] E.S. Dragan, Advances in interpenetrating polymer network hydrogels and their applications, Pure and Applied Chemistry 86(11) (2014) 1707-1721.

[80] H. Suo, D. Zhang, J. Yin, J. Qian, Z.L. Wu, J. Fu, Interpenetrating polymer network hydrogels composed of chitosan and photocrosslinkable gelatin with enhanced mechanical properties for tissue engineering, Mater Sci Eng C Mater Biol Appl 92 (2018) 612-620.

[81] A. Eltom, G. Zhong, A.J.A.i.M.S. Muhammad, Engineering, Scaffold techniques and designs in tissue engineering functions and purposes: a review, 2019 (2019).

[82] B. Dhandayuthapani, Y. Yoshida, T. Maekawa, D.S.J.I.j.o.p.s. Kumar, Polymeric scaffolds in tissue engineering application: a review, 2011 (2011).

[83] P. Gentile, V. Chiono, C. Tonda-Turo, A.M. Ferreira, G.J.B.j. Ciardelli, Polymeric membranes for guided bone regeneration, 6(10) (2011) 1187-1197.

[84] A.J. Nixon, E. Rickey, T.J. Butler, M.S. Scimeca, N. Moran, G.L. Matthews, A chondrocyte infiltrated collagen type I/III membrane (MACI(R) implant) improves cartilage healing in the equine patellofemoral joint model, Osteoarthritis Cartilage 23(4) (2015) 648-60.

[85] N. Mohan, P.V. Mohanan, A. Sabareeswaran, P. Nair, Chitosan-hyaluronic acid hydrogel for cartilage repair, Int J Biol Macromol 104(Pt B) (2017) 1936-1945.

[86] K. Duval, H. Grover, L.H. Han, Y. Mou, A.F. Pegoraro, J. Fredberg, Z. Chen, Modeling Physiological Events in 2D vs. 3D Cell Culture, Physiology (Bethesda) 32(4) (2017) 266-277.

[87] J. Lee, M.J. Cuddihy, N.A. Kotov, Three-dimensional cell culture matrices: state of the art, Tissue Eng Part B Rev 14(1) (2008) 61-86.

[88] W. Zhu, X. Ma, M. Gou, D. Mei, K. Zhang, S. Chen, 3D printing of functional biomaterials for tissue engineering, Current opinion in biotechnology 40 (2016) 103-112.

[89] K.M. Park, Y.M. Shin, K. Kim, H. Shin, Tissue Engineering and Regenerative Medicine 2017: A Year in Review, Tissue Eng Part B Rev 24(5) (2018) 327-344.

[90] P. Zhao, H. Gu, H. Mi, C. Rao, J. Fu, L.-s. Turng, Fabrication of scaffolds in tissue engineering: A review, Frontiers of Mechanical Engineering 13(1) (2017) 107-119.

[91] A. Mora-Boza, M.K. Włodarczyk-Biegun, A. del Campo, B. Vázquez-Lasa, J.S. Román, Glycerylphytate as an ionic crosslinker for 3D printing of multi-layered scaffolds with improved shape fidelity and biological features, Biomaterials Science 8(1) (2020) 506-516.

[92] N.E. Fedorovich, W. Schuurman, H.M. Wijnberg, H.J. Prins, P.R. van Weeren, J. Malda, J. Alblas, W.J. Dhert, Biofabrication of osteochondral tissue equivalents by printing topologically defined, cell-laden hydrogel scaffolds, Tissue Eng Part C Methods 18(1) (2012) 33-44.

[93] M. Bartnikowski, A.R. Akkineni, M. Gelinsky, M.A. Woodruff, T.J. Klein, A Hydrogel Model Incorporating 3D-Plotted Hydroxyapatite for Osteochondral Tissue Engineering, Materials (Basel) 9(4) (2016).

[94] A. Mora-Boza, M.L. Lopez-Donaire, Preparation of Polymeric and Composite Scaffolds by 3D Bioprinting, Advances in experimental medicine and biology 1058 (2018) 221-245.

[95] J. Yin, M. Yan, Y. Wang, J. Fu, H. Suo, 3D Bioprinting of Low-Concentration Cell-Laden Gelatin Methacrylate (GelMA) Bioinks with a Two-Step Cross-linking Strategy, ACS Appl Mater Interfaces 10(8) (2018) 6849-6857.

[96] Q. Wu, D. Therriault, M.-C. Heuzey, Processing and Properties of Chitosan Inks for 3D Printing of Hydrogel Microstructures, ACS Biomaterials Science & Engineering 4(7) (2018) 2643-2652.

[97] R. Levato, W.R. Webb, I.A. Otto, A. Mensinga, Y. Zhang, M. van Rijen, R. van Weeren, I.M. Khan, J. Malda, The bio in the ink: cartilage regeneration with bioprintable hydrogels and articular cartilage-derived progenitor cells, Acta Biomater 61 (2017) 41-53.

[98] S. Stratton, N.B. Shelke, K. Hoshino, S. Rudraiah, S.G. Kumbar, Bioactive polymeric scaffolds for tissue engineering, Bioact Mater 1(2) (2016) 93-108.

[99] M.K. Wlodarczyk-Biegun, A. Del Campo, 3D bioprinting of structural proteins, Biomaterials 134 (2017) 180-201.

[100] S. Derakhshanfar, R. Mbeleck, K. Xu, X. Zhang, W. Zhong, M. Xing, 3D bioprinting for biomedical devices and tissue engineering: A review of recent trends and advances, Bioact Mater 3(2) (2018) 144-156.

[101] A.V. Do, B. Khorsand, S.M. Geary, A.K. Salem, 3D Printing of Scaffolds for Tissue Regeneration Applications, Adv Healthc Mater 4(12) (2015) 1742-62.

[102] W. Jia, P.S. Gungor-Ozkerim, Y.S. Zhang, K. Yue, K. Zhu, W. Liu, Q. Pi, B. Byambaa, M.R. Dokmeci, S.R. Shin, A. Khademhosseini, Direct 3D bioprinting of perfusable vascular constructs using a blend bioink, Biomaterials 106 (2016) 58-68.

[103] K. Schutz, A.M. Placht, B. Paul, S. Bruggemeier, M. Gelinsky, A. Lode, Three-dimensional plotting of a cell-laden alginate/methylcellulose blend: towards biofabrication of tissue engineering constructs with clinically relevant dimensions, J Tissue Eng Regen Med 11(5) (2017) 1574-1587.

[104] H. Stratesteffen, M. Kopf, F. Kreimendahl, A. Blaeser, S. Jockenhoevel, H. Fischer, GelMA-collagen blends enable drop-on-demand 3D printablility and promote angiogenesis, Biofabrication 9(4) (2017) 045002.

[105] X. Wang, C. Wei, B. Cao, L. Jiang, Y. Hou, J. Chang, Fabrication of Multiple-Layered Hydrogel Scaffolds with Elaborate Structure and Good Mechanical Properties via 3D Printing and Ionic Reinforcement, ACS Appl Mater Interfaces 10(21) (2018) 18338-18350.

[106] H. Li, Y.J. Tan, S. Liu, L. Li, Three-Dimensional Bioprinting of Oppositely Charged Hydrogels with Super Strong Interface Bonding, ACS Appl Mater Interfaces 10(13) (2018) 11164-11174.

[107] G. Agrawal, R. Agrawal, Functional Microgels: Recent Advances in Their Biomedical Applications, Small 14(39) (2018) e1801724.

[108] W. Jiang, M. Li, Z. Chen, K.W. Leong, Cell-laden microfluidic microgels for tissue regeneration, Lab Chip 16(23) (2016) 4482-4506.

[109] J.P. Newsom, K.A. Payne, M.D.J.A.b. Krebs, Microgels: Modular, tunable constructs for tissue regeneration, (2019).

[110] T. Farjami, A. Madadlou, Fabrication methods of biopolymeric microgels and microgel-based hydrogels, Food Hydrocolloids 62 (2017) 262-272.

[111] N. Rajabzadeh, E. Fathi, R. Farahzadi, Stem cell-based regenerative medicine, Stem Cell Investig 6 (2019) 19-19.

[112] G. Choe, J. Park, H. Park, J.Y. Lee, Hydrogel Biomaterials for Stem Cell Microencapsulation, Polymers (Basel) 10(9) (2018).

[113] C.R. Harrell, C. Fellabaum, N. Jovicic, V. Djonov, N. Arsenijevic, V.J.C. Volarevic, Molecular mechanisms responsible for therapeutic potential of mesenchymal stem cell-derived secretome, 8(5) (2019) 467.

[114] G. Choe, J. Park, H. Park, J.Y.J.P. Lee, Hydrogel biomaterials for stem cell microencapsulation, 10(9) (2018) 997.

[115] F. Li, V.X. Truong, P. Fisch, C. Levinson, V. Glattauer, M. Zenobi-Wong, H. Thissen, J.S. Forsythe, J.E. Frith, Cartilage tissue formation through assembly of microgels containing mesenchymal stem cells, Acta Biomater 77 (2018) 48-62.

[116] A. Mora-Boza, L. García-Fernández, F.A. Barbosa, A.L. Oliveira, B. Vázquez-Lasa, J. San Román, Glycerylphytate crosslinker as a potential osteoinductor of chitosan-based systems for guided bone regeneration, Carbohydrate polymers 241 (2020) 116269.

[117] A. Skardal, J. Zhang, L. McCoard, X. Xu, S. Oottamasathien, G.D. Prestwich, Photocrosslinkable hyaluronan-gelatin hydrogels for two-step bioprinting, Tissue Eng Part A 16(8) (2010) 2675-85.

[118] S. Khunmanee, Y. Jeong, H. Park, Crosslinking method of hyaluronic-based hydrogel for biomedical applications, J Tissue Eng 8 (2017) 2041731417726464-2041731417726464.

[119] S. Ahmed, Annu, A. Ali, J. Sheikh, A review on chitosan centred scaffolds and their applications in tissue engineering, International journal of biological macromolecules 116 (2018) 849-862.

[120] A. Anitha, S. Sowmya, P.T.S. Kumar, S. Deepthi, K.P. Chennazhi, H. Ehrlich, M. Tsurkan, R. Jayakumar, Chitin and chitosan in selected biomedical applications, Progress in Polymer Science 39(9) (2014) 1644-1667.

[121] N. Kahya, Water soluble chitosan derivatives and their biological activities: A review, Polym. Sci 4(2) (2018) 1-16.

[122] J.B.M. Rocha Neto, T.B. Taketa, R.A. Bataglioli, S.B. Pimentel, D.M. Santos, A. Fiamingo, C.A.R. Costa, S.P. Campana-Filho, H.F. Carvalho, M.M. Beppu, Tailored chitosan/hyaluronan coatings for tumor cell adhesion: Effects of topography, charge density and surface composition, Applied Surface Science 486 (2019) 508-518.

[123] A.T. Iacob, M. Dragan, N. Ghetu, D. Pieptu, C. Vasile, F. Buron, S. Routier, S.E. Giusca, I.D. Caruntu, L. Profire, Preparation, Characterization and Wound Healing Effects of New

Membranes Based on Chitosan, Hyaluronic Acid and Arginine Derivatives, Polymers (Basel) 10(6) (2018).

[124] N.K. Saw, K. Chow, P.N. Rao, J.P. Kavanagh, Effects of inositol hexaphosphate (phytate) on calcium binding, calcium oxalate crystallization and in vitro stone growth, J Urol 177(6) (2007) 2366-70.

[125] J. Zhu, R.E. Marchant, Design properties of hydrogel tissue-engineering scaffolds, Expert Rev Med Devices 8(5) (2011) 607-626.

[126] A. Sannino, M. Madaghiele, L. Ambrosio, 5 - Biocompatibility and other properties of hydrogels in regenerative medicine, in: L. Di Silvio (Ed.), Cellular Response to Biomaterials, Woodhead Publishing2009, pp. 114-135.

[127] B. Page, M. PAGE, C. NOEL, A new fluorometric assay for cytotoxicity measurements in-vitro, International journal of oncology 3(3) (1993) 473-476.

[128] J. O'brien, I. Wilson, T. Orton, F. Pognan, Investigation of the Alamar Blue (resazurin) fluorescent dye for the assessment of mammalian cell cytotoxicity, European journal of biochemistry 267(17) (2000) 5421-5426.

[129] A.Y. Clark, K.E. Martin, J.R. Garcia, C.T. Johnson, H.S. Theriault, W.M. Han, D.W. Zhou, E.A. Botchwey, A.J. Garcia, Integrin-specific hydrogels modulate transplanted human bone marrow-derived mesenchymal stem cell survival, engraftment, and reparative activities, Nat Commun 11(1) (2020) 114.

Author's contributions

Publications

Ana Mora-Boza, Elena López-Ruiz, María Luisa López-Donaire, Gema Jiménez, María Rosa Aguilar, Juan Antonio Marchal, José Luis Pedraz, Blanca Vázquez-Lasa, Patricia Gálvez-Martín **Hyaluronic Acid-Based Hydrogel Membranes for Cartilage Regeneration**. (In preparation).

Ana Mora-Boza, Lina M. Mancipe Castro, Rebecca S. Schneider, Woojin M. Han, Andrés J. García, Julio San Román, Blanca Vázquez-Lasa. **Glycerylphytate-crosslinked chitosan microgels improve mesenchymal stem cell survival and upregulate secretory profile**. (In preparation).

Ana Mora-Boza, Luis García-Fernández*, Filipe A. Barbosa, Ana Leite Oliveira, Blanca Vázquez-Lasa*, Julio San Román**. Glycerylphytate crosslinker as a potential osteoinductor of chitosan-based systems for guided bone regeneration**. Carbohydrate Polymers, Volume 241, 116269 (2020).

Ana Mora-Boza, Malgorzata K. Włodarczyk-Biegun, Aránzazu del Campo, Blanca Vázquez-Lasa*, Julio San Román. **Glycerylphytate as an ionic crosslinker for 3D printing of multi-layered scaffolds with improved shape fidelity and biological features**. Biomaterials Science 8: 506-516 (2020).

Ana Mora-Boza, María Luisa López-Donaire; Laura Saldaña, Nuria Vilaboa, Blanca Vázquez-Lasa, Julio San Román. **Glycerylphytate compounds with tunable ion affinity and osteogenic properties.** Scientific Reports 9, Article number: 11491 (2019).

Luis García-Fernández, **Ana Mora-Boza**, Felisa Reyes-Ortega. **pH-Responsive Polymers: Properties, Synthesis, and Applications.** Chapter 3 of the book "Smart Polymers and Their Applications" (2nd edition). WoodHead Publishing, Elsevier (2019).

Ana Mora-Boza*, Maria Luisa Lopez-Donaire. **Preparation of polymeric and composite scaffolds by 3D Bioprinting**. Adv Exp Med Biol 1058: 221-245 (2018).

Ana Mora-Boza*, María Puertas-Bartolomé, Blanca Vázquez-Lasa, Julio San Román; Antonio Pérez-Caballer, Marta Olmeda-Lozano. **Contribution of bioactive hyaluronic acid and gelatin to regenerative medicine. Methodologies of gels preparation and advanced applications**. European Polymer Journal 95: 11-26 (2017).

**Corresponding author.*

No SCI papers

Ana Mora-Boza, Malgorzata K.Włodarczyk-Biegun, Aránzazu del Campo, Blanca Vázquez-Lasa, Julio San Román**. Chitosan-based inks: 3D printing and bioprinting strategies to improve shape fidelity, mechanical properties, and biocompatibility of 3D scaffolds**. Revista Biomecánica. Volumen 27 (2020).

María Puertas-Bartolomé, **Ana Mora-Boza**, Blanca Vázquez-Lasa. **Aplicaciones clínicas y biofabricación de sistemas poliméricos inyectables para la reparación de lesiones osteocondrales**. Revista de Plásticos Modernos 115: 731 (2018).

Conferences

2019 - **13th International Symposium Frontiers in Biomedical Polymers**. Oral Communication. Puerto de la Cruz, Tenerife (Spain). *3D bioprinting of soluble chitosan-lactate conjugate bioinks.* Ana Mora-Boza et al.

2019 - **XVII Conference on Biomaterial and Cellular Environment.** Oral Communication. Ávila (Spain). *In vitro osteoinductive and antioxidant properties of hydroxylic phytic acid derivatives*. Ana Mora-Boza et al.

2018 - **41st Edition of the Biomechanics and Biomaterials Iberian Society (SIBB) Congress**. Oral Communication. Madrid (Spain). *Improving shape fidelity in 3D printing of hydrogels*

Ana Mora-Boza et al. **Best Oral Communication Award.**

2018 - **XV edition of the Polymers Specialized Group (GEP)**. Punta Umbría (Spain). **Oral Communication**. *Synthesis and biological characterization of 3D bioprinted scaffolds using novel phytate crosslinker*. Ana Mora-Boza et al.

2018 - **29th Annual Meeting of the European Society for Biomaterials**. Maastricht (Netherlands). Poster. *Osteogenic properties of novel Phytate compounds*. Ana Mora-Boza et al.

2018 - **World Congress of the Tissue Engineering and Regenerative Medicine International Society**. Kyoto (Japan). Poster. *3D Bioprinting strategy for Chitosan-based bioinks*. Ana Mora-Boza et al.

2018 - **Comprehensive Summer School on Tissue Engineering: from biology to materials and products validation**. Trento (Italy). Oral Communication. *Development and biocompatibility of bioinks based on soluble chitosan conjugates*. Ana Mora-Boza et al.

2018 - **3rd International Conference on 3D Printing in Medicine**. Mainz (Germany). Oral Communication. *Novel bioactive crosslinker for hydrogel 3D bioprinting*. Ana Mora-Boza et al.

2017 - **28th Annual Conference for the European Society for Biomaterials**. Athens (Greece). **Poster.** *New polyfunctional crosslinking compounds for proteins and polysaccharides. Preparation of bioactive and biodegradable membranes*. Ana Mora-Boza et al.

2017 - **13th International Conference of the European Chitin Society and 8th Symposium of the Iberoamerican Chitin Society**. Seville (Spain). Poster and oral communication. *Hydrogel Membranes based on polysaccharides with potential as wound dressings in dermal applications*. Ana Mora-Boza et al.

Patents

2017 - **Novel crosslinker agents from phytic acid**. Patent reference: P201730794.

Inventors: **Ana Mora-Boza**, Luis García-Fernández, Filipe A. Barbosa, Ana Leite Oliveira, Blanca Vázquez-Lasa, Julio San Román.

Teaching

2019 - Teaching activities in **B.S. Degree in Biomedical Engineering** at Carlos III University of Madrid: Cell and Molecular Biology, and Biomaterials Experimental Design Smart-hydrogels for drug delivery.

Chapter 2

Glycerylphytate compounds with tunable ion affinity and osteogenic properties

Research article

Glycerylphytate compounds with tunable ion affinity and osteogenic properties

Ana Mora-Boza [1, 2, ‡], María Luisa López-Donaire [1, ‡], Laura Saldaña [2, 3], Nuria Vilaboa [3], Blanca Vázquez Lasa [1, 2, *], Julio San Román [1, 2]

[1] Institute of Polymer Science and Technology, ICTP-CSIC, 28006 Madrid, Spain.

[2] CIBER-BBN. Health Institute Carlos III, 28029 Madrid, Spain.

[3] Hospital Universitario La Paz-IdiPAZ, 28046 Madrid, Spain.

*corresponding author.

‡These authors contributed equally.

Scientific Reports 9, Article number: 11491 (2019)

Abstract

Phytic acid (PA) is a natural-occurring antioxidant, which plays an important role in many biological processes. PA is recognized as a potent inhibitor of lipid peroxidation because of its high affinity to multivalent cations, and it can play a role in osteogenic processes. However, its powerful chelating capacity is controversial because it can lead to a severe reduction of mineral availability in the organism. For this reason, compounds with beneficial biological properties of PA, but a modular ion binding capacity, are of high interest. In this work, we report the synthesis and physicochemical characterization of two hydroxylic derivatives of PA, named glycerylphytates (GPhy), through a condensation reaction of PA with glycerol (G). Both derivatives present antioxidant properties, measured by ferrozine/$FeCl_2$ method and chelating activity with calcium ions, depending on the content of glyceryl groups incorporated. Besides, the hydroxylic modification not only modulates the ion binding affinity of derivatives but also improves their cytocompatibility in human bone marrow mesenchymal cells (MSCs). Furthermore, GPhy derivatives display osteogenic properties, confirmed by *COL1A* and *ALPL* expression, depending

on composition. These positive features convert GPhy compounds into potent alternatives for those skeletal diseases treatments where PA is tentatively applied.

1. Introduction

Phytic acid (PA), or myo-inositol hexakisphosphate, is a powerful natural-occurring antioxidant, which constitutes up to 85% of the total phosphorus content in legumes and most cereals [1, 2]. PA is also present in mammalian cells as an endogenously synthesized compound that regulates essential biological processes [3-7]. As its name indicates, myo-inositol hexakisphosphate is a hexa-carbon carbohydrate with six phosphate groups, each one attached to a carbon group [8]. The presence of twelve ionizable protons in its structure makes PA form stable chelating complexes with multivalent cations, conferring it a potent antioxidant power. Complexes are formed with transition metals but also with amine groups and proteins [1, 9-12]. Iron-PA complexes formation has been widely studied since cell iron overload leads to the production of free radicals that can end in several degenerative processes [13]. Particularly, PA can maintain iron in the Fe(III) oxidation state by occupying all the available iron coordination sites and therefore, it can limit the formation of hydroxyl radicals [1]. Thus, PA has emerged as a powerful lipid peroxidation inhibitor [13-17]. This potent antioxidant character also makes PA play a role in diseases associated with bone loss due to the recently suggested connection between this type of pathogenesis and reactive oxygen species (ROS). ROS seem to promote osteoclastogenesis, and inhibit mineralization and osteogenesis processes [18]. In fact, an imbalance between the oxidant and antioxidant plasma biomarkers has been detected in patients with postmenopausal osteoporosis [18-20]. ROS are known to affect bone remodeling processes by activating NF-κB, a key factor involved in osteoclastogenesis [18], which stimulates the expression of cytokines such as tumor necrosis factor-α (TNF-α) and interleukin-6 (IL-6) [18, 21]. Therefore, taking into consideration the antioxidant properties of PA and the proposed influence of ROS in bone remodeling processes [21, 22], the use of PA as alternative treatment of musculoskeletal diseases is even of more interest.

On the other hand, bone mass loss is associated to an imbalance between new bone formation, mediated by osteoblasts, and bone resorption by osteoclasts [23, 24]. In this respect, in recent years

PA has arisen as an alternative antiosteoporotic agent as it has been claimed to play a key role in osteogenic processes [25]. Particularly, PA has demonstrated to be a potent *in vitro* inhibitor of osteoclastic activity, and it has also been suggested to modulate biomineralization [25, 26]. However, its mechanism of action in osteoblasts activity remains unclear and could depend on the cell type [3, 25, 26]. Thus, Arriero et al. observed that PA treatment decreased the mineralization ability of mouse MC3T3-E1 osteoblastic cells without affecting the mRNA levels of genes involved in matrix maturation such as alkaline phosphatase (ALP), osteocalcin or bone sialoprotein. Adison et al. also observed that, at physiologic concentrations, PA causes a dose-dependent inhibition of mineralization in MC3T3-E1 cultures, which was related to increased mRNA levels of osteopontin (an inhibitor of mineralization) without affecting the expression of osteocalcin and bone sialoprotein [3]. Interestingly, treatment of human umbilical cord mesenchymal stem cells (hUC-MSCs) with PA increased *ALPL* expression under osteogenic conditions [25].

Given the potential role of PA as a bone mass regulator, this paper is focused on the organic modification of PA by chemical anchorage of glyceryl moieties in different contents. This modification reduces the number of ionizable protons tuning the chelating activity with ions such as iron and calcium. It is expected that the novel chemical structure of hybrid phytate derivatives (named glycerylphytates, GPhy) also modulates some important biological properties such as cytocompatibility, cell-material interactions [27], lipid oxidation, and osteogenic activity. Thus, the synthesis of two novel hydroxylic PA derivatives was obtained by condensation reaction of glycerol (G) and PA in different feed molar ratios. GPhy products were characterized using Nuclear Magnetic Resonance (NMR), Attenuated Total Internal Reflectance Fourier Transform Infrared (ATR-FTIR), Energy Dispersive X-rays (EDX) and Induction Coupled Plasma (ICP) spectroscopic techniques. The chelating activity of GPhy compounds to Fe^{+2} and Ca^{+2} ions was analyzed. Finally, the *in vitro* biological effect of both glycerylphytate compounds was evaluated on human bone marrow mesenchymal cells (MSCs), measuring cytotoxicity, cell viability, ALP activity as well as the expression of key osteogenic genes.

2. Results and discussion

2.1 Synthesis and characterization of GPhy derivatives

The main goal of the present work was to obtain phytate derivatives with improved cytocompatibility without sacrificing the interesting biological properties of PA, and at the same time, to enlarge their applications in the biomedical and pharmaceutical fields. Thus, two phytate derivatives have been prepared by introducing glyceryl moieties in the chemical structure of PA, obtaining two compounds that were named as G_1Phy and G_3Phy, according to their G content, as it will be explained below. This type of strategy has been previously reported for different polyol-phosphate derivatives synthetized as prodrugs with enhancing bioavailability [27].

Figure 1 displays the synthetic procedure applied in the preparation of GPhy. Based on the work of He et al. [28] who proposed a 5-axial/1-equatorial structure of PA at alkaline solutions, we assumed a similar structure for solid PA. As illustrated in the synthetic scheme, there are different possibilities of reaction between the reactants due to the six phosphate groups in the PA structure and the two hydroxylic groups in the G molecule. In addition, other factors such as the PA:G ratio, the conformation of the cyclohexane ring and steric factors will have influence in the final reaction products [29]. In order to have an insight of the stoichiometry of the two condensates, structural characterization was performed. Table 1 shows the results obtained from Elemental Analysis (EA) and ICP. The formulas were deduced taking also into consideration the results of loss of water and percentage of residue at 800 ºC obtained from Thermogravimetric Analysis (TGA) of PA and both glycerylphytates. Results indicated an average number of 1 glyceryl residue for the compound obtained with a molar ratio PA:G of 5:1 and an average of 3 glyceryl groups for that obtained with a molar ratio PA:G of 1:7 (G_1Phy and G_3Phy compounds, respectively). This showed an agreement between the amount of G in the feed and the conjugation of glycerol moieties with phosphate groups. Additionally, the results suggested that the conjugation reaction was also determined by steric hindrance since the number of glyceryl conjugated moieties increased from 1 to 3 when the PA:G molar ratio varied from 5:1 to 1:7.

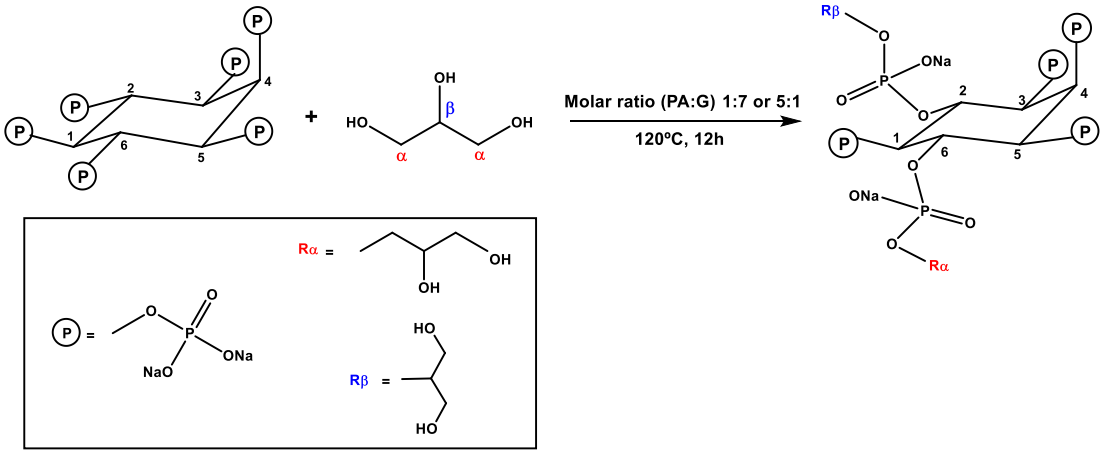

Figure 1. Synthetic procedure applied in the preparation of GPhy compounds, showing a GPhy derivative in which the PA has reacted with two glycerol molecules through α and β hydroxylic groups, respectively.

Table 1. Molecular empiric formula and elemental composition of GPhy derivatives.

Molecular formula[a]	C[b]		H[b]		Na[c]		P[c]	
	Cal%	Found%	Cal%	Found%	Cal%	Found%	Cal%	Found%
Phytic Acid $C_6H_{12}O_{24}P_6 \cdot 6Na \cdot 2H_2O$	8.70	8.34±0.01	1.95	2.50±0.02	16.66	15.26±0.81	22.45	19.81±1.59
G_1Phy $C_9H_{18}O_{26}P_6 \cdot 6Na \cdot 3H_2O$	11.75	8.85±0.03	2.63	2.99±0.10	14.99	13.33±0.72	20.20	17.10±0.68
G_3Phy $C_{15}H_{30}O_{30}P_6 \cdot 6Na \cdot 2H_2O$	17.16	17.36±0.80	3.26	4.53±0.10	13.13	10.34±1.33	17.70	12.20±1.84

[a] Determined by EA, ICP, and TGA
[b] Determined by EA
[c] Determined by ICP spectroscopy

EDX analysis confirmed the presence of expected elements and the absence of impurities (spectra not shown). The quantification of the elements content is shown in Figure S1 and results mainly reflected an increase of carbon content in the G_3Phy sample respect to those of PA and G_1Phy as it was expected due to the higher G conjugation in the former derivative. These results correlated well with those obtained by EA.

Figure 2 shows the infrared spectra of PA and GPhy derivatives. PA spectrum showed a band at 3284 cm^{-1} due to the stretching vibrations of O-H groups, which suffered a broadening in the spectra of GPhy derivatives with the glyceryl content, showing the contribution of the additional OH groups. The same observation was found in bands at 2974 and 2892 cm^{-1}, corresponding to asymmetric and symmetric stretching vibrations of C-H bonds of inositol rings and glyceryl groups. The intensities of these bands increased in both GPhy compounds, but the rise was considerably remarkable in G_3Phy due to the higher G conjugation. This feature was confirmed by the band at 1460 cm^{-1} attributed to δ CH_2 groups in glyceryl groups as we can observe in the region of interest (1500 - 400 cm^{-1}) in Figure 2 [30]. PA spectrum also showed a band at 1192 cm^{-1} corresponding to stretching vibration of P=O groups, and two bands at 1056 cm^{-1} and 913 cm^{-1}, which were attributed to P-O and C-O-P stretching vibrations in $COPO_3$ groups. Similar assignment for other phytates was given by Ishiguro et al. [31] and Guan et al. [32], who also assigned the two absorption bands at 1192 and 1056 cm^{-1} to asymmetric and symmetric stretching vibrations corresponding to P-O in HPO_3^- groups at alkaline conditions. In the synthetized glycerylphytates these absorption bands shifted to lower wave numbers respect to PA. In particular, the band due to υ P=O groups shifted from 1192 cm^{-1} in the PA spectrum to 1185 cm^{-1} in the GPhy spectra, and the intense peak at 1056 cm^{-1} attributed to υ C-O alcohols, υ P-O and P-O-C, and υ C-O glycosidic, moved to 1035 cm^{-1} in the GPhy spectra. Finally, the absorption band at 970 cm^{-1} assigned to -PO_3 groups, and peaks at 915 and 851 cm^{-1} assigned to υ P-O and P-O-C bonds shifted respect to PA. All these findings observed in the GPhy spectra indicated changes in the chemical environment of phosphate groups because of the condensation reaction [28, 31, 33].

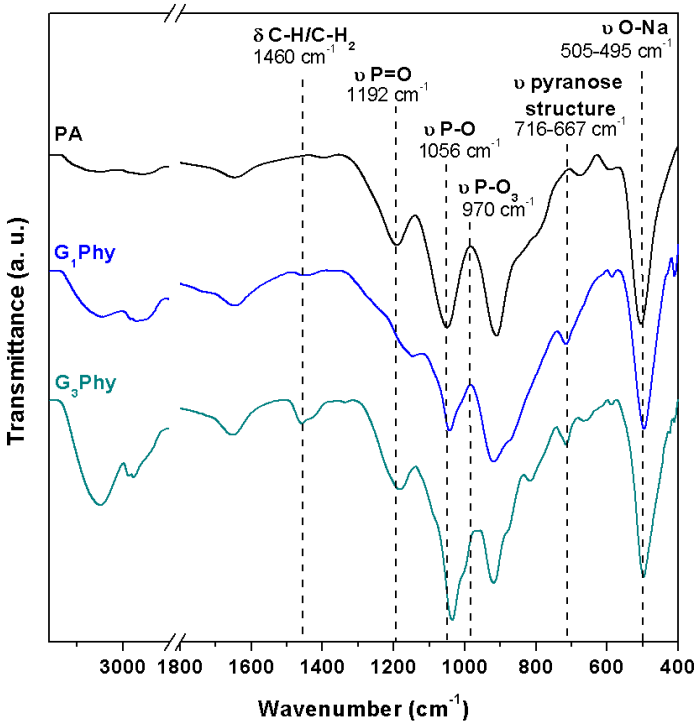

Figure 2. ATR-FTIR spectra obtained for PA, G_1Phy, and G_3Phy.

The GPhy compounds were subsequently characterized by NMR spectroscopy. The ^{13}C-NMR spectra of G_1Phy and G_3Phy and precursors are shown in Figure S2a. The spectrum of PA showed four peaks at 74.7, 76.8, 77.5 and 78.9 ppm. The assignment of these peaks was performed according to previous work of Crimella et al. [34] as follows: δ 75.3, C^4 and C^6; δ 78, C^2; δ 78.5, C^1 and C^3; and δ 79.3, C^5. The ^{13}C-NMR spectrum of G showed a peak at 63.9 ppm due to CH_2 carbons (C_α) and a peak at 73.5 ppm assigned to the CH carbons (C_β). Spectra of both derivatives were rather similar to each other and revealed notable changes in their signals respect to precursors, indicating the presence of different C atoms after the condensation reaction. ^{13}C-NMR spectrum of G_3Phy showed peaks at 63.6, 63.9, 67.3, 72.3, 72.6, 73.5, 73.7, 73.9 and 75.8 ppm. Signals in the range 63 – 68 ppm can be assigned to reacted C_α to form CH_2-O-PO_3- groups; the rest of the signals can be tentatively attributed to conjugated C_β in CH-O-PO_3- groups of the derivative and CH-O-PO_3- phytic carbons.

Figure S2b shows the ^{1}H-NMR spectra of both GPhy and precursors. Spectrum of G showed two doublet-of-doublet between 3.53 and 3.66 ppm that were assigned to no chemically equivalent H_α protons and a multiplet signal between 3.75 and 3.80 ppm assigned to H_β protons [35]. Spectrum of G_3Phy showed modified signals in the range 3.50 – 3.82 ppm and two new multiplet signals at lower field; one of them was in the range 3.82 – 3.98 ppm and it was tentatively attributed to H_α and H_β protons in the groups CH_2-O-P and CH-O-P of the glyceryl group. The other multiplet appeared in the range 4.05 – 4.10 ppm and it was attributed to H_β protons of CH-O-P groups in the glyceryl moieties. The spectra of G_1Phy differed somewhat respect to that of G_3Phy. The main difference lied in that the new multiplet in the range 3.82-3.98 ppm almost disappeared and the signal in the range 3.98 – 4.10 ppm attributed to resonance of H_β protons in glyceryl CH-O-P groups increased [34, 36]. Proton NMR analysis of GPhy derivatives varying in glyceryl content suggested that for low G content in the feed, the reactivity of β hydroxylic groups towards phosphate groups would be favoured whereas an increase in the G content would enhance the reactivity of α hydroxylic.

This hypothesis was further studied through 2D DEPT-HSQC NMR analysis. In this concatenated experiment, the carbon multiplicity information obtained from the DEPT-experiment (CH or CH_2 in our products) was detected in the 2D HSQC spectrum and illustrated in different colours (Figure 3). In the DEPT spectra of both glycerylphytates, carbons in the range 60 – 67 ppm appeared in red colour (CH_2) and carbons in the range 67 – 75 ppm appeared in blue colour (CH). Considering this information, in particular, in the 2D DEPT-HSQC spectrum of G_3Phy the intense signal at 3.8/65.8 ppm was attributed to the glyceryl CH_2-O groups conjugated with PA through CH_2-O-P bonds, and the signal at 3.8/70.7 ppm of lesser intensity to conjugated CH-O groups of glyceryl moieties forming CH-O-P bonds. In addition, another two intense signals were present in the 2D spectrum, one of them at 3.5/62.2 ppm that could be due to CH_2-O groups of reacted G, and the other one at 3.5/72.2 ppm due to reacted CH-O groups in the glyceryl moieties. As far as G_1Phy is concerned, its 2D DEPT-HSQC spectrum showed that the majority of the signals were due to association of protons with CH carbons (blue colour). Moreover, the 2D plot of G_1Phy showed less intense signals at 3.8/65.8 and 3.5/62.2 ppm as observed in G_3Phy and instead, intense signals at 4.1/72.4 and 4.1/78.5 ppm. These findings

suggest that conjugation reaction preferably proceeds between the β hydroxylic groups of G when this component is at low concentrations in the feed, whereas for higher G contents, the α hydroxylic groups are more likely to react, confirming the hypothesis previously proposed.

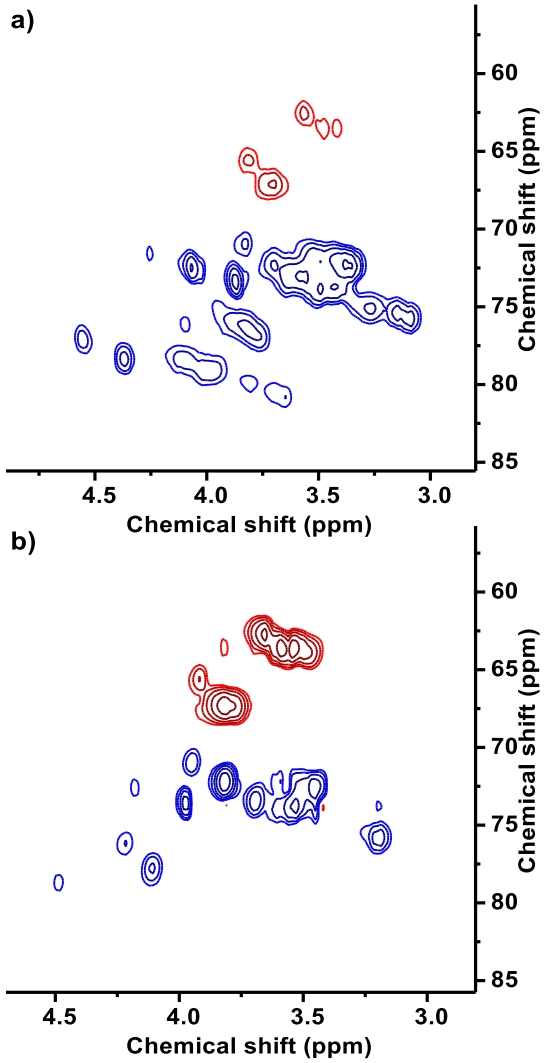

Figure 3. Two-dimensional HSQC spectra of ^{13}C-decoupled DEPT of G_1Phy **(a)** and G_3Phy **(b)** recorded in D_2O at 25ºC. For ^{1}H experiments chemical shifts were referenced to the residual proton absorption of D_2O (δ 4.79), while deuterated dioxane was used as external reference in ^{13}C experiments. In ^{13}C DEPT spectra, CH_2 signals are red while CH signals are blue.

Thermal properties of GPhy derivatives were analysed by Differential Scanning Calorimetry (DSC) and TGA techniques. DSC thermograms revealed a glass transition temperature of 50 ºC for both derivatives (thermograms not shown) indicating the amorphous character of these compounds because of the conjugation of glyceryl moieties in their structure. Table S1 summarizes the thermal degradation results of GPhy compounds and their precursors under inert atmosphere. Weight loss of glycerylphytates underwent in three stages in contrast to PA which showed four degradation steps. First stage was due to loss of water, 2 or 3 molecules for G_3Phy and G_1Phy, respectively, as explained above in the molecular formula analysis (Table 1). The second stage involved carbonization of conjugated glyceryl moieties and the dehydration of phytate structure by the decomposition of hydroxylic groups. Finally, the third and last degradation stage of GPhy (T_{max} around 340 ºC) corresponded to further decomposition of the phytate moieties (332 ºC) [37]. The residues of both derivatives obtained at 800 ºC notably decreased in comparison to PA, indicating the content of glyceryl groups after the condensation reaction.

2.2 Antioxidant properties

PA exhibits a powerful antioxidant activity due to its ion chelating capacity and hence, it is able to prevent Fenton reaction by inhibiting iron-catalysed hydroxyl radical formation [1, 14, 16, 38]. This property has repercussions on the bone mass loss, as it is known that iron-induced oxidative stress is directly linked to the activation of NF-kB, a key element in osteoclastogenesis [18, 21, 39, 40]. Then, to investigate the antioxidant properties of GPhy compounds, their chelating activity was examined by the ferrozine/$FeCl_2$ system and compared with that of PA [15]. As it can be observed in Figure 4a, PA and GPhy antioxidant properties were concentration dependent. Thus, ferrous chelating activity for PA was 33, 60, 73, and 78% at 10, 50, 100 and 300 μg/mL, respectively. Zajdel et al. [16] reported similar results regarding the powerful inhibitory capacity of PA in iron-catalysed oxidative reactions. The GPhy compounds exhibited a significantly lower antioxidant activity than PA at the lowest tested concentration (10 μg/mL). However, their antioxidant activity increased with concentration in both compounds, achieving values of 60% and 54% for G_1Phy and G_3Phy respectively at 100 μg/mL. In particular, the chelating activity of G_3Phy at all tested concentrations was significantly ($p<0.01$) lower compared to PA. G_1Phy, on the other hand, exhibited similar behaviour to G_3Phy in the range of 10-100 μg/mL, while antioxidant

activity reached to 84% at 300 μg/mL, being no significantly different ($p<0.5$) from PA value. These results indicate that antioxidant properties of GPhy compounds measured by ferrozine/$FeCl_2$ method are not only concentration dependent as occurs with PA, but also composition dependent, showing antioxidant activity in the range of 50 – 80 % for G_3Phy and G_1Phy respectively, at the highest studied concentration. This behaviour can be related to the incorporation of glyceryl moieties to PA structure, which reduces the number of ionizable protons and thus, chelating properties.

2.3 Calcium binding properties

Calcium deficiency plays a crucial role in bone-loss related diseases such as osteoporosis. Although calcium absorption can be affected with age, some dietary factors, and pharmaceutical compounds, can also act as potent chelating agents of calcium ions making them unavailable [41]. PA is shown to form insoluble complexes with Ca^{2+} [7, 42], which can lead to a decrease in calcium uptake. In fact, some studies have been focused on the adverse effects of mineral uptake mediated by PA and its strong chelation capacity, concluding that the bioavaibility of these essential minerals can be compromised [41, 43-45]. Particularly, magnesium and calcium deficiency has been linked to osteoporosis.

In this work, the Ca^{2+} binding capacity of GPhy derivatives was studied and compared with that of PA. After dropping a concentrated solution of the tested compound into a 4 mM solution of $CaCl_2$, the precipitation of a solid, white or brown for PA and GPhy compounds, respectively, was observed. The pellets were isolated and analysed by ICP spectroscopy. In Figure 4b, the stoichiometry of the Ca-phytate complexes at pH 7.5 is expressed in $moles_{Ca}/moles_{Phy}$ where Phy can be PA, G_1Phy or G_3Phy. The stoichiometry of Ca-G_1Phy complexes was quite similar to that of Ca-PA complexes. Interestingly, a notable decrease in the chelating capacity of G_3Phy was obtained. This can be explained by the higher content of glyceryl moieties in this derivative in comparison to G_1Phy. These results confirm that due to the introduction of glyceryl groups, G_3Phy derivatives show lower chelating activity than PA and they show how this modification can tune their binding ability.

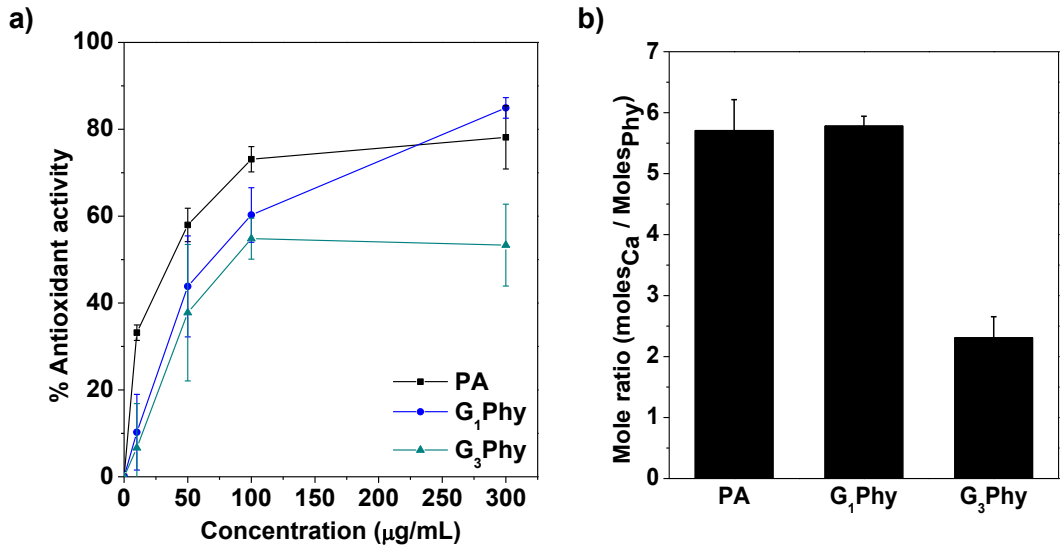

Figure 4. (a) Ferrous ions chelating activity effect of GPhy derivatives and PA at the indicated concentrations; **(b)** Chelating activity between Ca^{2+} and PA or GPhy compounds at pH 7.5.

2.4 *In vitro* biological effect of GPhy derivatives

2.4.1. Lipid peroxidation assay on RAW264.7 cells

Lipid peroxidation inhibition was measured *in vitro* by malondialdehyde-thiobarbituric acid (MDA-TBA) adduct formation after the induction of Fenton reaction with the Fe^{2+}/H_2O_2 system on RAW264.7 cells. Figure 5 shows the results of the inhibitory effect on lipid peroxidation for PA and its derivatives at 100 μg/mL concentration. A higher amount of MDA-TBA adduct is indicative of a higher oxidative stress, therefore a 100% MDA-TBA was the maximum lipid peroxidation induced in the cells (positive control). When cells were incubated with PA or its derivatives, iron-loaded related stress was reduced due to their strong ability to chelate iron species. A higher MDA concentration was observed for G_3Phy as compared to PA, which indicated a decrease in the ability to chelate iron ions as consequence of the higher content of glyceryl groups in its structure. Nevertheless, this compound was still able to prevent lipid peroxidation, as previously described for hydrolysis products of PA which maintain three or more phosphate groups [46, 47]. Accordingly, G_3Phy exhibited reasonable antioxidant iron stress properties in RAW264.7 cells in comparison to positive control. On the other side, G_1Phy showed lipid

peroxidation inhibition results comparable to PA, which correlated well with its antioxidant data obtained in previous analysis (Figure 5). These results demonstrate that G_1Phy and G_3Phy maintain and modulate both iron (II) chelation and antioxidant properties of PA in cell cultures using the RAW264.7 cell line.

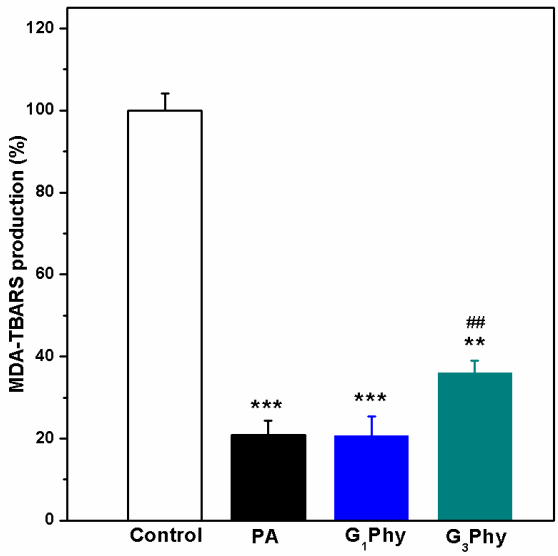

Figure 5. Effect of PA and its derivatives on MDA production. RAW267.4 cells were incubated overnight in presence of PA, G_1Phy and G_3Phy at a concentration of 100 μg/mL. Lipid peroxidation was induced with Fe^{2+}/H_2O_2 system. Analysis of variance (ANOVA) of the results for tested samples was performed with respect to positive control at significance levels of $^{**}p<0.01$ and $^{***}p<0.001$, and respect to PA at significance level of $^{\#\#}p<0.05$.

2.4.2. Cytotoxicity on MSCs

Biological properties of PA have been widely studied in different *in vitro* and *in vivo* models [2, 48-51]. Using healthy cells, Norhaizan et al. [50] reported that PA extracted from rice bran was not toxic up to 6 mM for 72 h in untransformed cultures of 3T3 cells, yielding <10% of dead cells, [50]. Similar results were reported by de Lima et al. [51] who did not observe PA cytotoxicity at 4.0 mM for 48 h in lymphocytes isolated from healthy human donors. In this work, cytotoxicity (IC_{50}) of PA and derivatives was tested in MSCs cultures using a standardized Alamar Blue assay. Viability of cells treated with G_1Phy or G_3Phy increased respect to PA. IC_{50} value of PA was 12.53±2.21 mg/mL (14.5±2.55 mM), while IC_{50} values of G_1Phy and G_3Phy were 22.81±2.64

(23.41±2.7 mM) and 29.81±2.43 mg/mL (27.45±2.23 mM), respectively. These results suggest that larger amounts of glycerylphytate derivatives than of PA could be safely used in different specific biomedical applications.

2.4.3. Osteogenic properties and biomineralization on MSCs

The osteogenic activity of glycerylphytates and PA was investigated in MSC cultures using Alamar Blue assay. To that end, firstly MSC cultures were treated with the tested compound at different concentrations for 1, 7 and 14 d. Figure 6 shows that the metabolic activity of treated cells was affected by each tested compound in a different trend depending on dose and time. Cellular viability progressively decreased with concentration and time at 7 and 14 d and the lowest values were obtained at 150-300 μg/mL. G_3Phy did not affect cell viability and even enhanced it at 300 μg/mL after long-term incubation time (14 d). The explanation of this enhancement is not clear yet but could be related to the less cytotoxicity of G_3Phy which has an IC_{50} value nearly double than that of PA. The behaviour of G_1Phy approached that of G_3Phy for a concentration range between 10 and 150 μg/mL and only a deleterious effect was observed when cells were treated for 14 d with the highest tested dose. These findings indicate that composition of the developed glycerylphytates plays a dominant role in their *in vitro* cytocompatibility and support previous results on their less cytotoxicity respect to PA.

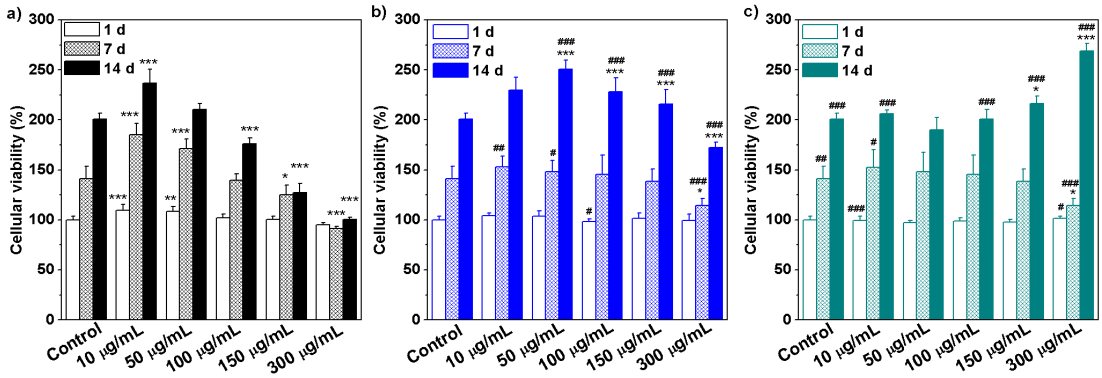

Figure 6. Cell viability (%) of PA **(a)**, G_1Phy **(b)**, and G_3Phy **(c)** at different concentrations for 1, 7 and 14 d. Mean ± SD values are relative to untreated MSCs culture for 1 d, which are given an arbitrary value of 100. ANOVA of the results for tested samples were performed with respect to control (untreated cells) at each concentration and time at significance levels of *$p<0.05$,

**p<0.01 and ***p<0.001, and respect to PA at each concentration and time at significance levels of #p<0.05, ##p<0.01 and ###p<0.001.

Since PA has been suggested to be involved in osteogenesis [3, 5], ALP activity, an early marker of osteoblast differentiation, was determined in MSCs treated with the compounds. Figure 7 depicts ALP activity of MSCs treated with 10 μg/mL PA or glycerylphytate compounds for 7 and 14 d in complete or differentiation LG-DMEM media (see experimental section). At the two incubation periods, ALP activity was higher in MSCs cultured in differentiation LG-DMEM than in complete LG-DMEM, either they were untreated or treated with compounds. Interestingly, a different response to the compounds was observed depending on the type of medium. In complete LG-DMEM, ALP activity of cells treated with PA or its derivatives slightly increased respect to control, except for the case of G_1Phy, in which ALP remained unaffected after 7 d. However, a different behaviour was observed in MSCs cultured in differentiating medium. ALP activity of cells treated with PA or G_1Phy for 7 d was similar to control, while treatment for 14 d resulted in lower ALP activity. Cells incubated with G_3Phy showed an interesting behaviour as ALP activity was slightly lower at 7 d respect to control and PA, but at 14 d it reached higher values than those found for PA and G_1Phy.

The mechanism by which PA participates in osteogenic processes is not well understood, but we can elucidate from these results that bioavailability of phosphate residues may be quite relevant. Furthermore, Addison et al. [3] proposed that the high negative charge of PA molecule also has an impact on cellular interaction and diffusion across the membrane. For this reason, a possible explanation can lie in the enhanced cell-material interactions for G_3Phy compound due to its major organic content. This hypothesis can be supported by the fact that this kind of modifications has been traditionally used for the protection of active phosphate groups, as those from PA [27]. An improved cytocompatibility would also enhance the metabolic effects that PA can trigger, as it has been demonstrated in this work. Thus, we can conclude that composition of GPhy compounds can tune the differentiation process of MSCs in comparison to PA itself.

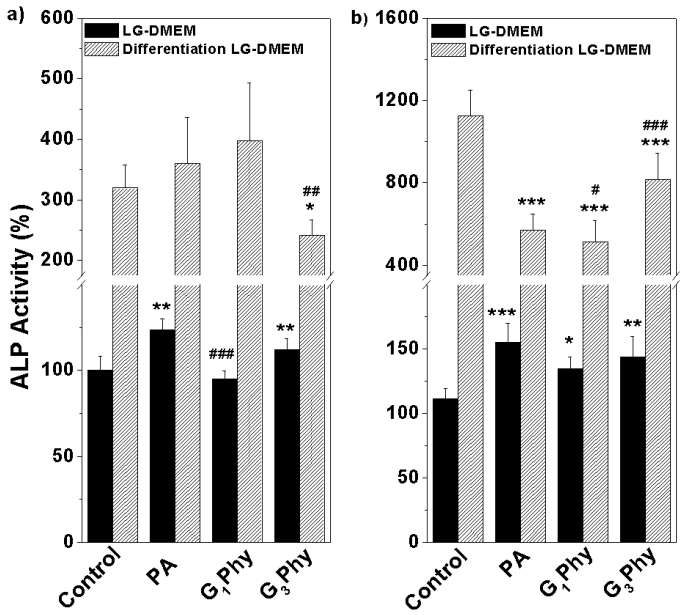

Figure 7. ALP activity normalized respect to DNA amount of MSCs treated for 7 d **(a)** or 14 d **(b)** with 10 μg/mL of PA, G_1Phy or G_3Phy. MSCs were incubated with PA or its derivatives in complete LG-DMEM (solid bars) or differentiation LG-DMEM (striped bars). Values represent the mean ± SD. ANOVA of the results for tested samples was performed with respect to the corresponding control at each time point and condition at significance levels of *p<0.05, **p<0.01 and ***p<0.001 and with respect to PA samples at each time and condition at significance levels of #p<0.05, ##p<0.01 and ###p<0.001.

2.4.4. Gene expression of osteogenic markers by RT-PCR

As previously mentioned, treatment of MSCs with PA or GPhy for 14 in complete LG-DMEM enhanced ALP activity (Figure 7b). Thus, further studies investigated whether these compounds regulate the expression, at the mRNA levels, of osteogenic differentiation markers in MSCs. Results showed that incubation of MSCs with PA for 14 d in complete LG-DMEM increased *COL1A* expression (Figure 8a). Interestingly, *COL1A* mRNA levels in MSCs treated with G_1Phy or G_3Phy were higher respect to PA suggesting that GPhy compounds could potentiate the deposition of collagen matrix, which nucleates mineral deposition during osteogenesis. On the other side, a previous study reported that treatment of hUC-MSCs with 4 μM PA for 14 d under osteogenic conditions increased *ALPL* expression [25]. Data obtained in

the present work indicated that incubation of MSCs with higher doses (10 μm/mL) of PA in complete LG-DMEM induced an increase in *ALPL* mRNA levels, suggesting that PA could promote the acquisition of osteoblastic features in MSCs populations even in the absence of osteogenic inductors. Notably, G_1Phy and G_3Phy also increased *ALPL* expression in MSCs and *ALPL* transcript levels in MSCs treated with G_1Phy were higher than those obtained in G_3Phy or PA treated cells (Figure 8b). It was not surprising that higher *ALPL* mRNA levels in G_1Phy treated MSCs were not associated to increased ALP activity levels (Figure 7b), as gene expression at the transcriptional levels does not necessarily correlate with protein activity, which is regulated by multiple post-transcriptional and post-translational mechanisms. Taken together, our results showed that PA and its derivatives might enhance MSC differentiation toward the osteoblastic lineage by regulating the expression of genes involved in matrix formation and maturation.

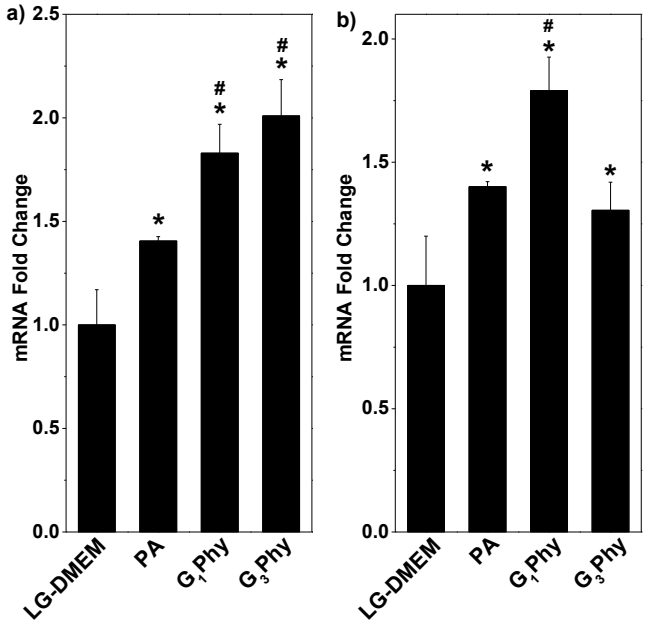

Figure 8. *COLA1A* **(a)** and *ALPL* **(b)** relative mRNA levels were determined after treating MSCs for 14 d with 10 μg/mL of PA, G_1Phy or G_3Phy. MSCs were incubated with the tested sample in complete LG-DMEM. Mean + SD values are relative to untreated MSCs, which were given an arbitrary value of 1. ANOVA of the results for tested samples was performed with respect to untreated cells at significance levels of $*p<0.05$, and with respect to PA treated cells at significance levels of $\#p<0.05$.

3. Conclusions

In this paper, we report two new glycerylphytate derivatives (G_1Phy, and G_3Phy) which have different content of glyceryl groups. The reaction conditions allow to modulate chelation properties of the compound through the amount of glyceryl moieties incorporated. The new derivatives have improved cytocompatibility and osteogenic properties in comparison to PA in MSCs. Besides, both of them possess antioxidant and *in vitro* lipid peroxidation inhibition properties, which are essential features in tissue remodelling processes.

In summary, the chelation activity and biological properties of glycerylphytate compounds can be tuned by the organic content. This approach can offer a library of compounds with different composition to be used as an alternative to PA in biomedical and pharmaceutical applications related to stress oxidative phenomenon and low bone mass density.

4. Methods

4.1 Synthesis of GPhy derivatives

PA sodium salt hydrate (PA) and glycerol (G) were purchased from Sigma-Aldrich and used without further purification. The synthesis of GPhy compounds was carried out at 120 ºC in bulk by reacting PA with the corresponding G volume for 12 h. The reaction products were dissolved in water, precipitated twice in 2-propanol, dried under reduced pressure to remove 2-propanol trace and lyophilized. Two GPhy derivatives were prepared using PA:G molar ratios of 5:1 and 1:7 which were named as G_1Phy and G_3Phy, respectively.

4.2 Physic-chemical characterization techniques

NMR experiments were performed using a Bruker AVANCE IIIHD-400 (399.86 MHz) spectrometer. Proton (^{1}H-NMR) and Carbon 13 (^{13}C-NMR) spectra were recorded in deuterated water (D_2O) at 25 ºC. ^{1}H chemical shifts were referenced to the residual proton absorption of the solvent listed as "residual internal D_2O (δ 4.79)". The acquisition conditions were as follows: spectral windows, 20.04 ppm; pulse width, 14 μs; and 128 scans with a recycle delay of 1 s. In case of ^{13}C, deuterated dioxane was use as external reference. The acquisition conditions were as follows: spectral windows, 396 ppm; pulse width, 15 μs; and 20000 scans with a recycle delay of 2

s between acquisitions. Two dimensional (2D) Heteronuclear Single-Quantum Coherence (HSQC) were recorded performing Distortionless Enhancement Polarization Transfer (DEPT) experiments (2D DEPT-HSQC). In this case, the acquisition conditions were: sweep width 165.00 ppm and 15.99 ppm for F_1 and F_2 dimensions, respectively; 256 and 8 scans for F_1 and F_2 dimensions, respectively. All measurements were conducted at 25 ºC.

ATR-FTIR spectra were obtained on a Perkin-Elmer (Spectrum One) spectrometer equipped with an ATR accessory for all samples. EA was performed with an elemental LECO model CHNS-932 microanalyzer. EDX spectrometry analysis was performed with a Bruker XFlash model with detector 5030. Inductively Coupled Plasma Optical Emission Spectrometry (ICP-OES) measurements were carried out in a 4300 DV Perkin-Elmer plasma emission spectrometer using a Gemcone (Perkin-Elmer) nebulizer. DSC experiments were carried out on a DSC model 8500 (PerkinElmer). Three heating-cooling cycles were analysed between 25 ºC and 180 ºC with a scanning rate of 10 ºC/min under nitrogen at 20 mL/min flow rate. From the thermograms, the glass transition temperature (T_g) was determined as the midpoint of the transition. TGA was performed in a thermogravimetric analyzer TGA Q500 (TA instruments) apparatus, under dynamic nitrogen at a heating rate of 10 ºC/min in a range of 40 - 800 ºC.

4.3 Formation of ions chelate complexes

The iron chelate complexes formation was studied by the method of Dinis et al. [15] PA and GPhy compounds at various concentrations (10-300 μg/ml) in dH_2O (0.4 mL) were added to a solution of 2 mM $FeCl_2$ (0.05 mL, Sigma Aldrich). The mixture was shaken vigorously and left at room temperature for 15 min under darkness conditions. Then, 0.2 mL of 5 mM ferrozine (Sigma Aldrich) solution was added, and the total volume was adjusted to 4 mL with ethanol. Absorbance of the solution was measured spectrophotometrically at 562 nm with a NanoDrop™ spectrophotometer. 10 mM EDTA solution and dH_2O were used as positive and negative controls, respectively. The experiments were conducted in triplicate for each sample and the data obtained were expressed as mean values ± standard deviations (SD).

The binding capacity of PA and GPhy derivatives to calcium ions was examined with an adapted method from Saw et al. [52] Particularly, aliquots of 50 µl at a concentration of 396 mg/mL of each compound were added to a 20 mL of a 4 mM solution of $CaCl_2$ in intervals of 2 min until achieving a final concentration of 5.27 mg/mL of each compound in the solution. The pH was controlled by preparing all the solutions in Tris-HCl 0.1M buffer pH 7.5. The pellet was isolated by centrifuging at 4 ºC and 8000 rpm (Eppendorf centrifuge 5810R model) for 10 min and washed with dH_2O. The final pellet was digested at 65 ºC with 65% v/v HNO_3. Finally, the phosphorus and calcium content of these pellets in 5% v/v HNO_3 solution were measured by ICP. The experiments were conducted in triplicate for each sample and the data obtained were expressed as mean values ± SD.

4.4 Cell culture

Human mesenchymal stem cells from bone marrow (MSCs, Innoprot) were grown and maintained in Mesenchymal Stem Cell Medium Kit (Innoprot) at 37 ºC in a humidified atmosphere of 5% CO_2. Cell culture media was refreshed every 48 h. For subsequent experiments, MSCs were cultured in Low Glucose Dulbecco's Modified Eagle Medium (LG-DMEM), supplemented with 20% fetal bovine serum (FBS), 200 mM L-glutamine, 100 units/mL penicillin and 100 µg/mL streptomycin (complete LG-DMEM). Differentiation medium consisted of complete LG-DMEM supplemented with dexamethasone (100 nM), ascorbic acid (50 µg/mL), and β-glycerolphosphate (10 mM). All the experiments were performed using MSCs at passages 4 to 8.

Murine RAW 264.7 macrophage cell line (Innoprot) were grown and maintained in DMEM supplemented with 10% FBS, 200 mM L-glutamine, 100 units/mL penicillin and 100 µg/mL streptomycin, at 37 ºC in a humidified atmosphere of 5% CO_2. Cell culture media was refreshed every 48 h and these cells were used at passages 5 to 6 for all the experiments.

4.5 Lipid peroxidation assay

Lipid peroxidation inhibition was tested in RAW264.7 cells, as macrophages are the major sources of oxidative stress and are used to evaluate the antioxidant function of dietary natural compounds [53]. $2x10^6$ RAW264.7 cells were seeded in 6-well plates and incubated for 24 h with

the corresponding solution of PA, G_1Phy or G_3Phy at final concentration of 100 μg/mL. For positive (lipid peroxidation induction but without any studied agent) and negative (no lipid peroxidation induction) controls, the same volume of dH_2O than for the studied samples was added. Lipid peroxidation was induced by incubating the samples with 50 μM $Fe_2SO_4 \cdot 7H_2O$ and 200 μM H_2O_2 solution at 37 ºC for 4 h in order to trigger the Fenton reaction [54]. Lipid peroxidation was evaluated using the Lipid Peroxidation Assay Kit (abcam), following the manufacturer instructions. The percentage (%) of lipid peroxidation inhibition was calculated respect to the positive control, considering it as the 100% of MDA producer. The experiments were conducted in triplicate for each sample and the data obtained were expressed as mean values ± SD.

4.6 Cytotoxicity

Cytotoxicity of PA and GPhy compounds was evaluated in MSCs cultures using the Alamar Blue assay. A stock solution of the corresponding tested compound in DMEM lacking FBS and containing 2% w/v D-sorbitol was prepared and successive dilutions were tested (5, 15, 20, 30, 50 mg/mL). 9000 of MSCs were seeded in 96-well plates and incubated for 24 h. Then, the medium was replaced, and the cells were treated with the tested compounds for 24 h. A 10% v/v Alamar Blue (Invitrogen) solution was prepared in DMEM without phenol red and the plates were incubated at 37 ºC for 3 h. Medium was collected and, after laser excitation at 590 nm, emitted fluorescence at 530 nm was quantified using a Biotek Synergy HT plate reader (Biotek Synergy HT spectrophotometer).

4.7 Cell viability

Alamar Blue assay was also used to analyse cell viability after incubation of MSCs with the tested compounds for 3, 7 and 14 d. For this experiment, 10^4 of MSCs were seeded in 48-well plates and cultured in Mesenchymal Stem Cell Medium Kit for 24 h. Then, the medium was replaced, and the cells were treated with the tested solutions at various concentrations in complete LG-DMEM (10, 50, 100, 150, and 300 μg/mL), and media containing the corresponding compounds were refreshed every 2 d. Medium was collected and, after laser excitation at 590 nm, emitted fluorescence at 530 nm was quantified using a Biotek Synergy HT plate reader (Biotek

Synergy HT spectrophotometer). The experiments were conducted in triplicate for each sample and the data obtained were expressed as mean values ± SD.

4.8 ALP activity quantification

ALP activity was evaluated after 3, 7 and 14 d of incubation of MSCs with the tested compounds. Total DNA amount was measured using the PicoGreen dSDNA quantitation kit (Molecular Probes). Determination of the ALP/DNA ratio is indicative of the amount of ALP activity per cell. For this experiment, 10^4 of MSCs were seeded in 48-well plates and cultured in Mesenchymal Stem Cell Medium Kit for 24 h. Then, the medium was replaced, and the cells were treated with PA and its derivatives solutions at 10 μg/mL. The media containing the corresponding compounds were refreshed every 2 d. Negative and positive controls correspond to cells cultured in complete or differentiation LG-DMEM media, respectively. The experiments were conducted in triplicate for each sample and the data obtained were expressed as mean values ± SD.

4.9 Analysis of differential gene expression by reverse transcription (RT) and real-time quantitative PCR (qPCR)

For this experiment, 10^6 of MSCs were seeded in 6-well plates and cultured in complete Mesenchymal Stem Cell Medium Kit for 24 h. Then, the medium was replaced, and the cells were treated with PA and its derivatives solutions at 10 μg/mL in complete LG-DMEM. Media containing the corresponding compounds were refreshed every 2 d. Total RNA was prepared using the RNeasy Mini Kit (Qiagen), following the manufacturer's instructions. To quantify the levels of *ALPL* and *COL1A1* mRNA, complementary DNA was prepared from total RNA using the Transcriptor Reverse Transcriptase and an anchored oligo (dT)18 primer (Roche Applied Science). qPCR was performed using LightCycler FastStart DNA Master SYBR Green I and LightCycler detector (both from Roche Applied Science). Quantitative expression values were extrapolated from standard curves and were normalized to the expression values of beta-2-microglobulin (*B2M*) and beta-glucuronidase (*GUSB*) which were used as endogenous controls. Specific oligonucleotide primers were*: COL1A1*, 5'-CGGGCCTCAAGGTATTGCT-3' (forward primer, F) and 5'-GGGACCTTGTTTGCCAGGTT-3' (reverse primer, R); *ALPL*, 5´-GACTAAGAAGCCCTTCACTGCCAT-3´ (F), 5´- GACTGCGCCTGGTAGTTGTT-3´ (R);

B2M, 5'-CCAGCAGAGAATGGAAAGTC-3' (F) and 5'-GATGCTGCTTACATGTCTCG-3' (R) ; *GUSB*, 5´-AAACGATTGCAGGGTTTCAC -3´ (F), 5´-CTCTCGTCGGTGACTGTTCA-3´(R).

4.10 Statistical analysis of data

Analysis of variance (ANOVA) of the results in each experiment for tested samples was performed with respect to LG-DMEM or differentiation LG-DMEM at each time and condition at significance level of *$p<0.05$, **$p<0.01$ and ***$p<0.001$, and with respect to PA samples at each time and condition at significance levels of #$p<0.05$, ##$p<0.01$ and ###$p<0.001$.

5. References

[1] E. Graf, J.W. Eaton, Antioxidant functions of phytic acid, Free Radical Biol. Med. 8(1) (1990) 61-69.

[2] L. Oatway, T. Vasanthan, J.H. Helm, Phytic Acid, Food Rev. Int. 17(4) (2007) 419-431.

[3] W.N. Addison, M.D. McKee, Inositol hexakisphosphate inhibits mineralization of MC3T3-E1 osteoblast cultures, Bone 46(4) (2010) 1100-7.

[4] K.H. Sun, Z. Liu, C. Liu, T. Yu, T. Shang, C. Huang, M. Zhou, C. Liu, F. Ran, Y. Li, Y. Shi, L. Pan, Evaluation of in vitro and in vivo biocompatibility of a myo-inositol hexakisphosphate gelated polyaniline hydrogel in a rat model, Sci Rep 6 (2016) 23931.

[5] A. Cordoba, M. Hierro-Oliva, M.A. Pacha-Olivenza, M.C. Fernandez-Calderon, J. Perello, B. Isern, M.L. Gonzalez-Martin, M. Monjo, J.M. Ramis, Direct Covalent Grafting of Phytate to Titanium Surfaces through Ti-O-P Bonding Shows Bone Stimulating Surface Properties and Decreased Bacterial Adhesion, ACS Appl Mater Interfaces 8(18) (2016) 11326-35.

[6] L.A. Hanakahi, M. Bartlet-Jones, C. Chappell, D. Pappin, S.C. West, Binding of inositol phosphate to DNA-PK and stimulation of double-strand break repair, Cell 102(6) (2000) 721-729.

[7] B.F. Harland, E.R. Morris, Phytate: A good or a bad food component?, Nutrition Research 15(5) (1995) 733-754.

[8] A. Matejuk, A. Shamsuddin, IP6 in Cancer Therapy: Past, Present and Future, Current Cancer Therapy Reviews 6(1) (2010) 1-12.

[9] M. Martínez-Tomé, M.A. Murcia, N. Frega, S. Ruggieri, A.M. Jiménez, F. Roses, P. Parras, Evaluation of antioxidant capacity of cereal brans, Journal of Agricultural and Food Chemistry 52(15) (2004) 4690-4699.

[10] M.V. Sidorova, A.K. Martusevich, A.G. Solov'eva, S.P. Peretyagin, A.R. Dorofeeva, L.N. Nistratova, N.B. Mel'nikova, Acid-Base and Antioxidant Properties of Complexes of Phytic Acid-Xymedone in Solution, Pharm. Chem. J. 49(1) (2015) 13-20.

[11] H. Lee, C. Jeong, K. Ghafoor, S. Cho, J. Park, Oral delivery of insulin using chitosan capsules cross-linked with phytic acid, Biomed Mater Eng 21(1) (2011) 25-36.

[12] R. Ravichandran, V. Seitz, J. Reddy Venugopal, R. Sridhar, S. Sundarrajan, S. Mukherjee, E. Wintermantel, S. Ramakrishna, Mimicking native extracellular matrix with phytic acid-crosslinked protein nanofibers for cardiac tissue engineering, Macromol. Biosci. 13(3) (2013) 366-75.

[13] F. Iemma, G. Cirillo, F. Puoci, S. Trombino, M. Castiglione, N. Picci, Iron (III) chelation and antioxidant properties of myo-inositol phosphorylated polymeric microspheres, The Journal of pharmacy and pharmacology 59(4) (2007) 597-601.

[14] F. Iemma, S. Trombino, F. Puoci, G. Cirillo, U.G. Spizzirri, R. Muzzalupo, N. Picci, Synthesis and antioxidant efficiency of a new copolymer containing phosphorylated myo-inositol, Macromol Biosci 5(11) (2005) 1049-56.

[15] T. Dinis, V. Madeira, L. Almeida, Action of phenolic derivatives as inhibitors of membrane lipid peroxidation and as peroxyl radical scavengers, Arch Biochem Biophys 315(161) (1994) 69.

[16] A. Zajdel, A. Wilczok, L. Weglarz, Z. Dzierzewicz, Phytic acid inhibits lipid peroxidation in vitro, Biomed Res Int 2013 (2013) 147307.

[17] A. Bhowmik, D. Ojha, D. Goswami, R. Das, N.S. Chandra, T.K. Chatterjee, A. Chakravarty, S. Chakravarty, D. Chattopadhyay, Inositol hexa phosphoric acid (phytic acid), a nutraceuticals, attenuates iron-induced oxidative stress and alleviates liver injury in iron overloaded mice, Biomed Pharmacother 87 (2017) 443-450.

[18] V. Domazetovic, G. Marcucci, T. Iantomasi, M.L. Brandi, M.T. Vincenzini, Oxidative stress in bone remodeling: role of antioxidants, Clinical Cases in Mineral and Bone Metabolism 14(2) (2017) 209-216.

[19] J.M.S. Davies, J. Cillard, B. Friguet, E. Cadenas, J. Cadet, R. Cayce, A. Fishmann, D. Liao, A.L. Bulteau, F. Derbre, A. Rebillard, S. Burstein, E. Hirsch, R.A. Kloner, M. Jakowec, G.

Petzinger, D. Sauce, F. Sennlaub, I. Limon, F. Ursini, M. Maiorino, C. Economides, C.J. Pike, P. Cohen, A.N. Salvayre, M.R. Halliday, A.J. Lundquist, N.A. Jakowec, F. Mechta-Grigoriou, M. Mericskay, J. Mariani, Z. Li, D. Huang, E. Grant, H.J. Forman, C.E. Finch, P.Y. Sun, L.C.D. Pomatto, O. Agbulut, D. Warburton, C. Neri, M. Rouis, P. Cillard, J. Capeau, J. Rosenbaum, K.J.A. Davies, The Oxygen Paradox, the French Paradox, and age-related diseases, GeroScience 39(5-6) (2017) 499-550.

[20] O. Altindag, O. Erel, N. Soran, H. Celik, S. Selek, Total oxidative/anti-oxidative status and relation to bone mineral density in osteoporosis, Rheumatology international 28(4) (2008) 317-21.

[21] J. Tsay, Z. Yang, F.P. Ross, S. Cunningham-Rundles, H. Lin, R. Coleman, P. Mayer-Kuckuk, S.B. Doty, R.W. Grady, P.J. Giardina, A.L. Boskey, M.G. Vogiatzi, Bone loss caused by iron overload in a murine model: importance of oxidative stress, Blood 116(14) (2010) 2582-2589.

[22] V. Domazetovic, G. Marcucci, T. Iantomasi, M.L. Brandi, M.T. Vincenzini, Oxidative stress in bone remodeling: role of antioxidants, Clinical cases in mineral and bone metabolism : the official journal of the Italian Society of Osteoporosis, Mineral Metabolism, and Skeletal Diseases 14(2) (2017) 209-216.

[23] N.A. Sims, T.J. Martin, Coupling the activities of bone formation and resorption: a multitude of signals within the basic multicellular unit, BoneKEy reports 3 (2014) 481.

[24] B.J. Kim, J.M. Koh, Coupling factors involved in preserving bone balance, Cellular and molecular life sciences : CMLS (2018).

[25] M. Arriero Mdel, J.M. Ramis, J. Perello, M. Monjo, Differential response of MC3T3-E1 and human mesenchymal stem cells to inositol hexakisphosphate, Cell. Physiol. Biochem. 30(4) (2012) 974-86.

[26] M. Arriero Mdel, J.M. Ramis, J. Perello, M. Monjo, Inositol hexakisphosphate inhibits osteoclastogenesis on RAW 264.7 cells and human primary osteoclasts, PLoS One 7(8) (2012) e43187.

[27] C. Schultz, Prodrugs of biologically active phosphate esters, Biorg. Med. Chem. 11(6) (2003) 885-898.

[28] Z. He, C.W. Honeycutt, T. Zhang, P.M. Bertsch, Preparation and FT-IR characterization of metal phytate compounds, J. Environ. Qual. 35(4) (2006) 1319-28.

[29] L.R. Isbrandt, R.P. Oertel, Conformational states of myo-inositol hexakis (phosphate) in aqueous solution. A carbon-13 NMR, phosphorus-31 NMR, and Raman spectroscopic investigation, Journal of the American Chemical Society 102(9) (1980) 3144-3148.

[30] Z. He, C.W. Honeycutt, B. Xing, R.W. McDowell, P.J. Pellechia, T. Zhang, Solid-state fourier transform infrared and ^{31}P nuclear magnetic resonance spectral features of phosphate compounds, Soil Science 172(7) (2007) 501-515.

[31] T. Ishiguro, T. Ono, K. Nakasato, C. Tsukamoto, S. Shimada, Rapid measurement of phytate in raw soymilk by mid-infrared spectroscopy, Biosci Biotechnol Biochem 67(4) (2003) 752-7.

[32] X.H. Guan, C. Shang, J. Zhu, G.H. Chen, ATR-FTIR investigation on the complexation of myo-inositol hexaphosphate with aluminum hydroxide, J. Colloid Interface Sci. 293(2) (2006) 296-302.

[33] D. Xiao, F. Yang, X. Zhou, Z. Chen, K. Duan, J. Weng, G. Feng, Small organic molecule-mediated hydrothermal synthesis of hierarchical porous hydroxyapatite microspheres by the incorporation of copper ions, RSC Advances 7(70) (2017) 44371-44375.

[34] T. Crimella, S. Villa, F. Rossi, G. Fiorelli, A. Zanella, Determination of purity of commercially available inositol hexaphosphate (phytates) and preparation of a reference material, Adv. Exp. Med. Biol. 326 (1992) 51-4.

[35] V. Govindaraju, K. Young, A.A. Maudsley, Proton NMR chemical shifts and coupling constants for brain metabolites, NMR in biomedicine 13(3) (2000) 129-53.

[36] L. Barrientos, J.J. Scott, P.P. Murthy, Specificity of hydrolysis of phytic acid by alkaline phytase from lily pollen, Plant Physiology 106(4) (1994) 1489-1495.

[37] A.L.M. Daneluti, J.d.R. Matos, Study of thermal behavior of phytic acid, Brazilian Journal of Pharmaceutical Sciences 49(2) (2013) 275-283.

[38] T. Obata, M. Nakashima, Phytic acid suppresses ischemia-induced hydroxyl radical generation in rat myocardium, Eur. J. Pharmacol. 774 (2016) 20-4.

[39] V. D Kancheva, O. T Kasaikina, Bio-antioxidants–a chemical base of their antioxidant activity and beneficial effect on human health, Current medicinal chemistry 20(37) (2013) 4784-4805.

[40] X. Wang, B. Chen, J. Sun, Y. Jiang, H. Zhang, P. Zhang, B. Fei, Y. Xu, Iron-induced oxidative stress stimulates osteoclast differentiation via NF-kappaB signaling pathway in mouse model, Metabolism: clinical and experimental 83 (2018) 167-176.

[41] T. Hou, W. Liu, W. Shi, Z. Ma, H. He, Desalted duck egg white peptides promote calcium uptake by counteracting the adverse effects of phytic acid, Food Chem. 219 (2017) 428-435.

[42] M.D. Ferrer, M.M. Perez, M.M. Canaves, J.M. Buades, C. Salcedo, J. Perello, A novel pharmacodynamic assay to evaluate the effects of crystallization inhibitors on calcium phosphate crystallization in human plasma, Sci Rep 7(1) (2017) 6858.

[43] Y. Wang, T. Zeng, S.E. Wang, W. Wang, Q. Wang, H.X. Yu, Fructo-oligosaccharides enhance the mineral absorption and counteract the adverse effects of phytic acid in mice, Nutrition 26(3) (2010) 305-11.

[44] S. Gupta, J. Lakshmi A, J. Prakash, In vitro bioavailability of calcium and iron from selected green leafy vegetables, Journal of the Science of Food and Agriculture 86(13) (2006) 2147-2152.

[45] L.H. Walter, L. Fanny, C. Charles, R. Christian, Minerals and phytic acid interactions: is it a real problem for human nutrition?, Int. J. Food Sci. Tech. 37(7) (2002) 727-739.

[46] S. Miyamoto, K. Murota, G. Kuwataz, M. Imai, A. Nagao, J. Terao, Antioxidant activity of phytic acid hydrolysis products on iron ion-induced oxidative damage in biological system, ACS Symposium Series, Washington, DC; American Chemical Society; 1999, 2002, pp. 241-250.

[47] S. Miyamoto, G. Kuwata, M. Imai, A. Nagao, J. Terao, Protective effect of phytic acid hydrolysis products on iron-induced lipid peroxidation of liposomal membranes, Lipids 35(12) (2000) 1411.

[48] Q. Xu, A.G. Kanthasamy, M.B. Reddy, Neuroprotective effect of the natural iron chelator, phytic acid in a cell culture model of Parkinson's disease, Toxicology 245(1-2) (2008) 101-108.

[49] M. Arya, P. Tiwari, C.B. Tripathi, P. Parashar, M. Singh, P. Sinha, N.P. Yadav, G. Kaithwas, K.P. Gupta, S.A. Saraf, Colloidal vesicular system of Inositol hexaphosphate to counteract DMBA induced dysregulation of markers pertaining to cellular proliferation/differentiation and inflammation of epidermal layer in mouse model, Mol. Pharm. 14(3) (2017) 928-939.

[50] M.E. Norhaizan, S.K. Ng, M.S. Norashareena, M.A. Abdah, Antioxidant and cytotoxicity effect of rice bran phytic acid as an anticancer agent on ovarian, breast and liver cancer cell lines, Malaysian Journal of Nutrition 17(3) (2011) 367-375.

[51] E.M. de Lima, C.C. Kanunfre, L.F. de Andrade, D. Granato, N.D. Rosso, Cytotoxic effect of inositol hexaphosphate and its Ni(II) complex on human acute leukemia Jurkat T cells, Toxicol. In Vitro 29(8) (2015) 2081-2088.

[52] N.K. Saw, K. Chow, P.N. Rao, J.P. Kavanagh, Effects of inositol hexaphosphate (phytate) on calcium binding, calcium oxalate crystallization and in vitro stone growth, J Urol 177(6) (2007) 2366-70.

[53] O.A. Castaneda, S.-C. Lee, C.-T. Ho, T.-C. Huang, Macrophages in oxidative stress and models to evaluate the antioxidant function of dietary natural compounds, journal of food and drug analysis 25(1) (2017) 111-118.

[54] B. Fuhrman, J. Oiknine, M. Aviram, Iron induces lipid peroxidation in cultured macrophages, increases their ability to oxidatively modify LDL, and affects their secretory properties, Atherosclerosis 111(1) (1994) 65-78.

Acknowledgments

The authors thank financial support to Ministry of Science, Innovation and Universities (Spain, MAT2017-2017-84277-R), Instituto Salud Carlos III (ISCIII)-Fondo Europeo de Desarrollo Regional (FEDER), MINECO-AES (PI18/00643 and PI15/01118). Ana Mora-Boza is supported by "La Caixa" Foundation (Scholarship code LCF/BQ/ES16/11570018), Laura Saldaña is supported by a Miguel Servet contract from ISCIII-MINECO-AES-FEDER-FSE. Nuria Vilaboa is supported by Program I2 from Comunidad Autónoma de Madrid. The authors are indebted to Rosana Ramirez (ICTP-CSIC) and Fatima Bensiamar (IdiPAZ and CIBER-BBN) for excellent technical assistance with cell culture experiments and gene expression analysis, respectively.

6. Supporting information

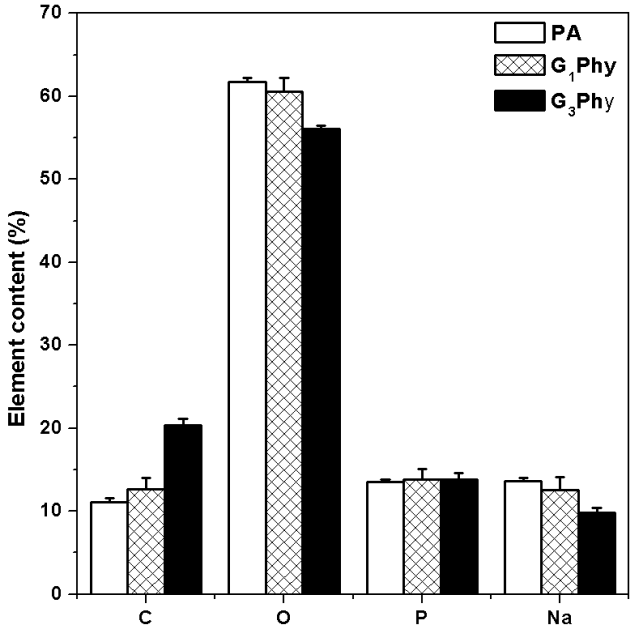

Figure S1. Elements content quantification of PA and GPhy derivatives by EDX spectroscopy.

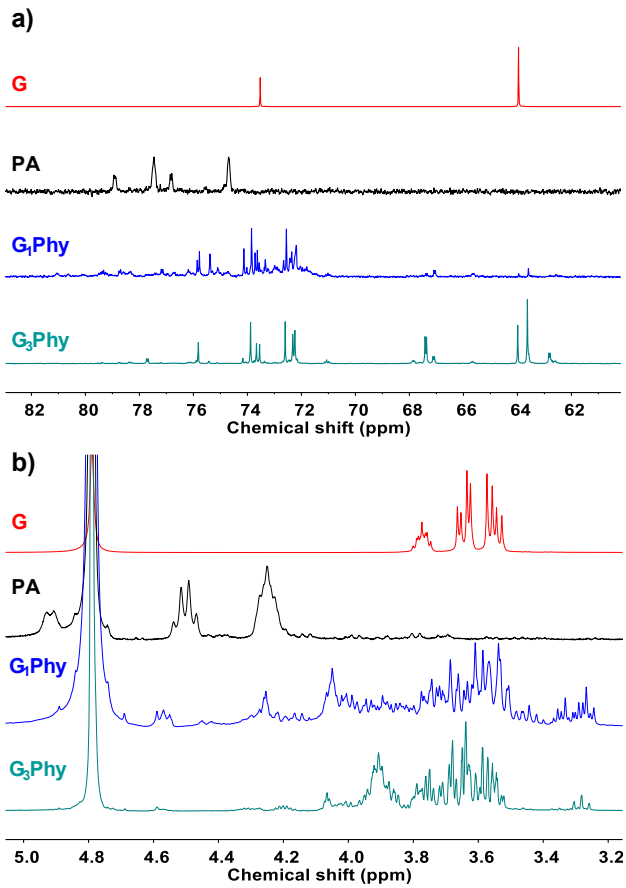

Figure S2. ^{13}C-NMR **(a)** and ^{1}H-NMR **(b)** spectra of G, PA and GPhy derivatives recorded in D_2O at 25ºC. For ^{13}C experiments chemical shifts were referenced to deuterated dioxane while the residual proton absorption of D_2O (δ 4.79) was used as external reference in ^{1}H experiments.

Table S1. Thermal degradation results for G, PA and GPhy compounds under inert atmosphere.

Sample	T_{max} (ºC)				Residue (%) at 800 ºC
	1st stage	2nd stage	3rd stage	4th stage	
G	228	-	-	-	0
PA	117	215	332	394	75
G_1Phy	137	242	356	-	69
G_3Phy	125	215	337	-	52

Chapter 3

Glycerylphytate crosslinker as a potential osteoinductor of chitosan-based systems for guided bone regeneration

Research Article

Glycerylphytate crosslinker as a potential osteoinductor of chitosan-based systems for guided bone regeneration

Ana Mora-Boza [a, b], Luis García-Fernández [a, b, *], Filipe A. Barbosa [c], Ana Leite Oliveira [c], Blanca Vázquez-Lasa [a, b, *], Julio San Román [a, b]

[a] Institute of Polymer science and Technology, ICTP-CSIC, 28006 Madrid, Spain.

[b] CIBER-BBN. Instituto de Salud Carlos III, 28029 Madrid, Spain.

[c] Universidade Católica Portuguesa, CBQF, 4169-005 Porto, Portugal.

*corresponding author.

Carbohydrate Polymers Volume 241, 116269 (2020).

Abstract

Chitosan-based membranes are promising systems for guided bone regeneration. In this work, we used glycerylphytate as ionic crosslinker and osteinductor compound for the fabrication of chitosan membranes as supports for human mesenchymal stem cells (hMSCs). Three different glycerylphytate-crosslinked membranes were developed by changing the crosslinker concentration, from 2.5 to 10 wt-% respect to chitosan. Physicochemical characterization in terms of composition, morphology, and thermal behavior was further analyzed. Swelling degree, crosslinking density, and crosslinker release showed a glycerylphytate content-dependent behavior. Glycerylphytate suggested to improve osteointegration ability of chitosan surfaces by the formation of apatite-like aggregates after incubation in body simulated fluid (SBF). Stem cells cultured on the membranes increased their viability over time, and the incorporation of glycerylphytate improved osteogenic and osteoinductivity potential of chitosan by increasing calcium deposition and alkaline phosphatase (ALP) activity on cultured stem cells. These results demonstrated a potential application of glycerylphytate-crosslinked chitosan systems for promising bone tissue regeneration.

1. Introduction

Despite healthy bone possesses a powerful regenerative capacity, critical bone defects usually require from the application of reconstructive surgeries, which are mainly based on autologous bone grafts, allografts, and demineralized bone matrix. Bone regeneration is usually limited by the growth of connective tissue in the graft, which can evolve in a deficient osteointegration and loosening of the graft. Thus, scaffolds applied to bone repair processes should provide excellence osteoinductivity and osteoinduction properties [1, 2]. Currently, autographs are the most effective methodology regarding bone reconstruction process due to their high osteoconduction and osteoinductivity. However, they exhibit severe limitations such as pain involved, possibility of infection, prolonged surgery time or the limited amount of tissue available [3]. Other bone substitutes like allographs does not possess the necessary osteoinduction activity which leads to a low osteointegration of the graph [4]. Finally, bone substitutes, which are not based on natural bone, are widely applied. They can be classified in three generations: the first one is based on pure materials, the second one include the coating of the pure material with additional materials which prevent from connective tissue formation, and the third one consists of materials closer to natural structure and characteristics of bone tissue. This last generation exhibits improved osteoconductivity and biodegradability properties in comparison to the other two [1, 5, 6].

Guided bone regeneration (GBR) consists of the use of membranes with osteogenic and osteoinductive properties that can promote bone growth and avoid the migration of epithelial cells, which derives in ectopic osteogenesis [7]. These membranes can contain inorganic phosphate components, osteogenic cations like Sr^{2+}, Zn^{2+}, or Mg^{2+} [8-10], or different bioactive compounds like growth factors [11]. Chitosan is a non-toxic natural polysaccharide that exhibits good biocompatibility properties [12, 13] due to its similitude with the glycosaminoglycans present in the extracellular matrix [14]. Moreover, chitosan has demonstrated to exert an osteogenic effect similar to those provided by dexamethasone when it is used as an additive in mineralization medium [15]. Taking together these beneficial properties, chitosan-based membranes have arisen as promising systems for GBR applications [16-18]. Chitosan membranes are usually crosslinked with other compounds or mixed with synthetic components, like hydroxyapatite, to enhance its bone regeneration capacity [7, 9, 19, 20]. Herein, we propose the fabrication of chitosan

membranes crosslinked with glycerylphytate (G_3Phy) to obtain systems with osteogenic properties and osteointegration potential. G_3Phy is a phytic acid derivative, which has previously demonstrated to improve cytocompatibility and osteogenic properties in comparison to its precursor [21]. G_3Phy has strong chelating activity against polyvalent cations such as Fe^{2+} and Ca^{2+}. Its ability to form complexes with Fe^{2+} confers it antioxidant properties and *in vitro* inhibition of lipid peroxidation on RAW267.4 macrophages [21]. Thus, the use of G_3Phy is of great interest for the development of osteogenesis promoter materials. In particular, G_3Phy demonstrated excellent osteogenic activity against human mesenchymal stem cells (hMSCs) by the enhancement of ALP activity and osteogenic markers expression like *ALPL* and *COLA1A* [21]. Chitosan-based materials that can support hMSCs proliferation and differentiation are of high interest because hMSCs possess the ability of self-renewal and differentiation towards osteogenic lineages when they are in presence of suitable osteoinductive compounds. Human MSCs can play a pivotal role in bone regeneration and repair *in vivo* to accelerate bone healing [9, 22].

In this work, three different G_3Phy-crosslinked chitosan systems were fabricated by changing the G_3Phy weight concentration from 2.5 to 10% respect to chitosan. Physicochemical characterization of G_3Phy-crosslinked membranes was performed in terms of composition, morphology and thermal properties. *In vitro* behavior was investigated in terms of swelling, crosslinking density, and crosslinker release. Moreover, *in vitro* deposition of apatite-like aggregates on G_3Phy-crosslinked chitosan surfaces was studied to evaluate the osteointegration potential of our membranes. Finally, *in vitro* biological properties regarding cell adhesion, viability, and osteogenic properties of G_3Phy-crosslinked chitosan surfaces were assessed on hMSCs. Osteoblastic differentiation of hMSCs seeded on the top of our systems was evaluated by ALP activity and alizarin red assay in absence of osteoinductor compounds. We envision that our systems based on G_3Phy and chitosan will have promising applications as osteogenic membranes for GBR.

2. Experimental section

2.1. Synthesis of G_3Phy

G_3Phy was synthesized as described by Mora-Boza et al. [21]. Briefly, phytic acid sodium salt hydrate (Sigma-Aldrich) and glycerol (G, Sigma-Aldrich) were mixed in a molar ratio of 1:7, respectively, and heated at 120 ºC for 12 h to allow the condensation reaction under mechanical stirring. The reaction product was dissolved in water, precipitated twice in 2-propanol, dried under reduced pressure to remove solvent traces, and lyophilized.

2.2. Preparation of G_3Phy-crosslinked chitosan membranes

Chitosan of medical grade and endotoxin free (<100 EU/g) with a degree of deacetylation of 90% and M_w = 300 kDa was purchased from Altakitin (São Julião do Tojal, Portugal) and dissolved (2 wt-%) in acetic acid (1 % v/v) solution. 10 mL of chitosan solution were placed into a glass mould and heated in a humid chamber at 37 ºC until complete evaporation of the solvent. The obtained chitosan membranes were neutralized with NaOH solution (1 N) and washed with double distilled H_2O (ddH_2O) until neutral pH.

G_3Phy-crosslinked chitosan membranes were obtained by immersion of the previous membranes in aqueous solution of G_3Phy at different concentrations (2.5, 5, and 10 wt-% with respect to chitosan) and kept overnight at 37 ºC. Nomenclature and composition of chitosan membranes crosslinked with G_3Phy are reported in Table 1.

Table 1. Nomenclature and composition of chitosan membranes synthetized in this work.

Sample	[G_3Phy] (wt-% respect to chitosan)
Ch	0
Ch/G_3Phy_2.5	2.5
Ch/G_3Phy_5	5
Ch/G_3Phy_10	10

2.3. Physicochemical characterization of G_3Phy-crosslinked chitosan membranes

Crosslinking reaction was verified by Fourier Transform Infrared Spectroscopy (FTIR) using the technique of Attenuated Total Internal Reflectance (ATR-FTIR, Spectrum-One Spectrometer, Perkin-Elmer).

Elemental composition of the different membranes was analyzed by Energy Dispersive X-rays (EDX, Bruker XFlash model with detector 5030) and Induction Coupled Plasma Optical Emission spectroscopies (ICP-OES, 4300 DV Perkin-Elmer spectrophotometer with a Gemcone nebulizer). For ICP-OES analysis, membrane pieces of 12 mm (≈ 100 mg) were dissolved in 65 % v/v HNO_3 solution at 65 ºC. Then, the samples were diluted 1:10 with ddH_2O. The G_3Phy amount incorporated in the membranes was calculated taking into consideration the phosphorus (P) content. The measurements were conducted in triplicate for each sample and the data obtained were expressed as mean values ± standard deviations (SD).

Surface morphology characterization was studied using scanning electron microscopy (SEM, HITACHI SU8000). Samples were platinum sputtered prior to analysis using a sputter coater Polaron SC7640 (Quorum Technologies).

Thermal degradation of the membranes was analyzed by thermogravimetric analysis (TGA) under nitrogen atmosphere using a thermogravimetric analyzer TGA Q500 (TA instruments). A heating rate of 10 ºC/min from 40 to 800 ºC was applied for the analysis.

2.4. Swelling degree and crosslinking density of G_3Phy-crosslinked chitosan membranes

G_3Phy-crosslinked chitosan membranes were cut in round pieces of 12 mm (≈ 100 mg) and were incubated in phosphate-buffered saline (PBS, Sigma-Aldrich) solution (pH 7.4) at 37 °C. The swelling degree of the different membranes over time was calculated gravimetrically. At each time point, the excess of PBS was carefully removed with an absorbent paper before weighing. Swelling degree percentage was calculated using equation 1:

$$Swelling\ (\%) = \frac{W_t - W_0}{W_0} x\ 100 \quad (1)$$

where W_0 is the initial weight of the dried sample and W_t is the mass at the specific time of incubation. The measurements were conducted in triplicate for each sample and the data obtained were expressed as mean values ± SD.

Crosslinking density of the hydrogel was calculated following the Flory-Rehner equation [23-26]:

$$M_c = \frac{V_s d_p[(V_p)^{1/3} - V_p/2]}{\ln(1-V_p) + V_p + \chi(V_p)^2} \quad (2)$$

where M_c is the average molecular weight between crosslinks and $1/M_c$ is considered as the crosslinking density (ϱ_x). χ represents the polymer solvent interaction parameter and can be calculated by Flory-Huggins theory [25, 26]:

$$\chi = \frac{\ln(1-V_p) + V_p}{{V_p}^2} \quad (3)$$

where V_p is the volume fraction of polymer in equilibrium state, calculated as follow:

$$V_p = \left[1 + \frac{d_p}{d_s}(Q-1)\right]^{-1} \quad (4)$$

where d_p and d_s are the densities of the polymer (0.57±0.03 g/cm^3, calculated with a Sartorius balance ME Series and a density Kit YDK-01) and the solvent (1 g/cm^3). V_s is the molar volume of solvent (V_s = 18.1 mL/mol). Q refers to swelling ratio and it is defined as:

$$Q = \frac{W_f}{W_0} \quad (5)$$

where W_0 is the initial weight of the dried sample and W_f is the mass when swelling equilibrium is reached.

2.5. Rheological study of G$_3$Phy-crosslinked membranes

Rheological measurements were determined using an advanced rheometer from TA instruments, model AR-G2, equipped with a Peltier and a solvent trap. The last one allows the measurement in a water-saturated atmosphere by avoiding water evaporation from the membrane.

Samples were previously stabilized by their immersion in 7.4 PBS for 24 hours at 37 ºC. All tests were carried out using a 25 mm diameter steel sand blasted parallel plate. Frequency sweeping tests of membranes were conducted with a frequency scanning from 0.01 to 40 Hz at 0.1 % strain and 37 ºC. Three replicates of each sample were evaluated.

2.6. Release of G_3Phy from crosslinked-chitosan films

To study G_3Phy release, round crosslinked-chitosan membranes pieces (12 mm, ≈ 100 mg) were incubated in 5 mL of 0.1 M Tris hydrochloride (Tris-HCl, pH 7.5, Mol. Biol., Fisher BioReagents) buffer solution at 37 °C. At different incubation times, the medium was taken and replaced with fresh one. The P amount of the medium was analyzed by ICP-OES.

2.7. *In vitro* biomimetic apatite deposition assay

The crosslinked membrane Ch/G_3Phy_10 was used for biomineralization studies using simulated body fluid (SBF) at 1.5 concentration (1.5SBF). Three replicates of the sample were placed into containers with 100 mL of 1.5SBF solution, and incubated at 37 ºC for 4, 7, and 14 days. The 1.5SBF solution was previously prepared according to the procedure previously described in the literature [27]. Membrane surfaces were dried at 37 ºC and analyzed by SEM and EDX.

2.8. *In vitro* biological study

2.8.1. Cell Culture

The biological behavior of G_3Phy-crosslinked chitosan membranes was assessed on human mesenchymal stem cells–bone marrows (hMSCs, Innoprot). Cells were cultured in Mesenchymal Stem Cell Medium Kit (Innoprot) at 37 ºC and 5 % CO_2. Cells were used from 4-8 passages for all the experiments. For subsequent experiments, hMSCs were cultured in Low Glucose-Dulbecco's Modified Eagle Medium (LG-DMEM) supplemented with 20% fetal bovine serum, 200 mM L-glutamine, 100 units/mL penicillin, and 100 μg/mL streptomycin (complete LG-DMEM).

G_3Phy-crosslinked chitosan membranes were sterilized by immersion in 70% v/v ethanol solution for 2 hours and washed with sterile culture medium to remove ethanol traces.

2.8.2. Cytotoxicity analysis

Cytotoxicity was evaluated by Alamar Blue (Invitrogen) assay [28]. The films were immersed in 5 mL of DMEM at 37 ºC. The medium was removed after 1, 2, 7, and 14 days of incubation, and replaced with 5 mL of fresh medium. The toxicity of these extracts was evaluated by seeding hMSCs at a density of 9×10^4 cells/mL in LG-DMEM in 96 well-plates. After 24 hours, the medium was replaced with the corresponding extracts and the cells were incubated for other 24 hours. Human MSCs cultured in LG-DMEM without any membrane extracts were used as control for comparison. Cell viability was analyzed by adding Alamar Blue solution (10 % v/v) to LG-DMEM without phenol red to cultured cells and incubating them at 37 ºC for 4 hours. Media were collected and, after laser excitation at 590 nm, emitted fluorescence at 530 nm was quantified using a plate reader (Biotek Synergy HT spectrophotometer). Cell viability (%) was calculated following the equation 6:

$$\text{Cell viability (\%)} = 100 \times (OD_S - OD_B) / (OD_C - OD_B) \qquad (6)$$

where OD_S, OD_B, and OD_C are the emitted fluorescence at 530 nm for the sample (S), blank (B, LG-DMEM without cells), and control (C, Thermanox™ coverslips), respectively. The experiments were conducted in triplicate for each sample and the data obtained were expressed as mean values ± SD.

2.8.3. Cell adhesion and proliferation assay

Alamar Blue assay was used to analyze cellular adhesion and proliferation hMSCs seeded on the films. Human MSCs were seeded on the films at a density of 10^4 cells/cm^2 in 24 well-plates. Human MSCs were also seeded at the same concentration in Thermanox™ coverslips (TMX, ThermoFisher Scientific), which were used as controls. Cells were cultured in complete LG-DMEM. Cell viability was analyzed after 2, 7, and 14 days of incubation by adding Alamar Blue solution (10 % v/v) to LG-DMEM without phenol red and incubating the cells at 37 ºC for 4 hours. Medium was collected and, after laser excitation at 530-560 nm, emitted fluorescence at 590 nm was quantified using a Biotek Synergy HT plate reader. Cell viability percentages were calculated following the equation 6. The experiments were conducted in triplicate for each sample and the data obtained were expressed as mean values ± SD.

The cells adhered to the membrane surfaces were stained using Calcein AM (Sigma Aldrich) at different incubation times. Calcein was added in a concentration 1:1000 to the culture media and incubated for 10 min. Fluorescent cells were visualized under fluorescence microscopy (Nikon Eclipse Microscopy model TE2000 equipped with a fluorescence light source CooLED model CoolLED's pE-300^{lite}).

2.8.4. ALP activity

For these experiments, hMSCs were seeded in the same conditions as previous assay. ALP activity was evaluated by measuring p-nitrophenol absorption at 405 nm after 14 days culture. ALP activity per cell was normalized by DNA quantification. Thus, ALP/DNA ratios indicate the amount of ALP activity per cell. Total DNA amount was measured using a PicoGreen dsDNA quantitation kit and following the manufacturer instructions (Molecular Probes, 231 P-7589). The experiments were conducted in triplicate for each sample and the data obtained were expressed as mean values ± SD.

2.8.5. Alizarin red assay

Calcium deposition on the membrane surfaces was evaluated by Alizarin red assay after 7 and 14 days of incubation. For this experiment, hMSCs were seeded on the films at a density of 10^4 cells/cm^2 in complete LG-DMEM. Cells were fixed with 70% v/v ethanol at 4 ºC for 1 hour. Then, the films were rinsed twice with ddH_2O, and subsequently stained with alizarin red staining solution (pH = 4.2, 40 mM) for 30 min at room temperature. Then, alizarin red solution was removed, and the membranes were washed five times with ddH_2O. Finally, alizarin red dye was extracted from the cell monolayer by incubating the membranes in 1 mL cetylpyridinium chloride (CPC, Sigma-Aldrich) buffer (10 wt%, 10 mM Na_2PO_4) for 15 min [29]. Absorbance values were read at 550 nm on a UV Biotek Synergy HT detector. The dye concentration in the membranes was calculated by a calibration curve of alizarin red solution staining in the same CPC solution previously used for dye extraction. The experiments were conducted in triplicate for each sample and the data obtained were expressed as mean values ± SD.

3. Results and discussion

The synthesis of G_3Phy-crosslinked chitosan membranes resulted in stable systems at physiological conditions. According to the molecular structures of chitosan and G_3Phy (Figure 1a), the main interactions that take place during the crosslinking process are the electrostatic attractions between protonated amino groups of chitosan and the phosphate groups present in G_3Phy. In addition, weak interactions consist of hydrogen bonds between hydroxyl groups of G_3Phy and hydroxyl/amino groups of chitosan, hydrogen bonds between intermolecular hydroxyl groups of chitosan, and hydrogen bonds between hydroxyl groups of chitosan and water molecules (Figure 1b). SEM micrographs of uncrosslinked chitosan and G_3Phy-crosslinked membranes are illustrated in Figure 1c. All images showed smooth and uniform surfaces without signs of phase segregation.

3.1. Physicochemical characterization of G_3Phy-crosslinked chitosan membranes

G_3Phy-crosslinked chitosan membranes were subjected to ATR-FTIR spectroscopy to observe the differences in bond structure due to G_3Phy incorporation into the polymer matrix. The infrared spectra of chitosan and G_3Phy/chitosan membranes are presented in Figure 1d. The main characteristic peaks of chitosan in uncrosslinked membrane spectrum were: peaks at 2867 and 2925 cm^{-1} corresponded to CH_2 stretching; 1647-1587 cm^{-1} peaks indicated the presence of amide I and II, respectively; and the band at 1378 cm^{-1} was assigned to N-CH_3 stretching. Finally, typical signals of saccharide structures appeared between 1160 and 900 cm^{-1} [17, 30]. Bands between 3600 and 3000 cm^{-1}, which are typically assigned to associated υ O-H and N-H [17], became narrower when G_3Phy amount increased from 2.5 to 10 %. After G_3Phy crosslinking process, analysis of ATR-FTIR spectra of these samples revealed other differences compared to the uncrosslinked chitosan membrane, mainly the appearance of a new peak at 2972 cm^{-1}, whose intensity increased proportionally to the incorporated amount of G_3Phy. This signal corresponded to the asymmetric and symmetric stretching vibrations of C-H bonds of the inositol rings of the crosslinker [21]. Another feature that showed the successful G_3Phy crosslinking of chitosan membranes was the displacement of the band at 1587 cm^{-1} to 1582 cm^{-1}, which indicated the presence of NH_3^+ groups due to the ionic interaction between the amino groups of chitosan and

phosphate groups of G_3Phy. Finally, changes in the intensities and displacements of different signals in the region of the saccharide structure (1160 to 900 cm^{-1}) confirmed the reorganization of polymeric matrix due to the ionic crosslinking. Our ATR-FTIR results were consistent with those previously reported for other phytic acid-crosslinked chitosan systems [31-33].

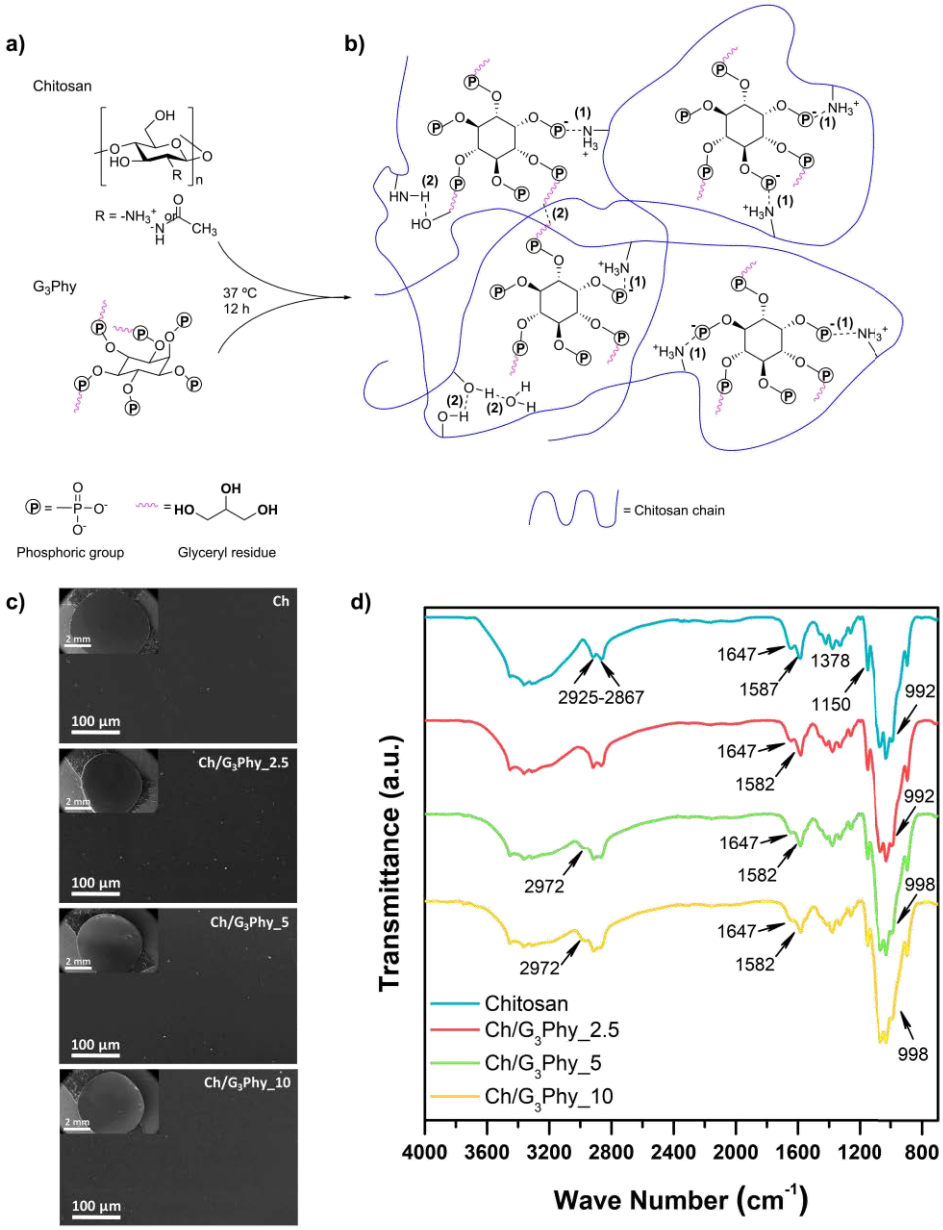

Figure 1. (a) Molecular structure of chitosan and G_3Phy; **(b)** Schematic illustration of interactions that take place between chitosan and G_3Phy: (1) electrostatic and (2) hydrogen bond interactions; **(c)** SEM micrographs of uncrosslinked and G_3Phy-crosslinked chitosan membranes; **(d)** ATR-FTIR spectra of uncrosslinked and G_3Phy-crosslinked chitosan membranes.

Elemental composition of G_3Phy-crosslinked chitosan membranes was evaluated by EDX and ICP-OES spectroscopies (Figure 2). EDX spectra of Ch/G_3Phy membranes (Figure 2a) showed the peaks of the main elements C, O, and N at their characteristic energy levels of 0.27, 0.52, and 0.39 keV, respectively. In addition, a peak at the energy level of P (2.01 keV), coming from the G_3Phy polyanions, was also observed and confirmed the ionic crosslinking reaction. The amounts of P incorporated to the membranes after ionic crosslinking process were measured by ICP-OES and are also displayed in Figure 2c.

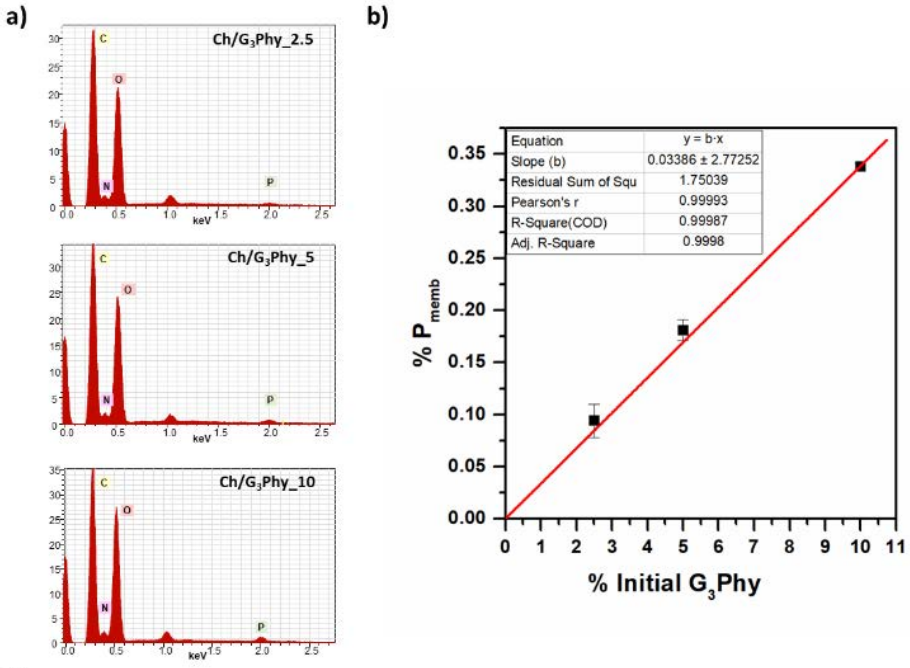

c)

	EDX		ICP-OES	
Membrane	**C/P**	**N/P**	**%P_{memb}**	**P_{memb}/P_{theor}**
Ch/G_3Phy_2.5	361.5	78.5	0.094 ± 0.016	0.270 ± 0.011
Ch/G_3Phy_5	126.7	30.0	0.181 ± 0.001	0.272 ± 0.011
Ch/G_3Phy_10	104.8	25.8	0.338 ± 0.003	0.268 ± 0.001

Figure 2. (a) EDX spectra of a representative sample of each membrane composition; **(b)** Linear regression adjustment curve for percentage of phosphorus incorporated in the membrane

(determined by ICP-OES) over percentage of initial amount of G_3Phy used during crosslinking reaction; **(c)** EDX results and P content measured by ICP-OES for the different G_3Phy-crosslinked membranes. P_{memb}: Amount of phosphorous found in the membranes. P_{theor}: Theoretical amount of phosphorous should be found in the membranes.

Figures 2b and 2c illustrate that the concentration of P in the membranes increased with the amount of initial G_3Phy, showing a linear regression adjustment with a R = 0.9998 (Figure 2b). In addition, the ratio between the final incorporated amount of P in the membranes (P_{memb}) and the initial amount of P used in crosslinking reaction (P_{theor}) was constant for all the systems, independently to the initial G_3Phy concentration. This result indicated that an average of 27 ± 0.01% of the total used G_3Phy was involved in the ionic interactions with amino groups of chitosan.

Taking EDX and ICP-OES results altogether, Figure 2c shows that both C/P and N/P ratios notably decreased as the content of G_3Phy increased in the membrane, demonstrating incorporation of P in the respective polymeric matrixes. These results confirmed the ionic crosslinking of chitosan membranes with G_3Phy at all the studied concentrations.

Thermal behavior of G_3Phy/chitosan membranes was studied by thermogravimetric analysis. Thermal degradation profiles (TGA and DTGA) and representative thermal parameters of all the studied films are represented in Table 2 and Figure S1, respectively.

Table 2. Maximum temperature values (DTGA curves), weight loss percentages (TGA curves) of the two main stages of thermal degradation and residue percentage values at 800 ºC for all the crosslinked systems.

Sample	First Stage		Second Stage		Remaining weight at 800 °C (%)
	$T_{max.}$ (°C)	Weight loss (%)	$T_{max.}$ (°C)	Weight loss (%)	
Ch	127.2	8.7	302.0	47.6	35.2
Ch/G_3Phy_2.5	147.3	8.5	295.6	46.9	38.2
Ch/G_3Phy_5	142.5	8.1	297.6	46.3	38.8
Ch/G_3Phy_10	128.4	8.0	290.4	45.2	40.4

Thermograms of uncrosslinked and G$_3$Phy-crosslinked membranes exhibited a similar thermogravimetric trend since thermal degradation occurred in two main stages in all the systems (Figure S1). Initial weight loss started at 60 ºC in all the samples and corresponded to vaporization of absorbed water. Considering the weight loss percentage values of the first degradation stage for chitosan and G$_3$Phy/chitosan systems, the water holding capacity differed in somewhat between the films. These results showed a different water-polymer interaction as a function of the incorporated G$_3$Phy [34], indicating that the membranes with higher concentration of G$_3$Phy crosslinker contained less water in their structure. The capacity of chitosan to retain water in its structure is based on the interaction of water with the hydroxyl and amino groups [35]. G$_3$Phy interacts ionically with these groups which can limit the water absorption capacity of chitosan from the surrounding medium. This behavior in water-polymer interaction will play a key role in other physicochemical properties, such as swelling, degradation or crosslinker release.

The second stage (between 302 and 290 ºC) corresponded to the thermal degradation of the polymer structure and indicated the thermal stability of the system since it is associated to chitosan pyranose ring degradation [36]. Similar values for chitosan depolymerization temperature have been reported by previous studies [17, 37]. In our systems, we observed that thermal stability of chitosan decreased as G$_3$Phy concentration increased. At low crosslinker amounts, the formation of intra-crosslinking reactions between polysaccharide chains that interfered with the formation of hydrogen bonds between structures is favored ,reducing the thermal stability of the systems [34]. Finally, residue percentages (remaining weight % at 800 ºC) increased from 35 %, for uncrosslinked chitosan, up to 40 %, for Ch/G$_3$Phy_10 sample, which confirmed the incorporation of G$_3$Phy in the membranes due to the presence of phosphate moieties that remained without degradation at high temperature.

3.2. Swelling degree and crosslinking density

Water adsorption capacity of a biomaterial is an essential feature to be studied because it will determine its ability to interact to body fluids. Consequently, swelling properties and crosslinking density due to the G$_3$Phy incorporation in the chitosan membranes will be decisive to discern their

biological properties. Swelling degree of uncrosslinked and G_3Phy-crosslinked membranes were studied in PBS at 37 ºC (Figure 3).

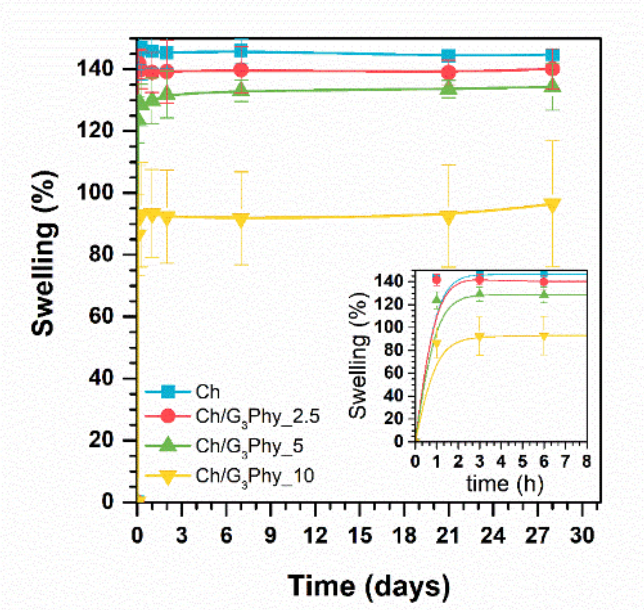

Figure 3. Swelling degree (%) profiles of the different chitosan-based membranes in PBS (pH 7.4) at 37 °C.

Swelling results showed that water-uptake equilibrium was reached after 8 hours of incubation for all the systems. However, swelling degree depended on G_3Phy content (147% for Ch; 139% for Ch/G_3Phy_2.5; 128% for Ch/G_3Phy_5, and 93% for Ch/G_3Phy_10, respectively). These results demonstrated that increasing G_3Phy contents leaded to higher crosslinking ratio and lower swelling degrees. As it can be observed in Figure 3, swelling degree of Ch/G_3Phy_10 sample was the lowest in comparison to the rest of the samples. For membranes crosslinked with 2.5 and 5 % of G_3Phy, swelling degrees were closer to those found for uncrosslinked chitosan film. These results correlated with thermal degradation analysis, which showed that the membranes with increasing G_3Phy content exhibited less water content in their structures. Then, it can be assumed that higher G_3Phy concentrations led to reduction of chitosan amino groups to interact with water molecules, and hence, the system exhibited less water adsorption capacity. Although swelling properties are important for nutrient diffusion in the scaffolds, high swelling degrees can

compromise scaffold integrity. In our systems, swelling degree was reduced by half with respect to chitosan for the membrane with higher content of G_3Phy. Recent studies claim that high initial swelling degrees are desirable for ensuring a suitable supply of nutrients to the whole scaffold, but moderate swelling degrees at equilibrium can enhance long-term mechanical stability of the membranes at physiological conditions, and even cellular adhesion and viability [38, 39].

Crosslinking densities for chitosan-based systems were calculated by applying the Flory-Rehner theory and using equations (2) to (5) described in subsection 2.4, taking the Q values at equilibrium state that are displayed in Table 3.

Table 3. Values of swelling ratio (Q), average molecular weight between nodes (M_c), crosslinking density (ϱ_x), and polymer solvent interaction (χ), of chitosan-based membranes.

Sample	Q	M_c (g/mol)	ϱ_x (g/cm^3)	χ
Ch	2.448 ± 0.008	11.416 ± 0.073	0.088 ± 0.001	0.819 ± 0.001
Ch/G_3Phy_2.5	2.402 ± 0.065	10.977 ± 0.613	0.091 ± 0.005	0.828 ± 0.012
Ch/G_3Phy_5	2.343 ± 0.075	10.425 ± 0.702	0.096 ± 0.006	0.839 ± 0.015
Ch/G_3Phy_10	1.965 ± 0.204	7.145 ± 1.635	0.140 ± 0.034	0.939 ± 0.075

As it was expected from swelling study, molecular weight between nodes (M_c) decreased as crosslinker concentration increased, whereas crosslinking density (ϱ_x) increased as G_3Phy content increased in the membranes. These results illustrated the hydrophilicity of the polymer systems in the sense that higher values of M_c resulted in higher swelling ratios in the films. Finally, solvent interaction parameters are related to the interaction between polymer and solvent. It is reported that high values of χ are indicative of weak interactions between polymers and solvent [40]. In our systems, high concentrations of G_3Phy resulted in less hydrophilic films due to the lower film-solvent interaction, as it was observed in swelling analysis.

Finally, mechanical properties of the Ch/G_3Phy_10 membranes were analyzed by rheology (Figure S2). Storage and loss moduli of uncrosslinked and G_3Phy-crosslinked samples exhibited a plateau in the studied frequency range, which indicated the stability of the polymeric networks. This plateau also evinced a solid-like behavior of the membranes, since storage moduli was

independent on the applied frequency [41]. Finally, crosslinked membranes showed lower storage moduli values in comparison to uncrosslinked chitosan, which indicated that G_3Phy crosslinker provided softer surfaces.

3.3. G_3Phy release from chitosan-based membranes

G_3Phy release from the G_3Phy-crosslinked membranes was analyzed by following P content of aliquots obtained by ICP-OES taken at different incubation times (Figure 4).

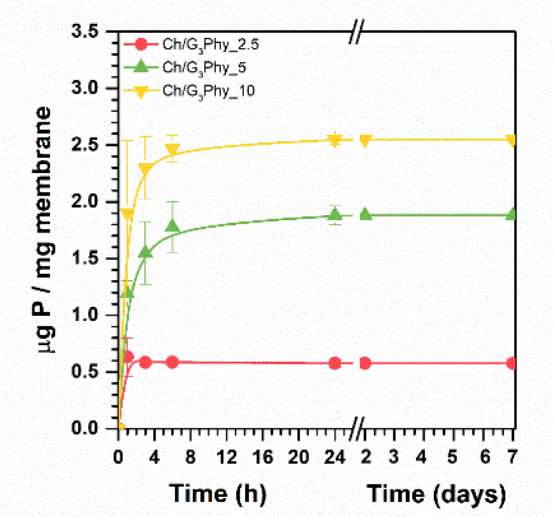

Figure 4. P release from G_3Phy-based membranes incubated in Tris-HCl buffer (pH 7.4) at 37 °C.

P release was observed in all the G_3Phy-crosslinked chitosan membranes. As it was expected, P release achieved higher values as G_3Phy content increased in the membranes. A burst release at the first 8-12 hours took place in all the G_3Phy-crosslinked membranes. This period agreed with the necessary time to achieve water-adsorption equilibrium in the membranes, as it was shown in swelling analysis (Figure 3). P release for all the studied systems achieved a plateau from 24 hours to the end of incubation period (7 days), giving P release values of 0.6, 1.9, and 2.5 µg P/mg membrane for Ch/G_3Phy_2.5, 5, and 10, respectively. Taking into consideration the final P release and the corresponding amount of P in the membrane (Figure 2c), it was estimated that an average of 80 % of the total crosslinking agent was released during the first 24 hours independently on the incorporated G_3Phy amount in the membranes.

3.4. *In vitro* 1.5SBF biomimetic study

In vitro biomimetic studies were carried out by immersion of Ch/G$_3$Phy_10 membrane in 1.5SBF solution [42]. Ch/G$_3$Phy_10 system was chosen because of its higher G$_3$Phy content in comparison to Ch/G$_3$Phy_2.5 and 5 samples. The formation of aggregates with apatite-like structure and composition was assessed by SEM and EDX after 4, 7, and 14 days of incubation (Figure 5).

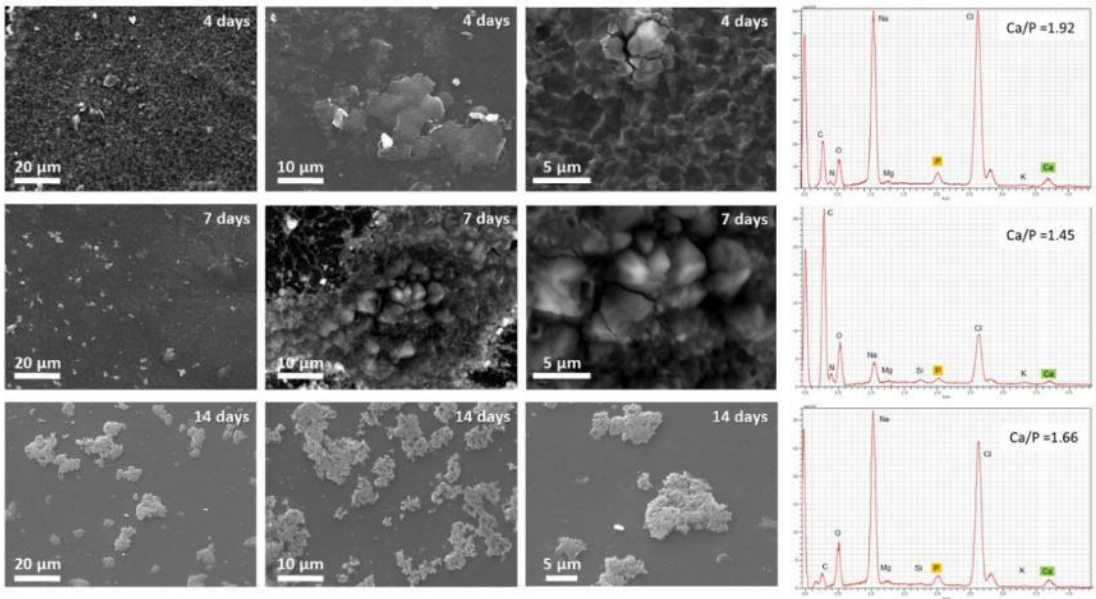

Figure 5. SEM micrographs of Ch/G$_3$Phy_10 membranes surfaces after different times (4, 7, 14 days) of soaking in 1.5SBF at different magnifications. EDX spectra of surface deposits of Ch/G$_3$Phy_10 films with their calculated Ca/P ratios.

Some disperse aggregates concentrated in localized zones, were observed on the membrane surfaces after 4 days of incubation. After 7 days, the deposits were more disseminated, and they colonized almost the whole surface after 14 days of incubation. At higher magnification (2000x) deposits resembled apatite-like phosphates. The morphology of these deposits agreed with that found by Yokoi *et al.,* corresponding to apatite deposits [43]. Yokio reported a granular apatite formed at high phosphate concentration on the surface of a polyacrylamide hydrogel. Elemental composition of surface aggregates at 4, 7, and 14 days was analyzed by EDX (Figure 5). EDX

spectra of the precipitates showed the characteristic peaks of Ca and P at any incubation time, obtaining Ca/P ratios of 1.92, 1.45, and 1.66 for 4, 7, and 14 days, respectively. These results confirmed that the aggregates formed in the Ch/G_3Phy_10 surface after 1.5SBF immersion exhibited a chemical composition close to that of biological apatite (Ca/P = 1.66).

Osteointegration, which consists of the direct bonding between bone substitute and new living bone, is one of the key properties an ideal bone-substitute must exhibit. This bonding should be sufficiently fast to avoid the generation and deposition of connective tissue between the bone and the implanted material. The formation of a fibrous layer will limit osteointegration and can result in loosening of the graft [1]. The rapid generation of an apatite-like layer in a bone-substitute material is an excellent indicator of an appropriate osteointegration [42, 44]. Some studies have been reported about the generation of Ca/P layers on chitosan-based materials. For example, Yokogawa *et al.* [42] performed a profound study of calcium phosphate layer growth on phosphorylated chitin fibers when they were soaked in 1.5SBF. Other studies have claimed the deposition of spherical Ca/P particles on titanium surfaces that were decorated with phytic acid and calcium hydroxide [45]. In this case, phytic acid seemed to act as the bridge between Ca ions and titanium surfaces due to its strong chelating capacity of phytic acid against divalent ions such as Ca^{2+} [10]. Because of the claimed stability of calcium-phytate complexes under *in vitro* neutral pH [46], phytic acid has been proposed as an inhibitor of bone resorption in animal models of osteoporosis [47-49]. In addition, phytic acid has been also applied as novel component in calcium phosphate cements due to its excellent Ca^{2+} chelating properties [46, 50, 51]. Meininger *et al.* [46] used phytic acid in their work as an alternative setting retarder, and these calcium phosphate cements demonstrated enhanced cells activity and proliferation, as well as, good *in vitro* stability of the formed Ca-Phytate complexes. G_3Phy is a hydroxylic derivative of phytic acid which demonstrated a tunable chelating ability against Ca^{+2} ion in comparison to phytic acid due to the incorporation of glyceryl moieties to the phytic acid structure [21]. In this sense, the present work demonstrated that G_3Phy chelating capacity is enough to promote *in vitro* biomineralization of chitosan membranes in a short incubation time (4 days). These results highlight the potential of the developed G_3Phy-crosslinked systems as promising candidates for direct bone-biomaterial bonding.

3.5. *In vitro* effect of G_3Phy-crosslinked membranes on hMSCs culture

3.5.1. Membrane cytotoxicity

The toxicity of lixiviates coming from different membranes was measured on hMSCs to evaluate the possible cytotoxic effects of the systems. Figure 6a shows that cell viability was not affected by lixiviates coming from any of the G_3Phy-crosslinked membranes as cell viability percentages were higher than 80% in all the systems. In addition, hMSCs exposed to extracts of Ch/G_3Phy_10 membranes taken at short incubation times (1 and 2 days) showed a significantly higher cell viability in comparison to TMX and chitosan membrane. This feature would be related to the highest P release, at short times (Figure 4) in comparison with the other membranes, since G_3Phy was claimed to exhibit excellent cytocompatibility and osteogenic properties against hMSCs culture [21].

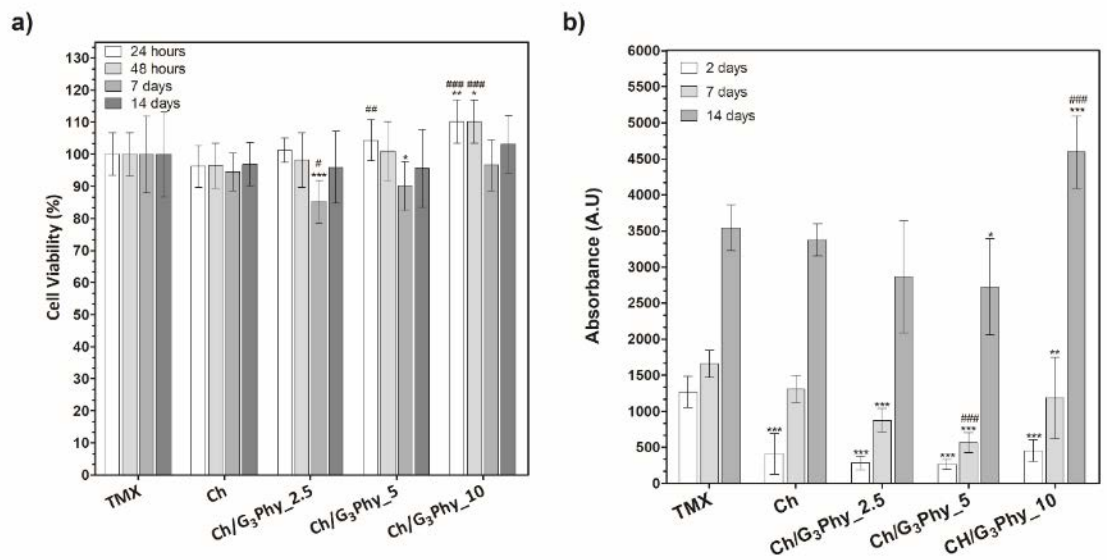

Figure 6. (a) Cell viability (%) of hMSCs cultured with extracts of chitosan and G_3Phy/chitosan membrane taken at 1, 2, 7, and 14 days of incubation. Significant differences with TMX samples at each time are marked with * (*$p < 0.05$, **$p < 0.01$, ***$p < 0.001$) and with chitosan membranes are marked with # (#$p < 0.05$, ##$p < 0.01$, ###$p < 0.001$); **(b)** Cell proliferation values of hMSCs seeded on the crosslinked membrane surfaces measured by Alamar Blue assay. Significant differences with respect to TMX sample at each time are marked with * (*$p < 0.05$, **$p < 0.01$,

***$p < 0.001$) and with chitosan membranes are marked with # (#$p < 0.05$, ##$p < 0.01$, ###$p < 0.001$).

3.5.2. Cell adhesion and proliferation

Human MSCs proliferation on uncrosslinked and G_3Phy-crosslinked membranes was evaluated by Alamar Blue and fluorescence microscopy assay at 2, 7 and 14 days (Figure 6b and S3). Human MSCs proliferation increased over time for all the systems. At short times (2 days), cell proliferation was significantly reduced in chitosan and Ch/G_3Phy membranes in comparison to TMX. However, cell proliferation in G_3Phy-crosslinked membranes was similar to those of chitosan membranes (no significant differences were found). For prolonged incubation times (7 days), cell proliferation significantly decreased in Ch/G_3Phy_5 system in comparison to chitosan membrane. The reduced cell proliferation in G_3Phy-crosslinked systems could be claimed to the G_3Phy release events that take place in these systems (Figure 4) and to the osteogenic differentiation processes that G_3Phy should lead on hMSCs [21], which could slow down cell proliferation at this incubation time. Finally, no significant differences on hMSCs proliferation were found between chitosan and Ch/G_3Phy_2.5 and _5 membranes, while Ch/G_3Phy_10 film demonstrated a significantly higher cell proliferation at 14 days. This behavior was attributed to the higher G_3Phy content in the system which notably improved cell adhesion and proliferation at prolonged incubation times. Collectively, these results confirmed that the incorporation of G_3Phy to chitosan at concentrations up to 10 wt-% with respect to chitosan improved cell cytocompatibility and proliferation. Previous studies have shown that phytic acid improved the proliferation of stem cells in different models [45, 50, 52]. For example, Sun *et al.* [52] demonstrated enhanced cell adhesion and proliferation in phytic acid polyaniline hydrogels. Konishi et al. [50], who developed a novel injectable cement using chitosan and phytic acid among other compounds, also observed that cell viability was improved at prolonged cell culture times in the systems containing phytic acid.

3.5.3. Osteogenic effect of G_3Phy-crosslinked membranes on hMSCs culture

The ALP activity and calcium deposition of hMSCs seeded on chitosan and Ch/G_3Phy membrane surfaces were evaluated to assess osteogenesis capacity of the systems (Figure 7).

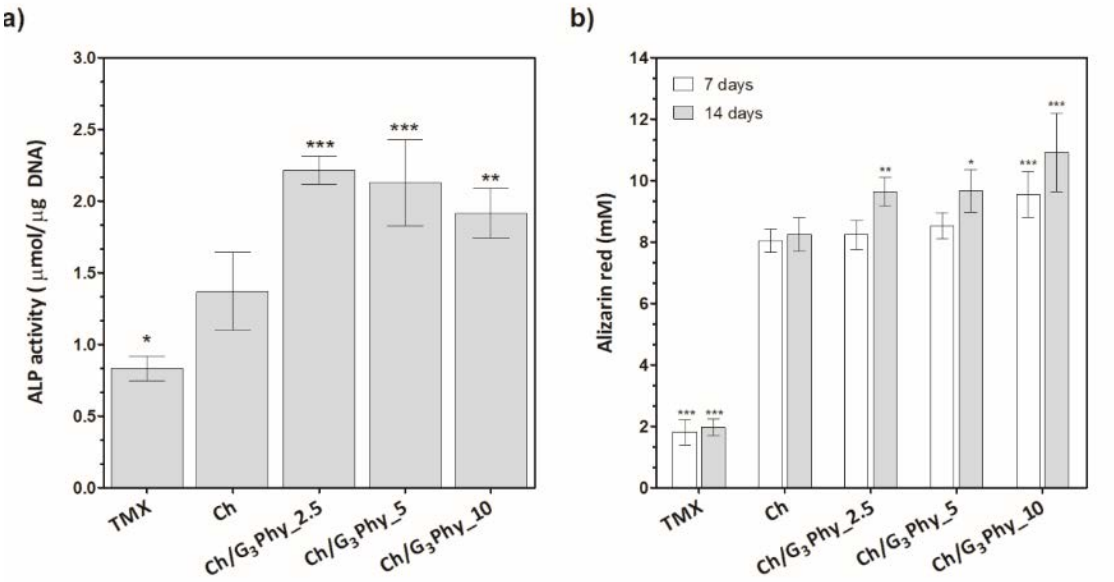

Figure 7. (a) ALP activity of hMSCs at 14 days seeded on chitosan and G_3Phy/chitosan membrane surfaces incubated in non-osteogenic medium; **(b)** Alizarin Red content (mM) on hMSCs cultured on the surface of different chitosan membranes. Significant differences with respect to chitosan sample at each time are marked with * (*$p < 0.05$, **$p < 0.01$, ***$p < 0.001$).

The ALP activity of the different Ch/G_3Phy membranes was evaluated after 14 days of incubation in non-osteogenic medium (Figure 7a). All G_3Phy-crosslinked membranes showed significantly higher ALP activity in comparison to uncrosslinked chitosan membrane. Although ALP activity decreased as G_3Phy content increased, no significant differences were found when Ch/G_3Phy compositions were compared one to each other ($p > 0.1$). These results indicated that even low contents of G_3Phy in the systems enhanced ALP activity of hMSCs seeded on membrane surfaces since ALP activity of Ch/G_3Phy_2.5 system increased 1-fold with respect to chitosan. Chitosan has been previously claimed to stimulate early osteogenic differentiation of dental pulp stem cells (DPSCs). Amir *et al.* [15] demonstrated in their work that the addition of chitosan to DPSCs cultured in mineralization medium increased ALP activity, and chitosan presence had an

osteogenic effect similar to that of dexamethasone. G_3Phy was previously demonstrated to exhibit osteogenic properties by increasing ALP activity respect to phytic acid after 14 days of incubation and upregulating early osteogenic markers such as *COLA1A* and *ALPL* at basal conditions (non-osteogenic medium) [21]. The showed ALP results in this work demonstrated that the combination of chitosan and G_3Phy led to a positive synergistic effect in the osteogenic differentiation of hMSCs seeded on membrane surfaces even in non-osteogenic stimulating conditions. Osteogenic activity has been observed in other systems based on phytic acid [45, 47, 53]. For example, Liu *et al.* [45] demonstrated that calcium and phytic acid-decorated titanium surfaces enhanced ALP activity and early osteogenic markers, which could lead to new bone formation and osteointegration. Likewise, Córdoba et al. [47], who developed a similar grafting of phytic acid molecules on titanium surfaces, also observed higher expression levels of osteogenic markers on MC3T3-E1 cells.

Biomineralization of cultured hMSCs on membrane surfaces was assessed by alizarin red assay at 7 and 14 days of incubation. Alizarin red stains the calcium deposits containing on hMSCs. Figure 7b shows that alizarin red concentration increased over time for Ch/G_3Phy systems, while it remained stable in uncrosslinked chitosan membrane from 7 to 14 days of incubation. Amir *et al.* demonstrated in their work that although chitosan upregulated osteogenic differentiation of DPSCs, no significant stimulation on mineral deposition was found [15]. At 7 days of incubation no significant differences were found between G_3Phy-crosslinked membranes and chitosan membranes. Nevertheless, after 14 days, alizarin red content was significantly higher in all Ch/G_3Phy systems in comparison to uncrosslinked chitosan. In addition, biomineralization increased with the G_3Phy content in the membranes. Thus, Ch/G_3Phy_10 sample exhibited the highest biomineralization capacity in comparison to the other G_3Phy-crosslinked compositions. These results correlated with the *in vitro* 1.5SBF biomineralization analysis (Figure 4). Other phytic acid-based systems have claimed to improve biomineralization [46, 47]. For example, high mineralization of MC3T3-E1 cells after 21 days was observed on titanium surfaces grafted with phytic acid molecules [47].

Taking the biological results in overall, we can claim that the G_3Phy crosslinking to chitosan membranes and its further release improved the osteogenic properties of chitosan. In this context,

we would like to highlight that all the *in vitro* experiments were conducted without osteogenic inductors typical for osteogenic differentiation of hMSCs [54]. We previously reported that G_3Phy exhibited osteogenic properties by its own and it has been proposed as promising candidate in bone-tissue engineering applications [21]. Here, we demonstrate that the use of G_3Phy as a polysaccharide crosslinker results in an osteogenic biomaterial that has great potential in the bone-tissue engineering field.

4. Conclusions

In this study, G_3Phy-crosslinked chitosan membranes as supports of hMSCs were developed for bone tissue engineering applications. Crosslinking reaction was confirmed by ATR-FTIR, EDAX, ICP-OES, and TGA analysis. Swelling and G_3Phy release exhibited a crosslinker content-dependent behavior. *In vitro* incubation of Ch/G_3Phy_10 system in SBF showed the deposition of apatite-like aggregates, which demonstrated the osteointegration potential of the chitosan surfaces crosslinked with G_3Phy. Human MSCs cultured on crosslinked-chitosan surfaces increased viability over time, and improved osteogenesis features in comparison to uncrosslinked chitosan. In particular, G_3Phy incorporation to chitosan membranes enhanced ALP activity and mineralization in absence of any typical osteogenic inducer. Taken together, these results evinced that G_3Phy-crosslinked chitosan membranes provide a suitable environment for hMSCs culture and differentiation into osteoblastic lineage. In conclusion, the developed systems could be applied as promising substrates for guided bone regeneration.

5. References

[1] M. Stepniewski, J. Martynkiewicz, J. Gosk, Chitosan and its composites: Properties for use in bone substitution, Polimery w medycynie 47(1) (2017) 49-53.

[2] A.S. Greenwald, S.D. Boden, V.M. Goldberg, Y. Khan, C.T. Laurencin, R.N. Rosier, Bone-graft substitutes: facts, fictions, and applications, The Journal of bone and joint surgery. American volume 83-A Suppl 2 Pt 2 (2001) 98-103.

[3] B. Stevens, Y. Yang, A. Mohandas, B. Stucker, K.T. Nguyen, A review of materials, fabrication methods, and strategies used to enhance bone regeneration in engineered bone tissues, Journal of biomedical materials research. Part B, Applied biomaterials 85(2) (2008) 573-82.

[4] W.R. Moore, S.E. Graves, G.I. Bain, Synthetic bone graft substitutes, ANZ journal of surgery 71(6) (2001) 354-61.

[5] A.R. Amini, C.T. Laurencin, S.P. Nukavarapu, Bone tissue engineering: recent advances and challenges, Crit Rev Biomed Eng 40(5) (2012) 363-408.

[6] V.P. Ribeiro, S. Pina, J.B. Costa, I.F. Cengiz, L. García-Fernández, M.D.M. Fernández-Gutiérrez, O.C. Paiva, A.L. Oliveira, J. San-Román, J.M. Oliveira, R.L. Reis, Enzymatically Cross-Linked Silk Fibroin-Based Hierarchical Scaffolds for Osteochondral Regeneration, ACS Applied Materials and Interfaces 11(4) (2019) 3781-3799.

[7] J.H. Luna-Domínguez, H. Téllez-Jiménez, H. Hernández-Cocoletzi, M. García-Hernández, J.A. Melo-Banda, H. Nygren, Development and in vivo response of hydroxyapatite/whitlockite from chicken bones as bone substitute using a chitosan membrane for guided bone regeneration, Ceramics International 44(18) (2018) 22583-22591.

[8] X. Wang, X. Li, A. Ito, Y. Sogo, Synthesis and characterization of hierarchically macroporous and mesoporous CaO–MO–SiO2–P2O5 (M = Mg, Zn, Sr) bioactive glass scaffolds, Acta Biomaterialia 7(10) (2011) 3638-3644.

[9] Y. Lei, Z. Xu, Q. Ke, W. Yin, Y. Chen, C. Zhang, Y. Guo, Strontium hydroxyapatite/chitosan nanohybrid scaffolds with enhanced osteoinductivity for bone tissue engineering, Materials Science and Engineering C 72 (2017) 134-142.

[10] B.M. Luttrell, The biological relevance of the binding of calcium ions by inositol phosphates, The Journal of biological chemistry 268(3) (1993) 1521-4.

[11] S. Yamano, K. Haku, T. Yamanaka, J. Dai, T. Takayama, R. Shohara, K. Tachi, M. Ishioka, S. Hanatani, S. Karunagaran, The effect of a bioactive collagen membrane releasing PDGF or GDF-5 on bone regeneration, Biomaterials 35(8) (2014) 2446-2453.

[12] A. De La Mata, T. Nieto-Miguel, M. López-Paniagua, S. Galindo, M.R. Aguilar, L. García-Fernández, S. Gonzalo, B. Vázquez, J.S. Román, R.M. Corrales, M. Calonge, Chitosan-gelatin biopolymers as carrier substrata for limbal epithelial stem cells, Journal of Materials Science: Materials in Medicine 24(12) (2013) 2819-2829.

[13] E. Khor, L.Y. Lim, Implantable applications of chitin and chitosan, Biomaterials 24(13) (2003) 2339-2349.

[14] R.L. Jackson, S.J. Busch, A.D. Cardin, Glycosaminoglycans: Molecular properties, protein interactions, and role in physiological processes, Physiological Reviews 71(2) (1991) 481-539.

[15] L.R. Amir, D.F. Suniarti, S. Utami, B. Abbas, Chitosan as a potential osteogenic factor compared with dexamethasone in cultured macaque dental pulp stromal cells, Cell and Tissue Research 358(2) (2014) 407-415.

[16] M. Masoudi Rad, S. Nouri Khorasani, L. Ghasemi-Mobarakeh, M.P. Prabhakaran, M.R. Foroughi, M. Kharaziha, N. Saadatkish, S. Ramakrishna, Fabrication and characterization of two-layered nanofibrous membrane for guided bone and tissue regeneration application, Materials Science and Engineering C 80 (2017) 75-87.

[17] S. Tamburaci, F. Tihminlioglu, Diatomite reinforced chitosan composite membrane as potential scaffold for guided bone regeneration, Materials Science and Engineering: C 80(Supplement C) (2017) 222-231.

[18] Q. Wang, J. Xu, H. Jin, W. Zheng, X. Zhang, Y. Huang, Z. Qian, Artificial periosteum in bone defect repair—A review, Chinese Chemical Letters 28(9) (2017) 1801-1807.

[19] A. Anitha, S. Sowmya, P.T.S. Kumar, S. Deepthi, K.P. Chennazhi, H. Ehrlich, M. Tsurkan, R. Jayakumar, Chitin and chitosan in selected biomedical applications, Progress in Polymer Science 39(9) (2014) 1644-1667.

[20] R. Guzman, S. Nardecchia, M.C. Gutierrez, M.L. Ferrer, V. Ramos, F. del Monte, A. Abarrategi, J.L. Lopez-Lacomba, Chitosan scaffolds containing calcium phosphate salts and rhBMP-2: in vitro and in vivo testing for bone tissue regeneration, PLoS One 9(2) (2014) e87149.

[21] A. Mora-Boza, M.L. López-Donaire, L. Saldaña, N. Vilaboa, B. Vázquez-Lasa, J. San Román, Glycerylphytate compounds with tunable ion affinity and osteogenic properties, Scientific Reports 9(1) (2019).

[22] W.B. Tsai, Y.R. Chen, W.T. Li, J.Y. Lai, H.L. Liu, RGD-conjugated UV-crosslinked chitosan scaffolds inoculated with mesenchymal stem cells for bone tissue engineering, Carbohydrate Polymers 89(2) (2012) 379-387.

[23] F. Reyes-Ortega, A. Cifuentes, G. Rodríguez, M.R. Aguilar, Á. González-Gómez, R. Solis, N. García-Honduvilla, J. Buján, J. García-Sanmartin, A. Martínez, J.S. Román, Bioactive bilayered

dressing for compromised epidermal tissue regeneration with sequential activity of complementary agents, Acta Biomaterialia 23 (2015) 103-115.

[24] N.A. Peppas, Y. Huang, M. Torres-Lugo, J.H. Ward, J. Zhang, Physicochemical foundations and structural design of hydrogels in medicine and biology, Annual Review of Biomedical Engineering 2(1) (2000) 9-29.

[25] S. Khan, N.M. Ranjha, Effect of degree of cross-linking on swelling and on drug release of low viscous chitosan/poly(vinyl alcohol) hydrogels, Polymer Bulletin 71(8) (2014) 2133-2158.

[26] N.M. Ranjha, G. Ayub, S. Naseem, M.T. Ansari, Preparation and characterization of hybrid pH-sensitive hydrogels of chitosan-co-acrylic acid for controlled release of verapamil, Journal of Materials Science: Materials in Medicine 21(10) (2010) 2805-2816.

[27] I.R.d. Oliveira, T.L.d. Andrade, R.M. Parreira, M. Jacobovitz, V.C. Pandolfelli, Characterization of calcium aluminate cement phases when in contact with simulated body fluid, Materials Research 18 (2015) 382-389.

[28] T. Mosmann, Rapid colorimetric assay for cellular growth and survival: Application to proliferation and cytotoxicity assays, Journal of Immunological Methods 65(1-2) (1983) 55-63.

[29] C.A. Gregory, W.G. Gunn, A. Peister, D.J. Prockop, An alizarin red-based assay of mineralization by adherent cells in culture: comparison with cetylpyridinium chloride extraction, Analytical Biochemistry 329(1) (2004) 77-84.

[30] K.D. Yao, T. Peng, M.F.A. Goosen, J.M. Min, Y.Y. He, pH-sensitivity of hydrogels based on complex forming chitosan: Polyether interpenetrating polymer network, Journal of Applied Polymer Science 48(2) (1993) 343-354.

[31] X.Z. Shu, K.J. Zhu, The influence of multivalent phosphate structure on the properties of ionically cross-linked chitosan films for controlled drug release, European Journal of Pharmaceutics and Biopharmaceutics 54(2) (2002) 235-243.

[32] X.Z. Shu, K.J. Zhu, Controlled drug release properties of ionically cross-linked chitosan beads: the influence of anion structure, International journal of pharmaceutics 233(1) (2002) 217-225.

[33] R. Ravichandran, V. Seitz, J. Reddy Venugopal, R. Sridhar, S. Sundarrajan, S. Mukherjee, E. Wintermantel, S. Ramakrishna, Mimicking native extracellular matrix with phytic acid-crosslinked protein nanofibers for cardiac tissue engineering, Macromolecular Bioscience 13(3) (2013) 366-75.

[34] C.G.T. Neto, J.A. Giacometti, A.E. Job, F.C. Ferreira, J.L.C. Fonseca, M.R. Pereira, Thermal analysis of chitosan based networks, Carbohydrate Polymers 62(2) (2005) 97-103.

[35] D.R. Rueda, T. Secall, R.K. Bayer, Differences in the interaction of water with starch and chitosan films as revealed by infrared spectroscopy and differential scanning calorimetry, Carbohydrate Polymers 40(1) (1999) 49-56.

[36] A. Pawlak, M. Mucha, Thermogravimetric and FTIR studies of chitosan blends, Thermochimica Acta 396(1-2) (2003) 153-166.

[37] J.M. Nieto, C. Peniche-Covas, G. Padro´n, Characterization of chitosan by pyrolysis-mass spectrometry, thermal analysis and differential scanning calorimetry, Thermochimica Acta 176 (1991) 63-68.

[38] I. Francolini, E. Perugini, I. Silvestro, M. Lopreiato, A. Scotto d'Abusco, F. Valentini, E. Placidi, F. Arciprete, A. Martinelli, A. Piozzi, Graphene oxide oxygen content affects physical and biological properties of scaffolds based on chitosan/graphene oxide conjugates, Materials 12(7) (2019) 1142.

[39] A.R. Unnithan, C.H. Park, C.S. Kim, Nanoengineered bioactive 3D composite scaffold: A unique combination of graphene oxide and nanotopography for tissue engineering applications, Composites Part B: Engineering 90 (2016) 503-511.

[40] G. Kali, S. Vavra, K. László, B. Iván, Thermally responsive amphiphilic conetworks and gels based on Poly(N-isopropylacrylamide) and polyisobutylene, Macromolecules 46(13) (2013) 5337-5344.

[41] L. Oatway, T. Vasanthan, J.H. Helm, Phytic acid, Food Reviews International 17(4) (2001) 419-431.

[42] Y. Yokogawa, J.P. Reyes, M. Mucalo, M. Toriyama, Y. Kawamoto, T. Suzuki, K. Nishizawa, F. Nagata, T. Kamayama, Growth of calcium phosphate on phosphorylated chitin fibres, Journal of Materials Science: Materials in Medicine 8(7) (1997) 407-412.

[43] T. Yokoi, M. Kawashita, K. Kikuta, C. Ohtsuki, Biomimetic mineralization of calcium phosphate crystals in polyacrylamide hydrogel: effect of concentrations of calcium and phosphate ions on crystalline phases and morphology, Materials Science and Engineering: C 30(1) (2010) 154-159.

[44] T. Miyazaki, K. Ishikawa, Y. Shirosaki, C. Ohtsukid, Organic-inorganic composites designed for biomedical applications, Biological and Pharmaceutical Bulletin 36(11) (2013) 1670-1675.

[45] K. Liu, H. Zhang, M. Lu, L. Liu, Y. Yan, Z. Chu, Y. Ge, T. Wang, C. Tang, Enhanced bioactive and osteogenic activities of titanium by modification with phytic acid and calcium hydroxide, Applied Surface Science 478 (2019) 162-175.

[46] S. Meininger, C. Blum, M. Schamel, J.E. Barralet, A. Ignatius, U. Gbureck, Phytic acid as alternative setting retarder enhanced biological performance of dicalcium phosphate cement in vitro, Scientific Reports 7(1) (2017) 558.

[47] A. Cordoba, M. Hierro-Oliva, M.A. Pacha-Olivenza, M.C. Fernandez-Calderon, J. Perello, B. Isern, M.L. Gonzalez-Martin, M. Monjo, J.M. Ramis, Direct covalent grafting of phytate to titanium surfaces through Ti-O-P bonding shows bone stimulating surface properties and decreased bacterial adhesion, ACS Applied Materials & Interfaces 8(18) (2016) 11326-35.

[48] Á.A. López-González, F. Grases, N. Monroy, B. Marí, M.T. Vicente-Herrero, F. Tur, J. Perelló, Protective effect of myo-inositol hexaphosphate (phytate) on bone mass loss in postmenopausal women, European Journal of Nutrition 52(2) (2013) 717-726.

[49] M. Arriero Mdel, J.M. Ramis, J. Perello, M. Monjo, Inositol hexakisphosphate inhibits osteoclastogenesis on RAW 264.7 cells and human primary osteoclasts, PLoS One 7(8) (2012) e43187.

[50] T. Konishi, M. Honda, M. Nagaya, H. Nagashima, E.S. Thian, M. Aizawa, Injectable chelate-setting hydroxyapatite cement prepared by using chitosan solution: Fabrication, material properties, biocompatibility, and osteoconductivity, Journal of biomaterials applications 31(10) (2017) 1319-1327.

[51] T. Konishi, M. Mizumoto, M. Honda, Y. Horiguchi, K. Oribe, H. Morisue, K. Ishii, Y. Toyama, M. Matsumoto, M. Aizawa, Fabrication of novel biodegradable α-tricalcium phosphate cement set by chelating capability of inositol phosphate and Its biocompatibility, Journal of Nanomaterials 2013 (2013) ID 864374.

[52] K.-H. Sun, Z. Liu, C. Liu, T. Yu, T. Shang, C. Huang, M. Zhou, C. Liu, F. Ran, Y. Li, Y. Shi, L. Pan, Evaluation of in vitro and in vivo biocompatibility of a myo-inositol hexakisphosphate gelated polyaniline hydrogel in a rat model, Scientific Reports 6 (2016) 23931.

[53] T. Zhu, H. Ren, A. Li, B. Liu, C. Cui, Y. Dong, Y. Tian, D. Qiu, Novel bioactive glass based injectable bone cement with improved osteoinductivity and its in vivo evaluation, Sci Rep 7(1) (2017) 3622.
[54] H. Hanna, L.M. Mir, F.M. Andre, In vitro osteoblastic differentiation of mesenchymal stem cells generates cell layers with distinct properties, Stem Cell Res Ther 9(1) (2018) 203-203.

Ackowledgments

This work was supported by the Ministry of Science, Innovation and Universities (Spain) [MAT2017-2017-84277-R], Instituto Salud Carlos III (ISCIII)-Fondo Europeo de Desarrollo Regional (FEDER), Centro de Investigación Biomédica en Red en Bioingeniería, Biomateriales y Nanomedicina (CIBER-BBN), Fundação para a Ciência e a Tecnologia [UID/Multi/50016/2019], Post-Doc grant to S. Baptista-Silva [SFRH/BPD/116024/2016]. Interreg V-A POCTEP Programme through FEDER European Union [0245_IBEROS_1_E.C.A.] and "Biotherapies: Bioengineered Therapies for Infectious Diseases and Tissue Regeneration" [NORTE-01-0145-FEDER-000012]. Ana Mora-Boza is supported by "La Caixa" Foundation [ID 100010434, scholarship code LCF/BQ/ES16/11570018].

6. Supporting information

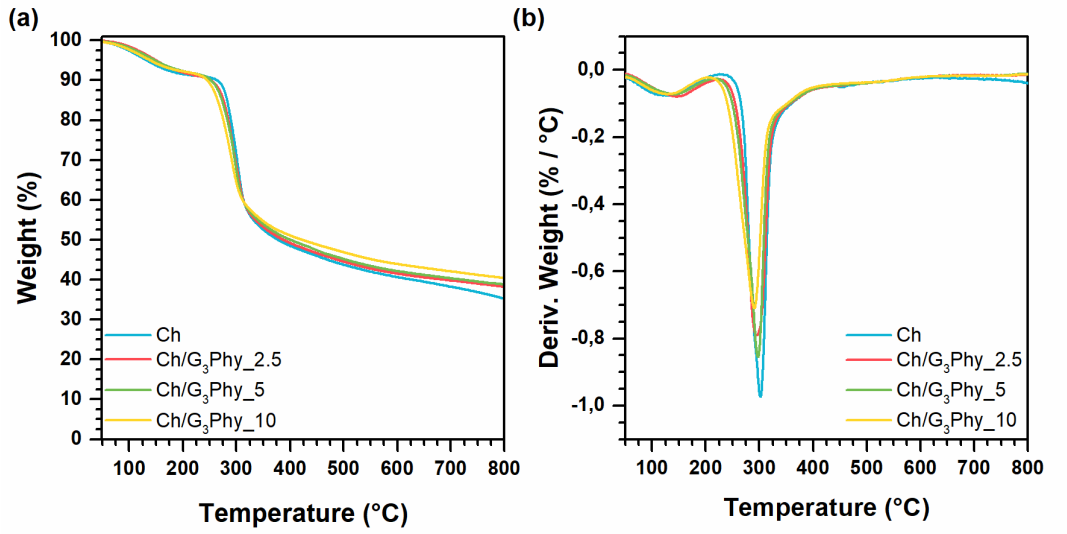

Figure S1. TGA **(a)** and DTGA **(b)** curves for uncrosslinked and G_3Phy-crosslinked chitosan membranes.

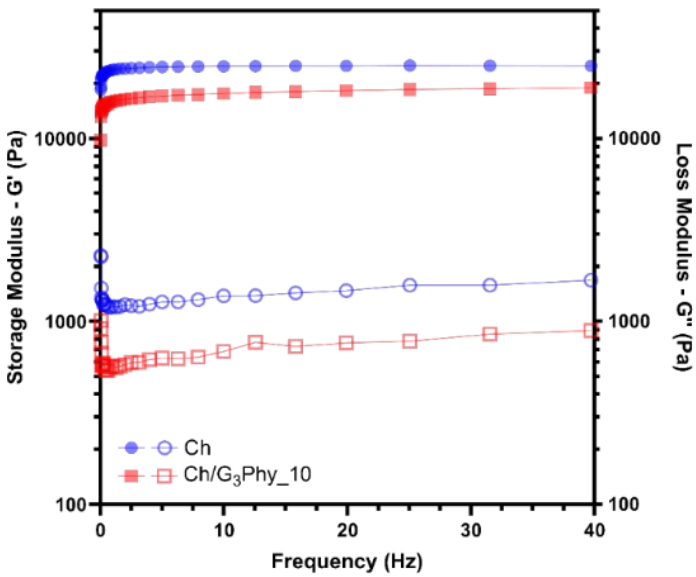

Figure S2. Storage (filled) and loss (empty) moduli evolution from 0.01 to 40 Hz at 37 ºC of uncrosslinked chitosan and chitosan membrane crosslinked with 10 wt-% of G_3Phy.

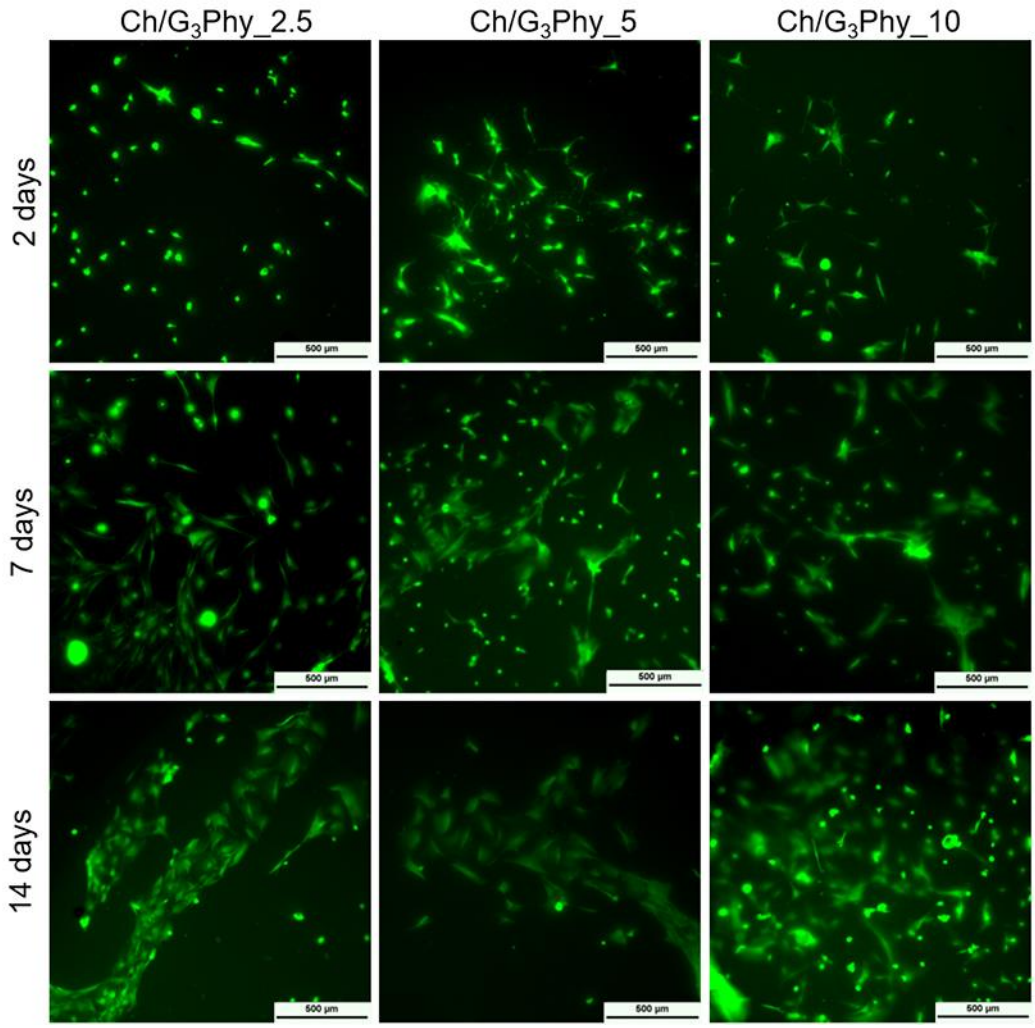

Figure S3. Fluorescence images of G_3Phy-crosslinked chitosan membranes at 2, 7, and 14 days of incubation after Calcein staining

Chapter 4

Hyaluronic acid-based hydrogel membranes for cartilage regeneration

Research article

Hyaluronic acid-based hydrogel membranes for cartilage regeneration

Ana Mora-Boza [1, 2, ‡], Elena López-Ruiz [3, 4, 5, 6, ‡], María Luisa López-Donaire [1, 2, *], Gema Jiménez [3, 4, 5, 6], María Rosa Aguilar [1, 2], Juan Antonio Marchal [3, 4, 6, 7], José Luis Pedraz [2, 8], Blanca Vázquez-Lasa [1, 2, *], Julio San Román [1, 2], Patricia Gálvez-Martín [9]

[1] Institute of Polymer Science and Technology, ICTP-CSIC, 28006 Madrid, Spain.

[2] CIBER-BBN. Health Institute Carlos III, 28029 Madrid, Spain.

[3] Biopathology and Regenerative Medicine Institute (IBIMER), Centre for Biomedical Research, University of Granada, Granada, E-18100, Spain.

[4] Instituto de Investigación Biosanitaria de Granada (ibs.GRANADA), University Hospitals of Granada-University of Granada, Granada E-18071, Spain.

[5] Department of Health Sciences, University of Jaén, 23071 Jaén, Spain.

[6] Excellence Research Unit "Modeling Nature" (MNat), University of Granada, Granada, E-18016, Spain.

[7] Department of Human Anatomy and Embryology, Faculty of Medicine, University of Granada, Granada, E-18016, Spain.

[8] NanoBioCel Group, Laboratory of Pharmaceutics, University of the Basque Country (UPV/EHU), School of Pharmacy, 01006 Vitoria- Gasteiz, Spain.

[9] R&D Human Health, Bioibérica S.A.U., Barcelona, Spain.

*Corresponding author.

‡These authors contributed equally.

In consideration for publication

Abstract

Current clinical procedures such as abrasion arthroplasty procedures, osteochondral transplantation, and autologous chondrocyte implantation fail to regenerate cartilage and make

necessary the development of new strategies. In this sense, crosslinked biomimetic and optimized degradable membranes can provide a stable and amenable environment for chondrocytes proliferation and stem cell differentiation, promoting in situ cartilage regeneration. Here, we developed novel semi- and interpenetrating polymer networks (IPN) membranes based on hyaluronic acid (HA) and chitosan (Ch) ionically crosslinked with the bioactive glycerylphytate (G_1Phy) compound. The second network of IPNs membranes is formed by a methacrylate derivative of HA covalently crosslinked through ultraviolet (UV) light irradiation. Semi-IPN and IPNs were physicochemically characterized in terms of composition, morphology, surface, and mechanical properties. Composition characterization by ICP-OES confirmed the incorporation of the G_1Phy crosslinker and values of C/N determined by elemental analysis (EA) indicated a hindered release of HA by the dual crosslinking processes in the IPNs membranes. Granular surfaces were observed for semi-IPN (Ra= 161.7±15.9) and IPN (Ra=58.9±11.6 nm) systems, being more marked in Ch/HA semi-IPN. Viscoelasticity of the systems was determined showing a loss tangent for the Ch/HA membranes (tan δ=0.17) in the range of native cartilage. Swelling and degradation of all membranes were evaluated at physiological conditions. Long-term stability was observed for all the systems in physiological media with a weight loss below 18% after 2 months. Biological performance was assessed on primary human mesenchymal stem cells (hMSCs). No cytotoxic effects were observed by confocal images as the total surface of the membranes was covered by live cells after 21 days culture. In agreement, cell proliferation increased over time for all the systems. Interestingly, Ch/HA semi-IPN showed a notable enhanced cell proliferation after 7 days culture. Thus, our findings suggest that Ch/HA semi-IPNs ionically crosslinked with G1Phy could be proposed as an effective promoter system of cartilage repair.

1. Introduction

Articular cartilage regeneration remains as a current challenge because of its limited self-renewal capacity mainly due to the absence of a vascular system and the presence of highly specialized phenotype cells (i.e. chondrocytes) [1-3]. Current clinical procedures for cartilage repair can be categorized into: (i) arthroscopic lavage and debridement, (ii) direct chondral replacement techniques by implantation of allografts or autografts, (iii) marrow stimulating

techniques, and (iv) cell-based implantation strategies like autologous chondrocyte implantation (ACI) [4, 5]. ACI has shown superior performance in comparison to the rest of methods from a clinical point of view, but its complex surgical requirements and the appearance of periosteal hypertrophy make necessary the development of new techniques [1].

Tissue engineering offers the possibility of using hydrogels-based scaffolds that can mimic the cartilage composition, structure, and intricate physicochemical features [2, 6]. The synthesis of crosslinked networks and matrices that provide an amenable environment for chondrocytes proliferation and differentiation maintenance offers the possibility of promoting *in situ* cartilage regeneration. In this sense, different strategies that use commercially available tissue engineering cartilage products have been developed and are being used in clinical practice [3, 7]. The matrix-induced autologous chondrocyte implantation (MACI) strategy is a marrow-stimulating technique that consists of a two-step procedure involving the implantation of a biodegradable polymeric construct that promotes cell differentiation and the formation of hyaline cartilage [5, 8]. In this technique, products such as the *in situ* formed gel BST Cargel® and the membrane Chondro-Gide® are being used. However, despite the currently used scaffolds and constructs give a certain level of success, optimized degradable systems directed towards more biomimetic grafts and improved joint environment are still in demand. In this sense, some research approaches are focused on the combination of different polymeric networks to form interpenetrating polymer networks (IPNs) or semi-IPNs. These systems have showed attractive properties in terms of enhanced stability and mechanical properties, mainly due to the molecular reinforcement resulted from the blend of different polymers [9-11]. Specifically, an IPN consists of a combination of two (or more) polymer networks, which are physically or chemically crosslinked and entangled with each other. For its part, in a semi-IPN, only one of the polymers is crosslinked and the linear polymer is entangled within the network [9].

Hyaluronic acid (HA) is a glycosaminoglycan found in cartilage extracellular matrix (ECM) that plays a critical role in maintaining cartilage homeostasis by the regulation of cell functions, including promotion of chondrogenic phenotype, and production and retention of matrix components [12, 13]. HA participates in important cell signalling pathways due to the presence

of cell surface receptors like CD44 and RHAMM, which is a receptor for hyaluronan-mediated motility [9]. Moreover, HA demonstrated to play powerful multifunctional activity in cartilage homeostasis and tissue remodelling processes [1, 14]. Different IPNs and semi-IPNs based on HA have been developed for cartilage repair applications [9, 15-17]. For example, Suri et al. [9] synthetized IPNs by sequential polymerization of collagen and photocrosslinkable HA, and semi-IPNs by HA entanglement in the polymerized collagen network. The fabricated IPNs exhibited improved mechanical properties and slower degradation in comparison to semi-IPNs due to the formation of a denser polymeric network. Other remarkable work was carried out by Pescosolido et al. [15], who developed a semi-IPN based on HA and photopolymerizable dextran for 3D bioprinting applications. Besides, different IPNs based on HA and sodium alginate have been also developed [16, 17]. Herein, we developed novel semi- and IPN systems based on HA and chitosan (Ch). Ch is a linear polysaccharide whose structure is similar to those glycosaminoglycans found in cartilage ECM. Ch has been widely applied to cartilage repair applications due to its attractive properties regarding biocompatibility and biodegradability [4, 12]. Some works have described the combination of HA and Ch to fabricate systems for cartilage regeneration [4, 8, 12, 14]. Neethu et al. [8] performed a profound study about the regeneration capacity of Ch/HA gels on critical osteochondral defects in knee joints of New Zealand white rabbits, claiming the potential regenerative capacities of their systems. In other work carried out by Erickson et al. [12], HA and Ch were used to fabricate a bilayer scaffold to repair osteochondral defects, showing excellent cellular proliferation results.

The novelty of our work lies in the development of HA and Ch formed semi- and IPN systems in which the Ch network is ionically crosslinked with glycerylphytate (G_1Phy) [18]. The second network of the IPN is formed by a methacrylic derivative of HA covalently crosslinked through ultraviolet (UV) light irradiation. G_1Phy is a bioactive crosslinker of reduced cytotoxicity whose crosslinking capacity against polymers containing amino groups (e.g. Ch, gelatin) has been widely demonstrated [19]. Moreover, it showed enhanced cellular adhesion and proliferation in comparison to traditionally used phosphate-based crosslinkers like tripolyphosphate [19]. In this work, we performed a parallel study of both semi- and IPN systems based on G_1Phy crosslinked Ch and HA in terms of composition, physicochemical, morphological, and mechanical

properties, observing clear differences that will determine its efficacy on their biological behaviour. Biological performance regarding viability, cell adhesion and proliferation was assessed on human mesenchymal stem cells (hMSCs). Our findings suggested that surface properties, as well as the presence of HA, can play a key role in the final application of semi- and IPN membranes as effective promoters of cartilage repair.

2. Experimental Section

2.1. Materials

HA (Ophthalmic grade, 800-1000 kDa, Bioiberica) and Ch with a degree of deacetylation of 90% (Medical grade, M_w: 200-500 kDa, Altakitin SA, Lisboa, Portugal) were used as received. Methacrylic anhydride (MA), poly(ethylene glycol) dimethacrylate (PEGDMA, M_n: 8000 Da) and the photoinitiator Irgacure 2959 were purchased from Sigma Aldrich and used as received. G_1Phy was prepared as previously described [18] by using phytic acid and glycerol from Sigma Aldrich. Solvents as isopropanol (Scharlau) and ethanol (BDH Chemicals) were used as received. Dialysis membranes (3500 Da cut off) were purchased from Spectrum®. Additional reagents such as phosphate buffered saline (PBS), calcium chloride, nitric acid 65% (v/v), acetic acid (AA) and sodium hydroxide were purchased from Thermo Fisher Scientific Corporation. Tris hydrochloride (Tris-HCl) 1 M solution (pH 7.5/Mol. Biol.) was purchase from Fisher BioReagents.

2.2. Synthesis of methacrylated hyaluronic acid (HAMA)

Methacrylated HA (HAMA) was synthesized through an esterification reaction in alkaline conditions following the protocol described by Khunmaneeet et al.[20]. Briefly, HA (1 g) was dissolved in 100 mL of double distilled water (ddH_2O) in a two necked glass flask for 24 h. Methacrylic anhydride was added to the HA solution at different MA:HA ratios (1:1, 2:1 and 5:1). The mixture was kept at 0 ºC using an ice bath and the pH was controlled at 8.5 by adding NaOH (5 M) with the help of an automatizater titrator (Metrohm) for 24 h. The final product was purified by precipitation in cold ethanol, subsequently centrifuged, redissolved in ddH_2O, and dialysed for 4 days. After freeze drying, a white powder was finally obtained. HAMA with different methacrylation degree (named HAMA-5, HAMA-20, HAMA-40) was characterized by

proton Nuclear Magnetic Resonance (^{1}H-NMR) and Attenuated Total Reflection–Fourier Transform Infra-Red (ATR-FTIR) spectroscopies.

2.3. Preparation of Ch membranes

Dried Ch was dissolved at a concentration of 2 wt-% in 1% AA water solution containing 13 wt-% $CaCl_2$ respect to Ch. Once it was dissolved, it was poured into a glass petri dish (internal diameter: 49 mm) and dried under moister conditions at room temperature until constant weight. Then, membranes were detached from the petri dishes after 5 min of incubation in 1 N NaOH solution and subsequently rinsed with ddH_2O until neutral pH was reached. Finally, membranes were ionically crosslinked by their immersion into a G_1Phy water solution at a concentration of 15 mg/mL for 24 h (30 wt-% respect to chitosan) and room temperature. The uncoupled G_1Phy was removed by rinsing twice the membranes with ddH_2O.

2.4. Preparation of Ch/HA and Ch/HAMA membranes

Either type of membranes, Ch/HA or Ch/HAMA, were prepared with a content of 75 % of chitosan and 25 % of HA or HAMA, respectively. Only HAMA with the lowest 5% methacrylation degree (HAMA-5) was used. HAMA-20 and 40 were not able to get dissolved in presence of Ch, which was dissolved as described in the above section. Either HA or HAMA solution in 1% AA with $CaCl_2$ (%) was added to the Ch solution together with additional drops of 2 M HCl to achieve the total dissolution of both polymers. In the case of Ch/HAMA membranes, the HAMA solution was supplemented with 5% PEGDMA crosslinker and 2% of photoinitiator Irgacure 2959, both respect to the HAMA content, in order to produce the photo-crosslinked process by UV-light. Therefore, the corresponding solution was poured into petri dishes and irradiated at 365 nm for 15 min using a UVP chamber photoreactor (CL-1000), equipped with 5 bulbs of 365-nm working at an intensity of 2.9 mW/cm^2. Finally, membranes were obtained following the same protocol as described in previous section for Ch membranes. Polymers and crosslinker compositions used for the fabrication of each system are summarized in Table 1.

Table 1. Polymer and crosslinker concentrations (wt-%) used for the fabrication of Ch membranes, semi-, and INPs developed in this work.

Membrane Sample	Ch (wt-%)	HA (wt-%)	HAMA (wt-%)	G_1Phy (wt-%) [a]	PEGDMA (wt-%) [b]
Ch (Network)	2	0	0	30	0
Ch/HA (Semi-IPN)	1.5	0.5	0	30	0
Ch/HAMA (IPN)	1.5	0	0.5	30	5

[a] Percentages calculated respect to Ch content.

[b] Percentage calculated respect to HAMA content

2.5. Characterization techniques

^{1}H-NMR spectra were recorded with a Varian Mercury 400 MHz. The spectra were carried out at 25 °C in deuterated H_2O (D_2O, 10% w/v) and referenced to the residual proton absorption of the solvent [δ 4.7].

ATR-FTIR of samples were carried out on a Perkin-Elmer Spectrum BX spectrophotometer. All spectra were recorded from 600 to 4000 cm^{-1} with a resolution of 4 cm^{-1} and 32 scans.

Elemental Analysis (EA) was performed with an elemental LECO model CHNS-932 microanalyzer. The determination of C and H was carried out with CO_2 and H_2O specific infrared detectors, while N (N_2) was determined by thermic conductivity. The measurements were conducted at 990 ºC using He as transporter gas.

Inductively Coupled Plasma-Optical Emission spectrometry (ICP-OES) measurements were carried out in a 4300 DV Perkin-Elmer plasma emission spectrometer under dynamic argon flow at 16 L/min using a Gemcone (Perkin-Elmer) nebulizer under dynamic argon flow at 0.8 L/min and 1300 W of plasma power.

Thermogravimetric Analysis (TGA) was performed in a thermogravimetric analyzer TGA Q500 (TA instruments) apparatus, under dynamic nitrogen at a heating rate of 20 ºC/min in a range of 30-640 ºC.

Field Emission Scanning Electron Microscopy (FE-SEM) images were taken in a Hitachi S-8000 instrument operating in transmission mode at 100 kV.

Atomic Force Microscopy (AFM) analysis was performed with an apparatus PicoLE (Molecular Imaging) operating in the acoustically driven, intermittent contact ("tapping") mode, using standard silicon AFM probes (NSC11/Cr-Au, Mikromasch, Estonia) having a cantilever spring constant of 48 N/m and a resonance frequency of 330 kHz. 10x10 mm^2. Topography was examined by AFM using the WSxM 5.0 Develop 9.1 software. Three acquisitions were made with roughness parameters analysis for each sample. Data were expressed as mean ± standard deviation (SD).

Contact angle measurements were performed at 25 °C on membranes dried by the sessile drop technique using a KSV instruments LTD CAM 200 Tensiometer and employing MilliQ water as a liquid with known surface tension. A minimum of 10 measurements were taken and averaged for each sample. Data were expressed as mean ± SD.

Rheological measurements were determined using an advanced rheometer from TA instruments, model AR-G2, equipped with a Peltier and a solvent trap. The last one allows leading the measurement in a water-saturated atmosphere by avoiding water evaporation from the membrane. Samples were previously stabilized by their immersion for 24 h in 7.4 PBS at 37 °C. All tests were carried out using a 25 mm diameter steel sand blasted parallel plate. Oscillatory shear tests with strain sweep step were performed at a frequency of 0.5 Hz and a strain ranging from 0.01 to 100% in order to determine the linear viscoelastic region (LVR) of the different membranes. Finally, frequency sweeping tests of membranes were conducted with a frequency scanning from 0.01 to 10 Hz at 0.1% strain and 37 °C to determine the elastic (G') and viscous (G") moduli. Three replicates of each sample were evaluated.

2.6. G_1Phy quantification

The amount of G_1Phy ionically crosslinked in the membranes was quantified measuring the P content using ICP-OES. Polymeric membranes were dried at 60 °C after their incubation in G_1Phy solution until constant weight. Afterwards, membranes were digested in nitric acid, 65% (v/v) at 60 °C for 24 h. Then, samples were diluted with ddH_2O to 5% nitric acid concentration in order to be compatible for ICP analysis. A blank solution was prepared with only nitric acid at 5% in ddH_2O. All measurements were performed in triplicate. A standard calibration curve of P

with concentration from 0-1000 mg/L was used. Three measurements were made for each sample. Data were expressed as mean ± SD.

2.7. Swelling

Dry membranes with a diameter of 12 mm and 0.2 mm thickness were soaked in 10 mL of PBS (pH=7.4) at 37 °C. The swollen membranes were removed at different periods of time. After removing the attached excess of water on the surface with filter paper, the membranes were weighed. The water uptake was calculated as described in equation (1):

$$\text{Swelling (\%)} = [(W_W - W_0) / W_0] \times 100 \quad (1)$$

where W_w and W_0 are the weight of the swollen membrane at time t, and the initial dried weight of the membrane, respectively. For each period of time and sample, a minimum of four replicates were measured and averaged. Data were expressed as mean ± SD.

2.8. Degradation

Dry membranes (12 mm and 0.2 mm) were weighed and then placed in 10 mL of PBS (pH 7.4) at 37 °C. The membranes were retrieved at predetermined time point and washed with ddH_2O to remove any remaining salts. The membranes were then dried at 60 °C until constant weight. The percentage of weight loss was calculated following the equation (2):

$$\text{Weight loss (\%)} = [(W_W - W_t) / W_0] \times 100 \quad (2)$$

where W_o and W_t are the weight of the initial dry membrane and the dried membrane at time t after incubation in PBS, respectively. For each period of time and sample, a minimum of four replicates were measured and averaged. Data were expressed as mean ± SD.

2.9. Release of G_1Phy

Dry membranes were sterilized using UV light on each side of the membrane for 1 h. Subsequently, each membrane was immersed into 10 mL of Tris-HCl 0.1 M buffer (pH 7.4) and incubated at 37 °C. Aliquots of 2 mL were taken at different periods of time (1, 2, 4, 7 and 14 days) and replaced with fresh media. The different aliquots were diluted to 5 mL with ddH_2O

and measured by ICP-OES. For each period of time and sample, a minimum of four replicates were measured and averaged. Data were expressed as mean ± SD.

2.10. Cell studies

2.10.1. Human MSCs isolation and culture from adipose tissue

Human MSCs used in this study were isolated from human abdominal fat obtained from healthy donors undergoing liposuction plastic surgery. Ethical approval for the study was obtained from the Ethics Committee of the Clinical University Hospital of Málaga, Spain. Informed patient consent was obtained for all samples used in this study. Human MSCs were isolated from human adipose tissue and characterized as previously reported [21, 22]. Cells were cultured in high-glucose Dulbecco's Modified Eagle's Medium (DMEM; Sigma-Aldrich, St Louis, MO, USA) supplemented with 10% fetal bovine serum (FBS; Sigma-Aldrich), 100 U/mL penicillin and 100 mg/mL streptomycin (Invitrogen Inc., Grand Island, NY, USA) at 37 °C in a humidified atmosphere containing 5% CO_2. Medium was regularly changed every 3 days. At 80% of confluence, cells were subcultured. For all the experiments cells were used between passages 4 and 6.

2.10.2. Human MSCs culture in hydrogel membranes

Hydrogel membranes were sterilized by immersion in 70% ethanol aqueous solution for 1 h, washed several times in phosphate buffered saline (PBS) and then subjected to UV light for 20 min each size. Then, hydrogel membranes were incubated in 24 well plates with complete medium overnight before cells were seeded. hMSCs suspension containing 30,000 cells in 200 μL of medium was slowly dropped onto the surface of each membrane and incubated for 2 h at 37 °C. After that, 1 mL of fresh medium was added to each well plate. All samples were incubated under a 5% CO_2 atmosphere at 37 °C. The culture medium was replaced every 2 days and the hydrogel membranes were processed for subsequent analysis.

2.10.3. Cell viability assay

Cell viability was determined on days 1, 7 and 21 using Live/Dead™ Viability/Cytotoxicity Kit (Invitrogen Inc., Grand Island, NY, USA). The hydrogel membranes were incubated in PBS containing Calcein AM (2 μM) and ethidium homodimer (4 μM) at 37 °C for 30 min to stain live

and dead cells, respectively. Membranes were imaged by confocal microscopy (Nikon Eclipse Ti-E A1, Amsterdam, Netherlands) and analyzed using NIS-Elements software (Amsterdam, Netherlands).

2.10.4. Cell proliferation assay

Cell proliferation was analyzed using Alamar Blue assay (Bio-Rad Laboratories, Inc., manufactured by Trek Diagnostic System. U.S.) after 1, 5, 7, 14 and 21 days. The hydrogel membranes were incubated with AlamarBlue® solution at 37 ºC for 3 h. Fluorescence of reduced AlamarBlue® was determined at 530/590 nm excitation/emission wavelengths (Synergy HT, BIO-TEK).

2.10.5. Environmental scanning electron microscopy (ESEM)

The hydrogel membranes were analyzed using a variable-pressure and environmental scanning electron microscope (ESEM) FEI, mod. Quanta 400 (Oregon, USA). The analysis was performed to characterize the surface structure of the membranes and cell growth after 21 days in culture. Samples were fixed with 2% glutaraldehyde and, then, were rinsed in 0.1 M cacodylate buffer and incubated overnight at 4 °C. For critical point the samples were then maintained with Osmium tetroxide 1% during 1 h and dehydrated in a series of ethanol solutions (50%, 70%, 90%, 100%) by soaking the samples in each solution for 15 min. Subsequently, samples were critical point dried (Anderson, 1951) in a desiccator (Leica EMCPD300), and covered by evaporating them in a carbon evaporator (Emitech K975X).

2.10.6. Statistical analysis

All graphed data represent the mean ± SD of at least three experiments. Two-tailed Student T-test analysis were performed for Ch/HA and Ch/HAMA samples with respect to Ch ones at each time point at significance level of $^{**}p<0.01$, and for Ch/HA samples with respect to Ch/HAMA samples at each time point at significance level of ($\#\#p<0.01$).

3. Results and Discussion

3.1. Synthesis of methacrylated hyaluronic acid (HAMA)

The chemical structure of HA allows easy modification of the (primary) hydroxyl-groups by esterification. This esterification is usually performed in aqueous solution mainly by using either methacrylic anhydride or glycidyl methacrylate. Alternative methods based on performing the same reaction in organic solution or water-organic solution have been described showing an improvement in the methacrylation degree [23]. In the present work, HAMA with three degrees of methacrylation were synthesized in water following the same protocol previously described by Smeds et al. [24], but with the implementation of an automatized titrator. This equipment allows controlling the reaction pH at 8.2 over time, which guarantees the efficiency of the reaction. The methacrylation degree was determined by ^{1}H-NMR spectroscopy (Figure S1A), considering the vinyl protons at 6.21 and 5.78 ppm (2H, s), and the pendant acetyl protons of HA at 2.04 ppm (3H, s). HAMA with a high methacrylation degree (43.5%, HAMA-40) was obtained for a 5-fold excess of MA, reaching higher values than the reported in the literature (~ 6 %) for a 20-fold excess and a HA of similar M_w (~ 1100 kDa) but without the computer controlled pH system [25]. This result confirmed the advantage of using an automatized method to synthetize HAMA, since high degrees of modification could be obtained without using excessive amounts of MA thanks to the precise pH control by the titrator. Additionally, by varying the HA excess from 2 to 1-fold excess, it was possible to obtain HAMA with methacrylation degrees of 19 and 4.5%, for HAMA-20 and HAMA-5, respectively.

The methacrylation of HA was also confirmed by ATR-FTIR spectroscopy (Figure S1B). HAMA with different methacrylation degrees showed the main characteristics bands of HA. The broad band at about 3300 cm^{-1} was attributed to hydrogen-bonded OH and NH stretching vibrations; the band at 2917 cm^{-1} to the CH stretching vibrations; and the band at 1407 cm^{-1} was attributed to the symmetric (CO_2^-) stretching modes of the planar carboxyl groups in the hyaluronate. The bands of amide I, II and II were observed at 1652 cm^{-1}, 1564 cm^{-1} and 1321 cm^{-1}; the band at 1150 cm^{-1} was due to COC (O-bridge); the band at 1072 cm^{-1} was assigned to the CO exocyclic and the band at 1036 cm^{-1} to the stretching of the C-OH bonds. At 947 cm^{-1} it appears the band due to the asymmetrical out of phase ring vibration [26]. An additional band

was observed at 1715-1710 cm^{-1}, which was attributed to the C=O ester bond vibration in the methacrylate group [27], which increases in intensity with the methacrylation degree. The band of the stretching of C-OH bonds also shifted from 1043 to 1036 cm^{-1}.

3.2. Physicochemical characterization and viscoelastic properties of membranes

Elemental composition of the membranes was determined by elemental analysis. Table 2 shows the theoretical and experimental elemental compositions (C, H, and N) for the different membranes. Experimental compositions correlated very well with those calculated theoretically, which revealed the absence of impurities. Table 2 also shows a decrease of the experimental C/N value respect to the theoretical one (from 6.1 to 5.25±0.07) for Ch/HA membranes. For Ch/HAMA membranes, the experimental C/N ratio (5.83±0.15) approached the theoretically expected (6.1). The decrease of C/N ratio in semi-IPN systems could indicate a possible release of HA from these membranes after washing steps since this phenomenon was not observed in IPN systems. This means that the covalent crosslinking of HAMA mediated by UV-light seemed to retain the HA polysaccharide in the IPN. In addition, this fact was confirmed by a decrease found in the yield percentage of Ch/HA membranes. Nevertheless, both semi- and IPN systems can be considered promising candidates for cartilage regeneration since both of them contain HA, an essential component of the cartilage ECM [12]. Likewise, the presence of HA in the membranes scaffolds will help to maintain the functionality and characteristic structure of regenerated cartilage, which is essential for the final success of these scaffolds [8, 14]. It is important to consider that the concentration range in which HA can provide these beneficial properties is quite wide [28].

The content of G_1Phy incorporated in the membranes resulted from the ionic crosslinking between amino and phosphate groups was analyzed by ICP-OES (Table 2). The amount of the phytate crosslinker decreased in Ch/HA and Ch/HAMA membranes compared to Ch sample. This feature was attributed to the lower chitosan content in these membranes (Ch:HA ratio = 75:25). This decrease become more pronounced in the IPN membranes in comparison to semi-

IPNs, maybe due to the fact that the covalently crosslinked HA could hindrance the availability of amine groups of Ch for ionic interactions with the phosphate groups of G_1Phy.

Table 2. Theoretical (Theo) and experimental (Exp) elemental compositions, crosslinker content, and yield percentage for Ch, Ch/HA and Ch/HAMA membranes.

Sample	C [a]		H [a]		N [a]		C/N [a]		G_1Phy content (%) [b, c]	Yield (%)
	Theo	Exp	Theo	Exp	Theo	Exp	Theo	Exp		
Ch	44.9	43.03 ±0.33	6.8	6.86 ±0.01	8.6	8.24 ±0.1	5.2	5.22 ±0.02	5.4 ±0.08	95.25 ±1.10
Ch/HA	44.7	42.72 ±0.11	6.53	6.77 ±0.09	7.36	8.12 ±0.11	6.1	5.25 ±0.07	4.9 ±0.49	74.96 ±0.60
Ch/HAMA	44.7	42.11 ±0.18	6.53	6.58 ±0.15	7.36	7.21 ±0.19	6.1	5.83 ±0.15	2.5 ±0.40	93.48 ±2.47

[a] Determined by elemental analysis

[b] Determined by ICP-OES

[c] Gram of G_1Phy per gram of membrane*100

The FTIR spectra of the membranes are represented in Figure S2. The FTIR spectra of semi- and IPN samples showed the characteristic bands of Ch and HA polysaccharides. The main bands appeared between 3600 and 3200 cm^{-1} (υ O-H and N-H associated); at 2924 and 2854 cm^{-1} (υ C-H); at 1720 cm^{-1} (υ C=O in carboxylic and ester groups); at 1643/1634 cm^{-1} (υ C=O of amide, amide I); at 1579 cm^{-1} (δ N-H); at 1420 cm^{-1} (υ COO^- and δ C-H); at 1373 cm^{-1} (δ -CH_3 symmetrical); at 1333 cm^{-1} (υ C-N, amide III); at 1258/1262 cm^{-1} (X P=O); at 1150 cm^{-1} (υ C-O-C asymmetric); at 1066, 1029, 995 and 984 cm^{-1} (υ C-O alcohols, υ P-O and P-O-C, υ C-O glycosidic linkages and vibration of pyranose structure); at 893 and 721 cm^{-1} (υ P-O and P-O-C) [29, 30].

Surface morphology is a critical factor for the development of biomaterials that effectively promote cell adhesion and proliferation [31]. Figure 1 shows a detailed examination of surface

topography for Ch (A), Ch/HA (B) and Ch/HAMA (C) by SEM and AFM, as well as the calculated roughness parameters (R_a and RMS) for the different systems. Topographic differences among the membranes can be observed in the SEM micrographs. Particularly, Ch system showed a very flat surface, while granular surfaces were observed in semi- and IPN systems, being more evident in Ch/HA membranes. This result illustrated a topographic change due to the incorporation of HA that can be a consequence of electrostatic interactions between carboxylic groups of HA and amino groups of Ch, which leads to polyelectrolyte complex formation [28]. The Ch-HA interaction could be hindered in IPN systems by UV curing process, resulting in flatter surfaces, as it is observed in Ch/HAMA micrographs. AFM 3D images show the micro features and the roughness of representative areas of the membranes. Ra and RMS values correlated very well with the topography observed by SEM. As it was expected, Ra and RMS values were significantly higher for Ch/HA membranes in comparison to those of Ch and Ch/HAMA. Therefore, we can conclude that covalent crosslinking of HAMA with UV-light resulted in a denser network in IPN systems compared to semi-IPNs, which leaded to a decrease of roughness at the nanoscale [9].

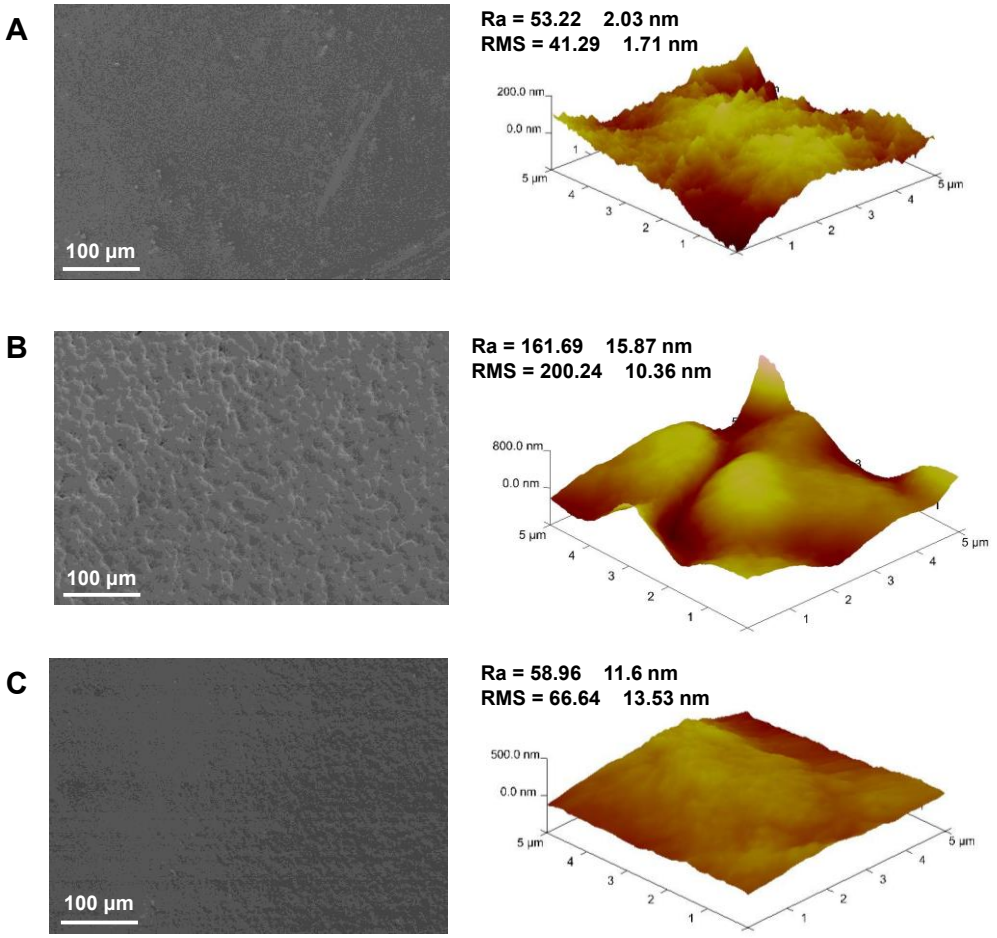

Figure 1. Scanning electron microscopy micrographs (left) and Atomic force microscopy 3D perspective images with their respective calculated roughness parameters (right) for Ch **(A)**, Ch/HA **(B)**, and Ch/HAMA **(C)** polymeric membranes.

Surface parameters such as wettability are important properties that must be studied since hydrophilic-hydrophobic balance greatly determines cell adhesion and proliferation properties of the scaffolds [32]. Surface-wetting characterization is currently carried out by contact angle measurements (WCA), the most common method being the sessile drop goniometry [33], which was used in this work. Measured WCA values for Ch, Ch/HA, Ch/HAMA membranes were 48.18 ± 2.71º, 40.97 ± 3.26º, and 47.73 ± 4.96º, respectively. All the systems showed hydrophilic surfaces (WCA<90º) as it was expected because of the characteristic water absorption nature of

these polysaccharides [34]. Different WCA for Ch samples are reported in literature. For instance, Tamer et al. found higher WCA values (89 ± 0.6°) for Ch surfaces [35] than those obtained in our work. However, it has been reported that Ch polarity highly depends on the type and concentration of the used neutralization solution as well as the time of washing steps. Noriega et al. [36] performed a profound study where they reported a wide range of WCA for Ch surfaces, from 45 to 65º, that highly depended on neutralization parameters. As expected, hydrophilicity increased as neutralization base concentration and incubation time increased. [36] In our samples, the relatively low WCA values observed for Ch could also be due to the contribution of available phosphate groups coming from the G_1Phy crosslinker on the membrane surface, which exhibits high affinity to polar liquids [37]. A decrease of WCA was observed for semi-IPN due to the presence of HA and its polyanionic character [38]. For its part, IPNs showed WCA values similar to those of Ch membranes, which could be due to the reduction of carboxylic groups of HA after methacrylation reaction and further covalent crosslinking. Since membrane surfaces showed different WCA values, we can conclude that wettability properties seem to be an easily tunable parameter in function of composition and applied crosslinking processes in our systems.

Rheological measurements were carried out to study the viscoelastic properties of our systems. The evolution of the elastic and viscous moduli of the membranes was studied in their LVR at a constant strain of 0.1%, and it is represented in Figure 2. All the systems exhibited a plateau in the studied frequency range, which indicated the stability of the crosslinked network. This plateau also showed a solid-like behavior of the membranes, since elastic moduli was independent on the applied frequency [39]. IPN showed higher G' values in comparison to Ch and semi-IPN systems due to the molecular reinforcement of the polymeric network after covalent crosslinking. IPNs have previously demonstrated to improve mechanical properties regarding semi-IPNs, since they provide denser structures because of double crosslinking mechanisms [9, 11]. Finally, loss tangent (tan δ = viscous modulus/elastic modulus), which is an index of the viscoelasticity of the systems, was calculated by taking the ratio between G" and G' at a frequency of 1 Hz. Values of 0.27, 0.17 and 0.24, were obtained for Ch, Ch/HA and Ch/HAMA membranes, respectively. Interestingly, loss tangent value found for Ch/HA semi-

IPN system approached that of native cartilage (0.14 ± 0.03) as previously reported by Hsu et al. [40]. This result makes this scaffold as a promising candidate for cartilage regeneration regarding mechanical properties.

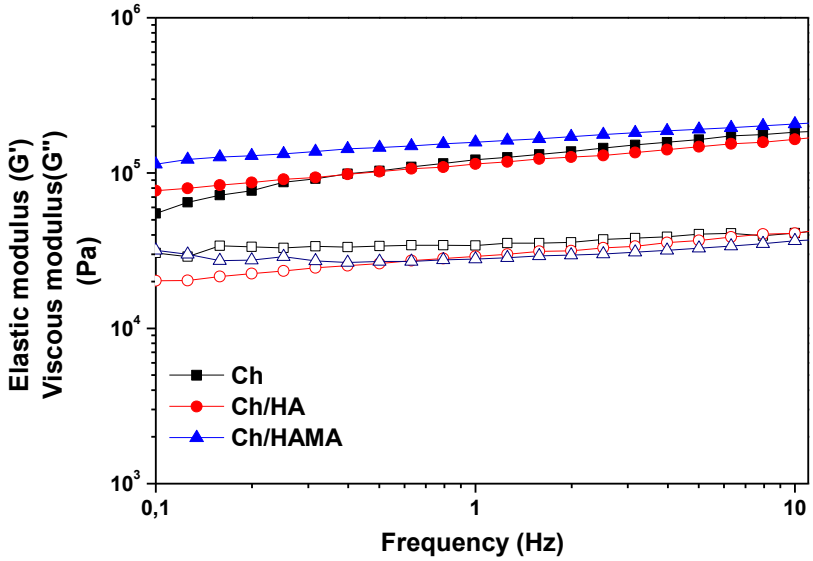

Figure 2. Evolution of elastic (G', filled) and viscous (G", unfilled) moduli as a function of applied frequency at constant strain of 0.1% of Ch, Ch/HA, and Ch/HAMA polymeric membranes.

Collectively, the results described in this subsection demonstrated clear differences regarding composition, surface topography, wettability and mechanical properties for the studied systems that are expected to also exert relevant differences on their swelling and degradation properties, as well as biological performance.

3.3. *In vitro* swelling and degradation studies

The swelling capability of cartilage mainly depends on the binding of water to polar groups of glycosaminoglycans (GAGs). [41] In this sense, the preparation of membranes that include natural polymers such as Ch, with similar structure to GAGs, and HA, both containing polar groups [42, 43] could be a good alternative to obtain systems that mimic water uptake of articular cartilage. Swelling of the developed membranes was studied under physiological conditions and the results are represented in Figure 3A. For all membranes a fast water uptake during the first

hour was observed, reaching a stable value after this period. Slight differences in water absorption were appreciated during the next 48 h when equilibrium was attained. Ch membranes showed the lowest swelling capacity, which is expected because the pKa value of Ch is 6.5. Under physiological conditions, Ch amino groups are not positively charged and the repulsive forces in the polymeric backbone are not induced, and therefore, this increase of the network water uptake does not take place [32]. Ch and Ch/HA membranes showed rather similar swelling profiles giving final swelling values ~100% (Figure 3B). For its part, Ch/HAMA membranes showed the highest equilibrium water absorption (up to 140%) which could be attributed to the formation of a dual crosslinked network able to locate a higher amount of water molecules in their interstices, but also to the presence of a higher HA content, whose residence time in the membrane increased thanks to covalent crosslinking. Nevertheless, all membranes showed moderate swelling that will contribute to maintain their structural stability. If necessary, swelling could be adjusted by varying the content of HAMA in the membrane [44].

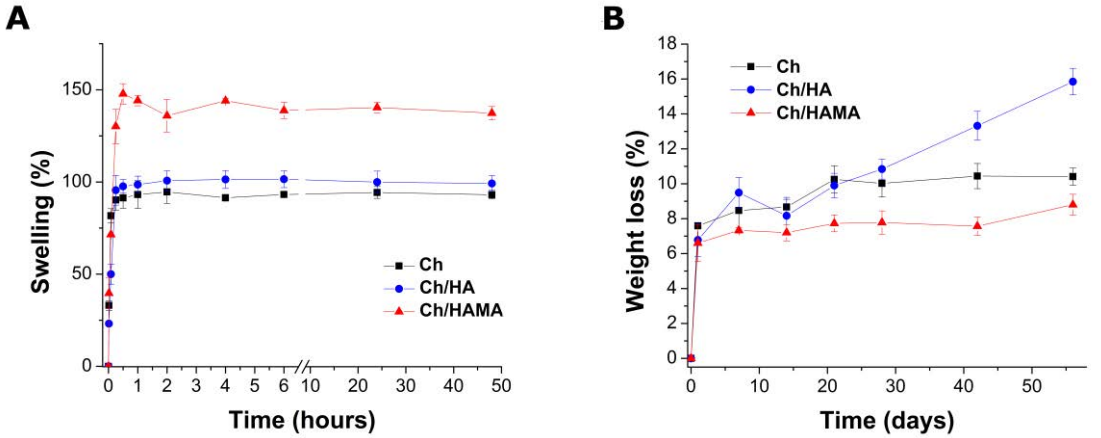

Figure 3. (A) Effect of hydrogel membrane composition on swelling after incubation in PBS 7.4 at 37 °C for different periods of time. **(B)** Weight loss of Ch, Ch/HA and Ch/HAMA membranes at different time points after soaking in PBS 7.4 at 37 °C under static conditions. Data represented the mean ± SD.

In vitro degradation of all hydrogel membranes immersed in a PBS solution at 37 ºC was below 10% over 14 days (Figure 3B) and it slightly increased after 28 days. However, for longer incubation time (~2 months), degradation of Ch and Ch/HAMA was maintained while Ch/HA

membranes suffered a slightly further degradation (~16%). The initial membrane weight loss could be attributed to the progressive breaking of the ionic bonds formed between the phosphates and amino groups, what produce release of the G_1Phy crosslinker and consequently, dissolution of HA and Ch polymeric chains. Similar results were reported for Ch/HA tissue engineering porous scaffolds where it was suggested than the degradation in PBS is only because of polymeric dissolution, being necessary the presence of enzymes such as lysozyme and hyaluronase to undergo an enzymatic degradation [42]. The higher weight loss of Ch/HA versus Ch membranes could be associated to the presence of entangled HA within the Ch network, favouring its dissolution. Accordingly, Ch/HAMA membranes displayed the highest stability. This fact, could be explained because the covalently crosslinked HA prevents its dissolution and the hydrolytically degradable ester bonds in the HAMA are sterically hindered [45].

3.4. G_1Phy release

The release profile of G_1Phy from the different hydrogels membranes is showed in Figure 4. All membranes showed a fast release (~72%) during the first 24 h. A plateau in the release profile is observed for the three systems after 7 days, where Ch and Ch/HA membranes reached an 85% release of the initial G_1Phy content, while Ch/HAMA membranes showed a slightly superior release (~90%). Electrostatic interaction between G_1Phy ions (PO_4^{2-} or HPO_4^{-}) and the amine groups of Ch and breaking of links with incubation time could be the cause of these release profiles. Finally, no complete release of initial G_1Phy content was achieved after 14 days. Physical mixture of Ch with phytic acid has been reported by Barahuie et al. [46] showing a complete release after 60 s. On the other hand, the slight increase of G_1Phy release observed in Ch/HAMA membranes respect to Ch and Ch/HA systems could be due to the higher water uptake of Ch/HAMA membranes, which can favour ion diffusion and subsequently ion exchange between G_1Phy anions and negative anions present in the Tris buffer. Finally, it is worth mentioning that the release profile is in agreement with the release of Ch/phytic acid systems reported in the literature [46, 47]. Thus, we can say that G_1Phy presents similar binding properties than phytic acid as has been recently reported by Mora-Boza et al. [18].

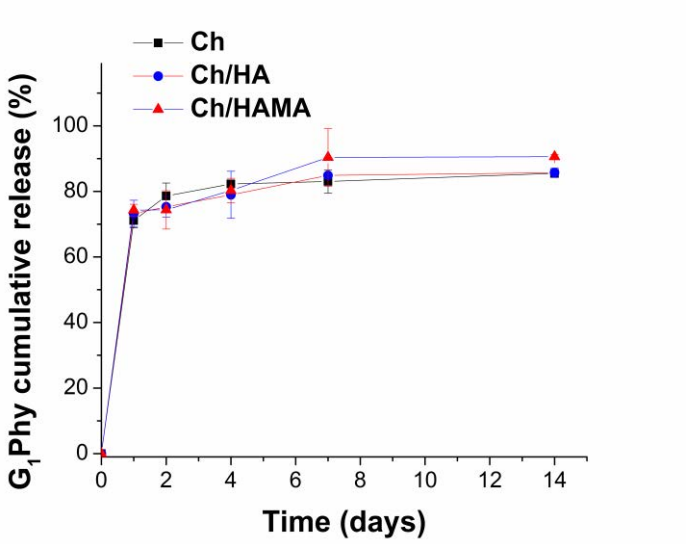

Figure. 4. Release profile of G_1Phy from the Ch, Ch/HA and Ch/HAMA membranes in 0.1 M Tris-HCl buffer (pH 7.4) at 37 °C. Data represented the mean ± SD.

3.5. Biological evaluation

3.5.1. Cell viability and proliferation assays

In order to evaluate the feasibility of Ch, Ch/HA and Ch/HAMA hydrogel membranes as an adequate support for cell survival, the viability of the seeded hMSCs on the top of the membranes was evaluated. The live/dead assay was employed to visualize the presence of living and dead cells after 1, 7 and 21 days in the hydrogel membranes (Figure 5A). Confocal images showed hMSCs growing on all the membrane surfaces at days 1 and 7. The number of living cells was much higher at day 21 and cells appeared covering the hydrogel membranes with few dead cells. These results indicated that Ch, Ch/HA and Ch/HAMA hydrogel membranes can provide an amenable environment that supports hMSCs growth and confirmed the cell viability with no cytotoxic effects.

Proliferation of hMSCs cultured in Ch, Ch/HA and Ch/HAMA hydrogel membranes was evaluated with Alamar Blue assay at 1, 5, 7, 14 and 21 days of cell culture (Figure 5B). Results demonstrated that cell proliferation increased from day 1 until 21 days in all the systems. No

significant differences were found between Ch/HAMA and Ch membranes regarding cell proliferation at any time. For its part, Ch/HA demonstrated a significantly enhanced cell proliferation in comparison to Ch at 5, 7, 14, and 21 days, and in comparison to Ch/HAMA system at 7, 14, and 21 days. This result may be due to the supportive microenvironment of semi-IPNs system for cell attachment and proliferation. Correira et al. [42] demonstrated that the biological performance of polysaccharides based systems was affected by their physicochemical factors, which could be tuned by the incorporation of HA to Ch at different proportions. In fact, they found that the addition of HA to Ch scaffolds up to 5% improved both physicochemical and biological properties of Ch scaffolds [42]. In our work, the better biological performance of the semi-IPN system can be attributed on the one hand, to its physicochemical features regarding surface roughness, mechanical properties approaching those of cartilage, and wettability. On the other hand, the enhancement of cell viability and proliferation of Ch/HA sample in comparison to Ch/HAMA system can derived from the presence of linear HA embedded in the semi-IPN and its higher ability to be interchanged with the medium respect to crosslinked HAMA which is longer retained in the IPN membrane [32, 42], thus in our case, the semi-IPN could mimic best the native cartilage ECM. Some authors have claimed the benefits of semi-IPN systems containing HA for cartilage regeneration due to its similarities to ECM composition [15, 48]. For example, Pescosolido et al. [15] combined HA with photocrosslinkable dextran to overcome instability problems of HA derived from its high hydrophilicity. Thus, the presence of the bioactive HA provided excellent biological properties to their systems. For its part, Skaalure et al. [48] developed a semi-IPN consisting on poly(ethylene glycol) and entrapped HA, whose incorporation clearly led to an enhanced cell adhesion and proliferation.

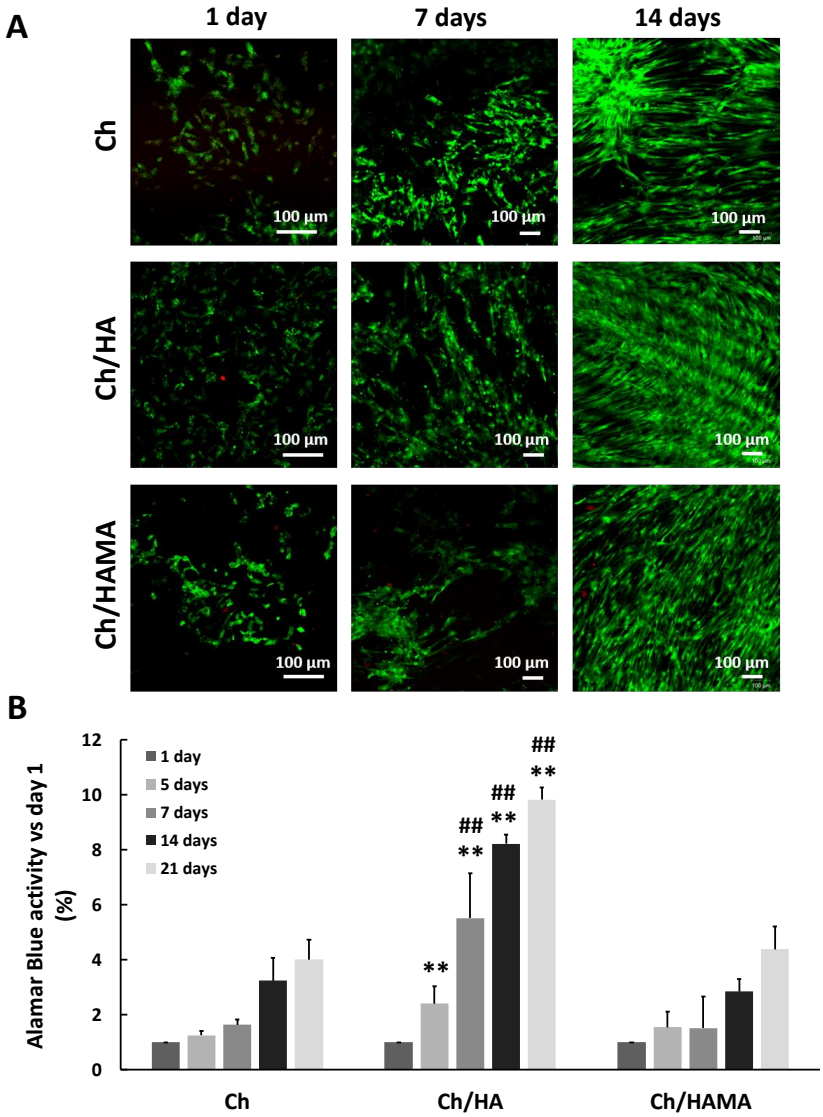

Figure 5. Cytocompatibility of Ch, Ch/HA and Ch/HAMA hydrogel membranes with hMSCs. **(A)** Representative confocal images of hMSCs stained with Calcein AM (living cells in green) and ethidium homodimer (dead cell in red) at days 1, 7 and 21 using the live/dead® assay. **(B)** Cell proliferation at the hydrogel membranes after 1, 5, 7, 14 and 21 days. Values are represented as mean ± SD (n=3) and normalized respect to day 1 values. Two-tailed Student T-test analysis were performed for Ch/HA and Ch/HAMA samples with respect to Ch samples at each time at significance level of **p<0.01, and for Ch/HA samples with respect to Ch/HAMA samples at each time point at significance level of (##p<0.01).

3.5.2. ESEM microscopy of hydrogel membranes

To characterize the microstructural architecture of Ch, Ch/HA and Ch/HAMA membranes and observe the morphology of hMSCs cultured on them, an ESEM analysis was carried out on day 21. It is known that the surface roughness is an important factor in promoting cell attachment [49]. ESEM images of Ch, Ch/HA and Ch/HAMA membranes (Figure 6A) revealed a rougher surface for the Ch/HA membrane compared to those of Ch/HAMA and Ch, corroborating the SEM observations for dried samples (Figure 1) but surfaces of all membranes were able to support cell growth (Figure 6B). ESEM images evidenced the cells covering the surface of Ch, Ch/HA and Ch/HAMA membranes, with good adhesion, spreading, and a homogenous distribution throughout the entire surface. Moreover, ESEM images showed an interconnected cell community that attached to the scaffold which also confirmed the biocompatibility of the membranes [50, 51].

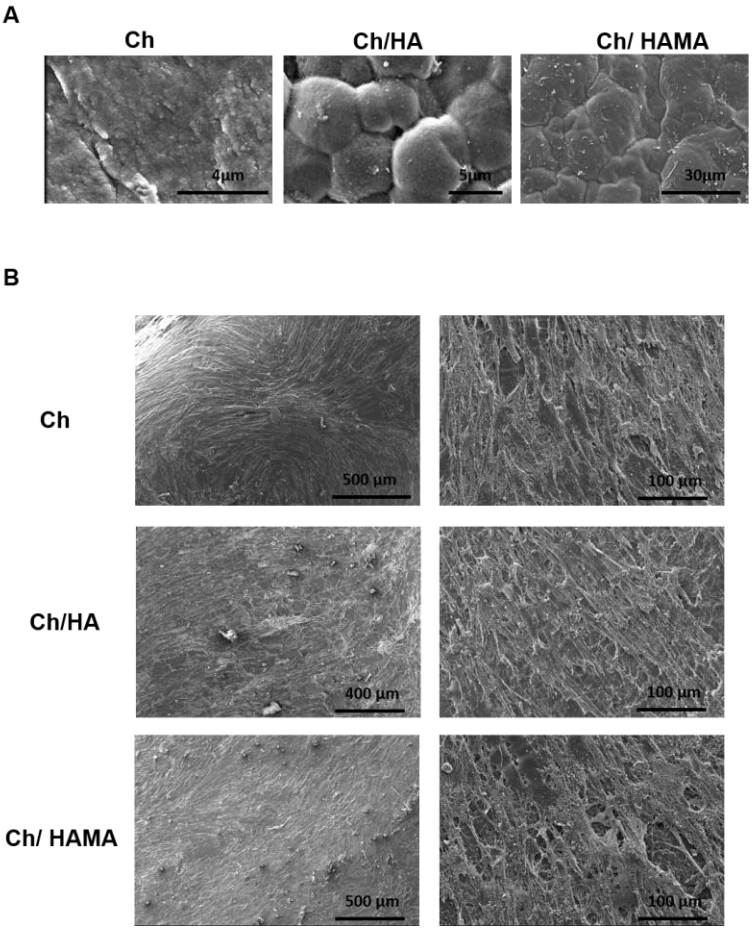

Figure 6. (A) Representative ESEM images of Ch/HAMA hydrogel membranes before hMSCs culture. **(B)** Representative ESEM images of hMSCs growing on hydrogel membranes after 21 days.

4. Conclusions

Semi-IPN and IPN systems based on HA and Ch were developed as biomimetic and degradable membranes with potential application in articular cartilage regeneration. Significant differences between semi-IPNs and IPNs were observed in terms of surface, mechanical, swelling and degradability properties. IPNs demonstrated to enhance HA retention, as well as, mechanical properties of the polymeric network thanks to covalent crosslinking mediated by UV-light irradiation. Dual crosslinking processes of IPNs, consisted of ionic crosslinking of Ch

and photopolymerization of HAMA, provided membranes with long-term stability and increased swelling. Moreover, the IPN framework led to flatter surfaces in comparison to semi-IPNs. All the studied systems demonstrated high biocompatibility, supporting hMSCs adhesion and proliferation on their surfaces. Semi-IPNs significantly increased cell proliferation over time respect to IPN, arising as the best candidate of the studied systems. This behavior could be due to the surface features of the semi-IPN (i.e. hydrophilic nature, granular topography and mechanical properties mimicking those of native cartilage), which seem to be key properties to favor hMSCs performance. These finding suggest that Ch/HA semi-IPNs ionically crosslinked with G_1Phy have potential to be proposed as an effective promoter system of cartilage repair. In the near future, further studies will be carried out to evaluate both *in vitro* and *in vivo* the chondrogenic differentiation of hMSCs and the maintenance of mature phenotype of chondrocytes seeded on these biomimetic ECM membranes.

5. References

[1] E. Tognana, A. Borrione, C. De Luca, A. Pavesio, Hyalograft C: hyaluronan-based scaffolds in tissue-engineered cartilage, Cells Tissues Organs 186(2) (2007) 97-103.

[2] C. Deng, J. Chang, C. Wu, Bioactive scaffolds for osteochondral regeneration, J Orthop Translat 17 (2019) 15-25.

[3] B.J. Huang, J.C. Hu, K.A. Athanasiou, Cell-based tissue engineering strategies used in the clinical repair of articular cartilage, Biomaterials 98 (2016) 1-22.

[4] A. Abarrategi, Y. Lopiz-Morales, V. Ramos, A. Civantos, L. Lopez-Duran, F. Marco, J.L. Lopez-Lacomba, Chitosan scaffolds for osteochondral tissue regeneration, J Biomed Mater Res A 95(4) (2010) 1132-41.

[5] A.J. Nixon, E. Rickey, T.J. Butler, M.S. Scimeca, N. Moran, G.L. Matthews, A chondrocyte infiltrated collagen type I/III membrane (MACI(R) implant) improves cartilage healing in the equine patellofemoral joint model, Osteoarthritis Cartilage 23(4) (2015) 648-60.

[6] L. Li, F. Yu, L. Zheng, R. Wang, W. Yan, Z. Wang, J. Xu, J. Wu, D. Shi, L. Zhu, X. Wang, Q. Jiang, Natural hydrogels for cartilage regeneration: Modification, preparation and application, J Orthop Translat 17 (2019) 26-41.

[7] R.M. Jeuken, A.K. Roth, R.J. Peters, C.C. Van Donkelaar, J.C. Thies, L.W. Van Rhijn, P.J. Emans, Polymers in cartilage defect repair of the knee: current status and future prospects, Polymers 8(6) (2016) 219.

[8] N. Mohan, P.V. Mohanan, A. Sabareeswaran, P. Nair, Chitosan-hyaluronic acid hydrogel for cartilage repair, Int J Biol Macromol 104(Pt B) (2017) 1936-1945.

[9] S. Suri, C.E. Schmidt, Photopatterned collagen-hyaluronic acid interpenetrating polymer network hydrogels, Acta Biomater 5(7) (2009) 2385-97.

[10] E.S. Dragan, Advances in interpenetrating polymer network hydrogels and their applications, Pure and Applied Chemistry 86(11) (2014) 1707-1721.

[11] H. Suo, D. Zhang, J. Yin, J. Qian, Z.L. Wu, J. Fu, Interpenetrating polymer network hydrogels composed of chitosan and photocrosslinkable gelatin with enhanced mechanical properties for tissue engineering, Mater Sci Eng C Mater Biol Appl 92 (2018) 612-620.

[12] A.E. Erickson, J. Sun, S.K. Lan Levengood, S. Swanson, F.C. Chang, C.T. Tsao, M. Zhang, Chitosan-based composite bilayer scaffold as an in vitro osteochondral defect regeneration model, Biomed Microdevices 21(2) (2019) 34.

[13] C.B. Knudson, Hyaluronan and CD44: strategic players for cell-matrix interactions during chondrogenesis and matrix assembly, Birth defects research. Part C, Embryo today : reviews 69(2) (2003) 174-96.

[14] R.A. Muzzarelli, F. Greco, A. Busilacchi, V. Sollazzo, A. Gigante, Chitosan, hyaluronan and chondroitin sulfate in tissue engineering for cartilage regeneration: a review, Carbohydr Polym 89(3) (2012) 723-39.

[15] L. Pescosolido, W. Schuurman, J. Malda, P. Matricardi, F. Alhaique, T. Coviello, P.R. van Weeren, W.J. Dhert, W.E. Hennink, T. Vermonden, Hyaluronic acid and dextran-based semi-IPN hydrogels as biomaterials for bioprinting, Biomacromolecules 12(5) (2011) 1831-8.

[16] C.W. Chung, J.Y. Kang, I.S. Yoon, H.D. Hwang, P. Balakrishnan, H.J. Cho, K.D. Chung, D.H. Kang, D.D. Kim, Interpenetrating polymer network (IPN) scaffolds of sodium hyaluronate and sodium alginate for chondrocyte culture, Colloids Surf B Biointerfaces 88(2) (2011) 711-6.

[17] P. Chen, C. Xia, J. Mo, S. Mei, X. Lin, S. Fan, Interpenetrating polymer network scaffold of sodium hyaluronate and sodium alginate combined with berberine for osteochondral defect regeneration, Mater Sci Eng C Mater Biol Appl 91 (2018) 190-200.

[18] A. Mora-Boza, M.L. López-Donaire, L. Saldaña, N. Vilaboa, B. Vázquez-Lasa, J. San Román, Glycerylphytate compounds with tunable ion affinity and osteogenic properties, Scientific Reports 9(1) (2019) 11491.

[19] A. Mora-Boza, M.K. Włodarczyk-Biegun, A. del Campo, B. Vázquez-Lasa, J.S. Román, Glycerylphytate as an ionic crosslinker for 3D printing of multi-layered scaffolds with improved shape fidelity and biological features, Biomaterials Science 8(1) (2020) 506-516.

[20] S. Khunmanee, Y. Jeong, H. Park, Crosslinking method of hyaluronic-based hydrogel for biomedical applications, J Tissue Eng 8 (2017) 2041731417726464-2041731417726464.

[21] P. Galvez, M.J. Martin, A.C. Calpena, J.A. Tamayo, M.A. Ruiz, B. Clares, Enhancing effect of glucose microspheres in the viability of human mesenchymal stem cell suspensions for clinical administration, Pharmaceutical research 31(12) (2014) 3515-28.

[22] E. Lopez-Ruiz, G. Jimenez, W. Kwiatkowski, E. Montanez, F. Arrebola, E. Carrillo, S. Choe, J.A. Marchal, M. Peran, Impact of TGF-beta family-related growth factors on chondrogenic differentiation of adipose-derived stem cells isolated from lipoaspirates and infrapatellar fat pads of osteoarthritic patients, European cells & materials 35 (2018) 209-224.

[23] E. Hachet, H. Van Den Berghe, E. Bayma, M.R. Block, R. Auzély-Velty, Design of Biomimetic Cell-Interactive Substrates Using Hyaluronic Acid Hydrogels with Tunable Mechanical Properties, Biomacromolecules 13(6) (2012) 1818-1827.

[24] K.A. Smeds, M.W. Grinstaff, Photocrosslinkable polysaccharides for in situ hydrogel formation, Journal of Biomedical Materials Research 54(1) (2001) 115-121.

[25] J.A. Burdick, C. Chung, X. Jia, M.A. Randolph, R. Langer, Controlled Degradation and Mechanical Behavior of Photopolymerized Hyaluronic Acid Networks, Biomacromolecules 6(1) (2005) 386-391.

[26] Y. Wu, Preparation of low-molecular-weight hyaluronic acid by ozone treatment, Carbohydrate Polymers 89(2) (2012) 709-712.

[27] F. Yousefi, S. Kandel, N. Pleshko, Infrared Spectroscopic Quantification of Methacrylation of Hyaluronic Acid: A Scaffold for Tissue Engineering Applications, Applied spectroscopy 72(10) (2018) 1455-1466.

[28] H. Liu, Y. Yin, K. Yao, D. Ma, L. Cui, Y. Cao, Influence of the concentrations of hyaluronic acid on the properties and biocompatibility of Cs-Gel-HA membranes, Biomaterials 25(17) (2004) 3523-30.

[29] S.A. de Oliveira, B.C. da Silva, I.C. Riegel-Vidotti, A. Urbano, P.C. de Sousa Faria-Tischer, C.A. Tischer, Production and characterization of bacterial cellulose membranes with hyaluronic acid from chicken comb, Int J Biol Macromol 97 (2017) 642-653.

[30] K.D. Yao, T. Peng, M.F.A. Goosen, J.M. Min, Y.Y. He, pH-sensitivity of hydrogels based on complex forming chitosan: Polyether interpenetrating polymer network, Journal of Applied Polymer Science 48(2) (1993) 343-354.

[31] J.B.M. Rocha Neto, T.B. Taketa, R.A. Bataglioli, S.B. Pimentel, D.M. Santos, A. Fiamingo, C.A.R. Costa, S.P. Campana-Filho, H.F. Carvalho, M.M. Beppu, Tailored chitosan/hyaluronan coatings for tumor cell adhesion: Effects of topography, charge density and surface composition, Applied Surface Science 486 (2019) 508-518.

[32] A.T. Iacob, M. Dragan, N. Ghetu, D. Pieptu, C. Vasile, F. Buron, S. Routier, S.E. Giusca, I.D. Caruntu, L. Profire, Preparation, Characterization and Wound Healing Effects of New Membranes Based on Chitosan, Hyaluronic Acid and Arginine Derivatives, Polymers (Basel) 10(6) (2018).

[33] T. Huhtamäki, X. Tian, J.T. Korhonen, R.H.A. Ras, Surface-wetting characterization using contact-angle measurements, Nature Protocols 13(7) (2018) 1521-1538.

[34] A.S. Hoffman, Hydrogels for biomedical applications, Advanced Drug Delivery Reviews 64 (2012) 18-23.

[35] T.M. Tamer, M.N. Collins, K. Valachova, M.A. Hassan, A.M. Omer, M.S. Mohy-Eldin, K. Svik, R. Jurcik, L. Ondruska, C. Biro, A.B. Albadarin, L. Soltes, MitoQ Loaded Chitosan-Hyaluronan Composite Membranes for Wound Healing, Materials (Basel) 11(4) (2018).

[36] S.E. Noriega, A. Subramanian, Consequences of Neutralization on the Proliferation and Cytoskeletal Organization of Chondrocytes on Chitosan-Based Matrices, International Journal of Carbohydrate Chemistry 2011 (2011) 1-13.

[37] I.F. Amaral, P.L. Granja, L.V. Melo, B. Saramago, M.A. Barbosa, Functionalization of chitosan membranes through phosphorylation: Atomic force microscopy, wettability, and cytotoxicity studies, Journal of Applied Polymer Science 102(1) (2006) 276-284.

[38] S. Yamanlar, S. Sant, T. Boudou, C. Picart, A. Khademhosseini, Surface functionalization of hyaluronic acid hydrogels by polyelectrolyte multilayer films, Biomaterials 32(24) (2011) 5590-5599.

[39] Y. He, C. Liu, X. Xia, L. Liu, Conformal microcapsules encapsulating microcarrier-L02 cell complexes for treatment of acetaminophen-induced liver injury in rats, Journal of Materials Chemistry B 5(10) (2017) 1962-1970.

[40] M.K. Kang, S.K. Hong, Y.C. Seo, Y.O. Kim, H.Y. Lee, J.-C. Kim, Chitosan microgel: Effect of cross-linking density on pH-dependent release, Korean Journal of Chemical Engineering 29(1) (2011) 72-76.

[41] M.N. Rodrigues, M.B. Oliveira, R.R. Costa, J.F. Mano, Chitosan/Chondroitin Sulfate Membranes Produced by Polyelectrolyte Complexation for Cartilage Engineering, Biomacromolecules 17(6) (2016) 2178-88.

[42] C.R. Correia, L.S. Moreira-Teixeira, L. Moroni, R.L. Reis, C.A. van Blitterswijk, M. Karperien, J.F. Mano, Chitosan scaffolds containing hyaluronic acid for cartilage tissue engineering, Tissue engineering. Part C, Methods 17(7) (2011) 717-30.

[43] Y. Yuan, B.M. Chesnutt, G. Utturkar, W.O. Haggard, Y. Yang, J.L. Ong, J.D. Bumgardner, The effect of cross-linking of chitosan microspheres with genipin on protein release, Carbohydrate Polymers 68(3) (2007) 561-567.

[44] J.E. Bean, D.R. Alves, M. Laabei, P.P. Esteban, N.T. Thet, M.C. Enright, A.T.A. Jenkins, Triggered Release of Bacteriophage K from Agarose/Hyaluronan Hydrogel Matrixes by Staphylococcus aureus Virulence Factors, Chemistry of Materials 26(24) (2014) 7201-7208.

[45] E. Tous, J.L. Ifkovits, K.J. Koomalsingh, T. Shuto, T. Soeda, N. Kondo, J.H. Gorman, 3rd, R.C. Gorman, J.A. Burdick, Influence of injectable hyaluronic acid hydrogel degradation behavior on infarction-induced ventricular remodeling, Biomacromolecules 12(11) (2011) 4127-35.

[46] F. Barahuie, D. Dorniani, B. Saifullah, S. Gothai, M.Z. Hussein, A.K. Pandurangan, P. Arulselvan, M.E. Norhaizan, Sustained release of anticancer agent phytic acid from its chitosan-coated magnetic nanoparticles for drug-delivery system, International journal of nanomedicine 12 (2017) 2361-2372.

[47] C.-Y. Yang, C.-H. Hsu, M.-L. Tsai, Effect of crosslinked condition on characteristics of chitosan/tripolyphosphate/genipin beads and their application in the selective adsorption of phytic acid from soybean whey, Carbohydrate Polymers 86(2) (2011) 659-665.

[48] S.C. Skaalure, S.O. Dimson, A.M. Pennington, S.J. Bryant, Semi-interpenetrating networks of hyaluronic acid in degradable PEG hydrogels for cartilage tissue engineering, Acta Biomater 10(8) (2014) 3409-20.

[49] R. Ayala, C. Zhang, D. Yang, Y. Hwang, A. Aung, S.S. Shroff, F.T. Arce, R. Lal, G. Arya, S. Varghese, Engineering the cell-material interface for controlling stem cell adhesion, migration, and differentiation, Biomaterials 32(15) (2011) 3700-11.

[50] A. Barlian, H. Judawisastra, N.M. Alfarafisa, U.A. Wibowo, I. Rosadi, Chondrogenic differentiation of adipose-derived mesenchymal stem cells induced by L-ascorbic acid and platelet rich plasma on silk fibroin scaffold, PeerJ 6 (2018) e5809.

[51] Z. Yang, Y. Wu, C. Li, T. Zhang, Y. Zou, J.H. Hui, Z. Ge, E.H. Lee, Improved mesenchymal stem cells attachment and in vitro cartilage tissue formation on chitosan-modified poly(L-lactide-co-epsilon-caprolactone) scaffold, Tissue engineering. Part A 18(3-4) (2012) 242-51.

Acknowledgments

The authors thanks to "La Caixa" Foundation (ID 100010434), which supported Ana Mora-Boza (scholarship code LCF/BQ/ES16/11570018), to the Spanish Ministry of Economy and Competitiveness for financial support (project RTC-2016-5451-1) and the Fundación Mutua Madrileña (project FMM-AP17196-2019). B. Vázquez-Lasa and M. R. Aguilar are members of the SusPlast platform (Interdisciplinary Platform for Sustainable Plastics towards a Circular Economy) from the Spanish National Research Council (CSIC).

6. Supporting information

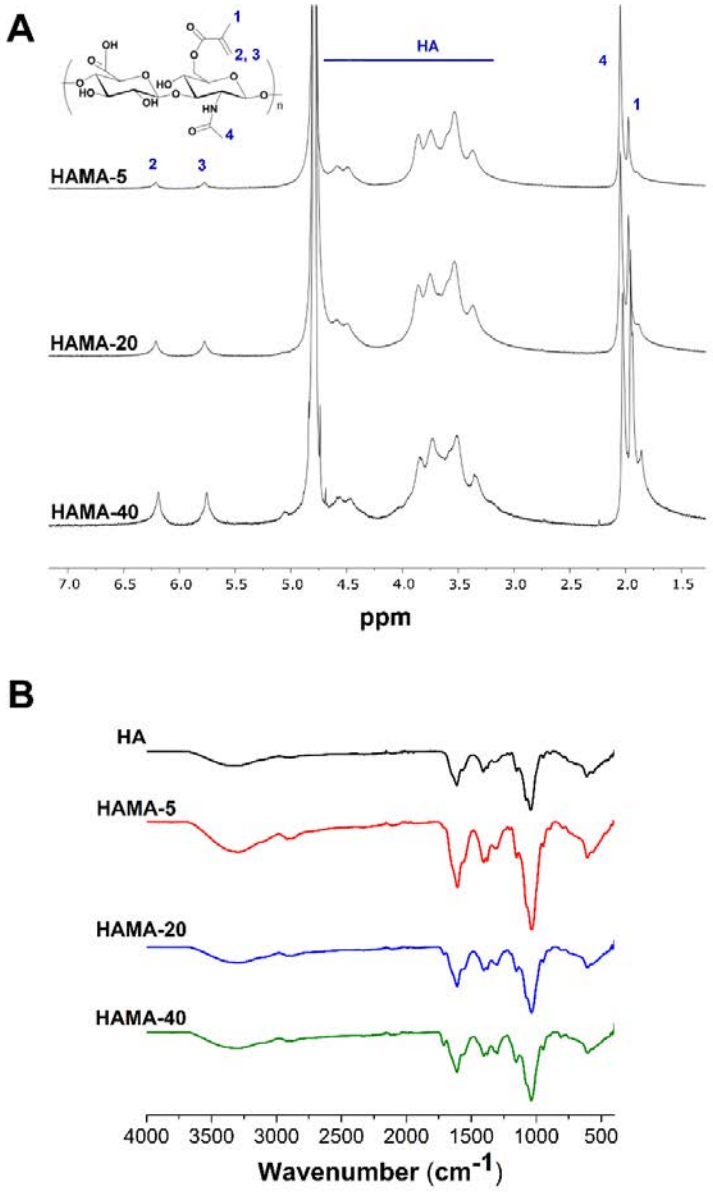

Figure S1. (A) ^{1}H-NMR spectra in D_2O, and **(B)** ATR-FTIR spectra of HA, HAMA-5, HAMA-20, and HAMA-40.

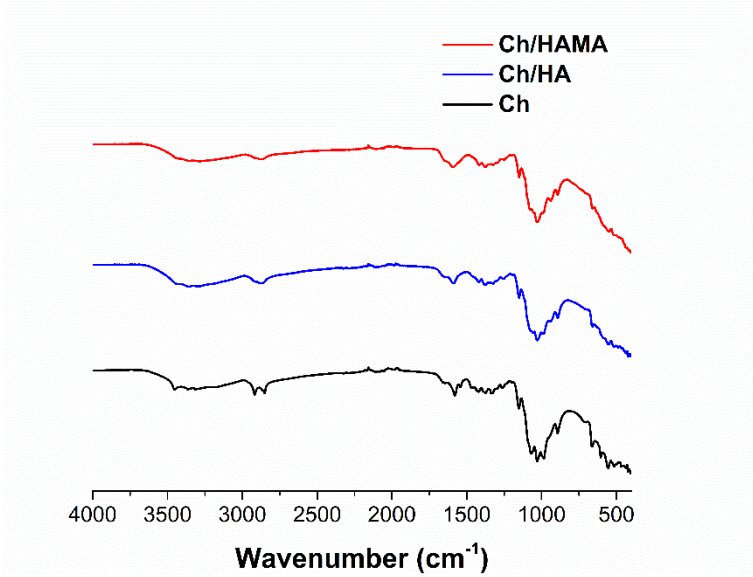

Figure S2. ATR-FTIR spectra of Ch, Ch/HA, and Ch/HAMA.

Chapter 5

Glycerylphytate as ionic crosslinker for 3D printing of multi-layered scaffolds with improved shape fidelity and biological features

Research article

Glycerylphytate as ionic crosslinker for 3D printing of multi-layered scaffolds with improved shape fidelity and biological features

Ana Mora-Boza [a, b], Małgorzata K.Włodarczyk-Biegun [c], Aránzazu del Campo [d, e], Blanca Vázquez-Lasa [a, b,*], Julio San Román [a, b]

[a] Institute of Polymer Science and Technology, ICTP-CSIC, 28006 Madrid, Spain.

[b] CIBER-BBN. Health Institute Carlos III, 28029 Madrid, Spain.

[c] INM – Leibniz Institute for New Material, 66123 Saarbrücken, Germany.

[d] Chemistry Department, Saarland University, 66123 Saarbrücken, Germany.

*corresponding author.

Biomaterials Science 8: 506-516 (2020)

Abstract

Fabrication of intricate and long-term stable 3D polymeric scaffolds by 3D printing technique is still a challenge. In the biomedical field, hydrogel materials are very frequently used because of their excellent biocompatibility and biodegradability, however improvement of their processability and mechanical properties is still required. This paper reports the fabrication of dual crosslinked 3D scaffolds, using a low concentrated (<10 wt-%) ink of gelatin methacryloyl (GelMA)/Chitosan and a novel crosslinking agent, glycerylphytate (G_1Phy), to overcome the current limitations in the 3D printing field using hydrogels. The applied methodology consisted of a first ultraviolet light (UV) photopolymerization followed by a post-printing ionic crosslinking treatment with G_1Phy. This crosslinker provides a robust framework and avoids the necessity of neutralization with strong bases. The blend ink showed shear-thinning behavior and excellent printability in the form of straight and homogeneous filament. UV curing was undertaken simultaneously to 3D deposition, which enhanced precision, shape fidelity (resolution ≈ 150 μm), and prevented from collapse of

the subsequent printed layers (up to 28 layers). In the second step, the novel G_1Phy ionic crosslinker agent provided swelling and long term stability properties to the 3D scaffolds. The multi-layered printed scaffolds were mechanically stable at physiological conditions for at least one month. Preliminary *in vitro* assays using L929 Fibroblasts showed very promising results in terms of adhesion, spreading, and proliferation in comparison to other phosphate-based traditional crosslinkers (i.e. TPP). We envision that the proposed combination of the blend ink and 3D printing approach can have widespread applications in the regeneration of soft tissues.

1. Introduction

Native organs and tissues are complex and highly organized structures. Fabrication of three-dimensional (3D) scaffolds which reproduce these intricate geometries is of great interest for tissue engineering and regenerative medicine. Traditional fabrication techniques, such as freeze drying or solution casting render random macro- and microstructures with poor control over the final architecture [1]. Porosity is a key parameter in the development of tissue-like structures: the pore size and distribution determine the colonization by cells, and their distribution within the scaffold [2, 3]. 3D printing has arisen as a promising tool for the development of scaffolds with complex and well defined geometries, as it allows layer-by-layer fabrication of 3D constructs with flexible selection of customized geometries, sizes, and materials [1, 4, 5]. Hydrogels are preferred materials for 3D printing because of their excellent biocompatibility and biodegradability. However, their high water content leads to poor processability for 3D printing methodologies [6]. Moreover, their intrinsic softness is insufficient for self-supporting of the printed structures [1, 4, 7-10]. A current trend to overcome these limitations is to combine different materials that can together fulfil the essential requirements for good printability [11-14]. Such properties are: (i) shear-thinning behaviour while printing, (ii) mechanical stability for keeping shape fidelity after printing, (iii) good structural integrity at physiological conditions, and (iv) cytocompatibility [15]. Extensive efforts have been recently made in the field to develop crosslinking processes that can stabilize the scaffold immediately after printing, such as photocuring of methacrylated polymers [4, 10, 16].

Gelatin hydrogels have been widely used for 3D printing in medical applications. Gelatin is a denatured form of collagen that has several advantages. Gelatin shows less antigenicity than

collagen, but it maintains in the backbone the RGD peptide sequences for cell attachment, and the matrix metalloproteinase-sensitive degradation domains, typical from collagen. Gelatin is commonly used in the tissue engineering and regenerative medicine fields due to its low cost and easy processability [16]. However, its gelation kinetics is too slow to be efficient for the printing process. Therefore, GelMA has been extensively used in the last years [6, 11, 13, 15-20]. Methacrylation allows fast covalent crosslinking in the presence of a photoinitiator and light exposure [16, 21]. Methacrylation does not affect the RGD domains and allows the synthesis of materials with tunable mechanical properties [21, 22]. Chitosan is a natural polysaccharide that can promote tissue regeneration through the activation of inflammatory and fibroblast cells [23-26]. Chitosan supports cell proliferation and differentiation better than alginate, the quintessential printable material [23]. However, its use in 3D printing has been limited due to its weak mechanical properties [27, 28]. In the last years, a few studies have reported the use of chitosan for 3D printing [5, 7, 23, 29-31]. Wu et al. studied different chitosan-based inks by dissolving the chitosan in a mix of different acids. Gelation of printed scaffolds was achieved by post-printing immersion in NaOH solution, which neutralized the amine groups of chitosan and reduced its solubility. However, the authors did not asses the biological response of the printed structures [7]. Demirtas et al. developed a bioprintable form of chitosan by adding β-glycerolphosphate to the ink, which provided thermosensitiveness to the system. In this case, the scaffold demonstrated favourable biological features, but the 3D printed structures showed poor shape fidelity [23]. Therefore, development of successful strategies to overcome current limitations in the 3D printing field using hydrogels is demanded. The present work proposes the use of the crosslinker glycerylphytate (G_1Phy) developed by our group [32] in the fabrication of dual crosslinked 3D scaffolds using a low concentrated (<10 wt-%) ink of GelMA/Chitosan. Although other studies have been focused on the combination of gelatin with chitosan because of their ability to form together polyelectrolyte complexes [15, 24, 25, 33], the blend ink composed of GelMA/Chitosan has not be reported so far.

G_1Phy plays a key role since it provides robust networks and avoids the necessity of neutralization and washing steps [32]. The as-obtained 3D printed structures exhibit good

printability, adequate mechanical properties and long-term stability. Thus, our approach involves a two-step crosslinking process that combined UV photopolymerization of GelMA followed by post-printing ionic crosslinking with G_1Phy. Two-step 3D printing approaches, which usually consist of the combination of GelMA photopolymerization and ionic crosslinking processes, has been widely applied in 3D printing field [11, 34-36]. In these works, ionic crosslinking is commonly first applied followed by photocuring of GelMA. In the present work, simultaneous deposition and photopolymerization of the 3D structures has been performed. This approach improves resolution and shape fidelity without the necessity of using sacrificial polymers or template agents, which are commonly techniques applied to water-based ink solutions [11, 37, 38]. This approach and the incorporation of a novel crosslinker such as G_1Phy for subsequent ionic gelation not only provides appropriate processability properties to the scaffolds but also bioactive properties [32] in comparison to traditional alginate-Ca^{+2} ionic crosslinking systems frequently applied in dual-step 3D printing technology.

In this work, 3D scaffolds printed with a pneumatic-based 3D printer show excellent shape fidelity (resolution ≈ 150 μm). Ionic post-treatment mediated by G_1Phy, a hybrid derivative of phytic acid of reduced toxicity, provides a fast and homogeneous ionic crosslinking between phosphate groups present in G_1Phy and amine groups of chitosan and GelMA, that is crucial for long-term stability properties of the crosslinked polymeric networks. Since, 3D printing technology aims to mimic intricate structures and geometries with high resolution, control over stability and swelling properties are essential for cell culture and tissue regeneration in the field of hydrogels 3D printing. Finally, preliminary *in vitro* results of the 3D printed scaffolds crosslinked with G_1Phy using L929 Fibroblasts display favourable biological performance in terms of biocompatibility, cell proliferation, and cytocompatibility.

2. Experimental section

2.1. Materials

Chitosan powder (with a degree of desacetylation of 90% and Mw = 300 kDa) was purchased from Altakitin (São Julião do Tojal, Portugal) and used as received. Gelatin from porcine skin (type A, ~300 bloom), methacrylic anhydride (MA), poly(ethylene glycol) dimethacrylate (PEGDMA,

Mn 20 kDa), Irgacure2959, sodium tripolyphosphate (TPP), triton, and Dulbecco's phosphate-buffered saline (DPBS) were purchased from Sigma-Aldrich (St. Louis, MO, USA). Bovine serum albumin (BSA) was purchased from PAN-Biotech and paraformaldehyde (PFA) from Electron Microscopy Sciences (Hatfield, PA, USA). G_1Phy crosslinker was synthesized in our lab as published elsewhere [32]. The dispensing tips were purchased from VIEWEG GmbH Dosier- und Mischtechnik (Kranzberg, Germany) and dispensing Optimum® cartridges from Nordson (Erkrath, Germany).

2.2. Ink design and preparation.

GelMA was synthetized by adapting a previously reported method [39]. 5 g of gelatin were dissolved in 50 mL of DPBS at 50 ºC and stirred for 30 min until completely dissolved. 8 mL of MA were added gradually to the solution and the reaction was allowed to proceed for 3 h at 50 ºC. The reaction was stopped by adding 150 mL of DPBS. The final solution was dialyzed against distilled water (MWCO 3.5 kDa) at 40 ºC for 7 days. The resulted product was freeze-dried and stored at 4 ºC in a dark container. The degree of methacrylation (70%) was calculated by ^{1}H-Nuclear Magnetic Resonance (RMN) in D_2O at 37 ºC [40] (Figure S1).

For the preparation of the polymeric ink, GelMA was dissolved at different concentrations (2 to 5 wt-%) in distilled water at 1% (v/v) of acetic acid and 1 wt-% of PEGDMA at 40 ºC. Chitosan powder was added to the solution to obtain different concentrations (1 to 4 wt-%) in the final ink volume. Irgacure 2959 was used as a photoinitiator and was added to the ink solutions at a final concentration of 0.5% (w/v). The ink solutions were stirred at 40 ºC for 3 h in dark conditions to obtain a homogeneous solution and transferred to 10 mL volume cartridges. Finally, the cartridges were centrifuged for 5 min at 800 rpm to remove air bubbles.

The viscosity of the ink solutions was measured with a rotational rheometer (DHR3, TA Instruments, USA) in oscillatory mode by increasing the shear rate from 1 to 1000 s^{-1} at 22 ºC using a stainless-steel parallel Peltier plate geometry (12 mm diameter) with solvent trap. The photocrosslinking reaction was followed on the same rheometer during *in-situ* illumination using a parallel plate geometry (20 mm) at room temperature (22 ºC), and a UV light source OmniCure

S2000 (Excelitas Technologies, Ontario, Canada). The UV light source was previously calibrated with a UV meter. The applied UV intensity was 50 mW/cm² and a 365 nm filter was used.

2.3. 3D printing methodology

The 3D printing approach is summarized in Figure 1. A pneumatic extrusion 3D printer (BioScaffolder 3.2, GeSiM, Germany) was used and the scaffolds were printed in 6 well-plates. Metal straight needles with an inner diameter of 150 μm and 200 μm were used. Printing speed and air pressure were adjusted to 5 mm/s and 500 kPa, respectively, for 150 μm tip, and 8 mm/s and 400 kPa for 200 μm tip. A dual-step crosslinking methodology was used. In the first step, simultaneously with material deposition, a UV light (OmniCure S1500, Excelitas Technologies, Ontario, Canada; Filter: 320-500 nm, 50 mW/cm²) was applied to initiate photopolymerization of GelMA in each layer of the scaffold. The light was focused on the needle outlet. After printing, the 3D scaffold was immersed for 5 min in a G_1Phy crosslinker solution (15 mg/mL, 16.3 mM) for ionic crosslinking of the amine groups present in chitosan and GelMA. Scaffolds were washed once with distilled water to remove crosslinker excess prior to further experiments. During printing, the temperatures in the cartridge and in the printer stage were maintained at 40 ºC and 15 ºC, respectively. Printing parameters (air pressure, printing speed and layer height) were adjusted depending on the needle used. For comparison, printed scaffolds were also crosslinked with TPP crosslinker solution (15 mg/mL, 40.7 mM).

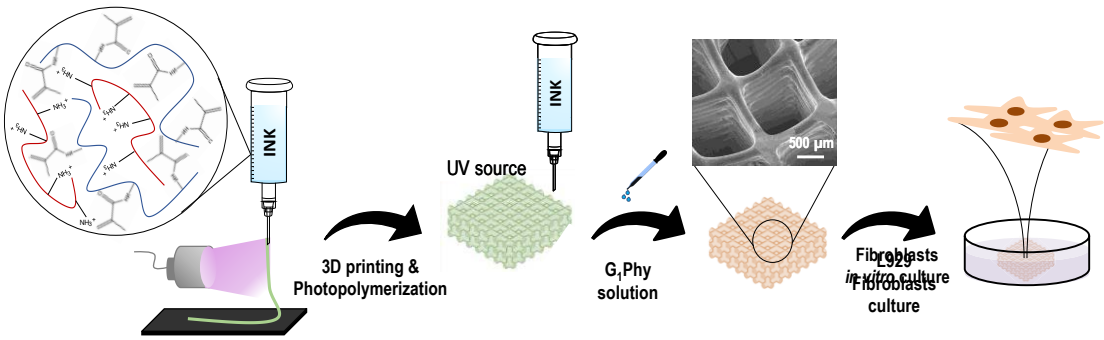

Figure 1. 3D printing approach applied for GelMA/Chitosan 3D polymeric scaffolds.

2.4. 3D scaffold characterization

2.4.1. Chemical composition and morphology

Phosphorus (P) content of the 3D printed scaffolds was studied by Inductively Coupled Plasma-Optical Emission Spectrometry (ICP-OES). The scaffolds were weighed and digested at 65 ºC with 65% v/v HNO_3. Then, the samples were diluted with pure water in a ratio 1:10. The quantification of P was performed with an ICP-OES Ultima 2 (HORIBA, Kyoto, Japan). A conical nebulizer at 2.15 bars and 0.81 L/min flow was used, and the analytical wavelength for P was 214.914 nm. The measurements were conducted in triplicate for each sample and the data obtained were expressed as mean values ± standard deviations (SD).

Energy Dispersive X-rays (EDX) analysis of P, C, N and O content was performed with a Bruker XFlash model with detector 5030. P maps were recorded for all fabricated samples.

Light microscopy characterization of the samples was done using an Olympus (Hamburg, Germany) SZX16 stereomicroscope under opaque illumination.

For cryo-Scanning Electron Microscope (SEM) evaluation, the samples were cut in 1cm x 2cm pieces and dried carefully with a Kimtech Science (Kimberly-Clark, Koblenz, Germany) tissue before plunging in liquid ethane at -165 ºC using a Gatan (Pleasanton, CA, USA) CP3 cryo plunger. Samples were transferred under liquid nitrogen to a self-made cryo-SEM holder and placed onto the stage of a FEI (Hilsboro, OR, United States) Quanta 400 FEG SEM. Cryo-SEM observation was performed under high vacuum conditions using accelerating voltage between 1.5 and 5 keV. Depending on the amount of ice generated at the sample surface during the preparation process, samples were freeze-dried carefully inside the SEM before taking secondary electron images using an Everheart-Thornley detector (ETD).

2.4.2. Physicochemical properties

Swelling of the printed scaffolds was evaluated by measuring the strand widths at different times of incubation in PBS at 37 ºC (2, 4, 7, and 10 days) by imaging with a light microscopy (stereomicroscope SMZ 800N with episcopic illumination, Nikon, Germany). The measurements were conducted in triplicate for three different samples.

Degradation rate was calculated gravimetrically by drying and weighing the scaffolds after incubation in PBS at 37 °C for different time points (2, 4, 7, 10, 20 and 30 days). The measurements were conducted in triplicate for each sample and the data obtained were expressed as mean values ± SD.

Crosslinker release was followed by measuring the content of P in the supernatant after incubating the scaffolds in medium at increasing times. G_1Phy and TPP samples were incubated in Tris-HCl buffer at pH 7.4 and 37 ºC in order to avoid interference between P in the sample and in PBS. Aliquots were taken at 2, 4, 7, 10 and 14 days of incubation and the P content was determined by ICP-OES. The measurements were conducted in triplicate for each sample and the data obtained were expressed as mean values ± SD.

2.4.3. Mechanical properties

Viscoelastic properties of the 3D printed scaffolds were evaluated in a rotational rheometer (DHR3, TA Instruments, USA) in oscillatory mode at frequency 1 Hz and strain 1%. 4 wt-%/4 wt-% GelMA/Chitosan solutions were photocrosslinked in 24 well-plates by illuminating for 5 min at 50 mW/cm^2, and incubated in 15 mg/mL solution of G_1Phy or TPP for 5 min. Their storage and loss moduli were measured in the rheometer.

2.5. Biological behaviour

2.5.1 Cell culture

L929 Fibroblasts (ATCC) were used to evaluate the *in vitro* biocompatibility of the scaffolds. Cells were grown and maintained in RPMI 1640 medium (Gibco, 61870-010) supplemented with 20% FBS (Gibco, 10270), 200 mM L-glutamine (Gibco), 100 units/mL penicillin and 100 µg/mL streptomycin (Invitrogen) at 37 ºC in a humidified atmosphere of 5% CO_2. Cell culture media was refreshed every 48 h. Cells from passage 25-30 were used.

2.5.2 Live/dead assay

For live/dead assay 10 µl microdroplets containing 10^5 cells were deposited on the surface of the scaffolds. 2 mL of cell culture medium were added to each well after 1 h. The samples were incubated for 24 h at 37 ºC in a humidified atmosphere of 5% CO_2 and cell viability was assessed

using a fluorescein diacetate (FDA) (Sigma-Aldrich) and propidium iodide (PI) (Sigma-Aldrich) double-staining protocol. 1 μg/mL PI solution and 1 μg/mL FDA solution were dissolved in PBS to achieve final concentrations of 20 μg/mL and 6 μg/mL, respectively. After removing culturing medium from the samples, 100 μL of staining solution was added to each well for 10 min incubation. Samples were 2 x washed with PBS and imaged with PolScope microscope (Zeiss, Germany).

2.5.3 Immunochemistry confocal staining

Cells were fixed with PFA 3.7% w/v for 10 min, permeabilized with 0.5% w/v Triton-X 100 (TX) for 10 min, and blocked with 0.1% TX and 5% w/v BSA for 20 min. Samples were incubated in 1:1000 vinculin rabbit antibody (Thermofisher) solution for cytoskeleton labelling and 1:200 Alexa fluor-546 Phalloidin (Thermofisher) solution for focal adhesions staining in red color for ~1 h. Then, they were rinsed twice with PBS and incubated with secondary antibody (Alexa flour-488 goat antirabbit, Thermofisher) 1:500 solution to visualize cytoskeleton in green. Finally, samples were stained with 1:1000 DAPI (4',6-Diamidino-2-Phenylindole, Dihydrochloride, Thermofisher) solution for nuclei visualization in blue color and washed with PBS (Sigma). Imaging was performed using Nikon Ti-Eclipse (Nikon Instruments Europe B.V., Germany) with a Sola SE 365 II (Lumencor Inc., Beaverton, USA) solid state illumination device and an Andor Clara CCD camera for detection.

2.5.4 Cytotoxicity

The evaluation of cytotoxicity of the scaffolds was determined by MTT assay. The corresponding scaffold was set in cell culture medium. Then, extracts of the medium were removed at different time periods (2, 4, 7 and 10 days) and replaced with fresh medium. The extracts were filtered and used for cytotoxicity assays. Thermanox® (TMX, Thermofisher, Waltham, MA, USA) discs were used as negative control. First, cells were seeded at a density of $9x10^4$ cells/mL in 96 well-plates and incubated to confluence. After 24 h of incubation the medium was replaced with the corresponding extract and incubated at 37 ºC in humidified air with 5 % CO_2 for 24 h. Cellular viability (%) was calculated for each sample respect to the control at each time of incubation. The

data were obtained from 3 independent series of experiments with triplicates for each sample and they were expressed as mean values ± SD. Analysis of variance (ANOVA) of the results for G^1Phy and TPP samples was performed with respect to control plate at each time at significance level of ***$p<0.001$, and for G_1Phy samples with respect to TPP sample at each time at significance level of ##$p<0.01$.

2.5.5 Proliferation over time.

Alamar Blue (Sigma-Aldrich) assay was used to analyze cellular proliferation at 2, 4, 7 and 10 days on the 3D scaffolds directly printed in cellular-repellent 6 well-plates (CELLSTAR®, Greiner Bio-One, Kremsmünster, Austria). The scaffolds were sterilized with ethanol and UV light for 1 h and 30 min, respectively. Cells were seeded at a density of $15x10^3$ cells/mL and incubated at 37 °C. The data were obtained from 3 independent series of experiments with triplicates for each sample and they were expressed as mean values ± SD. ANOVA of the results for G_1Phy samples was performed with respect to TPP samples at each time point at significance level of ***$p<0.001$.

3. Results

3.1. 3D Printability and rheological evaluation of GelMA/Chitosan polymeric inks

The printability, i.e. the extrusion of a continuous thread through the printer needle, of GelMA/Chitosan mixtures with different compositions was evaluated first (Figure 2a). Monocomponent GelMA solutions at concentrations below 5 wt-% were low viscous and formed droplet-like structures when printed (Figure 2a). Note that GelMA solutions at concentration ≥12.5 wt-% are printable [6]. Addition of chitosan at concentration <2 wt-% into GelMA solutions increased viscosity of the solution and allowed printing of mixed droplet and filament structures. Smooth filaments were deposited when chitosan concentration in the mix was increased from 2 wt-% to 4 wt-%, at total polymer concentrations between 6 wt-% and 8 wt-%, respectively, and GelMA/Chitosan ratios ≥1 (Figure 2a). These observations indicated that the addition of chitosan to GelMA improved the printability of GelMA at polymer concentrations >4 wt-%. Addition of higher concentrated solutions of chitosan (>5 wt-%) was not further investigated as the resulting inks had too high viscosity to be extruded. The composition 4 wt-% chitosan and 4 wt-% GelMA

was selected for the further studies and fabrication of 3D scaffolds because continuous, smooth and uniform filament could be easily extruded (Figure 2a). Better shape fidelity was also obtained in comparison to the other printable formulations (Figure 2b). The high content of amino groups due to the high chitosan content (4 wt-%) was positively taken into consideration because they can contribute to the ionic crosslinks for stabilization of the final scaffold. Figure 2c shows the viscosity of the blend ink compared to the viscosity of the monocomponent solutions of GelMA and chitosan at 4 wt-%. A clearly shear-thinning behavior was observed for the mixture at the studied shear rates. The zero-shear viscosity of the GelMA/Chitosan 4/4 w/w% ink was higher than the zero-viscosity of the tested individual components, which is expected because of to the higher polymer content.

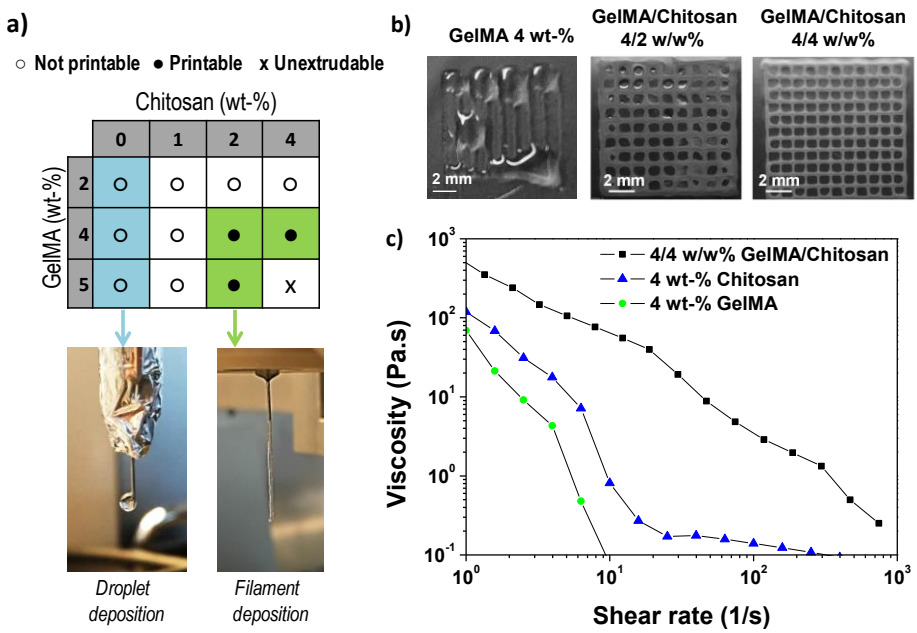

Figure 2. (a) Printability of GelMA/Chitosan inks with different polymer concentrations. Blue boxes indicate droplet-like deposition and green boxes indicate filament deposition; the photographs show the two types of depositions; **(b)** Light microscopy pictures of 3D scaffolds printed with GelMA 4 wt-%, GelMA/Chitosan 4/2 w/w% and GelMA/Chitosan w/w% mixtures; **(c)** Viscosity measurements for 4 wt-% GelMA (green circles), 4 wt-% chitosan (blue triangles), and mixture (black squares).

3.2. Optimization of printing parameters for improved shape fidelity and 3D printing

A dual-step crosslinking approach (Figure 1) was used for printing the 4/4 w/w% GelMA/Chitosan mixtures. The first crosslinking involves the radical polymerization of the acrylate groups and it occurs during ink deposition upon exposure to UV light. The light dose is a relevant parameter that determines the kinetics of the gelation process and the stability of the filament after extrusion. Using a power density of 50 mW/cm^2, a stable filament that retained its shape was obtained, and no obstruction of the tip occurred during printing. Lower exposure doses rendered to widespread strands and collapse between consecutive printed layers. A parallel rheological study of the UV-crosslinked solution indicated that the shear modulus of the UV-crosslinked mixture was G' = 20 kPa after full exposure (Figure S2). Adjustment of the printing parameters was necessary for each tip diameter. 150 and 200 μm metallic needles required printing speed and air pressure adjusted to 5 mm/s and 500 kPa, and 8 mm/s and 400 kPa, respectively. Under these conditions good shape fidelity and resolution were achieved during printing and the fabrication of scaffolds with several superposed layers was possible. It is worth pointing out that adherence between layers can be compromised when consecutive printed layers are fully photopolymerized. Optimization of printing height allowed better contact between consecutively printed layers and delamination was avoided. Layer heights of 80 and 100 μm were used when printing with 150 and 200 μm needles, respectively. Scaffolds of up to 28 layers were obtained without collapse nor delamination.The second crosslinking step involves ionic interactions and is performed after printing. The 3D scaffolds were immersed in a 15 mg/mL solution of G_1Phy crosslinker. The phosphate groups of G_1Phy are expected to form ionic crosslinks with the amine groups of chitosan and GelMA. This ionic crosslink forms instantaneously and permits fast gel formation and consolidation of structural integrity. In addition, this step provides long-term stability and allows tuning of the degradation kinetics of the 3D hydrogel structures. Figure 3 shows two 3D printed scaffolds: with and without ionic treatment. The dual crosslinked scaffold shows higher shape fidelity and controlled swelling, which were lost when the ionic post-treatment was skipped. This result indicates that both crosslinking processes, photopolymerization and ionic crosslinking, contribute to print 3D scaffolds with structural integrity and long-term stability. This

methodology allowed fast printing without using supporting templates [21, 36, 41-45] or neutralization and washing steps [5, 7, 24, 28, 30, 46]. The as-printed scaffolds were ready to be used for biological tests.

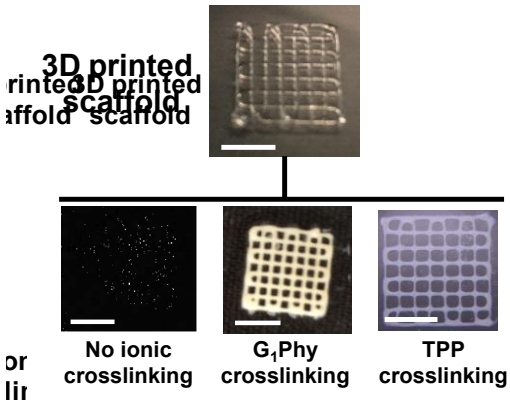

Figure 3. Visual examination and structural integrity changes that a photochemically 3D printed scaffold (four layers) immediately experienced after immersion in distilled water containing or not the G_1Phy or TPP. Scale bar is 0.5 cm.

The resolution of the 3D printed scaffolds fabricated with GelMA/Chitosan 4/4 w/w% composition was characterized by microscopy. The grid structures showed regular edges and corners (Figure 4 a-d), threads with uniform width (~ 150 μm), very close to the inner diameter of the used needle (= 150 μm) (Figure 4b). It is important to note that only a few studies in the ast years have reported strand diameters smaller than 200 μm for 3D printed hydrogel-based materials [14]. Cryo-SEM evaluation confirmed the structural integrity of the printed scaffolds and the interconnectivity between pores without internal collapse of the 3D structures (Figure 4 e-g). A maximum of 28 consecutive layers scaffold was printed with self-standing properties and good adherence between layers (Figure 4f). Finally, the 3D polymeric scaffolds showed inherent porosity in their microstructure (Figure 4h).

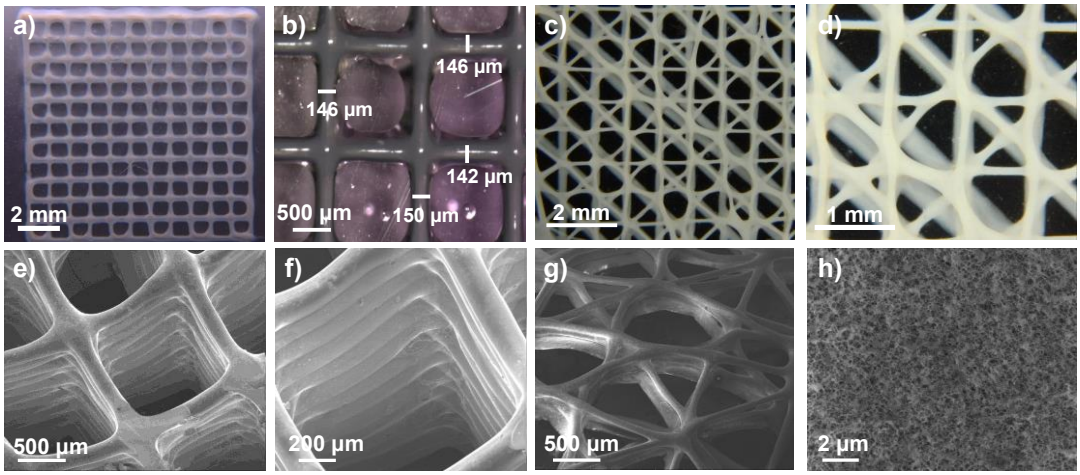

Figure 4. Light microscopy pictures of a 4-layer GelMA/Chitosan scaffold with quadrangular pore morphology **(a-b)** and angular geometries **(c-d)** at low **(a, c)** and higher **(b, d)** resolution. In b) the local width of the printed strand at three different positions is shown (150 µm needle). Images **(e-h)** show cryo-SEM micrographs of 3D printed scaffolds of 28 layers with quadrangular geometry **(e-f),** and 4 layers with angular geometry **(g)**. In **(h)** the microstructure of the printed hydrogel is shown.

3.3. 3D scaffold characterization

3.3.1. Crosslinker release, swelling, degradation, and mechanical properties of the scaffolds during incubation.

In further studies, the responses of our G_1Phy crosslinked 3D systems were compared with the scaffolds crosslinked with the traditional phosphate-based crosslinkers, TPP, as a control. The 3D printed structures crosslinked with G_1Phy solution will be referred further as "G_1Phy scaffolds", and scaffolds crosslinked with TPP solution will be named "TPP scaffolds". The amount of G_1Phy incorporated into the scaffolds after incubation with the corresponding crosslinker solution was quantified by ICP-OES. Thus, 0.53±0.03 mg of G_1Phy were detected in the scaffolds. The final TPP amount incorporated to the TPP scaffolds was of 0.13±0.02 mg. EDX maps (Figure 5a) showed a rather similar P distribution for both crosslinkers on the surface of the scaffolds but the distribution seemed to be somewhat more inhomogeneous in G_1Phy

scaffolds than in TPP ones. P is accumulated in some areas of the former, while less P in the centre of the fiber crossings than in the borders is observed in the latter.

Crosslinker release of the scaffold at physiological conditions (pH 7.4, 37 ºC) was studied (Figure 5b). G_1Phy showed a fast release (7.3 %, which corresponded to 10.32 μM) during the first 2 days of incubation, reaching a plateau after 4 days (11.2 %, which corresponded to 16.03 μM), which was maintained until 30 days of incubation. TPP showed a burst release (16.4 %, which corresponded to 14.74 μM) at 2 days. A plateau was achieved at 4 days (18.8%, which corresponded to 16.31 μM), which was sustained until the end of the incubation period. This different performance of the release crosslinkers can be associated to the differences in the distribution of the crosslinkers in the scaffold, and different ionic interactions of the crosslinkers with the polymeric backbones.

Swelling behaviour of the scaffolds was examined by measuring the strand widths by light microscopy (Figure S3). No swelling was observed for printed G_1Phy nor TPP crosslinked scaffolds after incubation in PBS at physiological conditions for 10 days. This indicated that the structures achieved their maximum water absorption after ionic crosslinking. The stability of the scaffolds was followed gravimetrically by measuring the weight loss after different incubation times (Figure 5c). G_1Phy crosslinked scaffolds showed a weight loss of 1.2±0.6 % during the first 2 days. Scaffolds remained stable for the following 10 days and degraded slowly up to 2.8±0.9 % during the next 20 days. At short time points (2 days), TPP crosslinked scaffolds showed a relatively higher degradation rate (2.0±0.2 %) than G_1Phy scaffolds and degradation progressively increased until 10 days (2.5±0.3%) to remain stable up to the end of the experiment (30 days). At the final time no significant ($p<0.5$) differences between G_1Phy and TPP samples were observed. Rheological characterization of UV cured GelMA/Chitosan discs after crosslinking with G_1Phy or TPP was performed to compare the viscoelastic properties of the 3D printed structures as a function of the type of ionic crosslinker. Figure 5d shows the shear and loss moduli for crosslinked discs. G_1Phy crosslinked discs exhibited lower storage modulus than TPP crosslinked discs and

GelMA/Ch photocrosslinked gel. Storage modulus values of TPP crosslinked scaffold approached those of GelMA/Ch photocrosslinked gel but higher loss modulus than this last one.

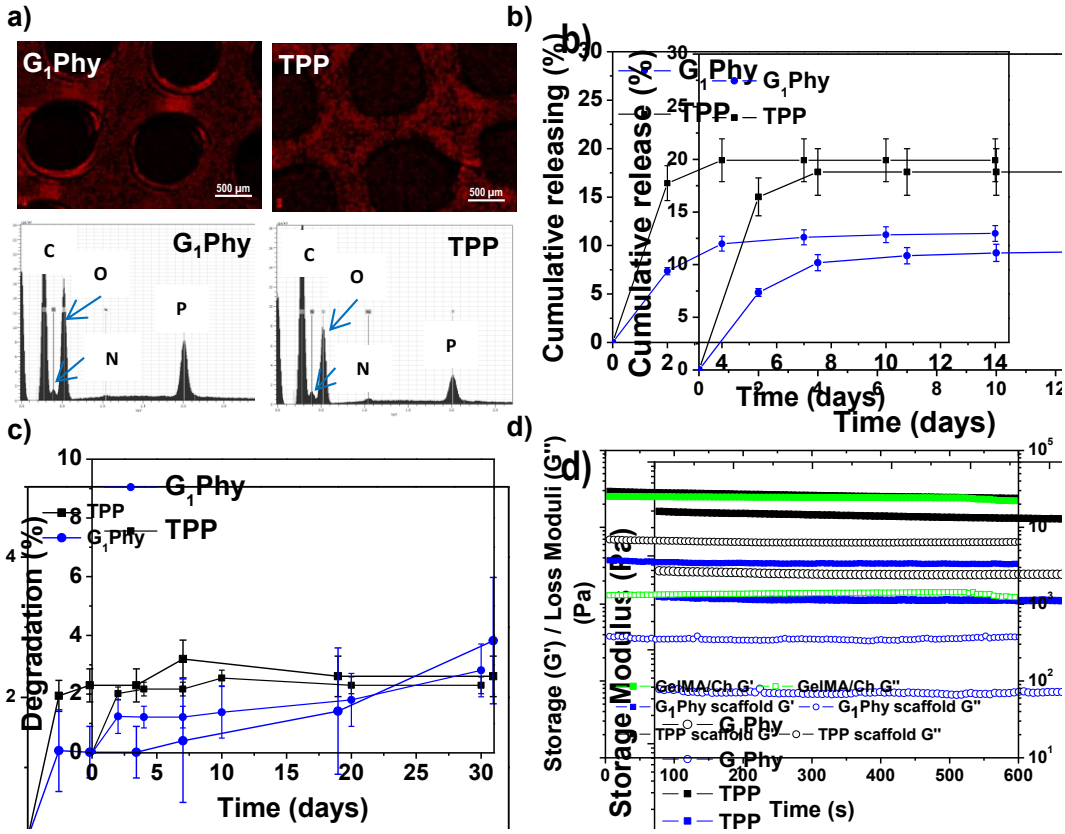

Figure 5. (a) EDAX map distribution of P in G_1Phy and TPP scaffolds, accompanied by EDAX spectra; **(b)** cumulative release crosslinker profiles for G_1Phy and TPP scaffolds incubated in Tris-HCl buffer at pH 7.4 and 37 ºC until 14 days; **(c)** degradation (%) for crosslinked scaffolds incubated in PBS at pH 7.4 and 37 ºC until 30 days; **(d)** Storage and loss moduli for UV-crosslinked GelMA/Ch gel and G_1Phy and TPP scaffolds.

3.3.2. Cytocompatibility results

The performance of G_1Phy scaffolds in biological experiments was assessed *in vitro* using L929 Fibroblasts, which were seeded on the top of the printed scaffolds. For comparison, TPP scaffolds were evaluated in a similar way. Live/dead staining showed high cellular viability and cell density attachment on the G_1Phy scaffolds after 1 day culture (Figure 6a), indicating no visible toxicity of

the materials. On the contrary, live/dead staining of cells seeded on the TPP scaffolds showed almost no cells attached to the 3D structure (Figure 6b), which migrated to the well-plate. Immunostaining results confirmed high cell attachment on G_1Phy scaffolds. Attached cells showed a spread morphology and formed focal adhesions stained in red (Figure 6c). TPP scaffolds showed fewer cells attached on their surface. Cells kept a rounded morphology characteristic of weak cell-material interaction with the scaffold surface, coherent with the results of the live/dead assay (Figure 6d).

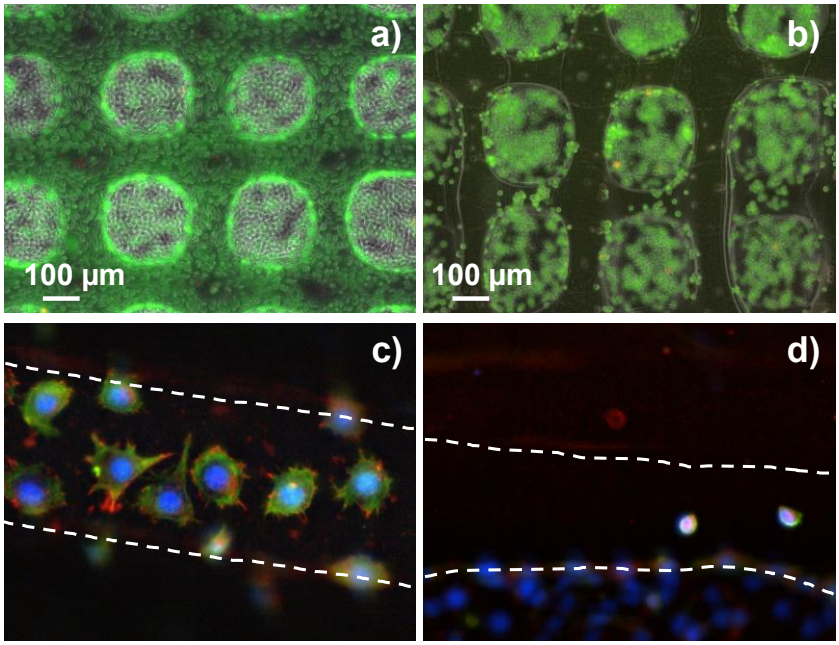

Figure 6. Live/dead assay on G_1Phy **(a)** and TPP **(b)** scaffolds after 24 h of incubation. Pictures were taken to scaffold strands; Confocal immunostaining assay performed on G_1Phy **(c)** and TPP **(d)** scaffolds after 24 h of incubation.

Proliferation of L929 Fibroblasts on the scaffolds was quantified using the Alamar Blue assay at days 2, 4, 7 and 10 of incubation. L929 proliferation on G_1Phy scaffolds increased over time and proliferation level was at any time higher than on TPP scaffolds (Figure 7a). Finally, the possible cytotoxic effects caused by the release of crosslinker or low molecular weight residues

from the 3D printed scaffolds was examined by incubating L929 Fibroblasts with the supernatants from the scaffolds after 2, 4, 7 and 10 days of soaked in cell culture medium. No cytotoxic effects were observed from any of the 3D printed scaffolds (Figure 7b).

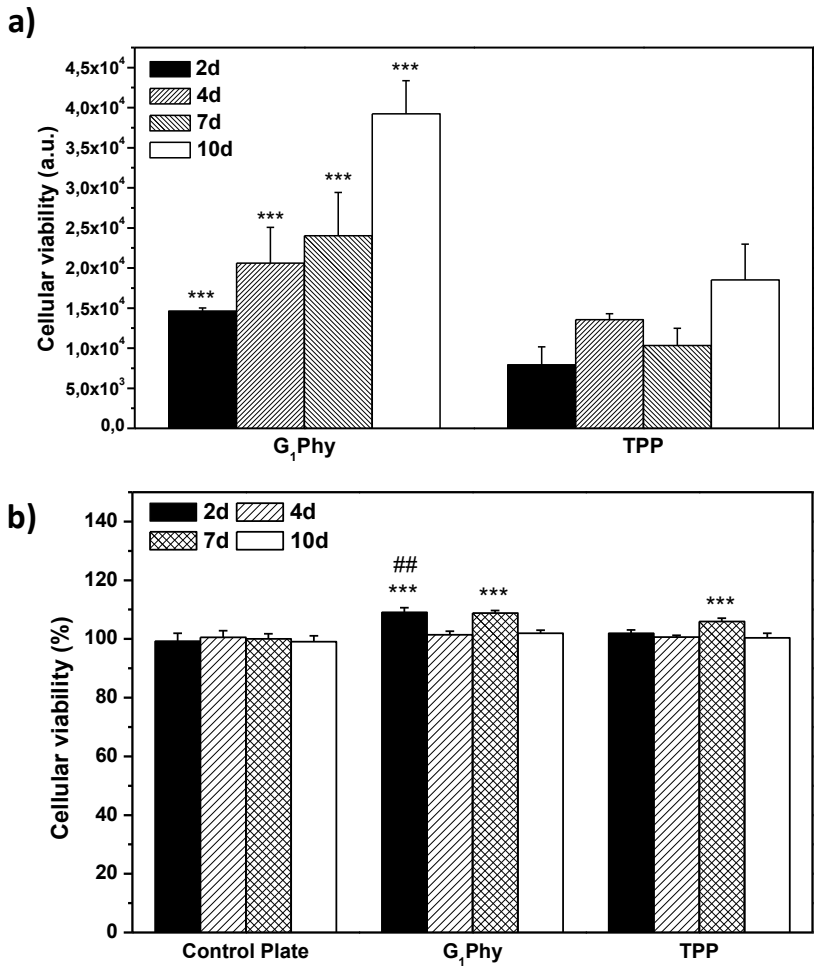

Figure 7. (a) Alamar Blue assay performed on G_1Phy and TPP scaffolds at 2, 4, 7 and 10 days of incubation. Analysis of variance (ANOVA) of the results for G_1Phy samples was performed respect to TPP samples at each time at a significance level of ***$p<0.001$; **(b)** MTT assay performed with extracts of G_1Phy and TPP scaffolds at 2, 4, 7 and 10 days. Control plate refers to cells incubated in DMEM. Analysis of variance (ANOVA) of the results for G_1Phy and TPP samples was performed with respect to control plate at each time at a significance level of ***$p<0.001$, and for G_1Phy samples with respect to TPP samples at each time at a significance level of ##$p<0.01$.

4. Discussion

Among all requirements that an ink must fulfil to allow successful printing homogeneity and deposition as uniform filament, shear-thinning behaviour, and appropriate viscosity are key features [23]. In addition, the 3D printed structures should be biocompatible and keep structural integrity at physiological conditions, avoiding delamination during and after printing [15, 47]. Blend inks that combine different types of polymers are commonly used to fulfil all the mechanical and biological requirements [48]. We decided to work with a mixture of polysaccharide (chitosan) and protein (GelMA) hydrogel. We expected the GelMA/Chitosan combination provides a printing ink with the biological advantages of both polymers, and this mixture overcomes the weak mechanical properties of chitosan [15]. Previous studies have reported the use of gelatin/chitosan blend inks [2, 15, 24, 25, 33, 49]. However, the mixture of chitosan with GelMA, which would result in superior biological properties and mechanical stability, has not been explored before.

Parameter optimization was performed to identify suitable printability windows for the GelMA/Chitosan ink. Wu et al. reported that 3D printing of chitosan using polymer concentrations below 10 wt-% was difficult because of low viscosity of the polymer solution [7]. On the other hand, other studies reported that it is possible to print scaffolds using low polymeric content, even with good cytocompatibility [50, 51]. For example, Yin et al. reduced total polymer concentration of the ink to 8/5 w/w% GelMA/gelatin mixture, and claimed that the obtained shape fidelity was similar to those found with 30 wt-% GelMA solutions [6]. In this work, we have developed a chitosan-based ink with low polymer concentration to favour cell growth, but with appropriate viscosity for free-standing filament dispensing. Among the tested formulations (green box Figure 2a), the GelMA/Chitosan 4/4 wt-% mixture showed the optimal properties combination of low polymer content and easy printability as uniform straight filament. The 8 wt-% polymer content falls within the range of published studies using gelatin/chitosan blends [25, 49], but since GelMA is used in our work, full comparison cannot be performed. Finally, scaffolds fabricated with this composition could be printed with high shape fidelity and maintained structural integrity after printing (Figure 4). Briefly, the selected composition of chitosan and GelMA polymers had synergistic effect, leading to better printability in comparison to each of

monocomponent polymers and made possible the deposition of a printed ink hydrogel with superior shape fidelity.

The optimization of printing parameters was done hand-in-hand with the formulation of the ink and the adjustment of the crosslinking parameters. A dual crosslinking process was applied (Figure 1): a first step based on covalent UV crosslinking while printing and a second step based on ionic crosslinking after material deposition. The dual-step approach is commonly used for processing inks at low polymer concentrations [6]. The GelMA/Chitosan 4/4 w/w% ink showed shear-thinning behaviour, which is a key property for successful deposition using extrusion-based 3D printing [15, 23]. In addition, the photopolymerization kinetics of the ink was suitable for the fabrication of 3D structures at speed of 5-8 mm/s depending on the used tip, with high printing fidelity and without the collapse of consecutive layers. Rheological tests of the crosslinked material demonstrated the viscoelastic properties and hydrogel formation, because storage modulus was constant and higher than loss modulus (Figure 5d).

The simultaneous photocrosslinking and 3D deposition allowed direct photocrosslinking of individual layers, avoiding common complications associated to post-printing photocrosslinking as consequence of low light penetration into the 3D structure [6]. It should be noted that simultaneous crosslinking might lead to a gradient in exposure dose across the layers. However, the post-printing characterization did not show differences in dimensions or swelling between individual layers. To date high number of 3D printing reports use post-printing photopolymerization [11, 15-18, 21, 22, 27, 45, 47], while only few studies have used simultaneous UV curing during printing [6, 39, 52, 53]. Yin et al., who performed a detailed study of GelMA/gelatin inks printability, used also the simultaneous photopolymerization and 3D deposition approach applying the same UV light intensity (50 mW/cm^2) than it is applied in this work. Although, comparisons are difficult since 3D printing approaches and ink composition differed in somewhat, in our work a lower total polymer content (8 vs 13 wt-%) can be printed with better filament resolution (150 vs 260 μm). Nevertheless, it is important to consider that a rigorous comparison of these results depends deeply on 3D printing parameters and used polymers.

The second crosslinking step took place after immersion of the 3D printed scaffolds in G_1Phy as ionic crosslinker. G_1Phy crosslinked scaffolds exhibited better biocompatibility than commonly used ionic crosslinking agents (i.e. TPP) [54]. In addition, the organic segment incorporated to the phytic acid structure favours interaction with cells [32]. This second crosslinking step contributed to maintained shape fidelity and positively influenced swelling and long-term stability of the scaffolds (Figure 4b). We speculate that the crosslinking of the amine groups of the chitosan and GelMA chains with the anionic crosslinker is essential to control the water uptake of the printed structures. This stabilization step did not require neutralization or washing steps, which is the commonly approach used for 3D printing of chitosan-based inks. For example, Wu et al. printed 10 wt-% chitosan solutions obtaining 3D structures with high resolution (~30 μm) and intricate shapes, but neutralization with 1 M NaOH solution for 4 h was required [7]. Elviri et al. were able to print lower chitosan solutions (6 wt-%) in a cryogenic chamber followed by the subsequent coagulation in a KOH (8 w/v %) bath [30]. Moreover, the described manufacturing protocols could potentially lead to shrinking and shape deformation of the scaffolds [5, 7, 24, 28, 30, 55], a post-printing phenomenon that it was not observed in our scaffolds after ionic crosslinking (Figure S4). Our polymer concentration is among the range of the published ones (± 2 wt-%), while it avoids such sophisticated post-processing techniques, being more similar to the traditional alginate-$CaCl_2$ system widely applied in 3D printing methodologies [29].

The dual step approach followed in our work also avoided the use of sacrificial or template materials, which is a widely used strategy to improve printing resolution with hydrogels [11, 37, 38]. G_1Phy crosslinking lead to improved mechanical properties of the scaffolds than TPP crosslinking. We expect G_1Phy to form less compact and softer networks because of two main reasons: (i) the organic content of this crosslinker provides some viscoelasticity to the network, and (ii) its higher molecular weight respect to TPP provides less dense frameworks. All these features together contributed to obtaining softer and viscoelastic gels with long-term stability and controlled swelling, which are essential characteristics for tissue engineering applications [1, 10, 56]. To the best of our knowledge, crosslinkers derived from phytic acid have not been used for the development of 3D printed scaffolds so far.

The 3D structures demonstrated excellent shape fidelity. The ink did not accumulate in the edges or in the corners of scaffolds, where printing speeds and direction changes abruptly. The scaffolds showed smooth surfaces and constant widths. Moreover, printing of multiple consecutive layers without collapsing was possible, leading to the structures of up to 28 layers height. The best reported line width for hydrogel printing was approximately 100-200 μm, which is among the best resolution degree that can be currently achieved with hydrogel inks [14]. This resolution is highly dependent on the diameter of the needle, and could be potentially improved using narrower tips. Porous and interconnected structures were printed, which are interesting geometries for tissue engineering applications [14, 57]. Finally, inherent microstructure (Figure 3h) of the polymeric scaffolds is also a decisive property for the correct distribution and diffusion of oxygen and nutrients of the ingrowth tissues [58, 59]. Summarizing, the developed GelMA/Chitosan hydrogel with dual crosslinking mechanism allows printing of 3D structures with complex designs at high resolution.

Cytocompatibility studies indicated that G_1Phy scaffolds supported better cell attachment and proliferation than TPP crosslinked scaffolds, which could be due to chemical composition as well as morphological properties of these scaffolds. Nevertheless, since the initial composition (GelMA/Chitosan) is the same for both crosslinked scaffolds and assuming that the chitosan surface exposure is rather similar in both types of scaffolds according to P distribution (Figure 5a), for short time periods, the different biological responses should only be due to the incorporation of G_1Phy or TPP to their structures. G_1Phy has demonstrated to be a highly biocompatible crosslinker which exhibits an organic composition that can enhance cellular interaction [32]. In addition, the different molecular weights of G_1Phy and TPP could play a role in the final mechanical properties of the ionically crosslinked networks. In fact, the rheological behaviour showed that the G1Phy crosslinked polymer network was softer than TPP crosslinked one. All this together with the sustained release of G_1Phy and the slower degradation of this scaffold can favourably contribute to the higher cell proliferation of the samples in long-term periods.

5. Conclusions

In summary, this work shows the implementation and optimization of a 3D printing methodology using the novel G_1Phy crosslinker. The methodology consisted of a dual-step crosslinking that allows the 3D printing of low concentrated GelMA/Chitosan based-ink (total polymer concentration <10 wt-%). This approach permitted the fabrication of 3D hydrogel scaffolds with excellent shape fidelity and resolution. The 3D printed scaffolds displayed long-term stability and excellent properties regarding swelling behaviour, mechanical and biological properties. In particular, the use of G_1Phy crosslinker enhanced cell adhesion and proliferation on the 3D scaffolds in comparison to TPP, widely used as a traditional ionic crosslinking agent. These results open a door for the extrusion of hydrogel-based inks employing phytic acid derived crosslinkers for the fabrication of complex structures with excellent biological properties that can be used in soft tissue engineering applications.

6. References

[1] A.V. Do, B. Khorsand, S.M. Geary, A.K. Salem, 3D Printing of Scaffolds for Tissue Regeneration Applications, Adv Healthc Mater 4(12) (2015) 1742-62.

[2] J. Huang, H. Fu, Z. Wang, Q. Meng, S. Liu, H. Wang, X. Zheng, J. Dai, Z. Zhang, BMSCs-laden gelatin/sodium alginate/carboxymethyl chitosan hydrogel for 3D bioprinting, RSC Advances 6(110) (2016) 108423-108430.

[3] Q.L. Loh, C. Choong, Three-dimensional scaffolds for tissue engineering applications: role of porosity and pore size, Tissue Eng Part B Rev 19(6) (2013) 485-502.

[4] M.K. Wlodarczyk-Biegun, A. Del Campo, 3D bioprinting of structural proteins, Biomaterials 134 (2017) 180-201.

[5] C. Intini, L. Elviri, J. Cabral, S. Mros, C. Bergonzi, A. Bianchera, L. Flammini, P. Govoni, E. Barocelli, R. Bettini, M. McConnell, 3D-printed chitosan-based scaffolds: An in vitro study of human skin cell growth and an in-vivo wound healing evaluation in experimental diabetes in rats, Carbohydr Polym 199 (2018) 593-602.

[6] J. Yin, M. Yan, Y. Wang, J. Fu, H. Suo, 3D Bioprinting of Low-Concentration Cell-Laden Gelatin Methacrylate (GelMA) Bioinks with a Two-Step Cross-linking Strategy, ACS Appl Mater Interfaces 10(8) (2018) 6849-6857.

[7] Q. Wu, D. Therriault, M.-C. Heuzey, Processing and Properties of Chitosan Inks for 3D Printing of Hydrogel Microstructures, ACS Biomaterials Science & Engineering 4(7) (2018) 2643-2652.

[8] R. Levato, W.R. Webb, I.A. Otto, A. Mensinga, Y. Zhang, M. van Rijen, R. van Weeren, I.M. Khan, J. Malda, The bio in the ink: cartilage regeneration with bioprintable hydrogels and articular cartilage-derived progenitor cells, Acta Biomater 61 (2017) 41-53.

[9] S. Stratton, N.B. Shelke, K. Hoshino, S. Rudraiah, S.G. Kumbar, Bioactive polymeric scaffolds for tissue engineering, Bioact Mater 1(2) (2016) 93-108.

[10] S. Derakhshanfar, R. Mbeleck, K. Xu, X. Zhang, W. Zhong, M. Xing, 3D bioprinting for biomedical devices and tissue engineering: A review of recent trends and advances, Bioact Mater 3(2) (2018) 144-156.

[11] W. Jia, P.S. Gungor-Ozkerim, Y.S. Zhang, K. Yue, K. Zhu, W. Liu, Q. Pi, B. Byambaa, M.R. Dokmeci, S.R. Shin, A. Khademhosseini, Direct 3D bioprinting of perfusable vascular constructs using a blend bioink, Biomaterials 106 (2016) 58-68.

[12] K. Schutz, A.M. Placht, B. Paul, S. Bruggemeier, M. Gelinsky, A. Lode, Three-dimensional plotting of a cell-laden alginate/methylcellulose blend: towards biofabrication of tissue engineering constructs with clinically relevant dimensions, J Tissue Eng Regen Med 11(5) (2017) 1574-1587.

[13] H. Stratesteffen, M. Kopf, F. Kreimendahl, A. Blaeser, S. Jockenhoevel, H. Fischer, GelMA-collagen blends enable drop-on-demand 3D printablility and promote angiogenesis, Biofabrication 9(4) (2017) 045002.

[14] X. Wang, C. Wei, B. Cao, L. Jiang, Y. Hou, J. Chang, Fabrication of Multiple-Layered Hydrogel Scaffolds with Elaborate Structure and Good Mechanical Properties via 3D Printing and Ionic Reinforcement, ACS Appl Mater Interfaces 10(21) (2018) 18338-18350.

[15] H. Li, Y.J. Tan, S. Liu, L. Li, Three-Dimensional Bioprinting of Oppositely Charged Hydrogels with Super Strong Interface Bonding, ACS Appl Mater Interfaces 10(13) (2018) 11164-11174.

[16] B.J. Klotz, D. Gawlitta, A. Rosenberg, J. Malda, F.P.W. Melchels, Gelatin-Methacryloyl Hydrogels: Towards Biofabrication-Based Tissue Repair, Trends Biotechnol 34(5) (2016) 394-407.
[17] N. Celikkin, S. Mastrogiacomo, J. Jaroszewicz, X.F. Walboomers, W. Swieszkowski, Gelatin methacrylate scaffold for bone tissue engineering: The influence of polymer concentration, J Biomed Mater Res A 106(1) (2018) 201-209.
[18] W. Liu, M.A. Heinrich, Y. Zhou, A. Akpek, N. Hu, X. Liu, X. Guan, Z. Zhong, X. Jin, A. Khademhosseini, Y.S. Zhang, Extrusion Bioprinting of Shear-Thinning Gelatin Methacryloyl Bioinks, Adv Healthc Mater 6(12) (2017).
[19] N.A. Chartrain, C.B. Williams, A.R. Whittington, A review on fabricating tissue scaffolds using vat photopolymerization, Acta Biomater 74 (2018) 90-111.
[20] M. Layani, X. Wang, S. Magdassi, Novel Materials for 3D Printing by Photopolymerization, Adv Mater 30(41) (2018) e1706344.
[21] K. Yue, G. Trujillo-de Santiago, M.M. Alvarez, A. Tamayol, N. Annabi, A. Khademhosseini, Synthesis, properties, and biomedical applications of gelatin methacryloyl (GelMA) hydrogels, Biomaterials 73 (2015) 254-71.
[22] Y.L. Cheng, F. Chen, Preparation and characterization of photocured poly (epsilon-caprolactone) diacrylate/poly (ethylene glycol) diacrylate/chitosan for photopolymerization-type 3D printing tissue engineering scaffold application, Mater Sci Eng C Mater Biol Appl 81 (2017) 66-73.
[23] T.T. Demirtas, G. Irmak, M. Gumusderelioglu, A bioprintable form of chitosan hydrogel for bone tissue engineering, Biofabrication 9(3) (2017) 035003.
[24] W.L. Ng, W.Y. Yeong, M.W. Naing, Polyelectrolyte gelatin-chitosan hydrogel optimized for 3D bioprinting in skin tissue engineering, International Journal of Bioprinting 2(0) (2016).
[25] W.L. Ng, W.Y. Yeong, M.W. Naing, Development of Polyelectrolyte Chitosan-gelatin Hydrogels for Skin Bioprinting, Procedia CIRP 49 (2016) 105-112.
[26] I.C. Carvalho, H.S. Mansur, Engineered 3D-scaffolds of photocrosslinked chitosan-gelatin hydrogel hybrids for chronic wound dressings and regeneration, Mater Sci Eng C Mater Biol Appl 78 (2017) 690-705.

[27] J. Radhakrishnan, A. Subramanian, U.M. Krishnan, S. Sethuraman, Injectable and 3D Bioprinted Polysaccharide Hydrogels: From Cartilage to Osteochondral Tissue Engineering, Biomacromolecules 18(1) (2017) 1-26.

[28] I.H. Liu, S.H. Chang, H.Y. Lin, Chitosan-based hydrogel tissue scaffolds made by 3D plotting promotes osteoblast proliferation and mineralization, Biomed Mater 10(3) (2015) 035004.

[29] A.R. Akkineni, T. Ahlfeld, A. Lode, M. Gelinsky, A versatile method for combining different biopolymers in a core/shell fashion by 3D plotting to achieve mechanically robust constructs, Biofabrication 8(4) (2016) 045001.

[30] L. Elviri, R. Foresti, C. Bergonzi, F. Zimetti, C. Marchi, A. Bianchera, F. Bernini, M. Silvestri, R. Bettini, Highly defined 3D printed chitosan scaffolds featuring improved cell growth, Biomed Mater 12(4) (2017) 045009.

[31] D. Lee, J.P. Park, M.Y. Koh, P. Kim, J. Lee, M. Shin, H. Lee, Chitosan-catechol: a writable bioink under serum culture media, Biomater Sci 6(5) (2018) 1040-1047.

[32] A. Mora-Boza, M.L. López-Donaire, L. Saldaña, N. Vilaboa, B. Vazquez-Lasa, J.S. Román, Glycerylphytate compounds with tunable ion affinity and osteogenic properties, Scientific Reports 9 (2019).

[33] A. Zolfagharian, A. Kaynak, S.Y. Khoo, A.Z. Kouzani, Polyelectrolyte Soft Actuators: 3D Printed Chitosan and Cast Gelatin, 3D Printing and Additive Manufacturing 5(2) (2018) 138-150.

[34] M.M. Fares, E. Shirzaei Sani, R. Portillo Lara, R.B. Oliveira, A. Khademhosseini, N. Annabi, Interpenetrating network gelatin methacryloyl (GelMA) and pectin-g-PCL hydrogels with tunable properties for tissue engineering, Biomaterials Science 6(11) (2018) 2938-2950.

[35] J. Visser, B. Peters, T.J. Burger, J. Boomstra, W.J.A. Dhert, F.P.W. Melchels, J. Malda, Biofabrication of multi-material anatomically shaped tissue constructs, Biofabrication 5(3) (2013) 035007.

[36] A. Tamayol, A.H. Najafabadi, B. Aliakbarian, E. Arab-Tehrany, M. Akbari, N. Annabi, D. Juncker, A. Khademhosseini, Hydrogel Templates for Rapid Manufacturing of Bioactive Fibers and 3D Constructs, Adv Healthc Mater 4(14) (2015) 2146-2153.

[37] P. Datta, B. Ayan, I.T. Ozbolat, Bioprinting for vascular and vascularized tissue biofabrication, Acta Biomater 51 (2017) 1-20.

[38] M. Muller, J. Becher, M. Schnabelrauch, M. Zenobi-Wong, Printing thermoresponsive reverse molds for the creation of patterned two-component hydrogels for 3D cell culture, J Vis Exp (77) (2013) e50632.

[39] C.D. O'Connell, C. Di Bella, F. Thompson, C. Augustine, S. Beirne, R. Cornock, C.J. Richards, J. Chung, S. Gambhir, Z. Yue, J. Bourke, B. Zhang, A. Taylor, A. Quigley, R. Kapsa, P. Choong, G.G. Wallace, Development of the Biopen: a handheld device for surgical printing of adipose stem cells at a chondral wound site, Biofabrication 8(1) (2016) 015019.

[40] M. Bartnikowski, R. Wellard, M. Woodruff, T. Klein, Tailoring Hydrogel Viscoelasticity with Physical and Chemical Crosslinking, Polymers 7(12) (2015) 1539.

[41] Y. Zhang, Y. Yu, I.T. Ozbolat, Direct Bioprinting of Vessel-Like Tubular Microfluidic Channels, Journal of Nanotechnology in Engineering and Medicine 4(2) (2013).

[42] Y.S. Zhang, K. Yue, J. Aleman, K.M. Moghaddam, S.M. Bakht, J. Yang, W. Jia, V. Dell'Erba, P. Assawes, S.R. Shin, M.R. Dokmeci, R. Oklu, A. Khademhosseini, 3D Bioprinting for Tissue and Organ Fabrication, Ann Biomed Eng 45(1) (2017) 148-163.

[43] I.S. Kinstlinger, J.S. Miller, 3D-printed fluidic networks as vasculature for engineered tissue, Lab Chip 16(11) (2016) 2025-43.

[44] J.S. Lee, J.M. Hong, J.W. Jung, J.H. Shim, J.H. Oh, D.W. Cho, 3D printing of composite tissue with complex shape applied to ear regeneration, Biofabrication 6(2) (2014) 024103.

[45] M. Costantini, J. Idaszek, K. Szöke, J. Jaroszewicz, M. Dentini, A. Barbetta, J.E. Brinchmann, W. Święszkowski, 3D bioprinting of BM-MSCs-loaded ECM biomimetic hydrogels forin vitroneocartilage formation, Biofabrication 8(3) (2016).

[46] J. Zhang, B.J. Allardyce, R. Rajkhowa, Y. Zhao, R.J. Dilley, S.L. Redmond, X. Wang, X. Liu, 3D Printing of Silk Particle-Reinforced Chitosan Hydrogel Structures and Their Properties, ACS Biomaterials Science & Engineering 4(8) (2018) 3036-3046.

[47] S. Sayyar, S. Gambhir, J. Chung, D.L. Officer, G.G. Wallace, 3D printable conducting hydrogels containing chemically converted graphene, Nanoscale 9(5) (2017) 2038-2050.

[48] K.W.M. Boere, M.M. Blokzijl, J. Visser, J.E.A. Linssen, J. Malda, W.E. Hennink, T. Vermonden, Biofabrication of reinforced 3D-scaffolds using two-component hydrogels, Journal of Materials Chemistry B 3(46) (2015) 9067-9078.

[49] K.D. Roehm, S.V. Madihally, Bioprinted chitosan-gelatin thermosensitive hydrogels using an inexpensive 3D printer, Biofabrication 10(1) (2017) 015002.

[50] J. Malda, J. Visser, F.P. Melchels, T. Jungst, W.E. Hennink, W.J. Dhert, J. Groll, D.W. Hutmacher, 25th anniversary article: Engineering hydrogels for biofabrication, Adv Mater 25(36) (2013) 5011-28.

[51] I. Pepelanova, K. Kruppa, T. Scheper, A. Lavrentieva, Gelatin-Methacryloyl (GelMA) Hydrogels with Defined Degree of Functionalization as a Versatile Toolkit for 3D Cell Culture and Extrusion Bioprinting, Bioengineering (Basel) 5(3) (2018).

[52] X. Cui, G. Gao, T. Yonezawa, G. Dai, Human cartilage tissue fabrication using three-dimensional inkjet printing technology, J Vis Exp (88) (2014).

[53] G. Gao, A.F. Schilling, K. Hubbell, T. Yonezawa, D. Truong, Y. Hong, G. Dai, X. Cui, Improved properties of bone and cartilage tissue from 3D inkjet-bioprinted human mesenchymal stem cells by simultaneous deposition and photocrosslinking in PEG-GelMA, Biotechnol Lett 37(11) (2015) 2349-55.

[54] HERA, Targeted Risk Assessment of Sodium Tripolyphosphate (STPP), (2003).

[55] A. Vitale, J.T. Cabral, Frontal Conversion and Uniformity in 3D Printing by Photopolymerisation, Materials (Basel) 9(9) (2016).

[56] K.N. Bardakova, T.S. Demina, E.A. Grebenik, N.V. Minaev, T.A. Akopova, V.N. Bagratashvili, P.S. Timashev, 3D printing biodegradable scaffolds with chitosan materials for tissue engineering, IOP Conference Series: Materials Science and Engineering 347 (2018).

[57] J. Wang, Z. Nor Hidayah, S.I.A. Razak, M.R.A. Kadir, N.H.M. Nayan, Y. Li, K.A.M. Amin, Surface entrapment of chitosan on 3D printed polylactic acid scaffold and its biomimetic growth of hydroxyapatite, Composite Interfaces (2018) 1-14.

[58] P. Thangavel, B. Ramachandran, V. Muthuvijayan, Fabrication of chitosan/gallic acid 3D microporous scaffold for tissue engineering applications, J Biomed Mater Res B Appl Biomater 104(4) (2016) 750-60.

[59] K. Zhang, Y. Fan, N. Dunne, X. Li, Effect of microporosity on scaffolds for bone tissue engineering, Regenerative biomaterials 5(2) (2018) 115-124.

Acknowledgements

Authors thank financial support to Ministry of Science, Innovation and Universities (Spain) (MAT2017-2017-84277-R), "La Caixa" Foundation (ID 100010434, scholarship of Ana Mora-Boza, code LCF/BQ/ES16/11570018) and DAAD Research Grants Short-term 2017.

The authors are indebted to Dr. Marcus Koch (Leibniz-INM) for excellent technical assistance with SEM and light microscopy experiments, and to Dr. Claudia Fink-Straube (Leibniz-INM) for ICP-OES experiments performance.

7. Supplementary Information

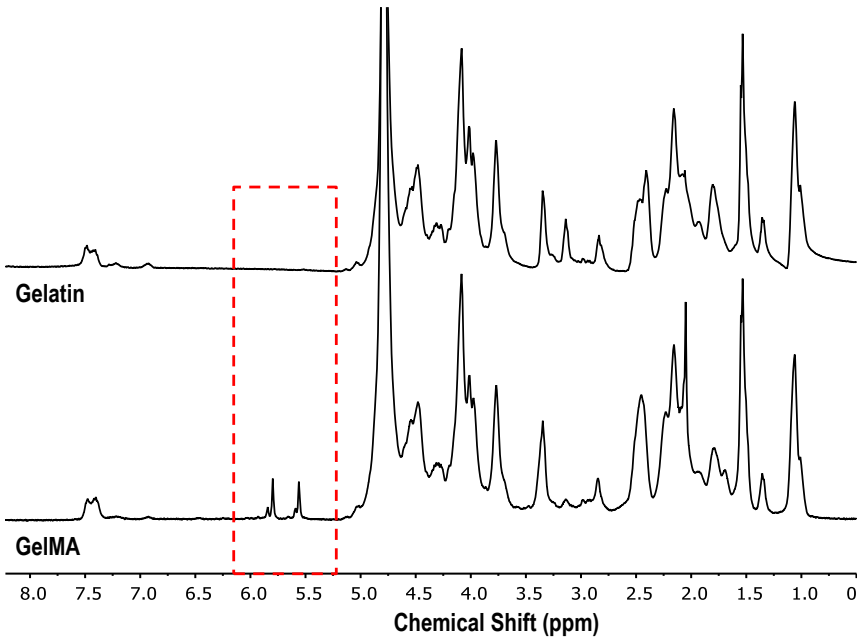

Figure S1. ^{1}H-RMN spectra of gelatin and GelMA recorded in D_2O at 37 ºC. Degree of methacrylation was calculated taking into consideration the methacrylate signals that appeared at a chemical shift of 5.8 and 5.6 ppm, which were normalized against the aromatic signals of phenylalanine at 7.4 ppm [40].

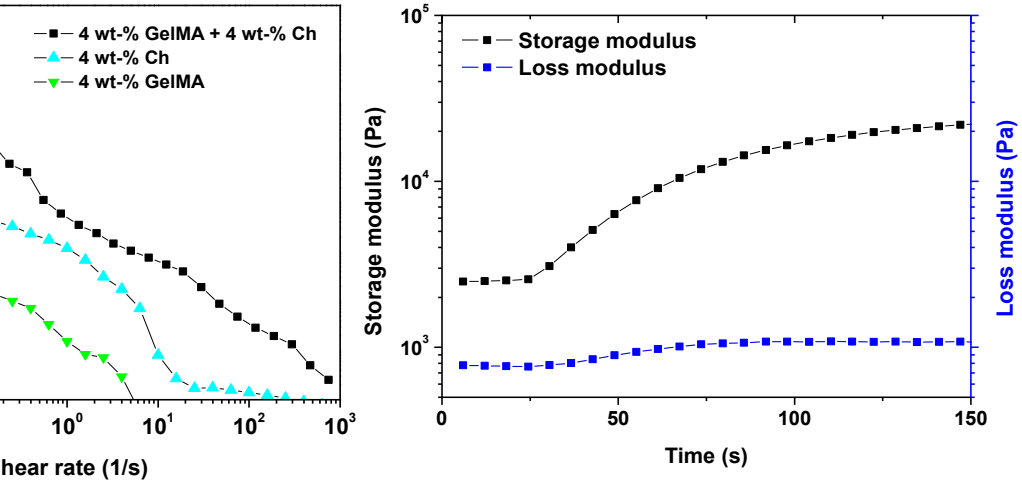

Figure S2. *In situ* photoinitiated crosslinking of the gel followed by rheology. The curves show the changes in the storage (black squares) and loss (blue squares) moduli of the gel during light exposure.

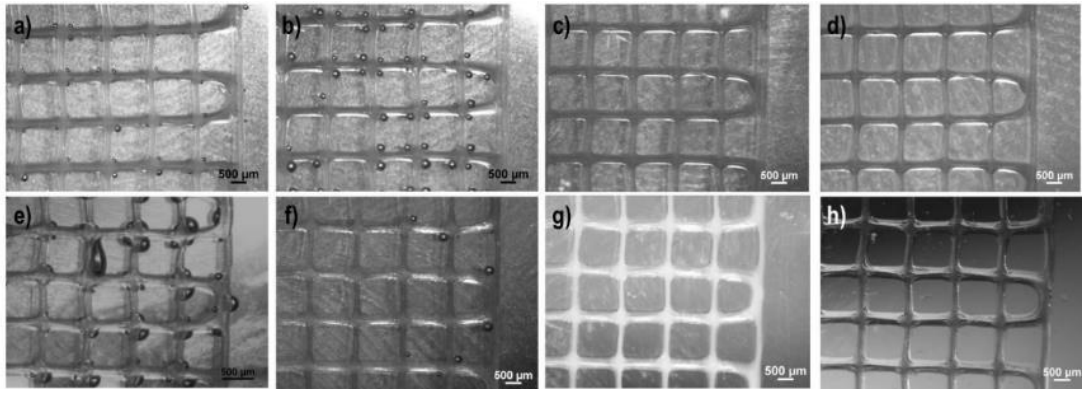

Figure S3. Qualitative examination under light microscopy of swelling for G_1Phy **(a-d)** and TPP **(e-h)** printed scaffolds at different times of incubation in PBS at 37 ºC (2, 4, 7 and 10 days).

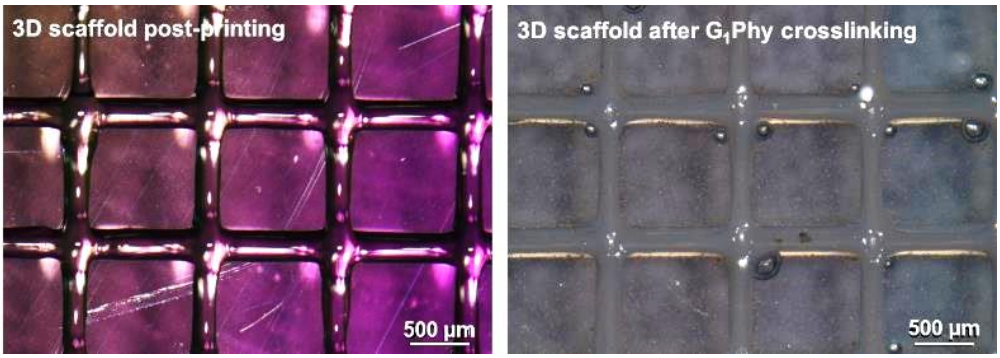

Figure S4. Light microscope images of a 3D printed scaffold after printing-photopolymerization process (left), and after ionic crosslinking with G_1Phy (right).

Chapter 6

Glycerylphytate-crosslinked chitosan microgels improve human mesenchymal stem cell survival and upregulate secretory profile

Research article

Glycerylphytate-crosslinked chitosan microgels improve human mesenchymal stem cell survival and upregulate secretory profile

Ana Mora-Boza [1, 2], Lina M. Mancipe Castro [3, 4], Rebecca S. Schneider [4, 5], Woojin M. Han [3, 4], Andrés J. García [3, 4], Julio San Román [1, 2], Blanca Vázquez-Lasa [1, 2, *]

[1] Institute of Polymer Science and Technology (ICTP-CSIC), Madrid, Spain.

[2] CIBER-BBN, Health Institute Carlos III, Madrid, Spain.

[3] Woodruff School of Mechanical Engineering, Georgia Institute of Technology, Atlanta, GA, USA.

[4] Petit Institute for Bioengineering and Bioscience, Georgia Institute of Technology, Atlanta, GA, USA.

[5] School of Chemical and Biomolecular Engineering, Georgia Institute of Technology, Atlanta, GA, USA.

*corresponding author.

In consideration for publication

Abstract

Human mesenchymal stem cells (hMSCs) are an attractive source for cell therapy since they exhibit multiple beneficial properties, most notably potent immunomodulation and tissue repair via their secretory factors. However, their clinical application remains limited due to their low survival and persistence, highlighting the need for new cell-carriers. Although chitosan microgel synthesis has been explored, its use as a cell microcarrier has been significantly limited by its poor solubility at neutral pH, the use of toxic crosslinking agents, and the need for harsh purification methods. Here, we examine the fabrication of bioactive hMSC-laden microcarriers based on *in situ* crosslinking of water-soluble chitosan in a microfluidic device. Encapsulation of hMSC was realized via the use of (i) chitosan lactate, a water-soluble chitosan derivative; and (ii) a combination of tripolyphosphate (TPP) and the antioxidant glycerylphytate (G_1Phy) as ionic crosslinkers to vary gelation kinetics. Reactive mixtures varying the ratio between TPP and G_1Phy were screened for the successful formation of bioactive chitosan-based microcarriers. G_1Phy in microgels (hydrogel

particles) maintained cell viability over time and upregulated paracrine factors secretion under stress conditions (e.g. oxidative stress and inflammation) compared to control microgels (microgels containing only TPP). Microgel-encapsulated hMSCs were easily delivered to the subcutaneous space of immunocompromised mice via injection, and the delivery process was as simple as the injection of unencapsulated cells. Immediately post-injection, equivalent signal intensities were observed between luciferase-expressing microgel-encapsulated and unencapsulated hMSCs, demonstrating no adverse effects in initial cell survival. Cell persistence, inferred by bioluminescence signal, decreased exponentially over time with average half-life values of 3 days and no statistically significant differences were observed among groups. These results position the bioactive G_1Phy-crosslinked microgels as a promising microcarrier for promoting hMSC survival and reparative activities.

1. Introduction

Therapies based on human mesenchymal stem cells (hMSCs) offer promising approaches for the treatment of diverse degenerative and inflammatory diseases [1]. Therapeutic interest in hMSCs originally focused on their self-renewal capacities and ability to differentiate into different cell lineages [2]. In recent years, paracrine signalling has been recognized to play an essential role in hMSC therapeutic efficacy via secretion of bioactive factors [3-5]. Secreted molecules influence tissue repair by enhancing processes such as angiogenesis, extracellular matrix (ECM) deposition, and by exerting immunoregulatory actions like macrophage activation and neutrophil recruitment, among others [3]. Nevertheless, the effective clinical application of hMSC-based therapy remains limited due to low cell survival and persistence *in vivo*, highlighting the need for developing new cell-carriers. Micron-scale hydrogels or microgels are attractive cell delivery platforms in comparison to bulk hydrogels because they can be delivered via minimally invasive techniques such as injection using small diameter needles. Microgels can be engineered to provide biological and physical support to enhance cell engraftment and sustain long-term release of paracrine molecules, enabling enhanced therapeutic actions [6].

Cell microencapsulation requires a polymer network that ensures cell viability during microgel synthesis and adequate crosslinking chemistry to form a polymer network under optimum gelation

conditions (e.g. gelation time, crosslinking pH, temperature) [2]. Chitosan is a natural polysaccharide obtained from the alkaline deacetylation of chitin. It is composed of randomly distributed β-(1→4)-linked D-glucosamine (deacetylated unit) and *N*-acetyl-D-glucosamine (acetylated unit) [7, 8], which are similar to glycosaminoglycans present in natural ECMs [9]. Chitosan is biodegradable, non-toxic, and its origin makes it a renewable and eco-friendly material [7]. The use of chitosan microgels as a delivery vehicle for growth factors [10, 11] and drugs [12-20] has been described. However, their application as cell carriers has been limited because of its scarce solubility at physiological pH [21, 22], as well as the lack of cytocompatible crosslinking reactions and the necessity of aggressive purification methods (e.g. organic solvents, freeze-drying) [23, 24]. In fact, few studies have reported fabrication methods that allow simultaneous cell encapsulation and chitosan microgel synthesis [25-28]. These reports focus on the combination of chitosan with a wide variety of polymers (e.g. collagen, chondroitin sulphate, dextran) or additives (e.g. hydroxyapatite) in an attempt to improve the weak mechanical strength of chitosan [29]. Daley et al. [27] fabricated chitosan-chondroitin sulfate polyelectrolyte microparticles for cartilage regeneration. They applied a single-step water/oil emulsification in a polydimethylsiloxane (PDMS) bath for MSCs embedding, obtaining microparticles of 80-90 μm that maintained *in vitro* cell viability after three weeks of culture. Wise et al. [28] also applied a water/oil emulsification in PDMS in combination with thermal gelation to fabricate encapsulated MSCs chitosan-collagen microgels for the enhancement of ectopic bone formation. Demir et al. [25] fabricated chitosan microgels containing hydroxyapatite for studying osteogenic differentiation of encapsulated MSCs and microgels were synthetized by ionic gelation of deposited polymer droplets in a tripolyphosphate (TPP) bath.

Despite this progress on chitosan-based microcarriers, further research on new crosslinking mechanisms would broaden cell encapsulation applications of chitosan microgels. Herein, bioactive chitosan lactate (ChLA) microgels are synthesized in a flow-focusing microfluidic device via *in situ* crosslinking reaction using TPP and the biologically active compound glycerylphytate (G_1Phy) as ionic crosslinkers. G_1Phy is a powerful antioxidant and bioactive compound [30], whose crosslinking capacity has also been applied in 3D printing technology [31]. Among microgel fabrication techniques, flow-focusing microfluidics is particularly attractive because it provides a

rapid and reproducible methodology for microgel generation of controlled size with simultaneous cell encapsulation [6, 32, 33]. Here, hMSC encapsulation is realized via the use of (i) ChLA, a water-soluble chitosan derivative; and (ii) a combination of crosslinkers with optimum gelation kinetics. Thus, reactive mixtures varying the ratio between TPP and G_1Phy are used for the successful formation of ChLA microcarriers. The optimum bioactive microgels composition (i.e. TPP:G_1Phy-microgels) is studied and compared to the microgels that do not contain G_1Phy (i.e. TPP-microgels) to evaluate the bioactive effect exerted by G_1Phy on hMSC viability, paracrine factors secretion, and *in vivo* persistence.

2. Experimental section

2.1. Materials

Chitosan with a degree of deacetylation of 90% (medical grade, ChitoScience, Heppe Medical Chitosan GmbH, Halle, Germany) was used as received. Lactic acid, 4-(4,6-dimethoxy-1,3,5-triazin-2-yl)-4-methylmorpholinium chloride (DMTMM), TPP, mineral oil, SPAN80, and polydimethylsiloxane (PDMS) were purchased from Sigma Aldrich and used as received. G_1Phy was prepared as previously described by Mora-Boza et al. [30], using phytic acid and glycerol from Sigma Aldrich.

2.2. ChLA synthesis

ChLA was synthesized through a condensation reaction with lactic acid. Briefly, 2 wt-% chitosan solution (1 % v/v acetic acid) was stirred for 24 h to allow complete dissolution of the polymer. DMTMM (2-fold excess with respect to lactic acid) was dissolved in lactic acid solution (30 wt% respect to chitosan) and stirred for 30 min. This solution was added dropwise to the chitosan solution and the reaction proceeded for 24 h. The final product was purified by precipitation in cold acetone, subsequently filtered, re-dissolved in distilled water, and dialysed (3500 Da cut off, Spectrum®) for 7 days. After freeze drying, a white powder was obtained. Lactic conjugation was confirmed by H^1-Nuclear Magnetic Resonance (H1-RMN, Figure S1). The degree of substitution (17.92%) of the chitosan amino groups was determined by formation of N-salicylidene, following the method reported by Qu et al. [34]

2.3. Cell culture

hMSCs were obtained from the Institute for Regenerative Medicine Texas A&M Health Science Center. Cells were cultured in α-minimum essential medium (α-MEM, Thermofisher/GIBCO) containing 16.5% fetal bovine serum (FBS, Thermofisher/GIBCO), 2 mM L-glutamine (Thermofisher/GIBCO), and 100 units/mL and 100 μg/mL of penicillin and streptomycin (ThermoFisher), respectively. Cells were incubated at 37 ºC and 5% CO_2, and subcultured at 70-80% confluence. Cells at passage 4 were used for all experiments. For *in vivo* experiments, luciferase-expressing hMSCs ($hMSCs^{Luc}$) were generated by transducing hMSC with lentivirus encoding for firefly luciferase as previously described [35].

2.4. Microfluidic device fabrication

PDMS flow-focusing devices with a nozzle size of 300 μm were fabricated using soft lithography from silicon and SU8 masters [32]. Devices were plasma treated and then bonded directly to glass slides. Devices were primed with continuous phase (mineral oil containing 3% v/v SPAN80 solution) prior to use.

2.5. TPP and G_1Phy-crosslinked ChLA microgel generation

ChLA microgels were synthesized by *in situ* crosslinking reaction in a flow-focusing microfluidic device (Figure 1a). ChLA phase consisted of 1 wt-% ChLA solution in phosphate buffered saline (PBS, pH 7.4, ThermoFisher) and crosslinker phase contained TPP and G_1Phy at different ratios (Table 1). Both solutions, polymer and crosslinker, were firstly focused at a T-junction to obtain a pre-crosslinked mixture that was then emulsified by the continuous phase to generate microdroplets. The ionic crosslinking reaction was subsequently completed along the serpentine channel of the device. Finally, the crosslinked-microgels were collected in α-MEM and centrifuged at 13000 rpm for 10 min to remove continuous phase and crosslinker traces. For encapsulated-hMSC microgels, cells were trypsinized, pelleted by centrifugation, and resuspended in ChLA solution at a final density of $2x10^9$ cells/mL. Flow rates were adjusted to 1.5 μL/min for both polymer and crosslinker phases, and 20 μL/min for continuous phase. Microgel compositions 1 and 3 (Table 1) were used for further cellular analysis, and will be henceforth referred to as TPP-microgels and TPP:G_1Phy-microgels, respectively.

Table 1. Crosslinker phase compositions varying the TPP:G_1Phy ratio.

Composition	TPP (wt-%)	G_1Phy (wt-%)
1	0.50	0
2	0.45	0.05
3	0.40	0.10

2.6. Morphological evaluation and microgel size distribution

Crosslinked-microgel morphology was evaluated by light microscopy (EVOS Imaging System, ThermoFisher). Pictures of the different microgel formulations were taken and diameters of at least 100 microgels per condition were measured using ImageJ software. Size distributions were analyzed using GraphPad Prism software.

2.7. *In vitro* cell viability

Encapsulated hMSCs in TPP- and TPP:G_1Phy-microgels were statically cultured for 10 days in complete α-MEM. At selected time points, microencapsulated cells were removed from culture and stained for 15 min with 2 μM Calcein-AM (live, Life Technologies) and 2 μM ethidium homodimer (dead, Life Technologies). At least 200 cells were imaged at each time point using confocal microscopy (Nikon Ti microscope equipped with C2+ confocal system). Viability over time was calculated by taking the ratio of live cells to total cells (average ± standard deviation (SD)). Two-way analysis of variance (ANOVA) using GraphPad Prism software was performed to study significant differences of cell viability percentages for TPP-microgels and TPP:G_1Phy-microgels.

2.8. *In vitro* secretory profile analysis

Paracrine factor secretion of encapsulated hMSCs in TPP- and TPP:G_1Phy-microgels was evaluated under two different conditions: oxidative stress and interferon-γ (IFN-γ) activation. For oxidative stress condition, Fenton reaction was induced by adding $Fe_2SO_4 \cdot 7H_2O$ (in 0.5% v/v H_2SO_4) and H_2O_2 solutions to microgel culture to obtain final concentrations of 50 mM and 20 mM, respectively. Encapsulated cells were treated for 4 h following a similar procedure reported by Fuhrman et al. [36]. Treatment with IFN-γ was carried for 30 h at a final concentration of 50

ng/mL. For both experiments, encapsulated hMSCs were cultured in α-MEM overnight before treatment. After finishing their respective incubation periods, the cell supernatant was collected and centrifuged at 14,000-xg for 20 min at 4 ºC. Samples were analysed for 23 analytes using a custom Luminex® Assay (R&D Systems), following the manufacturer's instructions. Analytes expression of encapsulated hMSCs in TPP and TPP:G_1Phy-microgels was analysed via partial least squares discriminant analysis (PLS-DA) using a custom MATLAB script. Analytes expression heat maps and clustering analysis were performed using JMP software. Individual analyte levels were plotted for each sample (average ± SD) for each condition, and unpaired t-tests were performed to detect differences between groups.

2.9. *In vivo* microgel injection and encapsulated hMSCs tracking

All animal experiments were performed with the approval of the Georgia Tech Animal Care and Use Committee with veterinary supervision and within the guidelines of the Guide for the Care and Use of Laboratory Animals. Cell persistence and survival were evaluated *in vivo* by tracking the bioluminescence of encapsulated $hMSC^{Luc}$ that were injected into dorsal subcutaneous spaces of immunocompromised mice. NSG male and female mice (5 weeks, Jackson Laboratories) were anesthetized under isoflurane, and 100 μL of microgel suspensions were injected subcutaneously in the dorsum. Each mouse received 4 separate injections (randomized groups) in each quadrant of the dorsum. D-Luciferin salt (Promega) was dissolved in saline and sterile filtered through 0.22 μm pore membranes. Mice received a 150 mg/Kg luciferin dose injected into the intraperitoneal cavity, as previously reported, and the bioluminescence signal was measured using the IVIS Spectrum CT System (Perkin Elmer) at specified time points [35]. Total flux was normalized to the obtained flux value of each group immediately after microgel suspension delivery in order to compare among samples. Data was fit to a one-phase decay curve and plotted over time using GraphPad Prism. Half-life values for each group were obtained from a one-phase decay curve fit.

3. Results

3.1. Generation of ChLA microgels using microfluidics

ChLA microgels were synthesized inside microfluidic devices by *in situ* crosslinking using TPP and G_1Phy. The ionic crosslinking mechanism of TPP and G_1Phy with chitosan is based on electrostatic interactions between phosphate groups present in the crosslinkers and protonated amino groups of chitosan [30, 37, 38]. Flow-focusing devices with 3 independent flow inlets (ChLA, crosslinker, and continuous phases) were used (Figure 1a) to produce crosslinked-ChLA microgels with and without encapsulated hMSCs. Firstly, ChLA (1 wt% in PBS) and crosslinker phases (Table 1) were merged at a T-junction to enable polymer-crosslinker interaction inside the device. The reactive mixture was then focused to the continuous phase to allow water/oil emulsion and droplet generation. The distance between the two junctions of the device was optimized to reduce interaction time between ChLA and the crosslinkers before emulsion. Thus, we avoided the formation of hydrogel pieces that clogged the device due to the fast kinetics of the crosslinkers. Once microdroplets were generated, residence time along the device was increased by the incorporation of a serpentine channel to ensure full crosslinking of ChLA microgels. Finally, resulting microgels were collected in α-MEM through the outlet tubing and centrifuged to eliminate oil, surfactant, and crosslinker traces (Figure 1b).

Different microgel formulations were synthesized varying the TPP:G_1Phy ratio in the crosslinker phase (Table 1). A minimum TPP concentration of 0.5 wt% was necessary to achieve fully crosslinked ChLA microgels. G_1Phy concentrations higher than 0.1 wt% resulted in the formation of hydrogel fibers that clogged the device. Therefore, the TPP:G_1Phy ratios were varied between these limits. It is important to note that G_1Phy has at least double the amount of anion groups capable to interact with ChLA compared with TPP. Thus, mixtures of TPP and G_1Phy at different ratios were a suitable strategy to modulate the ionic crosslinking kinetics and polymeric network formation. Notably, this approach allowed single-step fabrication of ChLA microgels containing G_1Phy. The size distributions of the tested mixtures were analysed (Figure 1c). Microgels showed relatively good homogeneous size distributions for all formulations. The average diameter decreased from 127±16 to 103±15 μm, as G_1Phy content increased from 0 to 0.1 wt% in the crosslinker phase. To conduct cellular encapsulation and bioactivity assays, composition 3

was selected because it represents the highest concentration of G_1Phy that could be successfully incorporated in the microgels. Composition 1 (not containing G_1Phy) was used as a control to test the bioactive effect of G_1Phy.

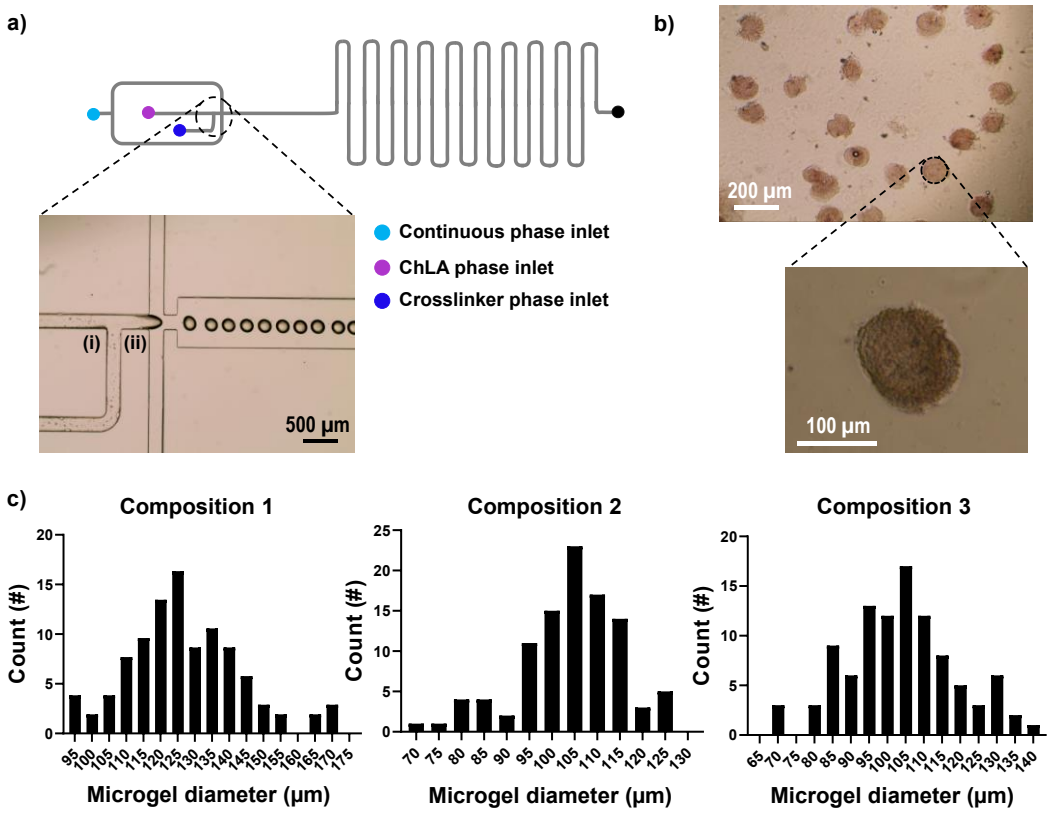

Figure 1. (a) Microfluidic device design that allowed (i) the mixture of ChLA and crosslinker phases; and (ii) the subsequent water/oil emulsion with continuous phase to generate microdroplets. The device serpentine allowed for microdroplets to fully crosslink and form microgels; **(b)** Light microscope images of TPP:G_1Phy-microgels at different magnifications after synthesis and purification; **(c)** Size distribution histograms for the three different microgel compositions (Table 1).

3.2. *In vitro* viability of encapsulated hMSCs

Viability of the encapsulated cells was evaluated by live/dead staining and confocal imaging at specified time points (Figure 2a). Confocal images showed high encapsulation efficiency after synthesis, with a low frequency (~ 10%) of cells remaining outside the microgels following encapsulation. Figure 2a shows cell viability percentages over time. A relatively high cell viability (79±2% and 67±2%, for TPP- and TPP:G_1Phy-microgels, respectively) was observed immediately following microgel synthesis (~ 2 h), demonstrating the cytocompatibility of the encapsulation and fabrication methods. However, encapsulated hMSCs showed a different survival profile in culture, varying with microgel composition. For TPP-microgels, cell viability was significantly reduced (~ 40±8%) after 1 day in culture ($p < 0.0001$), remaining constant until day 3. Cell viability significantly decreased down to 13±4% from 3 to 10 days in culture ($p < 0.0001$). In contrast, TPP:G_1Phy-microgels were more effective at supporting cell survival over time in comparison to TPP-microgels. G_1Phy-based microgels exhibited an initial viability of 67±2% which decreased to 60±7% after 1 day culture ($p < 0.01$), and remained constant over time. These results show that the presence of G_1Phy exerts a positive effect on the survival and maintenance of encapsulated hMSCs in ChLA microgels over time.

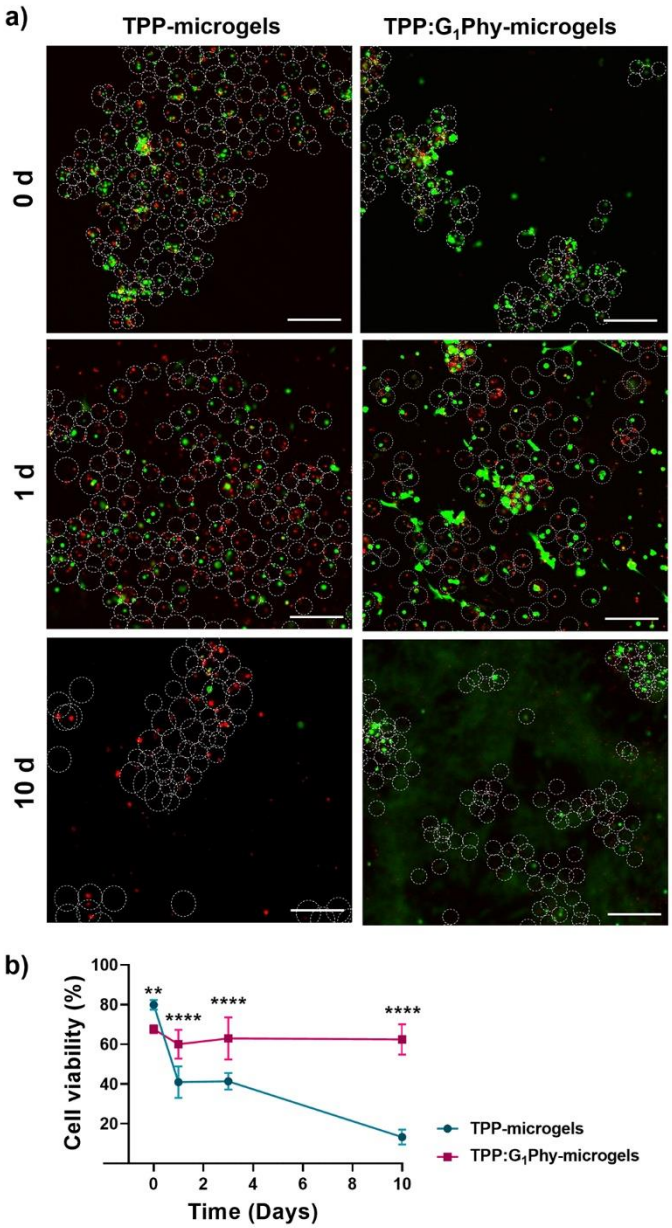

Figure 2. (a) Confocal images of encapsulated hMSCs in TPP- and TTP:G_1Phy-microgels after live/dead assay at 0, 1, and 10 days culture. Live (green) and dead (red) cells were stained with Calcein-AM and ethidium homodimer. Microgels are outlined with white dash lines. Scale bars: 500 μm; **(b)** Cell viability percentages (average ± SD) over time for TPP- and TPP:G_1Phy-

microgels calculated from confocal imaging analysis using ImageJ software. Two-way ANOVA analysis was performed to study significant differences between TPP-microgels and TPP:G_1Phy-microgels at each time point (**$p < 0.001$; ****$p < 0.0001$).

3.3. *In vitro* paracrine secretory profile of encapsulated hMSCs

hMSC secretome exerts powerful therapeutic actions on tissue regeneration processes [3-5]. Thus, we evaluated the effect of TPP:G_1Phy-microgel on paracrine signalling of encapsulated hMSCs cultured under oxidative stress or IFN-γ activation. To analyze the effect of G_1Phy on hMSC paracrine factor secretion under oxidative stress, we induced lipid peroxidation on cells encapsulated in the microgels by triggering the Fenton reaction [36]. PLS-DA of the complete collection of analytes showed clear clustering of the two experimental groups (Figure 3a), indicating that the crosslinker composition of the microgels had a considerable impact on analytes secretion profile under oxidative stress. Consistent with PLS-DA, heatmap analysis revealed clustering for both microgel compositions (Figure S2a). PLS-DA also provided information about the analytes that accounted for the majority of variance between the experimental groups after oxidative stress induction (Figure 3b). Secreted paracrine factors were analysed individually in order to compare secretory profiles of TPP- and TPP:G_1Phy-microgels. Figure 3c shows the results of analytes for which the two groups showed significant differences. The secretion of pro-angiogenic factors such as vascular endothelial growth factor (VEGF) and hepatocyte growth factor (HGF) for G_1Phy-containing microgels was higher than in control microgels. Furthermore, hMSCs encapsulated in TPP:G_1Phy-microgels showed elevated secretion of interleukin-8 (IL-8), which is related to monocyte activation and recruitment [39]. Other up-regulated paracrine factors in encapsulated cells in TPP:G_1Phy-microgels compared to control TPP microgels were fibroblast activation protein (FAP), macrophage colony-stimulating factor (M-CSF), monocyte chemoattractant protein-1 (MCP-1), insulin-like growth factor binding protein (IGFBP), and TNF R1, which belongs to tumour necrosis factors (TNF) family [40]. These cytokines have different immunoregulatory roles in tissue repair [4].

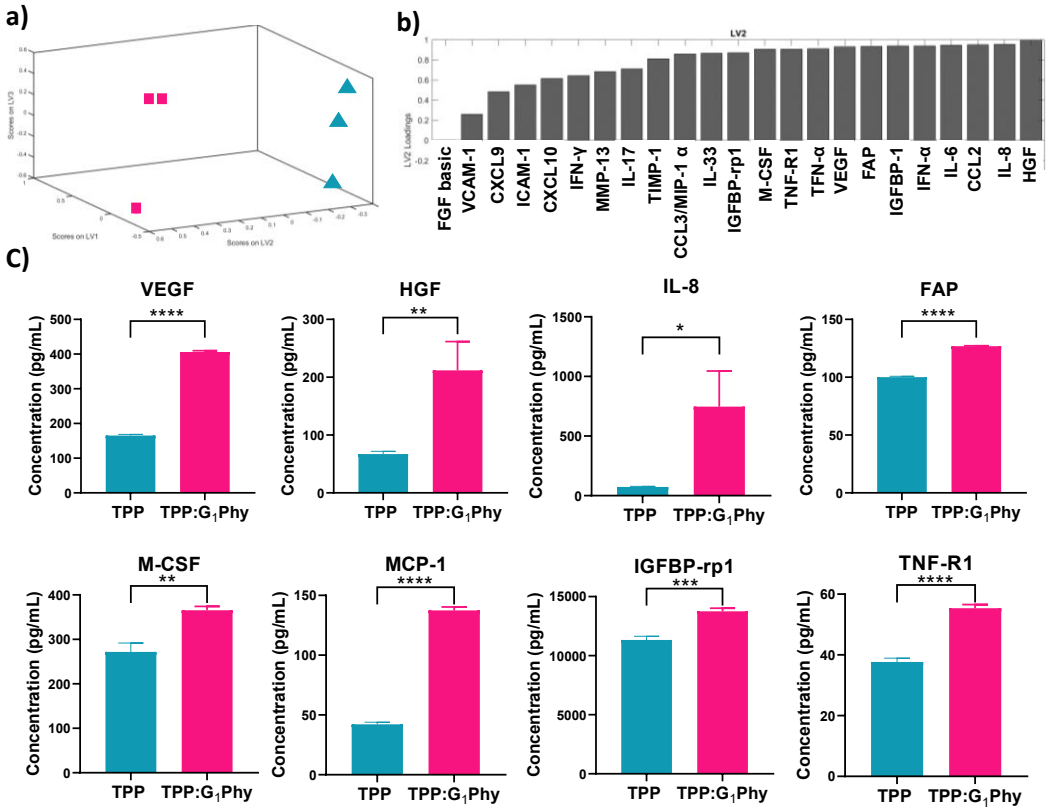

Figure 3. Analysis of secreted paracrine factors from encapsulated hMSCs in TPP-and TPP:G_1Phy-microgels under oxidative stress conditions studied using Luminex® assay. **(a)** PLS-DA of the total set of analyzed factors. Blue triangles and pink squares correspond to TPP-microgels and TPP:G_1Phy-microgel groups, respectively; **(b)** Normalized relative loading values given to each analyte during the PLS-DA; **(c)** Individual analysis of involved paracrine factors which were secreted from encapsulated hMSCs in function of microgel composition. n = 3 biologically independent samples, mean ± SD; *p<0.05, **p<0.01, ***p<0.001, ****p<0.0001. Unpaired t-test analysis was used to find significant differences between samples.

The hMSC secretome profile was also analysed after activation with IFN-γ, which induces inflammation-simulated conditions [41, 42]. PLS-DA revealed two well clustered groups corresponding to TPP- and TPP:G_1Phy-microgels (Figure 4a). Heatmap analysis showed a similar clustering organization (Figure S2b), supporting the PLS-DA results. Figure 3b displays the influence of each analyte on the variability between the experimental groups after IFN-γ in PLS-DA (Figure 4b). Analysis of individual analytes showed elevated expression for encapsulated

hMSCs in TPP:G$_1$Phy-microgels in comparison to TPP-microgels (Figure 4c). Thus, VEGF and basic FGF, which play key roles in tissue regeneration [4, 43, 44], were significantly up-regulated in TPP:G$_1$Phy-microgels compared to TPP-microgels. M-CSF, IL-8, and CXCL10 showed a significantly increased secretion in cells encapsulated in TPP:G$_1$Phy-microgels. CXCL10 is a chemokine involved in diverse immunomodulatory roles such as chemoattraction for monocytes and macrophages, and promotion of T cell adhesion to endothelial cells [45].

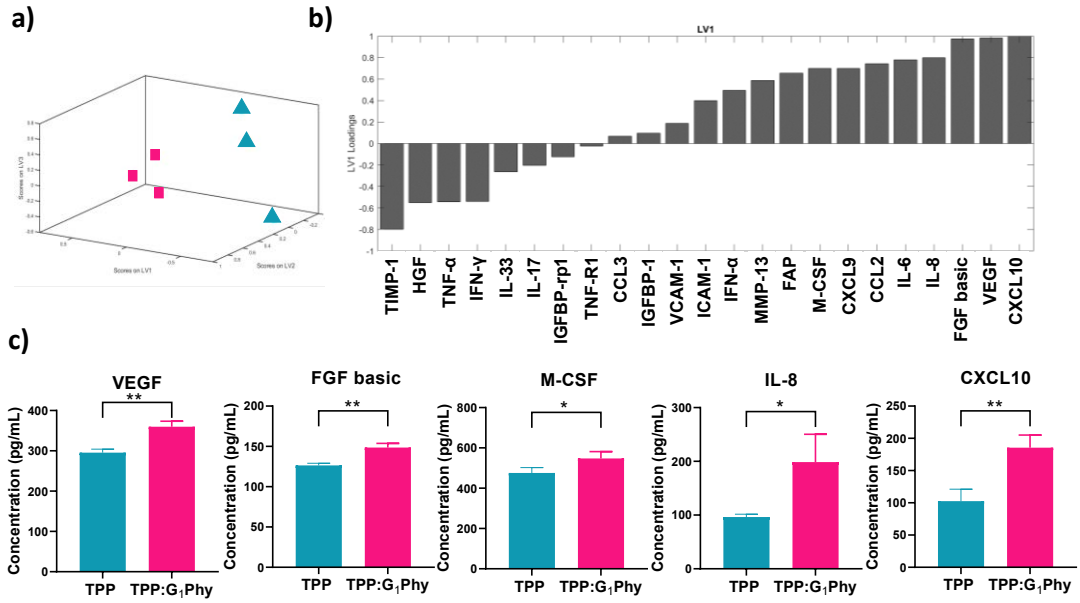

Figure 4. Analysis of secreted paracrine factors from encapsulated hMSCs in TPP-and TPP:G$_1$Phy-microgels activated with IFN-γ studied using Luminex® assay. **(a)** PLS-DA of the total set of analyzed factors. Blue triangles and pink squares correspond to TPP-microgels and TPP:G$_1$Phy-microgel groups, respectively; **(b)** Normalized relative loading values given to each analyte during the PLS-DA; **(c)** Individual analysis of relevant involved paracrine factors secreted from encapsulated hMSCs in function of microgel composition. n = 3 biologically independent samples, mean ± SD; *p<0.05, **p<0.01. Unpaired t-test analysis was used to find significant differences between samples.

Collectively, these results demonstrate that G_1Phy incorporation into microgel composition had a modulatory effect in the secretome of encapsulated hMSCs by enhancing the secretion of different pro-survival and pro-angiogenic factors (e.g. VEGF, HGF, FBF basic, among others) and immunoregulatory factors (e.g. CXCL10, IL-8, MCP-1) when exposed to oxidative and inflammatory environments. Thus, G_1Phy could be considered as a promising compound for enhancing paracrine signalling related to tissue repair capacities of encapsulated hMSCs in oxidative/inflammatory environments.

3.4. *In vivo* microgel-encapsulated hMSCs survival and persistence

Subcutaneous injection is an attractive route to evaluate the *in vivo* performance of microgels because it does not require invasive surgery and allows easily *in vivo* imaging. The survival and persistence of implanted microgel-encapsulated hMSCs were analyzed via *in vivo* imaging. Thus, TPP- and TPP:G_1Phy-microgels containing $hMSCs^{Luc}$ were subcutaneously injected in immunocompromised mice and bioluminescence was tracked (Figure 5a). Unencapsulated hMSCs (hMSCs-only) were used as control for comparison. At each time point (0, 3, 7, 10, 14, and 21 days) mice were injected with luciferin to measure bioluminescence signal. Microgel-encapsulated cells were easily delivered to the subcutaneous space via injection, and the delivery process was as simple as the injection of hMSCs-only. Immediately post-injection, equivalent signal intensities were observed between microgel-encapsulated cells and unencapsulated cells, demonstrating no adverse effects in initial cell survival. Normalized flux values (%) for each group are plotted over time in Figure 5b and half-life values of each sample were calculated from one-decay fit. Similar bioluminescence profiles over time were observed for all samples, but differences in the decay groups were found among groups (Figure 5b). Single-decay fit of the normalized total flux yielded half-life values of 3.7 ± 1.9, 2.2 ± 1.5, and 2.8 ± 1.3 days for TPP:G_1Phy-, TPP-microgels, and hMSCs-only, respectively. However, there were no statistical differences among groups.

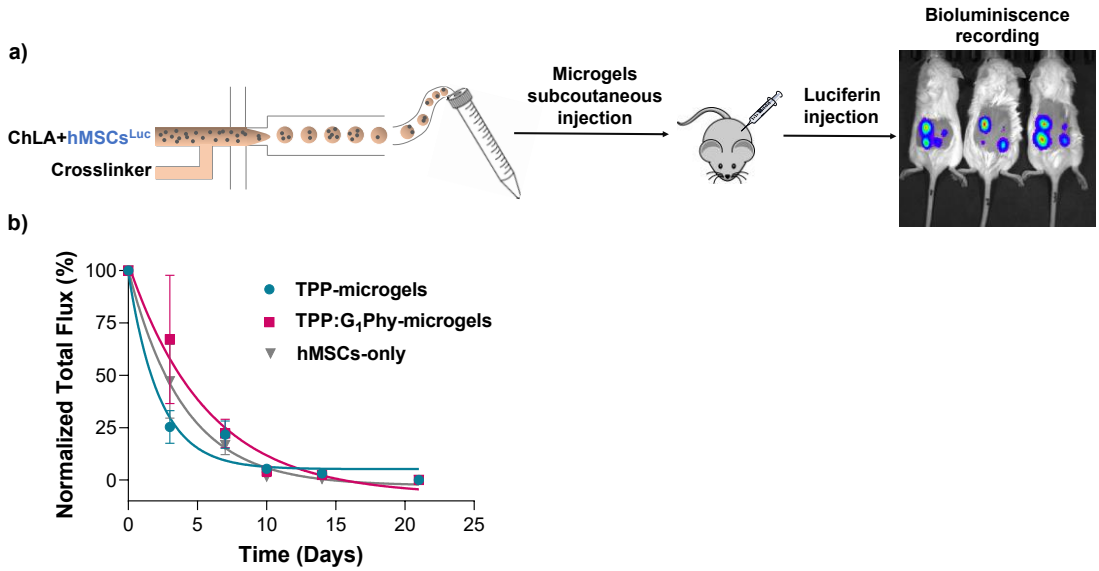

Figure 5. (a) Scheme of microfluidic synthesis of ChLA microgels containing hMCSs^{Luc} that were subcutaneously injected in dorsal sites of immunocompromised mice. Bioluminescence signal emitted by hMCSs^{Luc} after luciferin injection was monitored by IVIS Spectrum CT; **(b)** *In vivo* bioluminescence signal represented as normalized total flux (%) over time for TPP-, TPP:G_1Phy-microgels, and hMSC-only. Photon flux at each time and sample was normalized to flux value obtained immediately after sample injection; n = 7 per group; average ± SD.

4. Discussion

Microgels based on natural polymers are promising systems for cell delivery applications because they provide tissue-like structures that can improve cell survival and therapeutic activities of implanted cells [2]. Among their multiple advantages, microgels applications stand out due to their minimally invasive method of administration, which avoids surgical manipulations and complications associated with bulk hydrogel implantation (e.g. infection, trauma or scarring) [2, 46]. However, microencapsulation processes must ensure cell survival during fabrication [2, 47], and the used materials should exhibit excellent crosslinking capacities to maintain their structure and retain cells at the site of administration [2]. Although chitosan microgel synthesis has been explored [9, 10, 17, 24, 48-51], its use as a cell microcarrier has been significantly limited by (i) its poor solubility at neutral pH, (ii) the use of toxic crosslinking agents, and (iii) the need of harsh purification methods [21]. Here, we developed a strategy for the synthesis of bioactive chitosan

microgels by *in situ* crosslinking reaction in a flow-focusing microfluidic device. ChLA provided not only an adequate environment for cell encapsulation due to its excellent water-soluble properties, but the suitable amount of ionizable groups that can be successfully crosslinked at physiological conditions using phosphate-based agents. The combination of TPP and bioactive G_1Phy permitted the fabrication of ChLA microgels through ionic gelation that involved a one-step purification process by centrifugation without the necessity of using organic solvents. Crosslinker composition was adjusted to obtain optimum crosslinking kinetics. G_1Phy provided rapid crosslinking kinetics due to its higher content of phosphate groups, whereas the addition of TPP slowed down the gelation reaction, contributing to homogeneous microgel formation along the device. The blend of TPP and G_1Phy represents a new strategy to obtain stable microgels containing G_1Phy that provides the microgel formulation with bioactive properties. Furthermore, G_1Phy incorporation enhanced hMSC survival and paracrine factors secretion. TPP-chitosan gelation has been previously applied for MSCs encapsulation by Demir et al. [25]. In their work, they obtained chitosan microgels by precipitation of polymer droplets in a coagulation bath of TPP. Microcarriers obtained by precipitation-based methods generally show higher average diameter and polydispersity values than those obtained by microfluidic technology, which allows better control over particle size [52].

Encapsulated hMSCs with either microgel formulation showed relatively good cell viability after microencapsulation. TPP:G_1Phy-microgels exhibited lower initial viability than TPP-microgels. This result could be related to the faster crosslinking kinetics when G_1Phy was present. G_1Phy exhibits 6 phosphate groups per phytate ring that are susceptible to crosslink polymers containing positive charges providing rapid crosslinking kinetics. In this work, G_1Phy showed enhanced interaction ability against ChLA than TPP, giving rise to more robust polymeric frameworks than those obtained using only TPP. TPP:G_1Phy-microgels supported good *in vitro* cell viability over 10 days of culture. This result may be explained by the stronger interaction between G_1Phy and ChLA that contributed to maintain microgel shape and structure, providing a suitable matrix for prolonged cell culture. In this sense, G_1Phy has previously shown to improve biological behaviour in terms of cell adhesion and proliferation in comparison to TP. In particular, we applied G_1Phy as an ionic crosslinker for 3D printed scaffolds of other natural polymers,

finding out that G_1Phy-crosslinked 3D scaffolds showed better cellular adhesion and proliferation than when used only TPP [31]. Therefore, G_1Phy can play an important role in cell viability, providing an amenable environment for prolonged cell survival.

The therapeutic potential of hMSC secretome on tissue regeneration has gained great interest in recent years [3-5]. Antioxidant compounds, such as G_1Phy, are of great interest because injured tissues exhibit elevated levels of reactive oxidative species (ROS) [4]. In addition, although microgel injection is a minimally invasive method, it can prompt an adverse environment by the disruption of blood vessels and tissue damage [2]. In this work, G_1Phy incorporation modulated paracrine factor secretion in oxidative and inflammatory environments (Figure 3b and 4b, respectively) in comparison to the TPP crosslinker. G_1Phy-based microgels enhanced the secretion of vasculogenic factors like VEGF and HGF that could promote angiogenesis processes at similar oxidative conditions to those can be found in injured tissues. In this sense, studies on its precursor, phytic acid, demonstrated to improve vascularization of endothelial cells by increasing VEGF expression when used as crosslinker [53]. The incorporation of G_1Phy also promoted the expression of paracrine factors that play diverse immunomodulatory roles such as MCP-1 and M-CSF, which are related to the recruitment and proliferation and survival of monocytes, [5, 54, 55]; and IL-8, an angiogenic promoter with a key role in the recruitment and activation of neutrophils [39, 54]. Moreover, TNF-R1 (TNF-α family) secretion, was notably elevated in the presence of G_1Phy. TNF-α production has previously demonstrated to promote VEGF, IL-8, and IGF1 expression [54], and has been widely related to angiogenesis enhancement [56]. Finally, FAP, whose expression is closely related to tissue remodelling processes [57], was also upregulated in the presence of G_1Phy.

Similar findings were observed after IFN-γ treatment, which is a common *in vitro* model to simulate the inflammatory environment of injured or diseased tissues [41, 42] and has been shown to activate hMSCs. G_1Phy incorporation enhanced the secretion of pro-angiogenic factors such as VEGF, IL-8, and basic FGF. Basic FGF is an anti-inflammatory factor that belongs to the family of fibroblast growth factors, which regulates tissue repair signalling cascades [43]. Collectively, these results make TPP:G_1Phy-microgels attractive for applications in the regenerative medicine

field. The upregulation of paracrine signalling involved in tissue remodelling and healing by G_1Phy supports the use of these microgels for hMSC-based therapeutic applications.

Finally, we performed a pilot *in vivo* study examining hMSC survival and persistence for unencapsulated cells and microgel-encapsulated cells injected subcutaneously in immunocompromised mice. Microgel-encapsulated cells were easily delivered to the subcutaneous space via injection, and the delivery process was uneventful and as facile as injection of cells in saline (unencapsulated cells). Immediately post-injection, equivalent signal intensities were observed between microgel-encapsulated cells and cells in saline, demonstrating no adverse effects in initial cell survival. For all groups, cell persistence, inferred by bioluminescence signal, decreased exponentially over time with average half-life values of 3 days. In contrast to *in vitro* observations, no statistically significant differences in cell persistence were observed among groups. Further analyses are required to understand the relatively short persistence time of hMSCs in this pilot study.

4. Conclusions

Herein, we present a microfluidics approach for hMSC encapsulation in bioactive chitosan microgels. ChLA microgels crosslinked with the bioactive G_1Phy offer significant advantages as a hMSC delivery platform, including minimally invasive delivery by injection, cell viability maintenance over time and upregulation of paracrine signalling at adverse conditions (e.g. oxidative stress and inflammation). G_1Phy-crosslinked microgels emerge as a suitable and novel cell delivery platform since its therapeutic effect is not only due to support of encapsulated hMSC viability but also modulation of hMSC paracrine secretion. We envision that our G_1Phy-crosslinked ChLA microgels will impact on the hMSC therapeutic field.

5. References

[1] A.L. Facklam, L.R. Volpatti, D.G. Anderson, Biomaterials for Personalized Cell Therapy, Advanced Materials n/a(n/a) 1902005.

[2] G. Choe, J. Park, H. Park, J.Y. Lee, Hydrogel Biomaterials for Stem Cell Microencapsulation, Polymers (Basel) 10(9) (2018).

[3] D. Ascencio González, R. Hernández Pando, M. Ángel Gómez Lim, S. Ayala Fraustro, A. Torres Garcia, Therapeutic Strategies of Secretome of Mesenchymal Stem Cell, Stromal Cells - Structure, Function, and Therapeutic Implications2019.

[4] M. Gnecchi, M.C. Ciuffreda, M. Mura, Mesenchymal Stromal Cell Secretome for Tissue Repair, Cell Engineering and Regeneration2019, pp. 1-26.

[5] C.R. Harrell, C. Fellabaum, N. Jovicic, V. Djonov, N. Arsenijevic, V. Volarevic, Molecular Mechanisms Responsible for Therapeutic Potential of Mesenchymal Stem Cell-Derived Secretome, Cells 8(5) (2019).

[6] D.M. Headen, J.R. García, A.J. García, Parallel droplet microfluidics for high throughput cell encapsulation and synthetic microgel generation, Microsystems & Nanoengineering 4(1) (2018) 17076.

[7] A. Muxika, A. Etxabide, J. Uranga, P. Guerrero, K. de la Caba, Chitosan as a bioactive polymer: Processing, properties and applications, Int J Biol Macromol 105(Pt 2) (2017) 1358-1368.

[8] Q. Wu, D. Therriault, M.-C. Heuzey, Processing and Properties of Chitosan Inks for 3D Printing of Hydrogel Microstructures, ACS Biomaterials Science & Engineering 4(7) (2018) 2643-2652.

[9] K. Li, Y. Wang, Z. Miao, D. Xu, Y. Tang, M. Feng, Chitosan/gelatin composite microcarrier for hepatocyte culture, Biotechnol Lett 26(11) (2004) 879-83.

[10] M.S. Riederer, B.D. Requist, K.A. Payne, J.D. Way, M.D. Krebs, Injectable and microporous scaffold of densely-packed, growth factor-encapsulating chitosan microgels, Carbohydr Polym 152 (2016) 792-801.

[11] A. Das, D.A. Barker, T. Wang, C.M. Lau, Y. Lin, E.A. Botchwey, Delivery of bioactive lipids from composite microgel-microsphere injectable scaffolds enhances stem cell recruitment and skeletal repair, PLoS One 9(7) (2014) e101276.

[12] K. Wang, S. Lin, K.C. Nune, R.D. Misra, Chitosan-gelatin-based microgel for sustained drug delivery, J Biomater Sci Polym Ed 27(5) (2016) 441-53.

[13] C. Chen, M. Liu, S. Lii, C. Gao, J. Chen, In vitro degradation and drug-release properties of water-soluble chitosan cross-linked oxidized sodium alginate core-shell microgels, J Biomater Sci Polym Ed 23(16) (2012) 2007-24.

[14] R. Yin, K. Wang, S. Du, L. Chen, J. Nie, W. Zhang, Design of genipin-crosslinked microgels from concanavalin A and glucosyloxyethyl acrylated chitosan for glucose-responsive insulin delivery, Carbohydr Polym 103 (2014) 369-76.

[15] N. Isiklan, S. Tokmak, Development of thermo/pH-responsive chitosan coated pectin-graft-poly(N,N-diethyl acrylamide) microcarriers, Carbohydr Polym 218 (2019) 112-125.

[16] H. Liu, Z. Wei, M. Hu, Y. Deng, Z. Tong, C. Wang, Fabrication of degradable polymer microspheres via pH-responsive chitosan-based Pickering emulsion photopolymerization, RSC Adv. 4(55) (2014) 29344-29351.

[17] Y. Hong, Y. Gong, C. Gao, J. Shen, Collagen-coated polylactide microcarriers/chitosan hydrogel composite: injectable scaffold for cartilage regeneration, J Biomed Mater Res A 85(3) (2008) 628-37.

[18] S.-Y. Kim, H. Lee, S. Cho, J.-W. Park, J. Park, J. Hwang, Size Control of Chitosan Capsules Containing Insulin for Oral Drug Delivery via a Combined Process of Ionic Gelation with Electrohydrodynamic Atomization, Industrial & Engineering Chemistry Research 50(24) (2011) 13762-13770.

[19] H. Lee, C. Jeong, K. Ghafoor, S. Cho, J. Park, Oral delivery of insulin using chitosan capsules cross-linked with phytic acid, Biomed Mater Eng 21(1) (2011) 25-36.

[20] C.H. Yang, K.S. Huang, J.Y. Chang, Manufacturing monodisperse chitosan microparticles containing ampicillin using a microchannel chip, Biomed Microdevices 9(2) (2007) 253-9.

[21] X.-G. Chen, C.-S. Liu, C.-G. Liu, X.-H. Meng, C.M. Lee, H.-J. Park, Preparation and biocompatibility of chitosan microcarriers as biomaterial, Biochemical Engineering Journal 27(3) (2006) 269-274.

[22] B. Li, L. Wang, F. Xu, X. Gang, U. Demirci, D. Wei, Y. Li, Y. Feng, D. Jia, Y. Zhou, Hydrosoluble, UV-crosslinkable and injectable chitosan for patterned cell-laden microgel and rapid transdermal curing hydrogel in vivo, Acta Biomater 22 (2015) 59-69.

[23] Q. Zou, J. Li, Y. Li, Preparation and characterization of vanillin-crosslinked chitosan therapeutic bioactive microcarriers, Int J Biol Macromol 79 (2015) 736-47.

[24] Z. Lu, Y. Zhou, B. Liu, Preparation of chitosan microcarriers by high voltage electrostatic field and freeze drying, J Biosci Bioeng 128(4) (2019) 504-509.

[25] A. Koc Demir, A.E. Elcin, Y.M. Elcin, Osteogenic differentiation of encapsulated rat mesenchymal stem cells inside a rotating microgravity bioreactor: in vitro and in vivo evaluation, Cytotechnology 70(5) (2018) 1375-1388.

[26] Y. Jang, C. Cha, J. Jung, J. Oh, Interfacial Compression-Dependent Merging of Two Miscible Microdroplets in an Asymmetric Cross-Junction for In Situ Microgel Formation, Macromolecular Research 26(12) (2018) 1143-1149.

[27] E.L. Daley, R.M. Coleman, J.P. Stegemann, Biomimetic microbeads containing a chondroitin sulfate/chitosan polyelectrolyte complex for cell-based cartilage therapy, J Mater Chem B 3(40) (2015) 7920-7929.

[28] J.K. Wise, A.I. Alford, S.A. Goldstein, J.P. Stegemann, Synergistic enhancement of ectopic bone formation by supplementation of freshly isolated marrow cells with purified MSC in collagen-chitosan hydrogel microbeads, Connect Tissue Res 57(6) (2016) 516-525.

[29] A. Muxika, A. Etxabide, J. Uranga, P. Guerrero, K. de la Caba, Chitosan as a bioactive polymer: Processing, properties and applications, International journal of biological macromolecules 105(Pt 2) (2017) 1358-1368.

[30] A. Mora-Boza, M.L. López-Donaire, L. Saldaña, N. Vilaboa, B. Vázquez-Lasa, J. San Román, Glycerylphytate compounds with tunable ion affinity and osteogenic properties, Scientific Reports 9(1) (2019) 11491.

[31] A. Mora-Boza, M.K. Włodarczyk-Biegun, A. del Campo, B. Vázquez-Lasa, J.S. Román, Glycerylphytate as an ionic crosslinker for 3D printing of multi-layered scaffolds with improved shape fidelity and biological features, Biomaterials Science 8(1) (2020) 506-516.

[32] D.M. Headen, G. Aubry, H. Lu, A.J. Garcia, Microfluidic-based generation of size-controlled, biofunctionalized synthetic polymer microgels for cell encapsulation, Adv Mater 26(19) (2014) 3003-8.

[33] E.A. Phelps, N.O. Enemchukwu, V.F. Fiore, J.C. Sy, N. Murthy, T.A. Sulchek, T.H. Barker, A.J. Garcia, Maleimide cross-linked bioactive PEG hydrogel exhibits improved reaction kinetics and cross-linking for cell encapsulation and in situ delivery, Adv Mater 24(1) (2012) 64-70, 2.

[34] X. Qu, A. Wirsén, A.-C. Albertsson, Synthesis and characterization of pH-sensitive hydrogels based on chitosan and D,L-lactic acid, Journal of Applied Polymer Science 74(13) (1999) 3193-3202.

[35] A.Y. Clark, K.E. Martin, J.R. Garcia, C.T. Johnson, H.S. Theriault, W.M. Han, D.W. Zhou, E.A. Botchwey, A.J. Garcia, Integrin-specific hydrogels modulate transplanted human bone marrow-derived mesenchymal stem cell survival, engraftment, and reparative activities, Nat Commun 11(1) (2020) 114.

[36] B. Fuhrman, J. Oiknine, M. Aviram, Iron induces lipid peroxidation in cultured macrophages, increases their ability to oxidatively modify LDL, and affects their secretory properties, Atherosclerosis 111(1) (1994) 65-78.

[37] Y. Cai, Y. Lapitsky, Analysis of chitosan/tripolyphosphate micro- and nanogel yields is key to understanding their protein uptake performance, J Colloid Interface Sci 494 (2017) 242-254.

[38] V. Zamora-Mora, D. Velasco, R. Hernández, C. Mijangos, Chitosan microgels obtained by on-chip crosslinking reaction employing a microfluidic device, Optofluidics, Microfluidics and Nanofluidics 1(1) (2014).

[39] M. Akdis, S. Burgler, R. Crameri, T. Eiwegger, H. Fujita, E. Gomez, S. Klunker, N. Meyer, L. O'Mahony, O. Palomares, C. Rhyner, N. Ouaked, A. Schaffartzik, W. Van De Veen, S. Zeller, M. Zimmermann, C.A. Akdis, Interleukins, from 1 to 37, and interferon-gamma: receptors, functions, and roles in diseases, The Journal of allergy and clinical immunology 127(3) (2011) 701-21.e1-70.

[40] L. Yan, D. Zheng, R.H. Xu, Critical Role of Tumor Necrosis Factor Signaling in Mesenchymal Stem Cell-Based Therapy for Autoimmune and Inflammatory Diseases, Front Immunol 9 (2018) 1658.

[41] M. Goedhart, A.S. Cornelissen, C. Kuijk, S. Geerman, M. Kleijer, J.D. van Buul, S. Huveneers, M. Raaijmakers, H.A. Young, M.C. Wolkers, C. Voermans, M.A. Nolte, Interferon-Gamma Impairs Maintenance and Alters Hematopoietic Support of Bone Marrow Mesenchymal Stromal Cells, Stem Cells Dev 27(9) (2018) 579-589.

[42] N.A. Petinati, N.M. Kapranov, A.E. Bigil'deev, M.D. Popova, Y.O. Davydova, I.V. Gal'tseva, N.I. Drize, L.A. Kuz'mina, E.N. Parovichnikova, V.G. Savchenko, Changing the Properties of Multipotent Mesenchymal Stromal Cells by IFNgamma Administration, Bulletin of experimental biology and medicine 163(2) (2017) 230-234.

[43] L. Maddaluno, C. Urwyler, S. Werner, Fibroblast growth factors: key players in regeneration and tissue repair, Development 144(22) (2017) 4047-4060.

[44] P. Carmeliet, R.K. Jain, Molecular mechanisms and clinical applications of angiogenesis, Nature 473(7347) (2011) 298-307.

[45] Q. Zhao, T. Kim, J. Pang, W. Sun, X. Yang, J. Wang, Y. Song, H. Zhang, H. Sun, V. Rangan, S. Deshpande, H. Tang, M.E. Cvijic, R. Westhouse, T. Olah, J. Xie, M. Struthers, L. Salter-Cid, A novel function of CXCL10 in mediating monocyte production of proinflammatory cytokines, Journal of Leukocyte Biology 102(5) (2017) 1271-1280.

[46] G.A. Foster, D.M. Headen, C. Gonzalez-Garcia, M. Salmeron-Sanchez, H. Shirwan, A.J. Garcia, Protease-degradable microgels for protein delivery for vascularization, Biomaterials 113 (2017) 170-175.

[47] T.W. Yeung, E.F. Ucok, K.A. Tiani, D.J. McClements, D.A. Sela, Microencapsulation in Alginate and Chitosan Microgels to Enhance Viability of Bifidobacterium longum for Oral Delivery, Front Microbiol 7 (2016) 494.

[48] P. Xia, K. Zhang, Y. Gong, G. Li, S. Yan, J. Yin, Injectable Stem Cell Laden Open Porous Microgels That Favor Adipogenesis: In Vitro and in Vivo Evaluation, ACS Appl Mater Interfaces 9(40) (2017) 34751-34761.

[49] L. Zhang, J. Pan, J. Li, W. Wu, Y. Yu, Studies on the preparation of chitosan microcarriers cross-linked by oxidized lactose and culture of primary hepatocytes, Artif Cells Blood Substit Immobil Biotechnol 31(3) (2003) 293-301.

[50] L. Ye, S. Ding, Y.L. Cui, Q.S. Wang, Y. Zhang, Evaluation of the Preparation Technology on Chitosan-Gelatin Microcarrier by Orthogonal Design, Advanced Materials Research 282-283 (2011) 133-137.

[51] C.Y. Chui, A. Odeleye, L. Nguyen, N. Kasoju, E. Soliman, H. Ye, Electrosprayed genipin cross-linked alginate-chitosan microcarriers for ex vivo expansion of mesenchymal stem cells, J Biomed Mater Res A 107(1) (2019) 122-133.

[52] D.M. Headen, J.R. García, A.J. García, Parallel droplet microfluidics for high throughput cell encapsulation and synthetic microgel generation, Microsystems & Nanoengineering 4(1) (2018).

[53] X. Wang, K. Wen, X. Yang, L. Li, X. Yu, Biocompatibility and anti-calcification of a biological artery immobilized with naturally-occurring phytic acid as the crosslinking agent, Journal of Materials Chemistry B 5(40) (2017) 8115-8124.

[54] S.F.H. de Witte, M. Franquesa, C.C. Baan, M.J. Hoogduijn, Toward Development of iMesenchymal Stem Cells for Immunomodulatory Therapy, Frontiers in Immunology 6(648) (2016).

[55] A.C. Wu, N.A. Morrison, W.L. Kelly, M.R. Forwood, MCP-1 expression is specifically regulated during activation of skeletal repair and remodeling, Calcified tissue international 92(6) (2013) 566-75.

[56] Z.Y. Lu, W.C. Chen, Y.H. Li, L. Li, H. Zhang, Y. Pang, Z.F. Xiao, H.W. Xiao, Y. Xiao, TNF-alpha enhances vascular cell adhesion molecule-1 expression in human bone marrow mesenchymal stem cells via the NF-kappaB, ERK and JNK signaling pathways, Mol Med Rep 14(1) (2016) 643-8.

[57] K.-M. Chung, S.-C. Hsu, Y.-R. Chu, M.-Y. Lin, W.-T. Jiaang, R.-H. Chen, X. Chen, Fibroblast activation protein (FAP) is essential for the migration of bone marrow mesenchymal stem cells through RhoA activation, PloS one 9(2) (2014) e88772-e88772.

Acknowledgments

The authors thank the Spanish Ministry of Science and Innovation (project, MAT2017-84277-R) and U.S. National Institutes of Health (R01 AR062368) for financial support. B. Vázquez-Lasa and J. San Román are members of the *SusPlast platform (Interdisciplinary Platform for Sustainable Plastics towards a Circular Economy)* from the Spanish National Research Council (CSIC). Ana Mora-Boza was supported by "La Caixa" Foundation (ID 100010434, scholarship code LCF/BQ/ES16/11570018) and FORD ESPAÑA (Ford Motor Company Fund) - "Apadrina La Ciencia" Foundation research contract.

6. Supplementary information

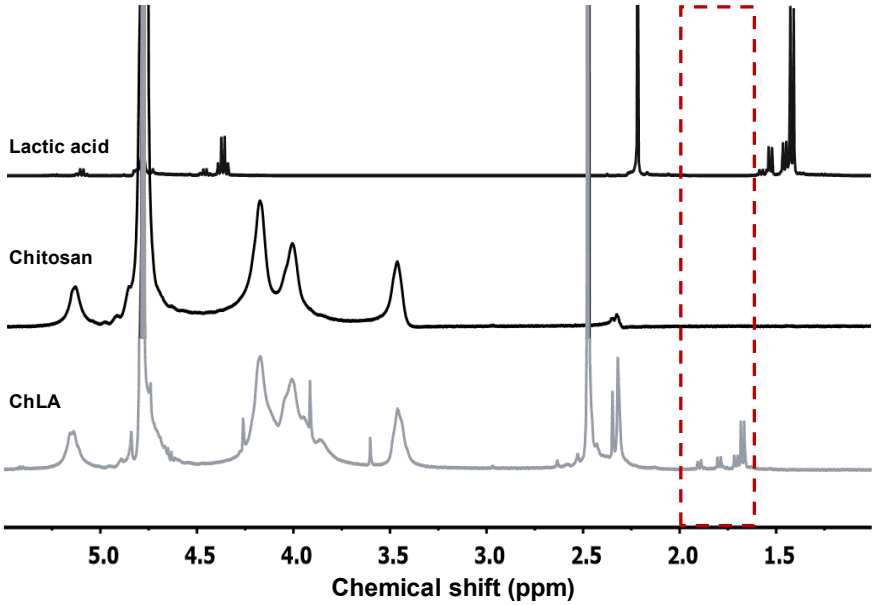

Figure S1. ^{1}H-RMN spectra of lactic acid, chitosan, and ChLA recorded in D_2O. The chitosan conjugated lactate groups in ChLA spectrum appeared at chemical shifts of δ 1.6, 1.7, 1.85 and 1.90 (red box).

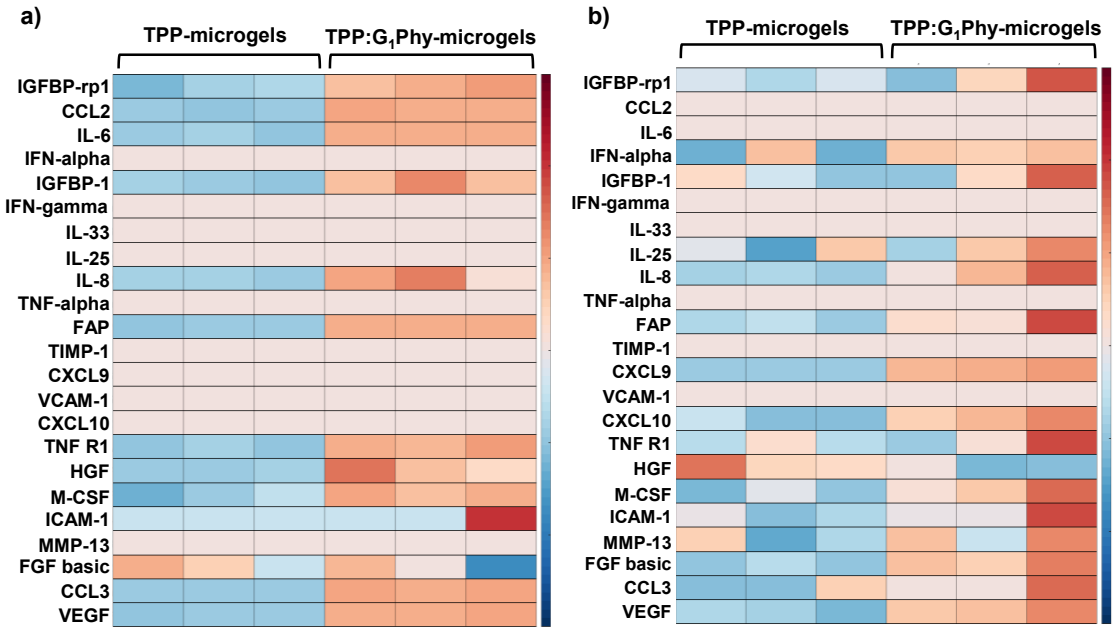

Figure S2. Heat maps of oxidative stress **(a)** and IFN-ɣ activation **(b)** experiments for TPP- and TPP:G_1Phy-microgels.

Appendix A

Preparation of polymeric and composite scaffolds by 3D Bioprinting

Book Chapter

Preparation of polymeric and composite scaffolds by 3D Bioprinting

Ana Mora-Boza [1, 2, *], María Luisa Lopez-Donaire [1]

[1]Institute of Polymer Science and Technology-ICTP-CSIC, 28006 Madrid, Spain.

[2]CIBER, Health Institute Carlos III, 28029 Madrid, Spain.

***Corresponding author.**

Book: Osteochondral Tissue Engineering. Advances in Experimental Medicine and Biology, vol 1058. Springer (2018)

Abstract

In the last few years, the advent of 3D Bioprinting technology has marked a milestone in osteochondral tissue engineering (TE) research. Nowadays, the traditional used techniques for osteochondral regeneration remain to be inefficient since they cannot mimic the complexity of joint anatomy and tissue heterogeneity of articular cartilage. These limitations seem to be solved with the use of 3D bioprinting which can reproduce the anisotropic extracellular matrix (ECM) and heterogeneity of this tissue. In this chapter, we will expose the most used 3D bioprinting approaches and then, discuss the main criteria that biomaterials must meet to be used as suitable bioinks, in terms of mechanical and biological properties. Finally, we highlight some of the challenges that this technology must overcome related to osteochondral bioprinting before its clinical implementation.

1. Introduction

Bioprinting has emerged in the last few years as a promising technique for osteochondral TE applications. 3D bioprinting is the technology through bioinks (biomaterials and bioactive cues) can be deposited in a spatiotemporal accurate layer-by-layer manner allowing high cell seeding density and strong cell-cell interactions [1-4]. This technology can be classified in two different categories in

function of the bioink contains living cells (cellular 3D bioprinting) or not (acellular 3D bioprinting). Although to the date, applications of 3D bioprinting have been focused on cardiovascular, skin regeneration, tracheal splints, cartilaginous structures, and hard tissues like bone, among others. The uniquely capacity of this technique to mimic heterogeneous and anisotropic properties of ECM has attracted much attention to osteochondral tissues [2, 5-9]. In this perspective, 3D fabrication techniques have raised as an alternative for grafting methodologies, which remain as the common gold standard treatment for joint degenerative diseases such as osteoarthritis (OA) or trauma [7]. Osteochondral grafts exhibit low integration at the bone-cartilage interface and poor tissue formation *de novo* [5, 8]. For its part, 3D bioprinting provides the fabrication of scaffolds with interconnected macro and micro-porosity which improves nutrients diffusion and removal of waste products, facilitates the ECM deposition and ingrowth of blood vessels [10, 11]. In the case of osteochondral tissue, considerations regarding to heterogeneity and anisotropy are of special importance due to mechanical and composition requirements, which differ from cartilage to bone tissues. Thus, 3D bioprinting can be advantageous.

To obtain effective and biological-relevant tissue constructions that mimic the native microenvironment, several specifications must be considered. Among these essential aspects, structural and physical specifications, such as bulk properties and surface topography, play a key role in the development of bioactive tissue constructs. 3D bioprinting is an appropriate fabrication technique with high spatial resolution by which achieves these aspects. However, appropriated biomaterials (bioinks) should be developed with optimal rheological and biological properties, since this is the main limitation of the technique as it will be exposed in this chapter [12-15]. Material viscosity, gelation method, and speed must be optimized to obtain 3D architectures with enough structural integrity and mechanical properties that allow interactions not only with the materials but also cell communication [2, 12, 16-19]. In addition, many manufacturing techniques can also be employed to improve the relatively weak mechanical properties of soft hydrogels, such as ultraviolet (UV) curing [20, 21], pre-crosslinking procedures or the incorporation of additional elements and materials such as polycaprolactone (PCL) [22] or graphene oxide (GO) elements [23, 24]. Some of these elements can be sacrificial since they will not form part of the final constructs.

Moreover, the 3D bioprinting processes must ensure compliance with some biological specifications. Certainly, biocompatibility and absence of cytotoxicity are essential requisites, but the considerable efforts made in the last decades on the TE field have demonstrated that bioactive constructs are indispensable. By this way, the need for vascularization remains as one of the most daunting challenge for the development of 3D complexes. The exchange of nutrients and oxygen cannot be facilitated without an adequate vascular network, being necessary ≈ 100 μm between cells and the nearest capillary due to molecular diffusion limitations [12, 25, 26]. Finally, for a succeed integration with surrounding environment, degradation and absorption kinetics of the constructs must be fast to avoid side effects. 3D bioprinting provides some advantages regarding to these biological aspects among other biofabrication techniques, since it can facilitate a controlled deposition of cells maintaining their viability during the process [12, 27].

Finally, economic issues regarding to manufacturing requirements, overall cost of materials and fabrication devices, and necessary production time are crucial aspects for the successfully clinical translation of 3D bioprinting in osteochondral restoration applications. Although the cost of specialized equipment and experienced personnel could be high, there are progressively more affordable 3D fabrication systems with intuitive interfaces for inexperienced users [5, 7, 12].

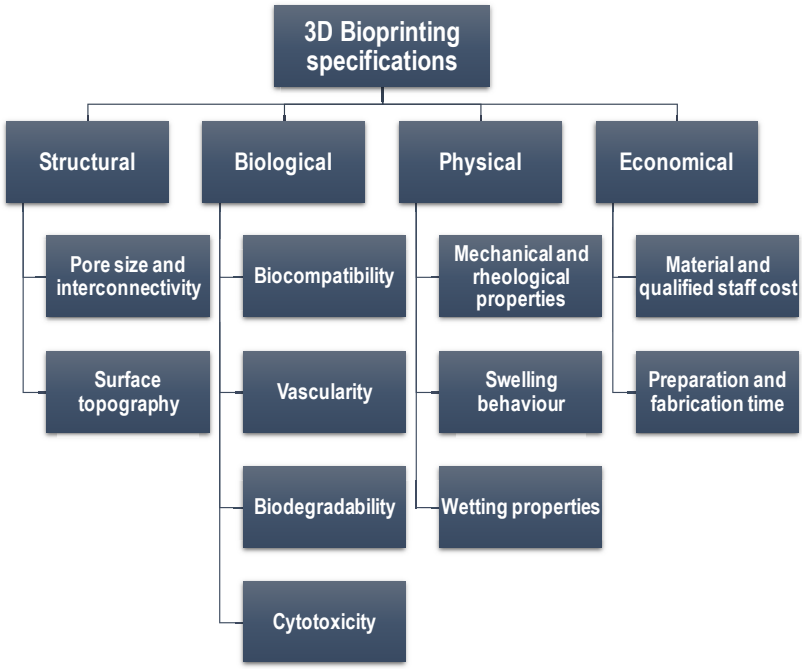

Figure 1. 3D bioprinting considerations regarding structural, physical, biological and economical specifications.

In this chapter, we will discuss how the advent of 3D bioprinting has provided new opportunities for osteochondral TE, and the current advances and challenges that must be addressed by current 3D bioprinting approaches and bioinks for the preparation of polymeric and composited scaffolds.

2. 3D Bioprinting fabrication strategies for Osteochondral TE

As it has been explained in the introduction, 3D bioprinting techniques have attracted much attention to the treatment of osteochondral degeneration and diseases such as OA through osteochondral tissue regeneration. Currently, autografts and allografts are being applied to reduce donor site morbidity and matching mainly in young patients. However, the research is moving towards developing *de novo* tissue structures to improve integration with host tissue and nutrient diffusion in larger macro-porous scaffolds through cell-based repairs such as autologous chondrocytes implementation [5, 7, 12, 28, 29].

Recently, bioprinting has been subclassified into two categories: scaffold-based and scaffold-free bioprinting. While scaffold-based bioprinting implies the generation by 3D printing of an scaffolding materials where cells can be seed during or post-fabrication, scaffold-free bioprinting is based on the self-assembly of cellular components mimicking embryonic development [30-32]. This chapter is focused only in the description of the scaffold-based bioprinting techniques for the development of osteochondral complex tissue. We have made a subdivision between cellular and acellular scaffold-based bioprinting depending on their bioink formulation containing living cells in its composition or not.

2.1. Cellular Bioprinting

In this first epigraph, the most used cellular 3D Bioprinting processes will be exposed extrusion-based bioprinting, droplet-based bioprinting, laser based bioprinting, and stereolithography, [5, 7, 9, 33, 34]. An illustration of these 3D bioprinting processes with its main components is shown in Figure 2.

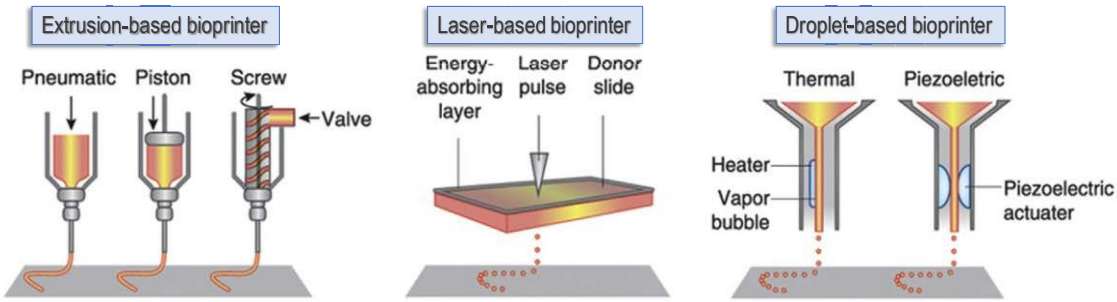

Figure 2. Schemes of 3D bioprinting process and its main components [35]. Adapted from Biomaterials 83, D. Tang. et al., Biofabrication of bone tissue: approaches, challenges and translation for bone regeneration, pp 363-382, Copyright 2016, with permission from Elsevier.

2.1.1. Extrusion-based bioprinting.

The extrusion-based bioprinting (EBB) consists of the dispensation of bioinks using an air-force pump, solenoid or mechanical screw plunger. EBB addresses the challenges of droplet bioprinting process, which cannot deposit very viscous materials or high cell density solutions [1, 12, 33]. As it will be shown later, high viscosity values of the bioinks are desirable to obtain high shape fidelity of

the tissue constructs but in some cases, high concentration of the components of the bioinks can result in less cell viability due to cytotoxicity [36]. Nevertheless, EBB is the most used technique for TE applications due to its moderate cost in comparison to the good resolution it provides, as well as, the high cellular concentrated-bioinks that can be printed [1]. In addition, good-shaped fidelity can be obtained through a fast phase change from a liquid bioink to a more solid network by different crosslinking procedures, that can be classified into chemical (irreversible) and physical (reversible) crosslinkings. Among all chemical crosslinkings processes, photo-initiated free radical polymerization reaction is a commonly used alternative for rapid crosslinking despite its cytotoxicity. This process is widely accepted due to its effectiveness, efficiency, and controllability. Duchi and collaborators developed a co-axial core/shell system for EBB to avoid the cytotoxicity that can trigger UV photocuring due to the generation of free radicals and UV exposure to the cells. They demonstrated that these problems can be addressed with an accurate control of the deposition parameters [37]. In other work, O'Connell et al. developed an easy-handle device for medical surgery, named as "biopen", in an attempt of bringing together 3D printing technology and surgical processes. The tool could print gelatin methacrylamide (GelMA) and hyaluronic acid methacrylate (HAMA) hydrogels, which were photocrosslinked. The process was compatible with the deposition of adipose stem cells at chondral wound side protocol [38].

Many authors have used of EBB for the development of multilayered compound scaffolds in the context of cartilage and osteochondral regeneration [10, 37, 39-41]. For example, Bartnikowski and collaborators developed a 3D plotted scaffold composed of alginate and hydroxyapatite (HAp), mixed with GelMA, or GelMA with HAMA for the regeneration of a zone of calcified cartilage, concluding that the incorporation of HAMA in these hydrogels improved chondrogenesis [11]. T. Ahlfeld and coworkers used EBB to obtain 3D constructs by printing alginate and methylcellulose with clinically relevant dimensions thanks to the addition of laponite, a nanosilicate clay that improve mechanical properties of the matrices. The cellular viability was maintained for 21 days, arising this approach as a promising alternative for 3D bioprinting materials [39].

Other important aspect to consider in EBB is the geometry of the needle, which can play a crucial role in cellular viability, since the shear stress under the extrusion can affect cellular behavior and well-being. Muller et al. developed an interesting study where they used different needle geometries and sizes to print alginate and nanocellulose bioinks for cartilage applications. The computational fluid dynamic analysis of different needle geometries is shown in Figure 3. In conclusion, they demonstrated that the appropriated selection of the needle geometry is as important as bioink optimization for high printing resolution and cell viability [13].

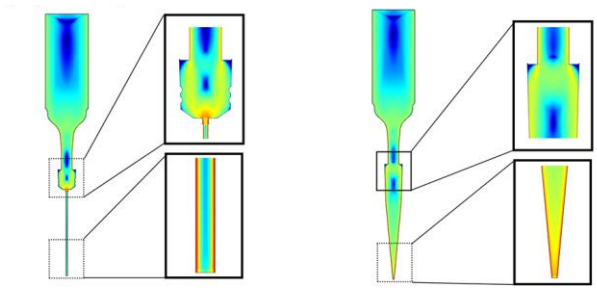

Figure 3. Computational fluid dynamic analysis for a straight and a conical needle, respectively. Regions of high shear stress are indicated in red/orange colors. Clear differences can be observed between the two geometries [13]. Reproduced from "Alginate Sulfate–Nanocellulose Bioinks for Cartilage Bioprinting Applications", Annals of Biomedical Engineering, Vol. 45, No. 1, January 2017, pp. 210–223, Muller et al. with permission of Springer.

2.1.2. Laser-based bioprinting and stereolithography

Laser-based bioprinting (LBB) is implemented by laser-induced forward transfer (LIFT), which is a method to deposit inorganic materials onto a platform construction through a patterned substrate. Odde and Renn, used this technique for the first time in 1999 for the deposition of biological materials and cell patterning into clusters to obtain 2 and 3D structures [12, 34, 42, 43]. LIFT uses very high-powered pulsed laser, and a glass or quartz print ribbon is coated with a thin film of metal or other laser-absorbing material to protect the cells from the laser power. Then, a cell suspension is spread onto the bottom of the ribbon. This suspension is vaporized with a laser pulse focused onto the metal layer, which propels the cell suspension from the ribbon to a receiving platform construction [44]. LBB is very useful for bioinks with very low viscosity allowing microscale

resolution. However, it is restricted only to very thin structures and presents a high cost and complex manufacturing [12, 45]. Gruene and collaborators demonstrated in their work that LBB is suitable for 3D scaffolds-free autologous tissue grafts with high cell density enough to promote chondrogenesis. In addition, the printed mesenchymal stem cells (MSCs) tolerated the complete process maintaining their functionality [46]. Other similar techniques to LIFT are used in LBB approaches. For example, absorbing film-assisted laser-induced forward transfer (AFA-LIFT) uses a 100 nm sacrificial metal layer to interact with the laser. There is also a version of AFA-LIFT, known as biological laser processing (BioLP), which uses motorized receiving stages and a charge-coupled device (CCD) camera to focus the laser. The sacrificial metallic layer allows having a rapid thermal expansion, to reduce the heating of the small cell suspension volume that is propel from the ribbon to the substrate. Finally, matrix-assisted pulsed laser evaporation direct writing (MAPLE DW), is similar to AFA-LIFT but it uses a low powered laser operating in the UV or near-UV region. In addition, the ribbon is coated with a sacrificial biological layer to allow the initial cell attachment [44].

On the other hand, stereolithography (SLA) consists of the irradiation of a photopolymerizable macromer solution with a laser to crosslink patterns with high resolution in the polymerization plane. This technique allows the fabrication of accurate microstructured scaffolds [1]. Thus, this technique is only valid for photopolymerizable materials, exhibiting high microscale resolution and printing speed [12]. X. Zhou et al. used SLA to produce GelMA, poly(ethylene glycol) diacrylate (PEGDA) and GO scaffolds that induced chondrogenic differentiation of human MSCs (hMSCs) by promotion of glycosaminoglycan (GAG) and collagen levels. A scheme of the scaffold fabrication is showed in Figure 4 [24].

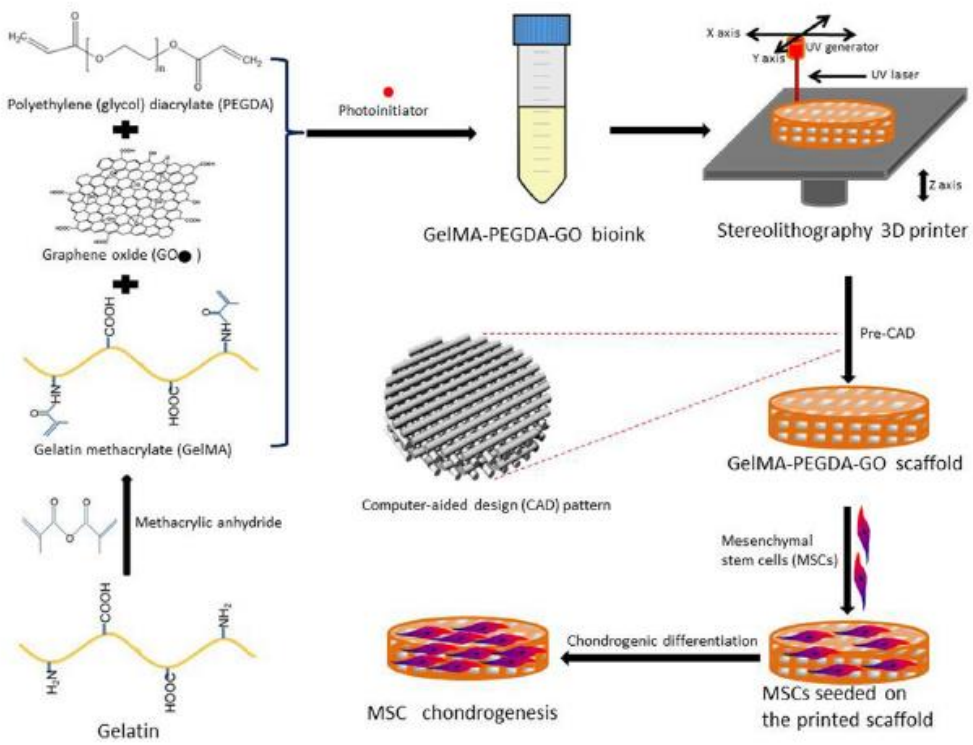

Figure 4. Illustration of 3D printed GO scaffolds for enhancing chondrogenesis of hMSCs through SLA approach [24]. Reprinted from 3D bioprinted graphene oxide-incorporated matrix for promoting chondrogenic differentiation of human bone marrow MSCs, Zhou et al., Carbon, volume 116, pp 615-624, Copyright 2017, with permission from Elsevier.

2.1.3. Droplet-based bioprinting.

Droplet-based biprinting (DBB) is a deposition method were prepolymer solution droplets are jetted onto a platform in a predefined pattern. It could be performed by the aid of piezoelectric or thermal actuators (Figure 2). The polymerization takes place after deposition by UV light, ionic, thermal or chemical crosslinking processes. The main advantages of this bioprinting technique are its low cost and the wide range of polymers that can be used. However, the viscosity range of this solution is very limited and cell density cannot be very high [12].

In addition, the bioprinting process can make a negative impact on cellular viability. Regarding to this and in order to understand better the process that can affect them, Hendriks et al. have developed an analytical model with which they can relate the cell survival to the cell membrane elongation and this last one, with the size and speed of the droplet, as well as, substrates characteristics [47]. Other interesting work is the one carried out by Graham et al., where they developed high-resolution 3D geometries by DBB, which consisted of the 3D printing of aqueous droplets containing human embryonic kidney (HEK) cells and ovine MSCs (oMSCs). These platforms included arborized cell junctions and osteochondral interfaces, exhibiting high viability. In addition, oMSCs showed a chondrogenic differentiation to cartilage-like structures after five weeks of culture [48].

2.2. Acellular Bioprinting techniques

Acellular bioprinting covers the generation of nonliving material constructs based on the pattern and assembly of materials and the successively cell post-printing seeding [3]. This strategy offers several advantages over printed cellular constructs such as higher resolution and greater shape complexity due to the manufacturing conditions in which is avoided the printing of either cells or heat-sensitive biological cues [49]. Acellular tissue scaffolds, alone or in combination with cellular techniques, have shown promising results for bone (BTE) and cartilage TE (CTE).

2.2.1. Fused deposition modeling (FDM)

FDM, also known as fused filament fabrication (FFF), is based on the extrusion through a computer-guided nozzle of a melting or semimolten thermoplastic filaments which are finally deposited onto a platform where its solidification takes place in a layer-by-layer fashion [23]. Thus, this printing technique, which later helps in the development of other bioprinting techniques, concretely extrusion based bioprinting [3], has been widely applied in the synthesis of acellular porous scaffolds for osteochondral TE due to the fact that the final construct provides a mechanical properties in a closer magnitude to articular cartilage and cancellous bone [50-52]. Strengths such as its rapid printing capability, the ability to obtain large construct with good mechanical integrity, easy scalability, and the no need of solvent and support structure have made this technique widely explored, especially for bone tissue. However, several disadvantages should be mentioned such as the reduce

number of filament materials that can be used, or the high temperature required to melt the filament which limits the printability with cells or temperature sensitive biological cues. In addition, it is very complicated the fabrication of constructs with small pore size while maintaining the porosity (100 μm) [53-55] .Thermoplastic polymers such as PCL, poly-lactic acid (PLA) and poly(lactic-co-glycolic acid) (PLGA) [52, 56, 57], which are the most common biodegradable synthetic polymers used in this manufacturing process, are the main responsible for this mechanical properties, especially in the case of PCL [55].

The replacement of the hot rollers system of FDM by a pressurized syringe with a thermostatically controlled heating jacket, defined as extrusion printing, has increased the number of synthetic materials used for 3D biofabrication [58]. For example, Woodfield et. al. has shown the success bioprinting of an amphiphilic biodegradable poly(ether ester) multiblock co-polymers as carrier materials for articular cartilage repair based on hydrophilic poly(ethylene glycol)-terephthalate (PEGT) and hydrophobic poly(butylene terephthalate) (PBT) (PEGT/PBT). Furthermore, constructs with a gradient in pore-size trying to mimic the complex zonal structure of cartilage were designed showing an efficiency inhomogeneous chondrocyte distribution but no differences in cartilage-like tissue formation related to cell density were observed [58]. More recently, Schuurman et. al have demonstrated the production of highly cartilage-like tissue abundance by improving the efficiency of cell seeding by distributing the cells along the PEGT/PBT scaffolds in form of pellets. However, additional options should be explored in order to generate *de novo* cartilage zonally organized [59].

The presence of nanoscale features in the constructs plays an important role in the generation of TE by affecting cell attachment, proliferation and cytoskeletal assembly. However, FDM, as well as other additive manufacturing (AM) techniques, have not fulfilled this biomimetic nano-resolution. In this sense and in order to overcome this limitation, recent strategies have been proposed for the post-fabrication functionalization with techniques such as layer-by-layer deposition (LbL) [60], plasma deposition [61], and the attachment based on mussel-inspired materials [62]. These strategies include not only the change of topography surface, also the incorporation of some thermal labile

biological cues which should be incorporated afterwards. Regarding to this, dexamethasone ,which is an osteoinductive drug, has been incorporated in 3D PCL/poloxamer scaffold during FDM without affecting its properties [63]. However, some labile compounds require their incorporation using the post-fabrication treatment mentioned before or being printed by other bioprinting techniques. Examples of the last one are described in section 3.3

2.2.2. Melt electrospinning writing.

Melt-electrospinning writing (MEW) is an emerging manufacturing approach wherein major principles of melt extrusion-based AM and electrospinning are combined. A melt polymer is extruded through a nozzle and beginning electrically charged due to the application of a high voltage between the nozzle tip and the collected platform where fibers are deposited upon each other [64]. The main difference in comparison with electrospinning is the lack of organic solvent as in MEW. This fact, allows to improve cell viability and the obtaining of really well orientated fibers by avoiding both their mechanical and electrical coiling [65]. On the other hand, this fibrous construct can be based on fibers with diameters down to 1 μm [66, 67], far away from the >200 μm provided by FDM manufacture technique [65]. All these aspects provide a really well organized network construct that can be built to millimeters thickness with a convenience pore size for allowing the cell invasion and vascularization of *de novo* tissue [65, 68]. The potential of this technique has been recently published for the reinforcement of soft hydrogel matrices because it is well known that the actual TE scaffolds based on hydrogels are unable to reach the stiffness and therefore the biological requirements to promote the neo-tissue. Concretely, electrospun PCL fibers obtained by MEW are infused with GelMA providing a scaffolds with mechanical properties in the range of articular cartilage [66]. More recently, and following the same strategy, constructs based on highly negatively charged star-shaped poly(ethylene glycol)/heparin hydrogel (sPEG/Hep) reinforced with medical grade PCL (mPCL) fibers by MEW were also obtained for articulate CTE. Despite the fibers provide an outstanding increase in the mechanical properties such as anisotropy, viscoelasticity and so on, the system does not met expectation under simulated dynamic load-bearing conditions, showing the necessity to explore different composite materials soft hydrogels-reinforcing fibers [69]. In this sense, it is interesting to mention the importance of trying to mimic the natural fiber structure in natural soft

tissue which is mainly based on collagen. Thus, Bas et al. has compared the behavior of soft network composites reinforced with either stretchable curvy or straight mPCL fibers presenting the curvy fibers the most similar behavior to natural soft tissue [70].

2.2.3. Selective laser sintering (SLS)

SLS, which was developed at the University of Texas [71], is an AM technique where a construct is obtained by sequential deposition of biopolymers, bioceramics or biocomposites powders which are spread in the bed with a roller following by their fusion via the increase in temperature coming from a computer controlled high-power carbon dioxide laser. Thus, a first thin layer (100-200 nm) is formed and the process is repeated layer-by-layer. Features of the powder such as particle size and shape can affect the SLS process [72]. In comparison with FDM, it might be ease to incorporate composite materials such as polymers-bioceramics due to there is not a requirement of being in filament form [73]. Other advantages are the high precision, the no need of solvent or porogens and the manufacturing of mimetic scaffolds with complicated geometries [74]. Therefore, SLS has found its potential application for BTE and more concretely in bone complex structure and intricate shapes such as maxillofacial and craniofacial [75]. Materials that do not decompose under the laser beam [73, 74] can be used for SLS. Thereby, apart from the metallic devices which are the most common one fabricated by SLS, it has also been explored for BTE using biodegradable polymers such as PCL [74], PLA [76], and polyvinil alcohol (PVA) [77], polymer-ceramics composites such as nano-HAp-PCL [78], aliphatic polycarbonate-HAp [79], PLA-HAp [80], PLA-carbonated HAp microsphere [24], calcium phosphate (Ca-P)/poly(hydroxybutyrate-co-hydroxyvalerate (PHBV) [75], polyamide-HAp [81], GO reinforced PVA [82], PLA-(Ca-P) [83], and PLGA/HAp and beta tricalcium phosphate (β-TCP) [84]. Nevertheless, this technique has hardly been applied for CTE but it is worth to mention the modification of SLS defined as microsphere-based SLS technique [85], where the powder used has a spherical shape in the micro scale. This version has led to the subsequent application in the manufacturing of scaffolds that mimic the complex multiple tissue structure of osteochondral defects (subchondral bone, intermediate calcified cartilage and the superficial cartilage region) [28, 86]. Pointedly, an approach trying to obtain HAp gradient scaffolds has been built by sintering PCL and PCL-HAp microparticles by SLS. The potential of SLS in the regeneration of osteochondral tissue

was showed *in vivo* experiments in a rabbit model by forming new tissue with both articular cartilage and subchondral bone regions [87].

2.2.4. Cellular/acellular bioprinting techniques

Cellular/acellular bioprinting techniques arise for the need to overcome the actual limitation of both main types of bioinks, natural and synthetic polymers. Hydrogel-based bioprinting constructs are restricted in terms of mechanical strength especially when their applications rely on the treatment of load-bearing tissue such as osteocondral tissue. On the other hand, synthetic polymers present limited cell affinity due to the lack of surface cell recognition sites [88, 89]. Furthermore, a common disadvantage for both of them is the inefficiency of *in vivo* hydrolytic and enzymatic degradation which should match the speed of tissue in-growth. For example, PCL presents a very low degradation rate (1.5 to 2 years) [90] while natural polymers such as chitosan shown a variable enzymatic degradation depending of the host response [91].

At this point, both the concept of substrate support and sacrificial templates are introduced due to the important role that they play in these hybrid bioprinting strategies. Sacrificial templates are usually synthetic polymers that are used during the manufacturing process of hydrogel-based bioink to provide to each layer with the requirement mechanical properties during the layer-by-layer deposition and they are removed in a second step [1]. Alternatively, they have found a great application when trying to obtain vascularized tissue such as BTE because the vascular channels in the scaffolds are printing with these sacrificial materials and subsequently removed [1, 3]. On the other hand, substrate support includes the pre-printing of templates that are not removed after hydrogel addition. Thus, the hybrid system can encompass the advantages of both systems, the good mechanical properties of the thermoplastic polymers and the good cells adhesion of natural polymers [92]. Examples of hybrid techniques for the development of these systems are described below.

Multi-head deposition system (MHDS) is a solid freeform fabrication which allows the obtaining of hybrid constructs with more than one bioinks. Concretely, those bioinks (thermoplastic polymers, natural polymers) are loaded in different thermostatically controlled syringes and parameters such as temperature, pneumatic pressure and motion are stablished independently to each syringe. Thus,

alternant layers of different bioinks either loaded or unloaded with cells, some reinforce additives and biological cues can be co-printed [93, 94]. Several works have been developed based on MHDS for bone and cartilage tissue regeneration based on the hybrid system PCL-Alginate [92, 94, 95]. Although, initial thought about MHDS techniques point to a possible reduction of cell viability when alternating thermoplastic polymer-natural polymer loaded with cells layer are deposited. Recent study based on the system PCL-Alginate loaded with primary chondrocytes isolated from chick embryos have demonstrated the high cell vitality after deposition (higher than 80%). The melting PCL cool down faster enough to minimize the effect on cell viability [95]. Furthermore, the mechanical stability conferred by the thermoplastic polymer allows the printing of hydrogels with lower crosslink density which could be beneficial for cells viability [92].

t-FDM have been used to create sacrificial templates. The template is printed by FDM and a crosslinkable material is poured onto the template where the polymerization takes places [96]. The template whether is removed or not should have biocompatible properties. An example of sacrificial template can be found in Guo et al. where a polyurethane construct was obtained with a well-define topological properties (in the range of trabecular bone) after its crosslinking polymerization on a PLA template [97]. An example where the template is not removed is described by Dong et al., where hybrid chitosan/PCL scaffolds have been described for their application in BTE. *In vitro* results of these systems when encapsulating Rabbit bone marrow mesenchymal stem cells (BMMSCs) in the chitosan matrix has shown an improvement of osteogenesis differentiation compared to PCL control scaffolds alone [98]. However, this hybrid system can fail under mechanical stresses due to an inefficiency thermoplastic-natural hydrogel interface adhesion. In this sense, a covalent attachment between both materials has been proposed for the hybrid system based on GelMA and poly(hydroxymethylglycolide-co-caprolactone)/PCL (pHMGCL/PCL) showing an increase of mechanical integrity while also keeping their ability to promote ECM formation [99]. Additional strategies to increase the mechanical properties are described in section 3.1.

3. 3D printing polymeric and composited materials for osteochondral TE

Biomaterials used for 3D printing fabrication must meet different criteria to the successful development of the scaffolds. The first requisite is having good rheological properties, which means that bioinks must be mechanically suitable for printing depending on the used bioprinting technique and provide an appropriate environment to the cells after bioprinting to promote adhesion, proliferation, and differentiation. Secondly, it is essential that the material maintains its structural integrity, in other words, high shape fidelity after the deposition process. This is directly related to printability, which refers to the relationship between the substrates and the bioinks. The brioprinting solutions should maintain vertical tension having a high contact angle with the substrate surface, and it normally depends on how fast the crosslinking process is. Finally, the bioinks must provide a biocompatible and not cytotoxic environment for cell encapsulation and deposition. However, many materials usually meet one or two requisites, being necessary the development of bioinks which present all these criteria. In this sense, materials that are printable and maintain their structure after bioprinting through a rapid crosslinking, make necessary the use of high temperature for thermal curing or UV light for photopolymerization, which compromise the encapsulation of cells in the bioinks. In addition, the most biocompatible materials do not exhibit good rheological properties for extrusion or bioprinting deposition, like for example hydrogels [1, 21, 100]. Hydrogels are very appropriated biomaterials for 3D bioprinted scaffolds for osteochondral TE due to its high biocompatibility, which make them suitable for cell encapsulation, and biodegradability properties [101]. Hydrogels are networks of 3D crosslinked polymers that able to uptake huge amount of water due to their inherent hydrophilic properties. This capability can be modulate depending on the biological tissue of interest. In addition, hydrogels pose injectability properties for minimally invasive therapies of cartilaginous-like tissues [8, 11, 101, 102]. One approach to improve mechanical properties of hydrogel bioinks is to increase the concentration of the components, obtaining highly viscous solutions with suitable printability. However, cell viability is usually decreased in high concentrated bioinks due to higher stress must be applied to the solution [6, 13, 36, 103].

Among all biomaterials explored for 3D bioprinting technology, we can distinguish between those derived from natural polymers, such as collagen, gelatin, alginate, chitosan or hyaluronic acid

(HA), or synthetic-derived polymers, such as PCL, PLGA, PLA, PEG or PEGDA. As it has been explained, synthetic materials exhibit robust mechanical properties, but poor biocompatibility and toxic degradation products. For these reasons, the use of composites is more widespread. Composites are a combination of two or more than three individual materials. They are used for enhancing mechanical strength and fabrication of more intricately designed constructs, as well as improving their long-term stability. Thanks to this combination, the suitable strength and mechanical properties of the scaffold can be modulated depending on the properties of the native tissue. [1, 8, 101]. Nanoclays and different PEGDA, for example, have been incorporated into some hydrogels solutions to control their viscosity [101]. One interesting example is the work developed by Yang et al., who synthetized a biphasic graft consisting of cartilage and subchondral bone using synthetic (PLGA) and natural (alginate) polymers and a multi-nozzle deposition system [14]. In the last years the use of decellurized extracellular matrix-derived (dECM) has been investigated for osteochondral regeneration. Decellurized ECM consists of a complex of GAGs, collagen and elastin that mimics the native tissue environment. In addition, the ECM can lead and mediate the differentiation of stem cells [101].

HA is a natural-derived polysaccharide that has been amply used in osteochondral tissue regenerative therapies. It is an anionic, GAG distributed widely throughout connective, epithelial, and neural tissues. As it is also one of the main components of the ECM, contributing significantly to cell proliferation and migration. All these properties make to HA a suitable material for 3D bioprinting application [11, 21, 38, 40, 104-106]. For example, Shaoquan et al. developed a semi-interpenetrating polymer network (semi-IPN) based on HA and hydroxyethylmethacrylate-derivatized dextran (dex-HEMA), which showed shear thinning rheology and mechanical strength. The scaffolds exhibited high porous structure, supporting the viability of encapsulated chondrocytes [107]. Ju Young and coworkers used HA with alginate and chondrocytes in Dulbecco's Modified Eagle Medium (DMEM) for chondral section, while collagen-I in DMEM constituted the osteo-section. Thus, they fabricated a two compartments scaffold for osteochondral tissue mimetic structures [105].

Gelatin is a natural-derived polysaccharide widely used in bioprinting techniques due to its thermosensitive properties which eases the development of shaped-fidelity structures [20, 21, 38, 104]. Gelatin is the denatured form of collagen, which resembles the ECM environments providing key biological motifs for cell adhesion and proliferation [102]. An example within numerous studies developed with gelatin or its methacrylate form, is the one carried out by Levato et al., who developed novel constructs consisting of GelMA and gellan gum for osteogenic and chondrogenic differentiation of MSCs [100, 108]. Gelatin has been also found to participate in some regulation ways for chondrogenesis. For example, Chameettachal et al. developed tyrosinase cross-linked silk-gelatin bioinks and demonstrated that these bioinks could upregulate the expression of hypoxia markers such as hypoxia inducible factor 1 alpha (HIF1A) which positively regulated also the expression of chondrogenic markers such as aggrecan or cartilage oligomeric matrix protein 1 (COMP1). The gelatin, particularly, showed the induction of matrix metalloproteinase 2 (MMP2) activity, which is known to promote the creation of a pericellular zone for the accumulation of growth factors and *de novo* matrix [109]. Costantini and collaborators also used GelMA for the development of 3D bioprinted constructs through a coaxial needle system. The bioinks, composed of GelMA, chondroitin sulfate amino ethyl methacrylate (CS-AEMA) and HAMA, showed the upregulated expression of chondrogenic markers, like *COL2A1* and aggrecan, as well as osteogenic markers like *COL1A1*. Thus, the presented approach demonstrated to be a suitable candidate for 3D bioprinted applications for cartilage TE field [40]. In addition, gelatin is usually combined with HA since this last one is known not only for promoting chondrogenesis in the 3D constructs but also, improving mechanical properties of the constructs during the bioprinting process [59, 106, 110].

Apart from bioink design, crosslinking mechanisms are another aspect to be optimized in order to obtain more complex constructs reducing undesirable side effects. Crosslinking procedures in bioprinting need to be secure for cell encapsulation and fast, promoting a state change from liquid (viscous) to almost solid network. The crosslinking can be physical, chemical or a combination of both, but it must maintain native cell adhesion properties of the biomaterial [8]. Chemical crosslinking processes are the most accepted due to its effectiveness, efficiency and controllability, being able to synthetize handle scaffolds with good mechanical properties and stiffness. Photopolymerization is

one of the most commonly approach used for the development of 3D bioprinted scaffolds. The chemical reaction can be triggered by the irradiation of a photoinitiator (PI) contained hydrogel at a specific wavelength. However, photocuring also shows some drawbacks due mainly to the cytotoxicity and inflammation reactions that are provoked by the generation of free radicals by UV exposure that can damage DNA and cellular components [20, 111, 112]. For this reason, activated PIs under visible or A-UV light are being extensively used during the last years [20, 113]. However, many authors have demonstrated in their studies that a proper adjustment of the UV irradiation time, intensity and wavelength, could ensure cell viability [37, 38, 104, 106, 110, 114, 115].

3.1. Incorporation of additives for enhancing mechanical properties

In order to achieve 3D bioprinted scaffolds with clinically relevant dimensions, there are two main strategies without using a bath as supporting medium. The first one consisted of the improvement of mechanical properties of the solution through a rapid crosslinking process, as it has been discussed in the previous section. The second one is the incorporation of support materials, such as PCL, which can confer space and structural integrity to low viscous bioinks [5, 39, 116, 117]. Daly and coworkers developed a study to compare the printability of different bioinks for 3D bioprinting of hyaline and fibrocartilage, using the most common hydrogels: agarose, GelMA, alginate and BioINK™, which consists of a poly(ethylene glycol) methacrylate (PEGMA) based hydrogel. The tissue staining for type II collagen revealed that alginate and agarose based bioinks supported properly the development of hyaline-like cartilage, while GelMA and BioINK™ supported the growth of fibrocartilage. They used PCL filaments to reinforce the mechanical properties of the hydrogels, being able to synthesized constructs with a compressive moduli similar to articular cartilage [22].

In another interesting work, Ahlfeld et al. used Laponite, a synthetic nanosilicate clay which is known for its drug delivery properties. They combined alginate and methylcellulose with Laponite to develop constructs with high printing fidelity as well as, controlled released of active compounds [39]. Co-printing approaches with PLGA or nanocellulose rather than PCL as supporting materials have also been boarded [118]. Nanocellulose, for example, is able to increase the viscosity of an alginate

solution bioink up to 7-fold, improving therefore the bioprintability [5]. In a work by Markstedt and collaborators, a bioink composed of nanofibrillate cellulose and alginate was developed to a patterned meniscus cartilage in a single-step bioprinting process [119, 120]. Müller et al. also developed a sulfate alginate-based bioink in combination with nanocellulose to make it printable. This mix was photocurable, arising as a good alternative for cartilage tissue regeneration applications [13]. In addition, to avoid the limitations of PCL as a reinforcing material, the increasing of porosity of the reinforcing phase can be also an alternative approach [9, 14].

3.2. Incorporation of bioactive compounds

The incorporation of active compounds such as growth factors and inorganic compounds is a very common approach to enhance cell adhesion and proliferation, as well as, differentiation to a specific tissue. Bartnikowski at al incorporated a paste of HAp to a GelMA, and GelMA-HAMA bioink for the development of a zone of calcified cartilage, as well as improvement of bioinks printability. They concluded that the incorporation of HAMA enhanced chondrogenesis and the bioprinted scaffolds showed good cell culture viability for 28 days [11]. In other interesting work, Wang et al. studied the effect of HAp in a HA-based bioink. They demonstrated that a small amount of HAp enhanced chondrogenesis and hypertrophic differentiation of adipose derived MSCs. In addition, they were able to develop stratified scaffolds with mineralized and nonmineralized layers (HA-HAp based and HA-based) [121]. In other work, Zhou and coworkers incorporated GO to their gelatin-based 3D bioprinted scaffolds to promote chondrogenic differentiation, demonstrating that multifunctional carbon-based nanomaterials can be a suitable additive for osteochondral TE approaches [24].

Traditionally, several growth factors including transforming growth factors (TGFs), insulin-like growth factors (IGFs) and bone morphogenetic protein (BMPs) have been incorporated to osteochondral TE scaffolds to promote chondrogenic or osteogenic stem cells differentiation as it has been reviewed recently [122]. Similar approach has been also used in AM scaffolds. Until now, TGF-β has been incorporated either as directly to the cell culture media [41, 123, 124] or by its physical encapsulation in the hydrogel [94, 125, 126]. An example of TGF-β physical encapsulation

has been reported by Kundu et al. where an alginate/TGF-β/BMMSCs printed scaffold reinforced with PCL has been manufactured by MHDS. Scaffolds loaded with TGF-β produced higher GAGs content after 4 weeks compared to the unloaded ones [94]. However, recent studies focus on silk-gelatin constructs incubated with TGF-β1 has shown the hypertrophy instead of articular cartilage MSCs differentiation. This evidence has led to an increasing need to find new strategies which could avoid the hypertrophy differentiation. In this sense, the over-expression of nuclear receptor subfamily 2 group F member 2 (NR2F2) in MSCs was promoted previous to scaffold cell implantation. This overexpression has provided the generation of abundant cartilage matrix [127]. Other strategy has been focus on the 3D bioprinting encapsulation of bioactive drug such asY27632, ([1R,4r)-4-(R)-1-aminoethyl)-N-(pyridin-4-yl)] cyclohexanecarboxamide (Y) which has been shown to reduce the hypertrophic market collagen X (Col X) in comparison with TGF-α when MSCs were seeded on polyurethane (PU)/HA constructs [126]. BMPs is another growth factor widely applied for promoting osteogenic differentiation. In a recent work, the surface of PLA constructs has been modified by the assembled of multilayer nanocoating based on gelatin (Gel) and polylysine (PLL) finally crosslinked with genipin (GnP). An increase cell adhesion of both human umbilical vein endothelial cells (HUVECs) and hMSCs respect to the control (unmodified PLA construct was reported. More interesting, this approach allowed the smart release of growth factors such as recombinant human bone morphogenetic protein (rhBMP-2) and recombinant human vascular endothelial (rhVEGF) by promoting osteogenic differentiation of hMSCs and .proliferation and differentiation of HUVECs Thus, it has been possible the generation of vascularized bone grafts [60]. In order to avoid undesirable growth factors degradation when adding directly to the cell culture media, Dong et al. has developed hybrids chitosan/PCL scaffolds loaded with BMP-2. A sustained *in vitro* release of BMP-2 promoted BMMSCs osteogenic differentiation [98].

4. Conclusion and future perspectives

In general, the arrival and development of 3D bioprinting has made a huge impact on tissue regeneration field. Its implementation in osteochondral TE field is much appropriated due to the particular heterogeneity and anisotropy that this tissue exhibits. 3D bioprinting allows fabricating

very intricate heterogeneous 3D constructs by an accurate spatiotemporal positioning of cells and biomolecules controlling the structure, size, shape, pore and orientation of each component with micrometer precision. In addition, the porosity and gradient created in the scaffolds by 3D bioprinting makes possible a good cell-cell communication and vascularization of the construct, which is essential for an appropriated distribution of oxygen and nutrients, and thus, for long-term stability.

However, despite all the advantages that this technology has provided to the field, some challenging aspects have to be solved before the translation of the technology to the clinic occurs. It cannot be denied that 3D bioprinting will be responsible for a new generation of personalized therapeutic approach, but to go to the clinic the materials and technology should be meticulously chosen. Currently, the most daunting challenges that restrict the translation of this technology are the capacity for large scale fabrication, sterilization process, stringent quality control for 3D scaffolds for human trials and the affordability of the medical expenditure. Although numerous preclinical studies are being developed, clinical trials are very limited due to regulatory issues, differences in patient responses, as well as implantation constraints. In addition, the necessity of skilled experts and cost-efficacy of the fabrication devices is still a bottleneck for the translation of the technology.

In conclusion, the emergence of printing technologies for the construction of mimetic scaffolds for the regeneration of osteochondral tissue seems to be a significant milestone. As all novel technologies, 3D bioprinting should face to regulatory hurdles for clinical translation that must be solved in the following years, as these technologies provide real benefits and advantages to really complicated osteochondral diseases and lesions.

5. References

[1] C. Mandrycky, Z. Wang, K. Kim, D.H. Kim, 3D bioprinting for engineering complex tissues, Biotechnol Adv 34(4) (2016) 422-434.

[2] S.V. Murphy, A. Atala, 3D bioprinting of tissues and organs, Nature biotechnology 32(8) (2014) 773-85.

[3] H. Cui, M. Nowicki, J.P. Fisher, L.G. Zhang, 3D Bioprinting for Organ Regeneration, Advanced Healthcare Materials 6(1) (2017) 1601118.

[4] A. Arslan-Yildiz, R.E. Assal, P. Chen, S. Guven, F. Inci, U. Demirci, Towards artificial tissue models: past, present, and future of 3D bioprinting, Biofabrication 8(1) (2016) 014103.

[5] G. O'Connell, J. Garcia, J. Amir, 3D Bioprinting: New Directions in Articular Cartilage Tissue Engineering, ACS Biomaterials Science & Engineering (2017).

[6] M. Muller, J. Becher, M. Schnabelrauch, M. Zenobi-Wong, Nanostructured Pluronic hydrogels as bioinks for 3D bioprinting, Biofabrication 7(3) (2015) 035006.

[7] I.T. Ozbolat, Bioprinting of osteochondral tissues: A perspective on current gaps and future trends, International Journal of Bioprinting 3(2) (2017).

[8] J. Radhakrishnan, A. Subramanian, U.M. Krishnan, S. Sethuraman, Injectable and 3D Bioprinted Polysaccharide Hydrogels: From Cartilage to Osteochondral Tissue Engineering, Biomacromolecules 18(1) (2017) 1-26.

[9] A.C. Daly, F.E. Freeman, T. Gonzalez-Fernandez, S.E. Critchley, J. Nulty, D.J. Kelly, 3D Bioprinting for Cartilage and Osteochondral Tissue Engineering, Adv Healthc Mater (2017).

[10] N.E. Fedorovich, W. Schuurman, H.M. Wijnberg, H.J. Prins, P.R. van Weeren, J. Malda, J. Alblas, W.J. Dhert, Biofabrication of osteochondral tissue equivalents by printing topologically defined, cell-laden hydrogel scaffolds, Tissue Eng Part C Methods 18(1) (2012) 33-44.

[11] M. Bartnikowski, A.R. Akkineni, M. Gelinsky, M.A. Woodruff, T.J. Klein, A Hydrogel Model Incorporating 3D-Plotted Hydroxyapatite for Osteochondral Tissue Engineering, Materials (Basel) 9(4) (2016).

[12] R.D. Pedde, B. Mirani, A. Navaei, T. Styan, S. Wong, M. Mehrali, A. Thakur, N.K. Mohtaram, A. Bayati, A. Dolatshahi-Pirouz, M. Nikkhah, S.M. Willerth, M. Akbari, Emerging Biofabrication Strategies for Engineering Complex Tissue Constructs, Adv Mater 29(19) (2017).

[13] M. Muller, E. Ozturk, O. Arlov, P. Gatenholm, M. Zenobi-Wong, Alginate Sulfate-Nanocellulose Bioinks for Cartilage Bioprinting Applications, Ann Biomed Eng 45(1) (2017) 210-223.

[14] S.S. Yang, W.H. Choi, B.R. Song, H. Jin, S.J. Lee, S.H. Lee, J. Lee, Y.J. Kim, S.R. Park, S.-H. Park, B.-H. Min, Fabrication of an osteochondral graft with using a solid freeform fabrication system, Tissue Engineering and Regenerative Medicine 12(4) (2015) 239-248.

[15] H.W. Kang, S.J. Lee, I.K. Ko, C. Kengla, J.J. Yoo, A. Atala, A 3D bioprinting system to produce human-scale tissue constructs with structural integrity, Nature biotechnology 34(3) (2016) 312-9.

[16] S. Ahadian, S. Yamada, J. Ramon-Azcon, M. Estili, X. Liang, K. Nakajima, H. Shiku, A. Khademhosseini, T. Matsue, Hybrid hydrogel-aligned carbon nanotube scaffolds to enhance cardiac differentiation of embryoid bodies, Acta biomaterialia 31 (2016) 134-143.

[17] K. Hölzl, S. Lin, L. Tytgat, S. Van Vlierberghe, L. Gu, A. Ovsianikov, Bioink properties before, during and after 3D bioprinting, Biofabrication 8(3) (2016) 032002.

[18] S. Ji, M. Guvendiren, Recent Advances in Bioink Design for 3D Bioprinting of Tissues and Organs, Frontiers in Bioengineering and Biotechnology 5 (2017).

[19] I. Donderwinkel, J.C.M. van Hest, N.R. Cameron, Bio-inks for 3D bioprinting: recent advances and future prospects, Polym. Chem. 8(31) (2017) 4451-4471.

[20] B.J. Klotz, D. Gawlitta, A.J. Rosenberg, J. Malda, F.P. Melchels, Gelatin-Methacryloyl Hydrogels: Towards Biofabrication-Based Tissue Repair, Trends Biotechnol 34(5) (2016) 394-407.

[21] A. Skardal, J. Zhang, L. McCoard, X. Xu, S. Oottamasathien, G.D. Prestwich, Photocrosslinkable hyaluronan-gelatin hydrogels for two-step bioprinting, Tissue Eng Part A 16(8) (2010) 2675-85.

[22] A.C. Daly, S.E. Critchley, E.M. Rencsok, D.J. Kelly, A comparison of different bioinks for 3D bioprinting of fibrocartilage and hyaline cartilage, Biofabrication 8(4) (2016) 045002.

[23] G. Brunello, S. Sivolella, R. Meneghello, L. Ferroni, C. Gardin, A. Piattelli, B. Zavan, E. Bressan, Powder-based 3D printing for bone tissue engineering, Biotechnol Adv 34(5) (2016) 740-753.

[24] X. Zhou, M. Nowicki, H. Cui, W. Zhu, X. Fang, S. Miao, S.-J. Lee, M. Keidar, L.G. Zhang, 3D bioprinted graphene oxide-incorporated matrix for promoting chondrogenic differentiation of human bone marrow mesenchymal stem cells, Carbon 116 (2017) 615-624.

[25] D.B. Kolesky, K.A. Homan, M.A. Skylar-Scott, J.A. Lewis, Three-dimensional bioprinting of thick vascularized tissues, Proceedings of the National Academy of Sciences of the United States of America 113(12) (2016) 3179-84.

[26] M.J. Dalby, N. Gadegaard, R. Tare, A. Andar, M.O. Riehle, P. Herzyk, C.D. Wilkinson, R.O. Oreffo, The control of human mesenchymal cell differentiation using nanoscale symmetry and disorder, Nature materials 6(12) (2007) 997-1003.

[27] Y. Ikada, Challenges in tissue engineering, Journal of the Royal Society, Interface 3(10) (2006) 589-601.

[28] M.K. Boushell, C.T. Hung, E.B. Hunziker, E.J. Strauss, H.H. Lu, Current strategies for integrative cartilage repair, Connective Tissue Research 58(5) (2016) 393-406.

[29] T.A.E. Ahmed, M.T. Hincke, Strategies for Articular Cartilage Lesion Repair and Functional Restoration, Tissue Engineering Part B: Reviews 16(3) (2009) 305-329.

[30] M. Hospodiuk, M. Dey, D. Sosnoski, I.T. Ozbolat, The bioink: A comprehensive review on bioprintable materials, Biotechnology Advances 35(2) (2017) 217-239.

[31] Y. Yu, K.K. Moncal, J. Li, W. Peng, I. Rivero, J.A. Martin, I.T. Ozbolat, Three-dimensional bioprinting using self-assembling scalable scaffold-free "tissue strands" as a new bioink, Scientific Reports 6 (2016) 28714.

[32] I.T. Ozbolat, Scaffold-Based or Scaffold-Free Bioprinting: Competing or Complementing Approaches?, Journal of Nanotechnology in Engineering and Medicine 6(2) (2015) 024701-024701-6.

[33] I.T. Ozbolat, M. Hospodiuk, Current advances and future perspectives in extrusion-based bioprinting, Biomaterials 76 (2016) 321-343.

[34] R.F. Pereira, P.J. Bártolo, 3D bioprinting of photocrosslinkable hydrogel constructs, Journal of Applied Polymer Science 132(48) (2015) n/a-n/a.

[35] D. Tang, R.S. Tare, L.Y. Yang, D.F. Williams, K.L. Ou, R.O. Oreffo, Biofabrication of bone tissue: approaches, challenges and translation for bone regeneration, Biomaterials 83 (2016) 363-82.

[36] G. Ahn, K.H. Min, C. Kim, J.S. Lee, D. Kang, J.Y. Won, D.W. Cho, J.Y. Kim, S. Jin, W.S. Yun, J.H. Shim, Precise stacking of decellularized extracellular matrix based 3D cell-laden constructs by a 3D cell printing system equipped with heating modules, Sci Rep 7(1) (2017) 8624.

[37] S. Duchi, C. Onofrillo, C.D. O'Connell, R. Blanchard, C. Augustine, A.F. Quigley, R.M.I. Kapsa, P. Pivonka, G. Wallace, C. Di Bella, P.F.M. Choong, Handheld Co-Axial Bioprinting: Application to in situ surgical cartilage repair, Sci Rep 7(1) (2017) 5837.

[38] C.D. O'Connell, C. Di Bella, F. Thompson, C. Augustine, S. Beirne, R. Cornock, C.J. Richards, J. Chung, S. Gambhir, Z. Yue, J. Bourke, B. Zhang, A. Taylor, A. Quigley, R. Kapsa, P. Choong, G.G. Wallace, Development of the Biopen: a handheld device for surgical printing of adipose stem cells at a chondral wound site, Biofabrication 8(1) (2016) 015019.

[39] T. Ahlfeld, G. Cidonio, D. Kilian, S. Duin, A.R. Akkineni, J.I. Dawson, S. Yang, A. Lode, R.O.C. Oreffo, M. Gelinsky, Development of a clay based bioink for 3D cell printing for skeletal application, Biofabrication 9(3) (2017) 034103.

[40] M. Costantini, J. Idaszek, K. Szoke, J. Jaroszewicz, M. Dentini, A. Barbetta, J.E. Brinchmann, W. Swieszkowski, 3D bioprinting of BM-MSCs-loaded ECM biomimetic hydrogels for in vitro neocartilage formation, Biofabrication 8(3) (2016) 035002.

[41] S. Chawla, A. Kumar, P. Admane, A. Bandyopadhyay, S. Ghosh, Elucidating role of silk-gelatin bioink to recapitulate articular cartilage differentiation in 3D bioprinted constructs, Bioprinting 7 (2017) 1-13.

[42] D.J. Odde, M.J. Renn, Laser-guided direct writing for applications in biotechnology, Trends in Biotechnology 17(10) (1999) 385-389.

[43] D.J. Odde, M.J. Renn, Laser-guided direct writing of living cells, Biotechnology and Bioengineering 67(3) (2000) 312-318.

[44] N.R. Schiele, D.T. Corr, Y. Huang, N.A. Raof, Y. Xie, D.B. Chrisey, Laser-based direct-write techniques for cell printing, Biofabrication 2(3) (2010) 032001.

[45] D.M. Kingsley, A.D. Dias, D.B. Chrisey, D.T. Corr, Single-step laser-based fabrication and patterning of cell-encapsulated alginate microbeads, Biofabrication 5(4) (2013) 045006.

[46] M. Gruene, A. Deiwick, L. Koch, S. Schlie, C. Unger, N. Hofmann, I. Bernemann, B. Glasmacher, B. Chichkov, Laser printing of stem cells for biofabrication of scaffold-free autologous grafts, Tissue Eng Part C Methods 17(1) (2011) 79-87.

[47] J. Hendriks, C. Willem Visser, S. Henke, J. Leijten, D.B. Saris, C. Sun, D. Lohse, M. Karperien, Optimizing cell viability in droplet-based cell deposition, Sci Rep 5 (2015) 11304.

[48] A.D. Graham, S.N. Olof, M.J. Burke, J.P.K. Armstrong, E.A. Mikhailova, J.G. Nicholson, S.J. Box, F.G. Szele, A.W. Perriman, H. Bayley, High-Resolution Patterned Cellular Constructs by Droplet-Based 3D Printing, Sci Rep 7(1) (2017) 7004.

[49] C.M. O'Brien, B. Holmes, S. Faucett, L.G. Zhang, Three-Dimensional Printing of Nanomaterial Scaffolds for Complex Tissue Regeneration, Tissue Engineering. Part B, Reviews 21(1) (2015) 103-114.

[50] D.W. Hutmacher, J.T. Schantz, C.X.F. Lam, K.C. Tan, T.C. Lim, State of the art and future directions of scaffold-based bone engineering from a biomaterials perspective, Journal of Tissue Engineering and Regenerative Medicine 1(4) (2007) 245-260.

[51] S.S. Chen, Y.H. Falcovitz, R. Schneiderman, A. Maroudas, R.L. Sah, Depth-dependent compressive properties of normal aged human femoral head articular cartilage: relationship to fixed charge density, Osteoarthritis and Cartilage 9(6) (2001) 561-569.

[52] S.A. Goldstein, The mechanical properties of trabecular bone: Dependence on anatomic location and function, Journal of Biomechanics 20(11) (1987) 1055-1061.

[53] S. Adepu, N. Dhiman, A. Laha, C.S. Sharma, S. Ramakrishna, M. Khandelwal, Three-dimensional bioprinting for bone tissue regeneration, Current Opinion in Biomedical Engineering 2(Supplement C) (2017) 22-28.

[54] C. Mota, D. Puppi, F. Chiellini, E. Chiellini, Additive manufacturing techniques for the production of tissue engineering constructs, Journal of Tissue Engineering and Regenerative Medicine 9(3) (2015) 174-190.

[55] M.A. Woodruff, D.W. Hutmacher, The return of a forgotten polymer—Polycaprolactone in the 21st century, Progress in Polymer Science 35(10) (2010) 1217-1256.

[56] J.C.H.G. Q. Huang, D.W. Hutmacher, and E.H. Lee, In Vivo Mesenchymal Cell Recruitment by a Scaffold Loaded with Transforming Growth Factor β1 and the Potential for in Situ Chondrogenesis Tissue Engineering 8(3) (2004) 469-482.

[57] I. Zein, D.W. Hutmacher, K.C. Tan, S.H. Teoh, Fused deposition modeling of novel scaffold architectures for tissue engineering applications, Biomaterials 23(4) (2002) 1169-1185.

[58] T.B.F. Woodfield, J. Malda, J. de Wijn, F. Péters, J. Riesle, C.A. van Blitterswijk, Design of porous scaffolds for cartilage tissue engineering using a three-dimensional fiber-deposition technique, Biomaterials 25(18) (2004) 4149-4161.

[59] W. Schuurman, P.A. Levett, M.W. Pot, P.R. van Weeren, W.J.A. Dhert, D.W. Hutmacher, F.P.W. Melchels, T.J. Klein, J. Malda, Gelatin-Methacrylamide Hydrogels as Potential Biomaterials for Fabrication of Tissue-Engineered Cartilage Constructs, Macromolecular Bioscience 13(5) (2013) 551-561.

[60] H. Cui, W. Zhu, B. Holmes, L.G. Zhang, Biologically Inspired Smart Release System Based on 3D Bioprinted Perfused Scaffold for Vascularized Tissue Regeneration, Advanced Science 3(8) (2016) 1600058-n/a.

[61] M. Domingos, F. Intranuovo, A. Gloria, R. Gristina, L. Ambrosio, P.J. Bártolo, P. Favia, Improved osteoblast cell affinity on plasma-modified 3-D extruded PCL scaffolds, Acta biomaterialia 9(4) (2013) 5997-6005.

[62] S.J. Lee, D. Lee, T.R. Yoon, H.K. Kim, H.H. Jo, J.S. Park, J.H. Lee, W.D. Kim, I.K. Kwon, S.A. Park, Surface modification of 3D-printed porous scaffolds via mussel-inspired polydopamine and effective immobilization of rhBMP-2 to promote osteogenic differentiation for bone tissue engineering, Acta biomaterialia 40(Supplement C) (2016) 182-191.

[63] P.F. Costa, A.M. Puga, L. Díaz-Gomez, A. Concheiro, D.H. Busch, C. Alvarez-Lorenzo, Additive manufacturing of scaffolds with dexamethasone controlled release for enhanced bone regeneration, International Journal of Pharmaceutics 496(2) (2015) 541-550.

[64] T.D. Brown, P.D. Dalton, D.W. Hutmacher, Direct Writing By Way of Melt Electrospinning, Advanced Materials 23(47) (2011) 5651-5657.

[65] O. Bas, E.M. De-Juan-Pardo, M.P. Chhaya, F.M. Wunner, J.E. Jeon, T.J. Klein, D.W. Hutmacher, Enhancing structural integrity of hydrogels by using highly organised melt electrospun fibre constructs, European Polymer Journal 72(Supplement C) (2015) 451-463.

[66] J. Visser, F.P.W. Melchels, J.E. Jeon, E.M. van Bussel, L.S. Kimpton, H.M. Byrne, W.J.A. Dhert, P.D. Dalton, D.W. Hutmacher, J. Malda, Reinforcement of hydrogels using three-dimensionally printed microfibres, 6 (2015) 6933.

[67] T.J. Gernot Hochleitner, Toby D Brown, Kathrin Hahn, Claus Moseke, Franz Jakob, Paul D Dalton and Jürgen Groll, Additive manufacturing of scaffolds with sub-micron filaments via melt electrospinning writing, Biofabrication 7(3) (2015).

[68] T.D. Brown, F. Edin, N. Detta, A.D. Skelton, D.W. Hutmacher, P.D. Dalton, Melt electrospinning of poly(ε-caprolactone) scaffolds: Phenomenological observations associated with collection and direct writing, Materials Science and Engineering: C 45(Supplement C) (2014) 698-708.

[69] B. Onur, M.D.-J.-P. Elena, M. Christoph, D.A. Davide, G.B. Jeremy, J.B. Laura, R.M. Wellard, K. Stefan, R. Ernst, W. Carsten, J.K. Travis, C. Isabelle, W.H. Dietmar, Biofabricated soft network composites for cartilage tissue engineering, Biofabrication 9(2) (2017) 025014.

[70] O. Bas, D. D'Angella, J.G. Baldwin, N.J. Castro, F.M. Wunner, N.T. Saidy, S. Kollmannsberger, A. Reali, E. Rank, E.M. De-Juan-Pardo, D.W. Hutmacher, An Integrated Design, Material, and Fabrication Platform for Engineering Biomechanically and Biologically Functional Soft Tissues, ACS Applied Materials & Interfaces 9(35) (2017) 29430-29437.

[71] C.R. Deckard, Apparatus for producing parts by selective sintering, Google Patents, 1997.

[72] M. Schmid, A. Amado, K. Wegener, Polymer powders for selective laser sintering (SLS), AIP Conference Proceedings 1664(1) (2015) 160009.

[73] Y. Almoatazbellah, J.H. Scott, D.D. Paul, Additive manufacturing of polymer melts for implantable medical devices and scaffolds, Biofabrication 9(1) (2017) 012002.

[74] J.M. Williams, A. Adewunmi, R.M. Schek, C.L. Flanagan, P.H. Krebsbach, S.E. Feinberg, S.J. Hollister, S. Das, Bone tissue engineering using polycaprolactone scaffolds fabricated via selective laser sintering, Biomaterials 26(23) (2005) 4817-4827.

[75] B. Duan, M. Wang, W.Y. Zhou, W.L. Cheung, Z.Y. Li, W.W. Lu, Three-dimensional nanocomposite scaffolds fabricated via selective laser sintering for bone tissue engineering, Acta biomaterialia 6(12) (2010) 4495-4505.

[76] J.M. Kanczler, S.-H. Mirmalek-Sani, N.A. Hanley, A.L. Ivanov, J.J.A. Barry, C. Upton, K.M. Shakesheff, S.M. Howdle, E.N. Antonov, V.N. Bagratashvili, V.K. Popov, R.O.C. Oreffo, Biocompatibility and osteogenic potential of human fetal femur-derived cells on surface selective laser sintered scaffolds, Acta biomaterialia 5(6) (2009) 2063-2071.

[77] S. Cijun, M. Zhongzheng, L. Haibo, N. Yi, H. Huanlong, P. Shuping, Fabrication of porous polyvinyl alcohol scaffold for bone tissue engineering via selective laser sintering, Biofabrication 5(1) (2013) 015014.

[78] Y. Xia, P. Zhou, X. Cheng, Y. Xie, C. Liang, C. Li, S. Xu, Selective laser sintering fabrication of nano-hydroxyapatite/poly-ε-caprolactone scaffolds for bone tissue engineering applications, International Journal of Nanomedicine 8 (2013) 4197-4213.

[79] S. XiaoHui, L. Wei, S. PingHui, S. QingYong, W. QingSong, S. YuSheng, L. Kai, L. WenGuang, Selective laser sintering of aliphatic-polycarbonate/hydroxyapatite composite scaffolds for medical applications, The International Journal of Advanced Manufacturing Technology 81(1) (2015) 15-25.

[80] D. Kuznetsova, N. Prodanets, S. Rodimova, E. Antonov, A. Meleshina, P. Timashev, E. Zagaynova, Study of the involvement of allogeneic MSCs in bone formation using the model of transgenic mice, Cell Adhesion & Migration 11(3) (2017) 233-244.

[81] S. M.M., H. L., D. P.M., Z. Y., T. K.E., H. R.A., The effects and interactions of fabrication parameters on the properties of selective laser sintered hydroxyapatite polyamide composite biomaterials, Rapid Prototyping Journal 18(1) (2012) 16-27.

[82] C. Shuai, P. Feng, C. Gao, X. Shuai, T. Xiao, S. Peng, Graphene oxide reinforced poly(vinyl alcohol): nanocomposite scaffolds for tissue engineering applications, RSC Advances 5(32) (2015) 25416-25423.

[83] W. Chong, Z. Qilong, W. Min, Cryogenic 3D printing for producing hierarchical porous and rhBMP-2-loaded Ca-P/PLLA nanocomposite scaffolds for bone tissue engineering, Biofabrication 9(2) (2017) 025031.

[84] W.Y. Zhou, S.H. Lee, M. Wang, W.L. Cheung, W.Y. Ip, Selective laser sintering of porous tissue engineering scaffolds from poly(l-lactide)/carbonated hydroxyapatite nanocomposite microspheres, Journal of Materials Science: Materials in Medicine 19(7) (2008) 2535-2540.

[85] Y. Du, H. Liu, J. Shuang, J. Wang, J. Ma, S. Zhang, Microsphere-based selective laser sintering for building macroporous bone scaffolds with controlled microstructure and excellent biocompatibility, Colloids and Surfaces B: Biointerfaces 135(Supplement C) (2015) 81-89.

[86] C. Di Bella, A. Fosang, D.M. Donati, G.G. Wallace, P.F.M. Choong, 3D Bioprinting of Cartilage for Orthopedic Surgeons: Reading between the Lines, Frontiers in Surgery 2 (2015) 39.

[87] Y. Du, H. Liu, Q. Yang, S. Wang, J. Wang, J. Ma, I. Noh, A.G. Mikos, S. Zhang, Selective laser sintering scaffold with hierarchical architecture and gradient composition for osteochondral repair in rabbits, Biomaterials 137(Supplement C) (2017) 37-48.

[88] Q. Cai, Y. Wan, J. Bei, S. Wang, Synthesis and characterization of biodegradable polylactide-grafted dextran and its application as compatilizer, Biomaterials 24(20) (2003) 3555-3562.

[89] G. Ciardelli, V. Chiono, G. Vozzi, M. Pracella, A. Ahluwalia, N. Barbani, C. Cristallini, P. Giusti, Blends of Poly-(ε-caprolactone) and Polysaccharides in Tissue Engineering Applications, Biomacromolecules 6(4) (2005) 1961-1976.

[90] H. Sun, L. Mei, C. Song, X. Cui, P. Wang, The in vivo degradation, absorption and excretion of PCL-based implant, Biomaterials 27(9) (2006) 1735-1740.

[91] C. Chung, J.A. Burdick, Engineering Cartilage Tissue, Advanced drug delivery reviews 60(2) (2008) 243-262.

[92] W. Schuurman, V. Khristov, M.W. Pot, P.R.v. Weeren, W.J.A. Dhert, J. Malda, Bioprinting of hybrid tissue constructs with tailorable mechanical properties, Biofabrication 3(2) (2011) 021001.

[93] J.-H. Shim, J.-B. Huh, J.Y. Park, Y.-C. Jeon, S.S. Kang, J.Y. Kim, J.-W. Rhie, D.-W. Cho, Fabrication of Blended Polycaprolactone/Poly (Lactic-Co-Glycolic Acid)/β-Tricalcium Phosphate Thin Membrane Using Solid Freeform Fabrication Technology for Guided Bone Regeneration, Tissue Engineering Part A 19(3-4) (2012) 317-328.

[94] J. Kundu, J.-H. Shim, J. Jang, S.-W. Kim, D.-W. Cho, An additive manufacturing-based PCL–alginate–chondrocyte bioprinted scaffold for cartilage tissue engineering, Journal of Tissue Engineering and Regenerative Medicine 9(11) (2015) 1286-1297.

[95] Z. Izadifar, T. Chang, W. Kulyk, X. Chen, B.F. Eames, Analyzing Biological Performance of 3D-Printed, Cell-Impregnated Hybrid Constructs for Cartilage Tissue Engineering, Tissue Engineering Part C: Methods 22(3) (2015) 173-188.

[96] A.N. Margaret, J.C. Nathan, W.P. Michael, Z. Lijie Grace, 3D printing of novel osteochondral scaffolds with graded microstructure, Nanotechnology 27(41) (2016) 414001.

[97] R. Guo, S. Lu, J.M. Page, A.R. Merkel, S. Basu, J.A. Sterling, S.A. Guelcher, Fabrication of 3D Scaffolds with Precisely Controlled Substrate Modulus and Pore Size by Templated-Fused Deposition Modeling to Direct Osteogenic Differentiation, Advanced Healthcare Materials 4(12) (2015) 1826-1832.

[98] L. Dong, S.-J. Wang, X.-R. Zhao, Y.-F. Zhu, J.-K. Yu, 3D- Printed Poly(ε-caprolactone) Scaffold Integrated with Cell-laden Chitosan Hydrogels for Bone Tissue Engineering, Scientific Reports 7(1) (2017) 13412.

[99] K.W.M. Boere, J. Visser, H. Seyednejad, S. Rahimian, D. Gawlitta, M.J. van Steenbergen, W.J.A. Dhert, W.E. Hennink, T. Vermonden, J. Malda, Covalent attachment of a three-dimensionally printed thermoplast to a gelatin hydrogel for mechanically enhanced cartilage constructs, Acta biomaterialia 10(6) (2014) 2602-2611.

[100] R. Levato, W.R. Webb, I.A. Otto, A. Mensinga, Y. Zhang, M. van Rijen, R. van Weeren, I.M. Khan, J. Malda, The bio in the ink: cartilage regeneration with bioprintable hydrogels and articular cartilage-derived progenitor cells, Acta biomaterialia 61 (2017) 41-53.

[101] J.E. Kim, S.H. Kim, Y. Jung, Current status of three-dimensional printing inks for soft tissue regeneration, Tissue Engineering and Regenerative Medicine 13(6) (2016) 636-646.

[102] Y.J. Chuah, Y. Peck, J.E. Lau, H.T. Hee, D.A. Wang, Hydrogel based cartilaginous tissue regeneration: recent insights and technologies, Biomater Sci 5(4) (2017) 613-631.

[103] X. Zhai, Y. Ma, C. Hou, F. Gao, Y. Zhang, C. Ruan, H. Pan, W.W. Lu, W. Liu, 3D-Printed High Strength Bioactive Supramolecular Polymer/Clay Nanocomposite Hydrogel Scaffold for Bone Regeneration, ACS Biomaterials Science & Engineering 3(6) (2017) 1109-1118.

[104] G. Camci-Unal, D. Cuttica, N. Annabi, D. Demarchi, A. Khademhosseini, Synthesis and characterization of hybrid hyaluronic acid-gelatin hydrogels, Biomacromolecules 14(4) (2013) 1085-92.

[105] P. Ju Young, C. Jong-Cheol, S. Jin-Hyung, L. Jung-Seob, P. Hyoungjun, K. Sung Won, D. Junsang, C. Dong-Woo, A comparative study on collagen type I and hyaluronic acid dependent cell behavior for osteochondral tissue bioprinting, Biofabrication 6(3) (2014) 035004.

[106] P.A. Levett, F.P. Melchels, K. Schrobback, D.W. Hutmacher, J. Malda, T.J. Klein, A biomimetic extracellular matrix for cartilage tissue engineering centered on photocurable gelatin, hyaluronic acid and chondroitin sulfate, Acta biomaterialia 10(1) (2014) 214-23.

[107] B. Shaoquan, M. He, S. Junhui, H. Cai, Y. Sun, J. Liang, Y. Fan, X. Zhang, The self-crosslinking smart hyaluronic acid hydrogels as injectable three-dimensional scaffolds for cells culture, 2016.

[108] L. Riccardo, V. Jetze, A.P. Josep, E. Elisabeth, M. Jos, A.M.-T. Miguel, Biofabrication of tissue constructs by 3D bioprinting of cell-laden microcarriers, Biofabrication 6(3) (2014) 035020.

[109] S. Chameettachal, S. Midha, S. Ghosh, Regulation of Chondrogenesis and Hypertrophy in Silk Fibroin-Gelatin-Based 3D Bioprinted Constructs, ACS Biomaterials Science & Engineering 2(9) (2016) 1450-1463.

[110] P.A. Levett, F.P. Melchels, K. Schrobback, D.W. Hutmacher, J. Malda, T.J. Klein, Chondrocyte redifferentiation and construct mechanical property development in single-component photocrosslinkable hydrogels, J Biomed Mater Res A 102(8) (2014) 2544-53.

[111] N. Annabi, A. Tamayol, J.A. Uquillas, M. Akbari, L.E. Bertassoni, C. Cha, G. Camci-Unal, M.R. Dokmeci, N.A. Peppas, A. Khademhosseini, 25th Anniversary Article: Rational Design and Applications of Hydrogels in Regenerative Medicine, Advanced Materials 26(1) (2014) 85-124.

[112] W.F. Hynes, N.J. Doty, T.I. Zarembinski, M.P. Schwartz, M.W. Toepke, W.L. Murphy, S.K. Atzet, R. Clark, J.A. Melendez, N.C. Cady, Micropatterning of 3D Microenvironments for Living Biosensor Applications, Biosensors (Basel) 4(1) (2014) 28-44.

[113] R.F. Pereira, P.J. Bartolo, 3D bioprinting of photocrosslinkable hydrogel constructs, Journal of Applied Polymer Science 132(48) (2015).

[114] B.V. Slaughter, S.S. Khurshid, O.Z. Fisher, A. Khademhosseini, N.A. Peppas, Hydrogels in regenerative medicine, Adv Mater 21(32-33) (2009) 3307-29.

[115] B. Duan, E. Kapetanovic, L.A. Hockaday, J.T. Butcher, Three-dimensional printed trileaflet valve conduits using biological hydrogels and human valve interstitial cells, Acta biomaterialia 10(5) (2014) 1836-46.

[116] B.S. Kim, J. Jang, S. Chae, G. Gao, J.S. Kong, M. Ahn, D.W. Cho, Three-dimensional bioprinting of cell-laden constructs with polycaprolactone protective layers for using various thermoplastic polymers, Biofabrication 8(3) (2016) 035013.

[117] E. Axpe, M.L. Oyen, Applications of Alginate-Based Bioinks in 3D Bioprinting, Int J Mol Sci 17(12) (2016).

[118] D. Nguyen, D.A. Hagg, A. Forsman, J. Ekholm, P. Nimkingratana, C. Brantsing, T. Kalogeropoulos, S. Zaunz, S. Concaro, M. Brittberg, A. Lindahl, P. Gatenholm, A. Enejder, S. Simonsson, Cartilage Tissue Engineering by the 3D Bioprinting of iPS Cells in a Nanocellulose/Alginate Bioink, Sci Rep 7(1) (2017) 658.

[119] K. Markstedt, A. Mantas, I. Tournier, H. Martínez Ávila, D. Hägg, P. Gatenholm, 3D Bioprinting Human Chondrocytes with Nanocellulose–Alginate Bioink for Cartilage Tissue Engineering Applications, Biomacromolecules 16(5) (2015) 1489-1496.

[120] S.E. Bakarich, R. Gorkin, M. in het Panhuis, G.M. Spinks, Three-Dimensional Printing Fiber Reinforced Hydrogel Composites, ACS Applied Materials & Interfaces 6(18) (2014) 15998-16006.

[121] Y. Wang, S. Wu, M.A. Kuss, P.N. Streubel, B. Duan, Effects of Hydroxyapatite and Hypoxia on Chondrogenesis and Hypertrophy in 3D Bioprinted ADMSC Laden Constructs, ACS Biomaterials Science & Engineering 3(5) (2017) 826-835.

[122] J. Yang, Y.S. Zhang, K. Yue, A. Khademhosseini, Cell-laden hydrogels for osteochondral and cartilage tissue engineering, Acta biomaterialia 57(Supplement C) (2017) 1-25.

[123] X. Cui, K. Breitenkamp, M. Lotz, D. D'Lima, Synergistic action of fibroblast growth factor-2 and transforming growth factor-beta1 enhances bioprinted human neocartilage formation, Biotechnology and Bioengineering 109(9) (2012) 2357-2368.

[124] M. Kesti, C. Eberhardt, G. Pagliccia, D. Kenkel, D. Grande, A. Boss, M. Zenobi-Wong, Bioprinting Complex Cartilaginous Structures with Clinically Compliant Biomaterials, Advanced Functional Materials 25(48) (2015) 7406-7417.

[125] C.H. Lee, J.L. Cook, A. Mendelson, E.K. Moioli, H. Yao, J.J. Mao, Regeneration of the articular surface of the rabbit synovial joint by cell homing: a proof of concept study, The Lancet 376(9739) (2010) 440-448.

[126] K.-C. Hung, C.-S. Tseng, L.-G. Dai, S.-h. Hsu, Water-based polyurethane 3D printed scaffolds with controlled release function for customized cartilage tissue engineering, Biomaterials 83(Supplement C) (2016) 156-168.

[127] G. Gao, X.F. Zhang, K. Hubbell, X. Cui, NR2F2 regulates chondrogenesis of human mesenchymal stem cells in bioprinted cartilage, Biotechnol Bioeng 114(1) (2017) 208-216.

Appendix B: List of Abbreviations

^{13}C-NMR	Carbon 13 Nuclear Magnetic Resonance
^{1}H-NMR	Proton Nuclear Magnetic Resonance
2D	Bidimensional
3D	Three-dimensional
AA	Acetic acid
ACI	Autologous Chondrocyte Implantation
AFA-LIFT	Absorbing Film-Assisted Laser-Induced Forward Transfer
AFM	Atomic Force Microscopy
ALP	Alkaline phosphatase
AM	Additive manufacturing
ANOVA	Analysis of variance
ATR-FTIR	Total Reflection–Fourier Transform Infrared
B2M	Beta-2-microglobulin
bFGF	Basic fibroblast growth factor
BioLP	Biological Laser Processing
BMMSCs	Rabbit bone marrow mesenchymal stem cells
BMPs	Bone morphogenetic protein
BSA	Bovine serum albumin
BTE	Bone tissue engineering
Ch	Chitosan
ChLa	Chitosan lactate
COMP1	Cartilage oligomeric matrix protein 1
CPC	Cetylpyridinium chloride
CTE	Cartilage tissue engineering
D_2O	Deuterated water
DBB	Droplet-based Bioprinting
dH_2O	Distilled water
ddH_2O	Double distilled water

dECM	Decellurized extracellular matrix-derived
DEPT	Distortionless Enhancement Polarization Transfer
DMEM	Dulbecco's modified Eagle medium
DPBS	Dulbecco's phosphate-buffered saline
DSC	Differential Scanning Calorimetry
EA	Elemental Analysis
EBB	Extrusion-based Bioprinting
ECM	Extracellular matrix
EDX	Energy-Dispersive X-Ray Spectroscopy
ESEM	Environmental Scanning Electron Microscopy
FAP	Fibroblast activation protein
FBS	Fetal bovine serum
FDA	Food and Drug Administration
FDM	Fused Deposition Modeling
FE-SEM	Field Emission Scanning Electron Microscopy
FFF	Fused Filament Fabrication
G	Glycerol
G'	Storage modulus
G”	Loss modulus
GAG	Glycosaminoglycan
GBR	Guided bone regeneration
Gel	Gelatin
GelMA	Methacrylated gelatin/gelatin methacryloyl
GnP	Genipin
GO	Graphene oxide
GRAS	Generally Recognized as Safe
GUSB	Beta-glucuronidase
G_xPhy/GPhy	Glycerylphytate
HA	Hyaluronic acid
HAMA	Methacrylated hyaluronic acid

HAp	Hydroxyapatite
HEK	Human embryonic kidney cells
Hep	Heparin
HGF	Hepatocyte growth factor
HIF1A	Hypoxia inducible factor 1-alpha
hMSCs	Human mesenchymal stem cells
hMSCs^{luc}	Luciferase-expressing human mesenchymal stem cells
HSQC	2D Heteronuclear Single-Quantum Coherence
hUC-MSCs	Human umbilical cord mesenchymal stem cells
HUVECs	Human umbilical vein endothelial cells
ICP-OES	Inductively Coupled Plasma-Optical Emission Spectroscopy
IFN-γ	Interferon-gamma
IGFBP	Insulin-like growth factor binding protein
IGFs	Insulin-like growth factors
IL-6	Interleukin-6
IL-8	Interleukin-8
IPN	Interpenetrated polymer network
LBB	Laser-based Bioprinting
LG-DMEM	Low Glucose Dulbecco's modified Eagle medium
LIFT	Laser-Induced Forward Transfer
LVR	Linear viscoelastic region
MA	Methacrylic anhydride
MACI	Matrix-Induced Autologous Chondrogenesis Implantation
MAPLE DW	Matrix-Assisted Pulsed Laser Evaporation Direct Writing
MCP-1	Monocyte chemoattractant protein-1
M-CSF	Macrophage colony-stimulating factor
MDA	Malondialdehyde
MEW	Melt-Electrospinning Writing
MHDS	Multi-Head Deposition System
MMP	Matrix metalloproteases

mPCL	Medical grade polycaprolactone
MSCs	Mesenchymal stem cells (In Chapter 2, MSCs refers to hMSCs)
NMR	Nuclear Magnetic Resonance
OA	Osteoarthritis
oMSCs	Ovine mesenchymal stem cells
P	Phosphorus
PA	Phytic acid
PBS	Phosphate-buffered saline
PBT	Poly(butylene) terephthalate
PCL	Polycaprolactone
PCR	Polymerase Chain Reaction
PDMS	Polydimethylsiloxane
PEC	Polyelectrolyte complex
PEG	Poly(ethylene glycol)
PEGDA	Poly(ethylene glycol) diacrylate
PEGDMA	Poly(ethylene glycol) dimethacrylate
PEGT	Poly(ethylene glycol)-terephthalate
PFA	Paraformaldehyde
PI	Photoinitiator
PLA	Poly-lactic acid
PLGA	Poly(lactic-co-glycolic) acid
PLL	Polylysine
PLS-DA	Partial Least Squares-Discriminant analysis
PU	Polyurethane
PVA	Polyvinil alcohol
RGD Sequence	Arginine-Glycine-Aspartic acid peptide sequence
ROS	Reactive oxygen species
RT-qPCR	Reverse Transcription and Real-Time Quantitative Polymerase Chain Reaction
SBF	Simulated body fluid

SD	Standard deviation
SEM	Scanning Electron Microscopy
SLA	Stereolithography
SLS	Selective Laser Sintering
TE	Tissue engineering
T_g	Glass transition temperature
TGA	Thermogravimetric Analysis
TGFs	Transforming growth factors
TMX	Thermanox™ coverslip
TNF-α	Tumor necrosis factor-alpha
TPP	Tripolyphosphate
TX	Triton-X 100
UV	Ultraviolet
VEGF	Vascular endothelial growth factor
WCA	Water contact angle
α-MEM	Alpha-Minimum Essential medium
β-TCP	Beta-tricalcium phosphate

Appendix C: Journal information

The Journal information provided in this Appendix was checked in the "Journal Citation Report®" tool available in "Web of Knowledge" database.

1. **Glycerylphytate compounds with tunable ion affinity and osteogenic properties.**
   Ana Mora-Boza, María Luisa López-Donaire, Laura Saldaña, Nuria Vilaboa, Blanca Vázquez-Lasa, Julio San Román. Scientific Reports 9, Article number: 11491 (2019).
   DOI: 10.1038/s41598-019-48015-5.
   - Impact Factor 2018: 4.011.
   - Theme area: Multidisciplinary Science.
   - As co-author of this publication together with Dr. María Luisa López-Donaire, we conducted the physicochemical and biological characterization of GPhy derivatives, except the experiments of differential gene expression by reverse transcription (RT) and real-time quantitative PCR (qPCR) that were carried out in collaboration with the Hospital Universitario La Paz-IdiPAZ. I also contributed to the analysis and discussion of the results and wrote the main draft manuscript text.

2. **Glycerylphytate crosslinker as a potential osteoinductor of chitosan-based systems for guided bone regeneration.**
   Ana Mora-Boza, Luis García-Fernández, Filipe A. Barbosa, Ana Leite Oliveira, Blanca Vázquez-Lasa, Julio San Román. Carbohydrate Polymers, Volume 241, 116269 (2020)
   DOI: 10.1016/j.carbpol.2020.116269.
   - Impact Factor 2018: 6.044.
   - Theme area: Polymers Science, Applied Chemistry, Organic Chemistry.

3. **Glycerylphytate as an ionic crosslinker for 3D printing of multi-layered scaffolds with improved shape fidelity and biological features.**
   Ana Mora-Boza, Malgorzata K. Włodarczyk-Biegun, Aránzazu del Campo, Blanca Vázquez-Lasa, Julio San Román. Biomaterials Science 8: 506-516 (2020).
   DOI: 10.1039/C9BM01271K.
   - Impact Factor 2018: 5.251.
   - Theme area: Materials Science, Biomaterials.